Novel approaches in Hadron Spectroscopy

Miguel Albaladejo[a,b], Łukasz Bibrzycki[c], Sebastian M. Dawid[d,e], César Fernández-Ramírez[f,g], Sergi Gonzàlez-Solís[d,e,h], Astrid N. Hiller Blin[a], Andrew W. Jackura[a,i], Vincent Mathieu[j,k], Mikhail Mikhasenko[l,m], Victor I. Mokeev[a], Emilie Passemar[a,d,e], Alessandro Pilloni[n,o,*], Arkaitz Rodas[a,p], Jorge A. Silva-Castro[f], Wyatt A. Smith[d], Adam P. Szczepaniak[a,d,e], Daniel Winney[d,e,q,r],

(Joint Physics Analysis Center)

[a] *Theory Center and Physics Division, Thomas Jefferson National Accelerator Facility, Newport News, VA 23606, USA*
[b] *Instituto de Física Corpuscular (IFIC), Centro Mixto CSIC-Universidad de Valencia, E-46071 Valencia, Spain*
[c] *Pedagogical University of Krakow, 30-084 Kraków, Poland*
[d] *Department of Physics, Indiana University, Bloomington, IN 47405, USA*
[e] *Center for Exploration of Energy and Matter, Indiana University, Bloomington, IN 47403, USA*
[f] *Instituto de Ciencias Nucleares, Universidad Nacional Autónoma de México, Ciudad de México 04510, Mexico*
[g] *Departamento de Física Interdisciplinar, Universidad Nacional de Educación a Distancia (UNED), Madrid E-28040, Spain*
[h] *Theoretical Division, Los Alamos National Laboratory, Los Alamos, NM 87545, USA*
[i] *Department of Physics, Old Dominion University, Norfolk, VA 23529, USA*
[j] *Departament de Física Quàntica i Astrofísica and Institut de Ciències del Cosmos, Universitat de Barcelona, E-08028, Spain*
[k] *Departamento de Física Teórica, Universidad Complutense de Madrid and IPARCOS, E-28040 Madrid, Spain*
[l] *ORIGINS Excellence Cluster, 80939 Munich, Germany*
[m] *Ludwig-Maximilian University of Munich, Germany*
[n] *Dipartimento di Scienze Matematiche e Informatiche, Scienze Fisiche e Scienze della Terra, Università degli Studi di Messina, I-98122 Messina, Italy*
[o] *INFN Sezione di Catania, I-95123 Catania, Italy*
[p] *College of William & Mary, Williamsburg, VA 23187, USA*
[q] *Guangdong Provincial Key Laboratory of Nuclear Science, Institute of Quantum Matter, South China Normal University, Guangzhou 510006, China*
[r] *Guangdong-Hong Kong Joint Laboratory of Quantum Matter, Southern Nuclear Science Computing Center, South China Normal University, Guangzhou 510006, China*

Abstract

The last two decades have witnessed the discovery of a myriad of new and unexpected hadrons. The future holds more surprises for us, thanks to new-generation experiments. Understanding the signals and determining the properties of the states requires a parallel theoretical effort. To make full use of available and forthcoming data, a careful amplitude modeling is required, together with a sound treatment of the statistical uncertainties, and a systematic survey of the model dependencies. We review the contributions made by the Joint Physics Analysis Center to the field of hadron spectroscopy.

Keywords: Hadron spectroscopy, Exotic hadrons, Three-body scattering, Resonance production
Preprint numbers: LA-UR-21-31664

*Corresponding author
Email address: alessandro.pilloni@unime.it (Alessandro Pilloni)

Contents

1. Introduction

In the last two decades the quark model lore of baryons with three quarks and mesons with a quark-antiquark pair has been challenged by the many unexpected exotic hadron resonances found in high-energy experiments. Tetraquarks, pentaquarks, molecules, hybrids and glueball candidates have copiously sprung revitalizing the field of hadron spectroscopy [1–9]. Discovering and characterizing an exotic resonance is not a goal by itself but a step further to identify complete multiplets and study the emerging patterns and properties of the states. We still lack a comprehensive and consistent picture of this sector of the QCD spectrum, as many of the candidates have been identified in a single production or decay channel. Nevertheless, this research needs to be pursued as this kind of knowledge would provide insights not only into the nature of said exotics, but on the inner workings of the nonperturbative regime of QCD, given that an analytic solution of QCD in this regime will not be available in the foreseeable future.

The analyses at lepton colliders have been limited by statistics so far, although this situation is expected to improve with the forthcoming data from Belle II [10]. Moreover, the measurements usually present multibody final states, which make a challenge to perform a model-independent determination of an exotic candidate.

On the theoretical front, Lattice QCD provides the most rigorous, albeit computationally expensive, tool to calculate observables from first principles [11, 12]. However, it cannot explain the emergence of confinement and mass generation, or *why* quarks and gluons organize themselves in the observed hadron spectrum. Functional methods [13, 14] and models of QCD (as the quark model, or the holography-inspired description [15, 16]) are employed to fill in that gap.

Together with these top-down approaches, bottom-up strategies are also feasible: one can write ansätze for the amplitudes that respect the fundamental principles as much as possible, at least in a given kinematical domain, and fit to data. If the amplitude model space is large enough, the resonance properties obtained will be as unbiased as possible.

Once the theoretical modeling of the reaction amplitude has been achieved, it can be combined with a sound statistical data analysis. Moreover, one can use clustering methods to separate the physical resonances from the artifacts of the amplitude parametrizations. All these studies allow one to give a robust determination of resonances and of their properties. These analyses are computationally expensive and require high-performance computing resources, but they will become mandatory for the interpretation of present and future high-precision data.

Besides the direct analysis of resonances, studying their production rates and the underlying mechanisms offers a complementary window to determine their nature. In particular, the dual role of resonances as particles and forces implies that one can probe their properties in both regimes. These ideas motivate a program to impose duality constraints to the standard amplitude analysis.

In this review we summarize the contributions of the Joint Physics Analysis Center (JPAC) to the field. JPAC started in 2013 impulsed by Mike Pennington, originally to provide theory support to the most delicate spectroscopy analyses at Jefferson Lab (JLab). In the following years, it has become an example of collaboration between theorists and experimentalists aiming to develop amplitude analysis tools and best practices for hadron spectroscopy. The methods require complementary sets of skills in QCD, reaction theory, computer science, and experimental data analysis. The group has a strong record of interactions with experiments: JPAC members have contributed to analyses by BaBar, BESIII, CLAS, COMPASS, GlueX, and LHCb, and to several proposals of future spectroscopy experiments and facilities. The review is organized as follows. In Section 2 we discuss the physics of resonances: the generalities of the QCD spectrum, the methods, and some practical applications, both to the light and heavy sectors. Section 3 is devoted to the study of three-body physics, a quickly developing topic within Lattice QCD with important applications in the experimental analyses. The production of resonances is discussed in Section 4. A brief summary is presented in Section 5.

2. Resonance studies

2.1. The S-matrix and amplitude parameterizations

The excited spectrum of QCD is composed by states with lifetimes $\lesssim 10^{-21}$ s, which need to be reconstructed from the energy and angular dependence of their decay products. The measured rates are proportional to the modulus squared of the *reaction amplitude*, which encodes the information at the quantum level. While the reaction amplitude's angular dependence is determined by the spin of the particles involved, the energy behavior is dynamical.

The S-matrix theory traces back to the late 50s, as a possible formalism that circumvented the apparent inconsistencies of perturbative quantum field theory. The idea was that, even if no theory of strong interactions was available, the underlying S-matrix must satisfy certain properties. Lorentz invariance requires that the S-matrix elements, and therefore amplitudes, depend on particle momenta only through Mandelstam invariants. In particular, Landau argued that causality of the interaction implies that the amplitudes must be analytic functions of the invariants [17]. Similar analyticity requirements were argued by Regge, studying the Schrödinger equation for complex values of angular momentum [18]. Analyticity, together with unitarity, which stems from probability conservation, and crossing symmetry, which is proper of relativistic quantum theories, constitute the so-called S-matrix principles. The hope was that these principles were sufficient to uniquely determine the strong interaction S-matrix, once proper additional assumptions and initial conditions were given. The main additional hypothesis was the maximal analyticity principle, *i.e.* that the only singularities appearing in an amplitude are the ones required by unitarity and crossing symmetry. This was verified at all orders in perturbative field theory, but has not yet been proven to hold nonperturbatively. Chew led the so-called bootstrap program, which, using an input model for resonances exchanged in the cross-channel, allowed one to recover self-consistently the same resonances in the direct channel. The main obstacle to this was that the dispersion relations one derives suffer from Castillejo-Dalitz-Dyson (CDD) ambiguities [19], and the solution cannot be determined uniquely. In modern terms, the S-matrix principles are not specific to the strong interactions, and the information about what theory they are applied to must be encoded in these ambiguities. When QCD was established as the underlying theory of strong interactions, it was proposed that CDD poles reflect the presence of bound states of quarks, about which the S-matrix theory knows nothing *a priori*, and must be imposed from data. With the discovery of J/ψ and the triumph of quantum field theory, the bootstrap program was abandoned. Fifty years later, we still do not have a constructive solution of QCD. There is no simple connection between the interaction at the quark- and hadron-level, so there is a renewed interest in what one can learn from amplitude properties alone, and if possible, to constrain the space of feasible solutions rather than to look for a unique one. The new program is thus to postulate *ansätze* for the amplitudes that depend on a finite number of parameters and fit them to data. Ideally, one requires the amplitudes to fulfill the constraints given by the S-matrix principles, to obtain physical results as sound as possible. It should be stressed, however, that implementing all the constraints simultaneously is extremely difficult, and the problem has to be approached on a case-by-case basis, in order to enforce the constraints that are most relevant for the physics at hand.

We review here the basics of $\mathbf{2} \to \mathbf{2}$ scattering and $\mathbf{1} \to \mathbf{3}$ decay, that will be used in the rest of the paper. Consider a $\mathbf{2} \to \mathbf{2}$ scattering process of scalar particles $a(p_1)\, b(p_2) \to c(p_3)\, d(p_4)$, and and the $\mathbf{1} \to \mathbf{3}$ decay $a(p_1) \to b(p_2)\, c(p_3)\, d(p_4)$ one obtains by crossing particle b, as depicted in Figure 1. The Mandelstam variables, for scattering, are defined through

$$s = (p_1 + p_2)^2 = (p_3 + p_4)^2 \ , \tag{1a}$$

$$t = (p_1 - p_3)^2 = (p_2 - p_4)^2 \ , \tag{1b}$$

$$u = (p_1 - p_4)^2 = (p_2 - p_3)^2 \ , \tag{1c}$$

$$s + t + u = m_1^2 + m_2^2 + m_3^3 + m_4^2 \equiv \Sigma \ , \tag{1d}$$

where for the $\mathbf{1} \to \mathbf{3}$ decay, $p_2 \to -p_2$. In order to describe the s-channel center of mass frame it is convenient

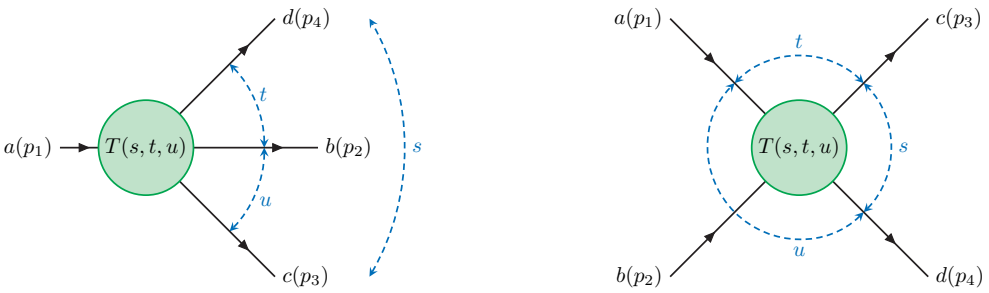

Figure 1: (left) Representation of the decay $a(p_1) \to b(p_2)\, c(p_3)\, d(p_4)$ and the kinematical variables involved. (right) Representation of the scattering process $a(p_1)\, b(p_2) \to c(p_3)\, d(p_4)$ and its kinematical variables.

to introduce the initial- and final-state 3-momenta,

$$p(s) = \frac{\lambda^{\frac{1}{2}}(s, m_1^2, m_2^2)}{2\sqrt{s}} \qquad\qquad q(s) = \frac{\lambda^{\frac{1}{2}}(s, m_3^2, m_4^2)}{2\sqrt{s}} \ , \tag{2}$$

where $\lambda(x,y,z) = x^2 + y^2 + z^2 - 2(x\,y + y\,z + z\,x)$ is the triangle or Källén function [20]. The four-momenta in the s-channel center-of-mass frame read

$$p_1 = \left(\frac{s + m_1^2 - m_2^2}{2\sqrt{s}}, p(s)\hat{z}\right), \qquad p_3 = \left(\frac{s + m_3^2 - m_4^2}{2\sqrt{s}}, q(s)\hat{n}\right), \tag{3a}$$

$$p_2 = \left(\frac{s + m_2^2 - m_1^2}{2\sqrt{s}}, -p(s)\hat{z}\right), \qquad p_4 = \left(\frac{s + m_4^2 - m_3^2}{2\sqrt{s}}, -q(s)\hat{n}\right). \tag{3b}$$

The cosine of the scattering angle z_s is defined by $\hat{z} \cdot \hat{n} \equiv z_s$. It is given as a function of the Mandelstam variables as

$$z_s = \frac{s(t-u) + \left(m_1^2 - m_2^2\right)\left(m_3^2 - m_4^2\right)}{4s\, p(s)\, q(s)}. \tag{4}$$

Similar expressions can be obtained for the scattering angle z_t and z_u of the crossed processes in the respective center-of-mass frame. We will omit its $s-$, $t-$, and $u-$dependence when no ambiguity can arise. For simplicity, we consider the spinless case. The customary partial wave expansion of the amplitude $T(s,t,u)$ is

$$T(s,t,u) = \sum_{\ell=0}^{\infty} (2\ell+1) P_\ell(z_s)\, t_\ell(s) \ , \tag{5}$$

where $P_\ell(z_s)$ are the Legendre polynomials, $t_\ell(s)$ are the partial waves of angular momentum ℓ, and z_s is the cosine of the scattering angle in the s-channel center of mass system. Note that for symmetry and compactness reasons we have left the explicit u-dependence in Eq. (5), although the sum of the three Mandelstam variables is constrained, and as a result the full amplitude $T(s,t,u)$ depends only on two of them. The partial waves $t_\ell(s)$ can be obtained from the full amplitude by inversion of the aforementioned equation

$$t_\ell(s) = \frac{1}{2}\int_{-1}^{+1} \mathrm{d}z\, P_\ell(z)\, T(s, t(s,z), u(s,z)) \ . \tag{6}$$

The physics of the unstable states we are interested in is encoded in these partial waves. A resonance of spin ℓ appears in $t_\ell(s)$ as a pole located at complex values of energy, the real and imaginary parts being the mass and half-width of the resonance, respectively. It is thus necessary to consider amplitudes that can be

analytically continued from the physical real axis—where data exist—to the complex plane. Such partial waves diagonalize unitarity,

$$\mathrm{Im}\, t_\ell(s) = t_\ell(s)\, \rho(s)\, t_\ell(s)^\dagger\,, \tag{7}$$

where $\rho(s)_{ij} \propto \delta_{ij}\, q_j(s)/\sqrt{s}$ is the diagonal matrix of the phase space of all possible two-body channels. Unitarity provides us with the means to continue our partial waves into the next continuous Riemann sheets, where resonances live. The existence of a non-zero imaginary part due to this principle produces a multi-valued complex function, which has a physical branch cut produced by s-channel unitarity. A parametrization that fulfills this principle is the customary K-matrix formalism [21, 22],

$$t_\ell(s) = K_\ell(s)\, \left[1 - i\rho(s) K_\ell(s)\right]^{-1}\,, \tag{8}$$

where $K_\ell(s)$ is a real symmetric matrix. The simplest parametrizations for $K_\ell^{ij}(s) = g^i g^j/(M^2 - s)$ contain the "bare" information about the resonance: formally Eq. (8) can be expanded as

$$t_\ell(s) \simeq K_\ell(s) + K_\ell(s) i\rho(s) K_\ell(s) + K_\ell(s) i\rho(s) K_\ell(s) i\rho(s) K_\ell(s) + \dots\,. \tag{9}$$

In this limit, the resonance basically behaves like a quasi-stable particle of mass M propagated between different initial (i) and final (j) states, and acquires a width due to the couplings with the continuum. However, the physical objects are the poles of $t_\ell(s)$, and not of $K_\ell(s)$. As we will see in the following sections there is no one-to-one correspondence between the two, and so this interpretation of K must be taken with a grain of salt.

Finally, in order to describe the data by means of analytic functions, we will make use of the *Chew-Madelstam formalism* [23], for which the ordinary phase space $\rho(s)$ is replaced by its dispersive form.

In addition to right hand cuts produced by unitarity, the partial waves can exhibit more complicated structures, like left-hand cuts as a result of crossing symmetry and unitarity in the crossed channels (we refer the reader to [24] for a reference textbook on the topic). The N/D formalism [23, 25–27] makes the splitting between these left and right hand cuts explicit. The partial wave can be recast as

$$t_\ell(s) = N_\ell(s)\, D_\ell^{-1}(s), \tag{10}$$

which is designed to separate the constraints coming from unitarity in the direct (D) and cross-channels (N). The latter can be often interpreted in terms of the intensity of the produced resonances. Although the two functions should be related through complicated dispersive equations, in practice we will use a simple functional form for N. The main reason is that we mostly study energy regions far from crossed channel cuts.

When looking at the final state of $\mathbf{1} \to \mathbf{3}$ decay products, one must consider that there are several processes that could produce a local enhancement in the cross section. Besides poles, if the kinematics overlap, a resonance of the crossed channel could rescatter into these final products, enhancing the cross section and mimicking a resonance in the direct channel. At leading order these rescattering processes are called triangle singularities, first by Landau [17]. These singularities appear in the integrand of the corresponding Feynman diagram and 'pinch' the integration domain, producing a logarithmic branch point as a result. The implications fro phenomenology have been widely discussed in the literature, see for example [7]. We will discuss examples of these processes in Sections 2.5.1 and 2.5.3.

We recall that more complications arise from particle spin, even though they are purely kinematic in nature. For example, consider a $\mathbf{1} \to \mathbf{3}$ decay of particles with spin. The Legendre polynomials discussed above will be promoted to Wigner D-matrices. Writing helicity amplitudes for the three two-body subchannel in the different resonance frames requires boosts that do not conserve the helicity of the various particles. To add the various contributions coherently, one has to take into account the so-called Wigner rotations (crossing matrices), associated with precession of particle spins when moving from one frame to another. There is a recent interest in this, motivated by the fact that the practical implementation of such rotations is highly nontrivial [28, 29]. A proposal to write the $\mathbf{1} \to \mathbf{3}$ reaction as a sum over subchannels in the same reaction plane, and then rotate the whole sum together, was given in [30], and is referred to as "Dalitz plot

decomposition". In this way, the dependence of the Wigner rotations on the relevant Mandelstam variables is apparent. Explicitly, the amplitude factorizes in

$$T^{\Lambda}_{\lambda_1,\lambda_2,\lambda_3} = \sum_{\lambda_1} D^{j_4 *}_{\Lambda,\lambda_4}(\alpha,\beta,\gamma)\; A_{\lambda_4,\lambda_1,\lambda_2,\lambda_3}\,, \tag{11}$$

where $D^{j_1 *}_{\Lambda,\lambda_1}(\alpha,\beta,\gamma)$ is the Wigner D-matrix that takes into account the alignment of the reaction plane in the laboratory frame in terms of the Euler angles α, β, γ, and

$$A_{\lambda_4,\lambda_1,\lambda_2,\lambda_3}(s,t,u) = \sum_j A^{(12),j}_{\lambda_4,\lambda_1,\lambda_2,\lambda_3}(s,t,u) + \sum_j A^{(23),j}_{\lambda_4,\lambda_1,\lambda_2,\lambda_3}(s,t,u) + \sum_j A^{(31),j}_{\lambda_4,\lambda_1,\lambda_2,\lambda_3}(s,t,u)\,. \tag{12}$$

This decomposition looks like a partial wave expansion, but is performed over all the two-body subchannels, and is known as *isobar decomposition*. This will be discussed further in Section 3.1. The isobar amplitude $A^{(xy),j}_{\lambda_4,\lambda_1,\lambda_2,\lambda_3}$ contains resonances in the (xy)-channel of spin j, with particle z as spectator. The isobars can be aligned with additional rotations,

$$\begin{aligned} A^{(xy),j}_{\lambda_4,\lambda_1,\lambda_2,\lambda_3} = \sum_{\lambda'_4,\lambda'_1,\lambda'_2,\lambda'_3} & h^{(z),j}_{\lambda'_z+\lambda'_4,\lambda'_z}(\sigma_{xy})\,(-1)^{j_z-\lambda'_{z'}}\, d^{j}_{\lambda'_4+\lambda'_z,\lambda'_x-\lambda'_y}(\theta_{xy})\, h^{(xy),j}_{\lambda'_x,\lambda'_y}(\sigma_{xy})\,(-1)^{j_y-\lambda'_y} \\ & \times d^{j_4}_{\lambda_4,\lambda'_4}(\zeta^4_{z(r_4)})\, d^{j_1}_{\lambda'_1,\lambda_1}(\zeta^1_{z(r_1)})\, d^{j_2}_{\lambda'_2,\lambda_2}(\zeta^2_{z(r_2)})\, d^{j_3}_{\lambda'_3,\lambda_3}(\zeta^3_{z(r_3)})\,, \end{aligned} \tag{13}$$

where index r indicates the frame where helicity is defined. The angles $\zeta_{z(r)}$ depend on s,t,u and vanish when $r=z$. The explicit expressions for nontrivial cases are found in [30]. The functions $h^{(z),j}_{\lambda'_z+\lambda'_4,\lambda'_z}$, and $h^{(xy),j}_{\lambda'_x,\lambda'_y}$ depend on a single Mandelstam variable $\sigma_{(xy)} = (p_x+p_y)^2 = \{s,t,u\}$. Here we have make explicit the phases $(-1)^{j-\lambda}$ due to the Jacob-Wick particle-2 convention, that leads to a natural matching with the LS decomposition [30, 31]. A practical method to validate the spin alignment is suggested in Ref. [28].

Another consequence of spin is the presence of kinematical singularities, that must be removed before studying dispersion relations. One can argue what are the simplest factors needed to control these singularities, and what is the minimal energy dependence that one therefore expects. This was done in the context of $\bar{B}^0 \to J/\psi\pi^+K^-$ and $\Lambda_b^0 \to J/\psi p K^-$ in [32, 33].

As a final remark, when dealing with all these different reactions, exploring a number of possible parametrizations minimizes the model dependence. It enables us to assess sound systematic uncertainties to our results. Furthermore, if combined with a proper statistical analysis allows us to distinguish the poles corresponding to physical resonances from model artifacts. This will be shown in detail in Section 2.2.3. Hence, we will adopt this approach for our analyses in this review.

2.2. Statistics tools

The determination of the existence of each resonance and its properties relies on fitting experimental data accompanied by an uncertainty analysis. We review the general strategy and some of the techniques employed by JPAC. This is particularly relevant for pole extraction, where the error propagation through standard means is complicated. In doing so we mostly take a frequentist point of view [34, 35].

2.2.1. Fitting data

The standard approach to fitting data is through maximizing the likelihood,

$$L(\{\theta\}|\{y\}) = \prod_i^N P_i(y_i|\theta_i)\,, \tag{14}$$

where $P_i(y_i|\theta_i)$ stands for the probability density function at fixed parameter θ_i and y_i is the experimental datapoint. If chosen as Gaussian for binned data,

$$P_i(y_i|\theta_i) = \frac{1}{\sqrt{2\pi}\sigma_i}\exp\left[-\frac{1}{2}\left(\frac{f_i(\{\theta\})-y_i}{\sigma_i}\right)^2\right]\,, \tag{15}$$

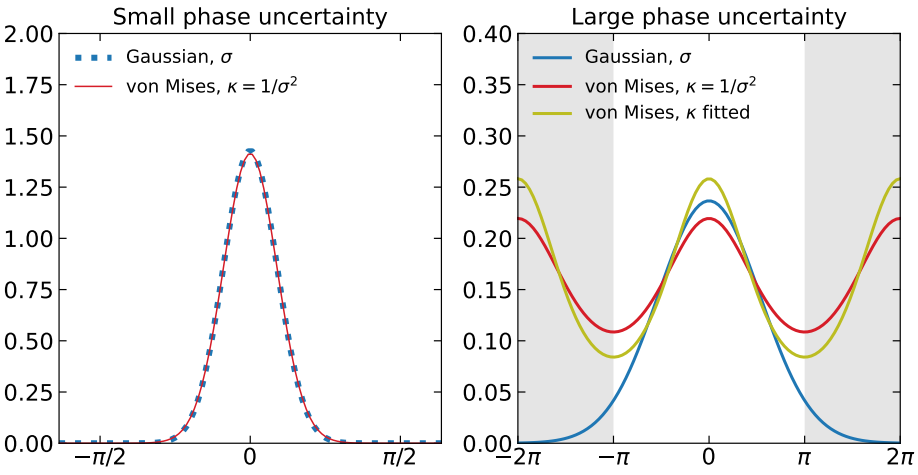

Figure 2: Comparison between the Gaussian and von Mises distributions for small (top) and large (bottom) phase shift uncertainties, centered in $\mu = 0$. In the upper plot the Gaussian distribution has $\sigma = 0.28$ (dotted blue), and von Mises has $\kappa = 1/\sigma^2 = 12.82$ (solid red). In the lower plot the Gaussian has $\sigma = 1.69$ (solid blue), von Mises has $\kappa = 1/\sigma^2 = 0.35$ (solid red), and another von Mises has $\kappa = 0.56$ (solid gold) obtained by fitting to the Gaussian distribution. The grey bands hide the region outside the $[-\pi, \pi]$ range. Figures from [36].

where y_i is the binned experimental datapoint value and σ_i its uncertainty. $f_i(\{\theta\})$ is the objective function to be fitted. This expression assumes each bin to be statistically independent, as customarily done. Maximizing the likelihood is equivalent to minimizing the χ^2 function,

$$\chi^2(\{\theta\}) = \sum_i^N \left(\frac{f_i(\{\theta\}) - y_i}{\sigma_i} \right)^2 . \tag{16}$$

The choice of a Gaussian distribution is standard in many physical problems, and is adequate if the experimental uncertainties are of statistical origin. However, there are situations where other probability densities should be chosen. For example, in the case that the y observable is positively defined (*e.g.* an intensity) and, because of the values of y_i and σ_i there is a significant overlap with unphysical negative values, a Gamma distribution is more adequate,

$$H(y_i|\theta_i, \sigma_i) = \left(\frac{y_i \theta_i}{\sigma_i^2} \right)^{\frac{\theta_i^2}{\sigma_i^2}} \frac{\exp\left(-y_i\theta_i/\sigma_i^2\right)}{\theta_i \Gamma\left(y_i^2/\sigma_i^2\right)} . \tag{17}$$

This was used for example in [37, 38]. Another relevant case happens when the observable is periodic, for example a relative phase. A simple solution is to redefine the distance to take the periodicity into account,

$$\chi^2(\{\theta\}) = \sum_i^N \min_{k\in\mathbb{Z}} \left(\frac{f_i(\{\theta\}) - y_i - 2k\pi}{\sigma_i} \right)^2 , \tag{18}$$

as done in [38, 39]. However, using a von Mises distribution is more rigorous,

$$f(y_i|\theta_i, \kappa_i) = \frac{1}{2\pi I_0(\kappa_i)} \exp\left[\kappa_i \cos\left(f_i(\{\theta\}) - y_i\right)\right] , \tag{19}$$

where $I_0(\kappa_i)$ is the modified Bessel function. The concentration parameter κ_i is the reciprocal measurement of the dispersion. If the uncertainty is small, the Gaussian distribution with σ_i equal to the experimental uncertainty is almost equal to the von Mises distribution with $\kappa_i = 1/\sigma_i^2$. For larger values of the uncertainty,

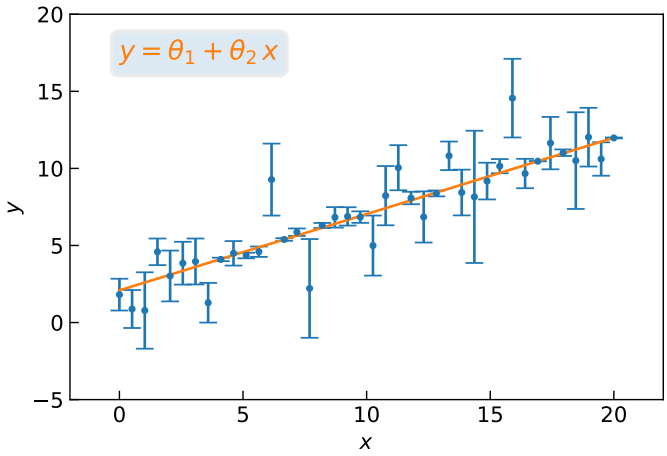

Figure 3: Datapoints and BFF for the linear fit example.

Gaussian and the von Mises distribution with $\kappa_i = 1/\sigma_i^2$ are quite different, and it is better to refit the concentration parameter to the (y_i, σ_i) Gaussian distribution as done in [36] and shown in Figure 2. Of course, the χ^2 is no longer the correct estimator to maximize the likelihood. The best strategy is to compute the logarithm of the likelihood from Eq. (14) using the appropriate distributions, and maximize the obtained function. A special situation happens when we need to fix the normalization in a fit to events. In that case we can minimize the extended negative loglikelihood function $\mathcal{L}$ [40–42],

$$\mathcal{L}(\{\theta\}|\{y\}) = \sum_i^N \left[f_i(\{\theta\}) - y_i \log f_i(\{\theta\}) \right] , \tag{20}$$

as was employed in [36]. As normalization correlates all the datapoints, one has to be careful on how the D'Agostini bias might impact the fit [43].

The minimization is usually performed using a gradient-based optimization method such as MINUIT [44] or Levenberg-Marquardt [45, 46]. Unfortunately, multiple local minima can appear, preventing the optimizer from finding the physically sensible minimum. The typical strategy is to try many initial values for the parameters at the beginning of the optimization process and then compare all the minima obtained. Another approach is to explore the parameter space using a genetic algorithm [47–49], and then improve the result with a gradient-based method. Knowing about the existence of nearby local minima is necessary to have a better interpretation of the results. Also, a good set of initial parameters is required to apply the bootstrap method detailed below.

2.2.2. Uncertainties estimation with bootstrap

The fit needs to be accompanied by an error analysis, as well as a method to propagate the uncertainties from the fit parameters to the physical observables, whose relation might highly nontrivial. A standard approach is to use the covariance matrix obtained from the Hessian of the likelihood as given by, for example, MIGRAD [44]. This relies on the parabolic approximation of the likelihood function around the minimum, which always provides symmetric uncertainties for the fitted parameters. The main advantage is that this is computationally cheap, and in many circumstances the approximation is good enough. For more refined determinations of the uncertainties, the high-energy physics community usually relies on MINOS, which samples the likelihood in the neighbourhood of the minimum and is able to provide asymmetric uncertainties for the fit parameters. However, propagating errors from parameters to observables using MINOS is unattainable for nontrivial functions, as for pole extractions. To overcome this, we can use the method of bootstrapping, a Monte Carlo based method [50, 51]. Although computationally expensive, its results are robust and rigorous.

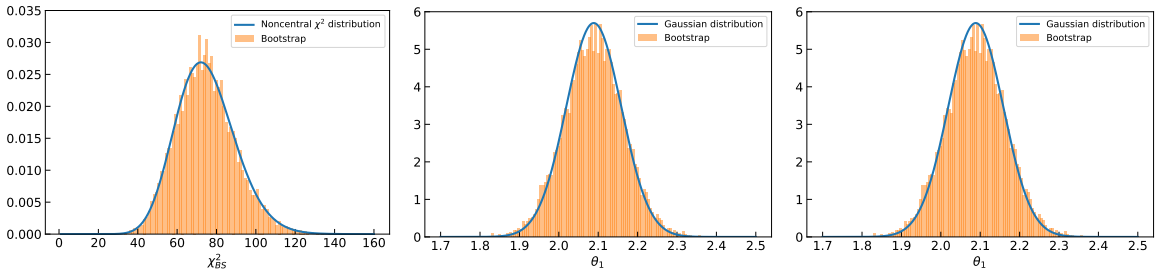

Figure 4: (left) Theoretical noncentral χ^2 distribution *vs.* the histogram from the bootstrap fits for $\chi^2_{\rm BS}$. (center) Theoretical Gaussian distribution *vs.* the histogram from the bootstrap fits for θ_1 parameter. (right) Theoretical Gaussian distribution *vs.* the histogram from the bootstrap fits for θ_2 parameter.

For pedagogical reasons we explain the technique through a linear fit example, and compare to the results of MIGRAD and MINOS.[1] We consider a model $y = 0.5 + 2\,x$. We generate $N = 40$ datapoints uniformly in $x \in [0, 20]$, and for each of them generate an uncertainty Δy_i extracted from a Gaussian distribution with zero mean and $\sigma = 1.5$. Then, we compute the noise $\nu_i = \hat{\nu} \times \Delta y_i$ where $\hat{\nu}$ is generated from a Normal distribution. Finally, the datapoint is $y_i = 0.5 + 2\,x_i + \nu_i$ with associated error Δy_i. Figure 3 shows the computed datapoints. We use MINUIT χ^2 minimization to fit these data to a linear model $y = \theta_1 + \theta_2\,x$. The best fit found (BFF) has $\chi^2_{\rm BFF}/{\rm dof} = 36.75/\,(40-2) = 0.967$, $\theta_1 = 0.495 \pm 0.004$, and $\theta_2 = 2.09 \pm 0.07$. The error is computed using MIGRAD, but MINOS gets the same results, as the likelihood is symmetric by construction.

We repeat the fit with bootstrap. We find the best fit by minimizing the χ^2. We can resample each datapoint, generating a new one from a Gaussian distribution having by mean the original y_i value and $\sigma_i = \Delta y_i$. In this way we generate a new pseudodata set $\{\tilde{y}\}$ that is compatible with the experimental measurement. The uncertainties of the new pseudodata set are fixed to original ones $\{\Delta y\}$. The new pseudodata set can be refitted with the original model, obtaining a set of parameters $\{\theta\}_1$ and the associated $\left[\chi^2_{\rm BS}\right]_1$. Then, we repeat the procedure until acquiring the desired statistical significance. We call each fit to one pseudodata set a *bootstrap* (BS) *fit*. The results of the process are the histograms of the parameters $\{\theta\}$ and the $\{\chi^2_{\rm BS}\}$. Since Δy_i is assumed Gaussian, the $\{\chi^2_{\rm BS}\}$ follow a noncentral χ^2 distribution,

$$\chi^2_{nc}(x|k,\lambda) = \frac{1}{2}\exp\left[-\frac{\lambda+x}{2}\right]\left(\frac{x}{\lambda}\right)^{(k-2)/4} I_{(k-2)/2}\left(\sqrt{\lambda x}\right)\,, \tag{21}$$

where $\lambda = \chi^2_{\rm BFF}$, k the number of degrees of freedom. Figure 4 shows the comparison between Eq. (21) and the $\{\chi^2_{\rm BS}\}$ distribution from the $M = 10^4$ BS fits, which approximately peaks at $\sim 2\,\chi^2_{\rm BFF}$. Figure 4 also shows the $\{\theta_1\}$ and $\{\theta_2\}$ histograms, which are Gaussian and give $\theta_1 = 0.495 \pm 0.004$, and $\theta_2 = 2.09 \pm 0.07$, same as MIGRAD. The expected value of the parameters is computed as the mean of the $\{\theta_1\}$ and $\{\theta_2\}$ histograms, and the 1σ uncertainties (68% confidence level) from the 16th and 84th quantiles. Any desired confidence level can be computed selecting the appropriate quantiles, given that enough BS fits are computed, since the accuracy scales as $1/\sqrt{M}$. For example, if $M = 10^3$ BS fits are performed, the accuracy of our results would be 3.2%; not good enough to claim a 2σ (95.5%) confidence level.

The covariance and correlation matrices are straightforward to compute from the BS fits,

$$\mathrm{cov}(\theta_i,\theta_j) = \sum_{k=1}^{M}\frac{\left([\theta_i]_k - \langle\theta_i\rangle\right)\left([\theta_j]_k - \langle\theta_j\rangle\right)}{M}\,;\;\mathrm{corr}(\theta_i,\theta_j) = \frac{\mathrm{cov}(\theta_i,\theta_j)}{\sqrt{\mathrm{cov}(\theta_i,\theta_i)}\sqrt{\mathrm{cov}(\theta_j,\theta_j)}}\,. \tag{22}$$

[1] The Python code for this example can be downloaded from [52].

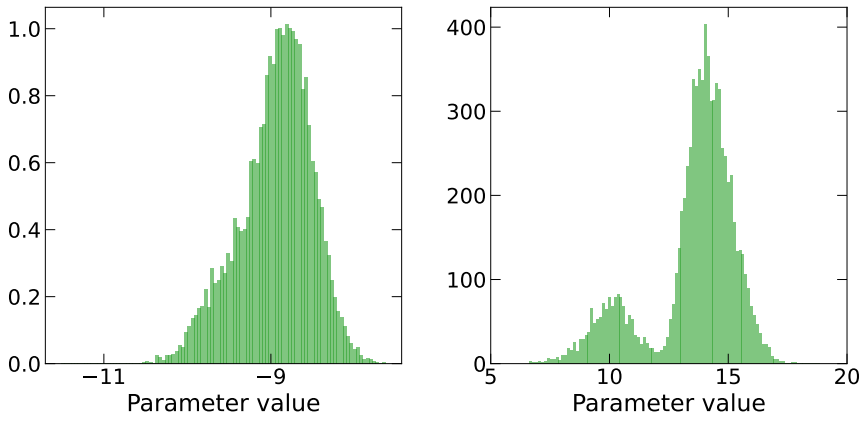

Figure 5: Examples of a realistic case from [36] where one parameter histogram is well behaved (left) and follows a Gaussian-like behavior while another has two nearby minima (right).

The covariance and correlation matrices are very similar to the ones obtained with MIGRAD.

$$\mathrm{cov}(\theta_0,\theta_1)_{\mathrm{Hessian}} = \begin{bmatrix} 55.7 & -3.27 \\ -3.27 & 0.19 \end{bmatrix} \times 10^{-4}\,; \qquad \mathrm{corr}(\theta_0,\theta_1)_{\mathrm{Hessian}} = \begin{bmatrix} 1 & -0.996 \\ -0.0996 & 1 \end{bmatrix};$$

$$\mathrm{cov}(\theta_0,\theta_1)_{\mathrm{Bootstrap}} = \begin{bmatrix} 54.8 & -3.22 \\ -3.22 & 0.19 \end{bmatrix} \times 10^{-4}\,; \qquad \mathrm{corr}(\theta_0,\theta_1)_{\mathrm{Bootstrap}} = \begin{bmatrix} 1 & -0.996 \\ -0.0996 & 1 \end{bmatrix};$$

as expected in this simple example. Hence, we showed how bootstrap and a standard Hessian method are equivalent, given enough BS fits are computed.

The calculation of any observable $g(\{\theta\})$ and the propagation of the uncertainties is straightforward. For each set of parameters $[\{\theta\}]_i$ obtained from a BS fit, we compute the observable $g_i = g([\{\theta\}]_i)$, obtaining M values of g_i. From the histogram we can compute the expected value $\langle g \rangle$ and the uncertainties as done for the parameters $\{\theta\}$. This procedure is independent of the functional form of g and fully propagates the uncertainties in the parameters and their correlations to the derived observable.

For simplicity we explained the method using data from a linear model who are statistically independent and whose uncertainties follow Gaussian distributions. Hence, there was only one minimum for the BFF and the histograms of $\{\theta\}$ and the $\{\chi^2_{\mathrm{BS}}\}$ were Gaussian and noncentral χ^2-distributed, respectively. However, extending the method to any other distribution is straightforward, both at the level of the likelihood function and at the generation of the pseudodata sets. If the experimental datapoints are correlated, one can generate the pseudodata according to the correlation matrix. Similarly, one can incorporate correlated errors, as systematic uncertainties. The only disadvantage is that systematic and statistical uncertainties propagate together, so they cannot be disentangled in the observables.

If the BFF has a local minimum closeby, it is possible for the bootstrap to jump from the global minimum to the local one. In that case, the parameter distribution can follow a two peak structure (see Figure 5) and the expected value, the uncertainties and any other computed quantities have be taken with a grain of salt.

Bootstrap results can be exploited to compare two models of, apparently, similar quality in terms of χ^2_{BFF} and $\{\chi^2_{\mathrm{BS}}\}$ distribution. Given the two models, for each pseudodata set we can fit both and compare them for each BS fit. If one model systematically outperforms the other, it is a signature of better quality. This was exploited in [36] for the case of extended negative loglikelihood [Eq. (20)] fits to $\eta^{(\prime)}\pi$ data from COMPASS collaboration. The results for $\eta\pi$ are shown in Figure 6, where two models with the same amount of parameters provided similar best likelihoods and likelihood distributions, but if bootstrap fits are individually compared, a systematic pattern emerges favoring a particular model.

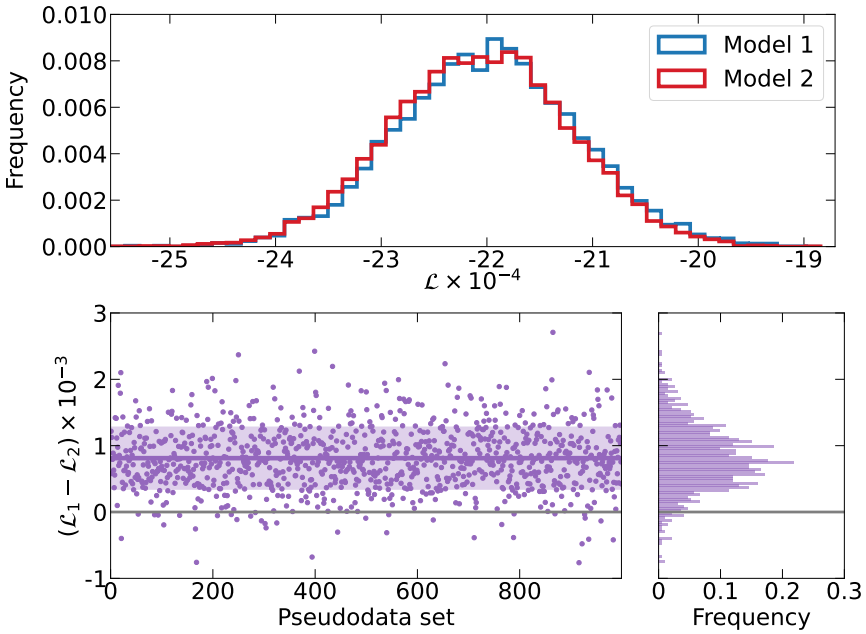

Figure 6: Example from [36]. (top plot) Extended negative log-likelihood for two models. (bottom row) Difference in negative log-likelihood at every one of the first 1000 pesudodata sets (left) and frequency for the 10^4 computed pseudodata sets (right). The purple line represents the mean, the band the 68% confidence level. The distribution sits mostly above the zero difference (gray line).

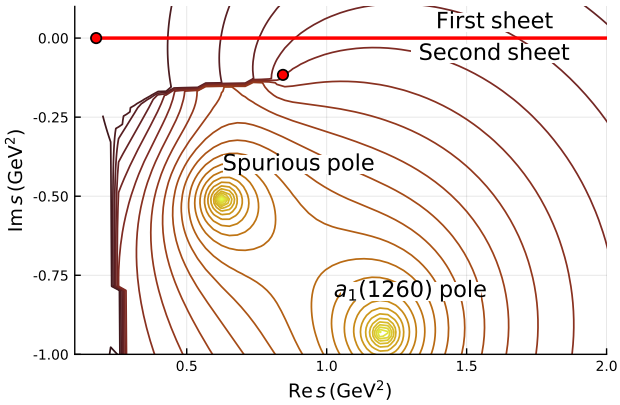

Figure 7: Example of a spurious pole in the pole extraction of the $a_1(1260)$ resonance form the $\tau^- \to \pi^-\pi^+\pi^-\nu_\tau$ decay. The brown curve represents the ρ cut. Figure from [53].

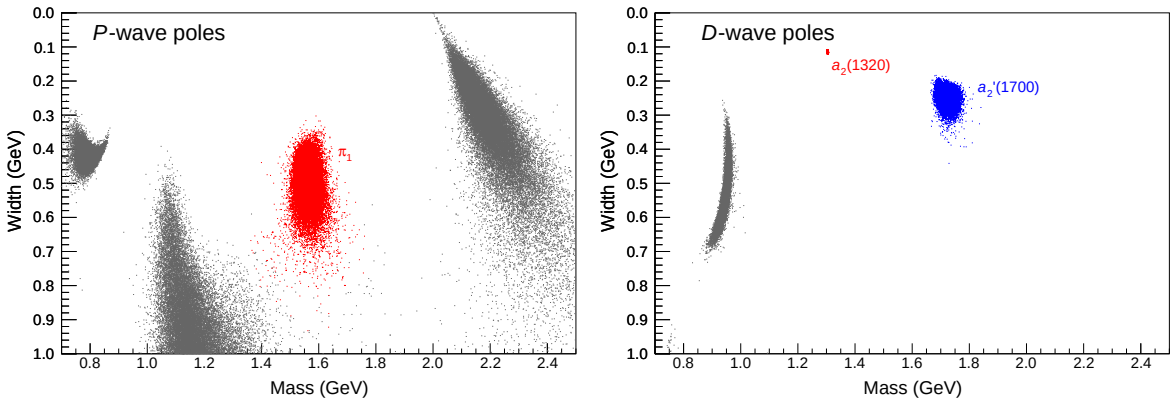

Figure 8: Poles clusters generated by bootstrap for the P- (left) and D-waves (right). The π_1, $a_2(1320)$, and $a_2'(1700)$ resonances are labeled.

2.2.3. Physical and spurious poles

Once the data have been fitted and the poles extracted, the question of whether the found poles are truly physical resonances or artifacts of the parametrization looms ahead of any physical interpretation. This is because: (a) we fit a given energy range and poles can appear outside the fitting region; (b) data have statistical noise, so an apparent signal can be compatible with statistical fluctuations; and (c) the amplitude models are incomplete, *i.e.* they do not encompass the full physics of QCD, and sometimes are unwillingly biased. If data are cut in a certain energy range, poles outside or at the edge of the fitting region can allow the model to reproduce the behavior of the data at the edge, acting as an effective background, and their physical meaning is highly debatable. Other poles can be forced by features of the model. For example, the unitarization of left-hand singularities can create poles in the unphysical Riemann sheets close to threshold. Without a careful examination of the model, of the data and of the uncertainites, these poles can be mistakenly hailed as new resonances, when they are not really demanded by the data. Figure 7 shows an example of a spurious pole in the extraction of the $a_1(1260)$ resonance from the $\tau^- \to \pi^-\pi^+\pi^-\nu_\tau$ decay [54], discussed in Section 3.3.1. In this case, the model is simple enough that its appearance can be tracked down to a second-sheet unphysical singularity generated by the phase space function.

We have found that the error analysis based on the bootstrap method, besides providing a proper uncertainty analysis, often helps discerning true resonant poles from those which are artifacts of the parametrization or due to statistical noise, *aka* spurious poles, reducing the possibility of signal misinterpretation. Moreover, it also helps to assess the reliability of the extracted pole, *i.e.* if it truly represents a resonance or it is an spurious effect. As an example, we describe an actual physics example from the analysis of COMPASS $\eta^{(\prime)}\pi$ P- and D-waves in the resonance region [39], that we will discuss in detail in Section 2.4.2. The BFF in this analysis has four poles in the P-wave and three in the D-wave. Figure 8 shows the pole positions of the $\mathcal{O}(10^5)$ BS fits. The three clusters that appear in the D-wave are associated to each one of the three poles found in the BFF. The two higher mass clusters are Gaussian, and stable against statistical fluctuations. However, the lowest mass cluster has a nongaussian shape, with the mass close to threshold and the width as deep as 1 GeV. Given their position, it is intuitive that these poles cannot have a direct influence on data, nevertheless the cluster is relatively narrow and well accumulated, as if the data were actually constraining it. The reason is that such pole is actually built in in the model, for similar reasons to what was discussed above. This pole is, therefore, not demanded by the data. For the single channel analysis in [55] we could track down its origin by turning off the imaginary part of the amplitude we find out it arises from a left-hand pole in the model that mimics the effects due to the left-hand cut. Hence, it is an artifact consequence of the model.

In the P-wave we find four clusters. Only the one labeled as π_1 has the correct behavior and is the one we associate to a exotic resonance. We deem the other three spurious. The heavier cluster is at higher masses than the fitted data (2 GeV). This pole right above the fitted region, and the model tries to overfit

the last few data points by placing a pole. When the bootstrap is performed, the pole position is completely unstable, showing its unphysical origin as an artifact of the data selection. The lowest mass one is equivalent to the left-hand pole found in the D-wave, as its mass is very close to threshold. The remaining cluster at $\sim 1.2\,\text{GeV}$, that did not appear in the BFF, is unstable against bootstrap, as it often escapes deep in the complex plane, so it is associated to the statistical fluctuations. However, it could have happened that the BFF found such a pole, say at a width of 500 MeV, and could have misidentified as a new state. This type of analyses allows us to distinguish such cases from the physical ones. Additional examples can be found in Section 2.4.1 and Ref. [38] for the J/ψ radiative decays.

2.3. Machine Learning for hadron spectroscopy

There are two factors which have allowed Machine Learning (ML) to thrive in recent years: The first one is an enormous progress in hardware, related mostly to the use of massive parallel GPU processors [56]. This development makes it significantly easier to tackle problems involving "big data". The second factor is related to rapid and multifaceted development of architectures, algorithms and computational techniques like convolutional neural networks [57], rectified linear unit (ReLU) [58, 59], improved stochastic gradient optimization [60] or batch normalization [61]. ML in nuclear and high-energy physics has already quite a long history: Applications to experimental studies include event selection [62–64], jet classification [65, 66], track reconstruction [67, 68], and event generation [69, 70]. On the theory front, ML has been extensively used for fitting [47, 48, 71–75] and to provide model-independent parametrizations of structure and spectral functions [72, 73, 76, 77], as well as of solutions of Schrödinger equations [74, 75]. Several reviews cover these applications extensively [78, 79].

In hadron spectroscopy, ML methods have not been explored so thoroughly. Among the many techniques available, we focus on classifiers, which are a kind of discriminative models. These are designed to capture the differences between groups of data (*e.g.* canonical "cat *vs.* dog" classification) and estimate a conditional probability of the output to belong to a class given the input. Recently, the use of classifiers has been proposed as a method to identify the nature of a given hadron state [80–83]. The idea is that different natures of the states reflect into different lineshapes, and ML can be used to discriminate the most favored interpretation by data. In particular, this has been applied to the $P_c(4312)$ pentaquark candidate in [83]: since the peak appears very close to a two-body threshold, the amplitude can be expanded model-independently, and the resulting simple form permits a direct characterization of the P_c. Details about the physics that determines the different classes will be presented in Section 2.5.2, while here we focus on the methodology.

Formally, the classification problem can be stated as seeking the function f which maps the space of input data $x \in X^N$ (*aka* feature vectors) into a set of target classes $t \in T$. [2] Here the feature vectors consist of values of intensity in bins of energy, and labels were four possible interpretations of the $P_c(4312)$. The problem hides in the choice of f [84–86]. In what follows we focus on the simplest version of a neural network classifier, *i.e.* a dense feed-forward network in which the trained parameters are encoded in weights of the network node (neuron) connections. The typical architecture is depicted in Figure 9. The values read in the output layer are obtained by passing the values of the feature vectors through consecutive hidden layers. For this process to be more than mere matrix multiplication (thus being able to model arbitrary nonlinear input-output dependence), the output value of each neuron is obtained by subjecting the weighted values from all nodes of the preceding layer to an activation function σ. Thus the output value of the m-th neuron of the n-th layer can be expressed as

$$x_{m,n} = \sigma\left(\sum_{i=1}^{N} w_{im} x_{i,n-1} + b_{m,n}\right) , \tag{23}$$

where N is the dimension of the $(n-1)$-th layer and b is known as the bias vector of the n-th layer. Nonlinearities of the σ function can be modelled in many different ways (step function, sigmoid, tanh, etc.),

[2] With this definition, the only difference between classification and regression tasks is that the target set is finite for classification and continuous for regression.

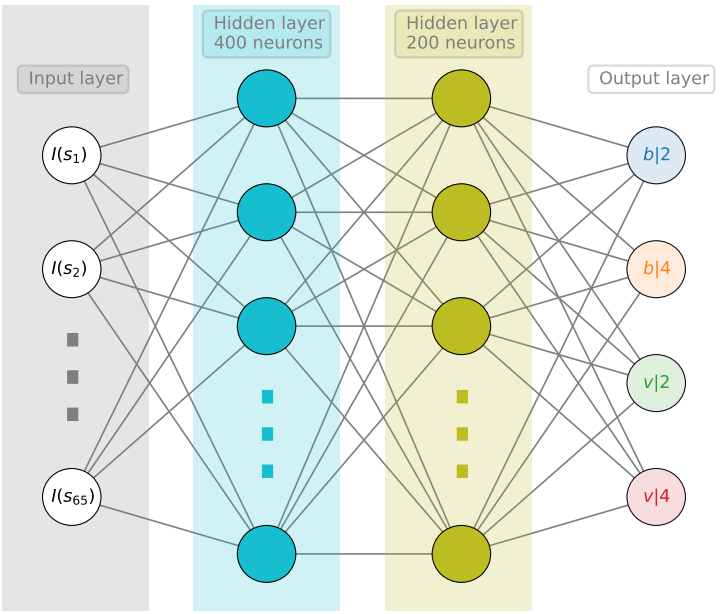

Figure 9: The neural network architecture of the classifier used in [83]. In the input layer, the feature vectors contain the intensity of the amplitude in each energy bin. The output layer is composed by the four classes which correspond to the various interpretations of the $P_c(4312)$. Figure from the Supplemental Material of [83].

but ReLU was employed in [83]. By continuing this procedure for all nodes in all layers, we finally obtain the values at the output layer that can be compared with ground truth labels (classification) or values (regression). To measure the quality of this comparison one uses a cost function, *e.g.* a cross entropy or a χ^2 (*aka* mean squared error). Thus learning is basically the minimisation of the cost function by varying the model parameters, in this case the weights of the neural network. This is a difficult optimization problem and, along with a proper choice of the cost function, it has a large body of literature discussing devoted to it it [87–89]. The network is trained by matching the feature vectors with ground truth labels: we generated a set of 10^5 line shapes for the four classes, sampling uniformly the amplitude parameters within a wide range of values. For each line shape, the intensities in energy bins provide the feature vectors that feed the network. It is clear that the stability of the optimisation process and the precision of eventual inference are largely impacted by the size of the training dataset.

The feature vectors in this example have 65 elements. This is less than in typical ML problems and far less than the amount of data input to Convolutional Neural Networks. But even here one expects substantial correlation which is related to information redundancy. Moreover, the system is governed mainly by threshold dynamics, so the relevant features should be just a few. Last but not least, working in a smaller dimensional space allows us to plot 2D projections to represent the data and to acquire a better intuition on the properties of the training set and the data to classify. To isolate the relevant features one customarily employs the Principal Component Analysis (PCA) [90], which boils down to extracting the eigenvectors and eigenvalues of the covariance matrix built from the standardized feature vectors (see Figure 10). The covariance matrix expressed in terms of eigenfeatures is diagonal with diagonal elements summing up to the total variance. So, in the PCA one retains those diagonal elements (and associated features) which "explain most of the variance".

Tracing the path that leads the classifier to assign the input to a particular class is impossible except for the simplest models. This makes the ML tools as black boxes whose decisions we are bound to trust rather

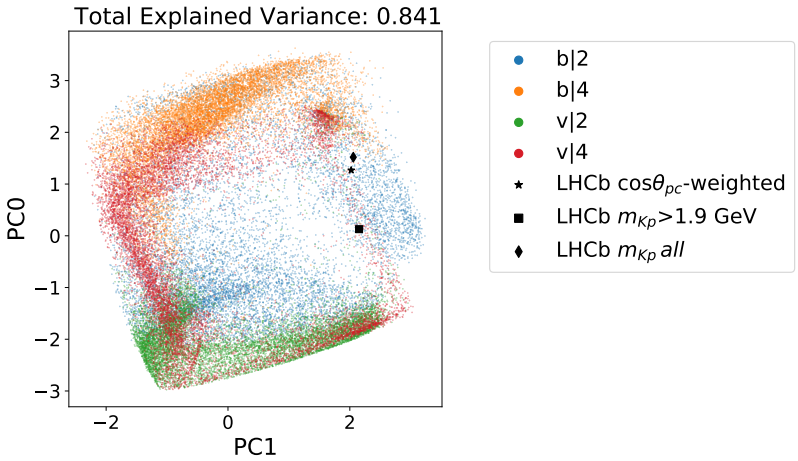

Figure 10: Training sets projected onto 2D space using PCA, compared with the values obtained from the LHCb datasets. Experimental data are located in a region well represented in the training set. Figure from the Supplemental Material of [83].

than understand. This is uncomfortable not only in physics where we aim at understanding the dynamics that leads to a given choice, but also in other fields like medicine or economics. However, we can at least select the features decisive for the classifier to make its class assignment. Partially, PCA already address this task, by selecting "principal directions" expressed in terms of combinations of the underlying features. These in turn may be difficult to interpret, and it is better to use SHapley Additive exPlanations (SHAP) values [91]. This approach originates in game theory, and it shows whether an individual feature favors (positive) or disfavors (negative) a certain classification.

The SHAP values in Figure 11 show that most of the class assignment explanation comes from the $v|4$ class in the near-threshold region. This conclusion is both expected and valuable: it confirms the conjectured dominance of the threshold effects in shaping the experimental signal, thus providing an *ex post* justification of the assumed scattering length approximation. Also it narrows the interval of energies relevant for the analysis to those neighboring the resonance peak.

Having established that our training set covers the region of the feature space where the experimental data are situated, and having identified the energy region of importance for the class assignment, we are ready to infer the nature of the $P_c(4312)$ from the experimental data. A probabilistic interpretation of the classification can be obtained by subjecting the signal t produced by the neurons of the output layer to a softmax function,

$$\text{softmax}(t_i) = \frac{\exp(t_i)}{\sum_{j=1}^{4} \exp(t_j)}, \tag{24}$$

where i, j run over the four classes. Obviously, this function is positive definite and normalized to 1. We obtain a probability by resampling the data with the bootstrap procedure explained in Section 2.2.2. Alternatively, one can apply the Monte Carlo dropout to the trained layers [92], which approximates the Bayesian inference in the deep Gaussian process. The results of these two procedures are shown in Figure 11. Both the dropout and bootstrap distributions show the clear dominance of the $v|4$ class, in other words based on the experimental data the neural network assigns the highest probability for the $P_c(4312)$ to have a $v|4$ nature. As said, the meaning of the different classes will be given Section 2.5.2.

One of the benefits of using Machine Learning and Artificial Intelligence at large is that of generalisation, *i.e.* one hopes that using ML or AI it is possible to classify features the network was not explicitly trained on. In realistic cases this generalisation ability is rather modest. Still, in the context of hadron spectroscopy, one may ask what would be the recognition rate for the classifier trained on the $P_c(4312)$ if applied to other resonances. One can speculate that for the resonance emerging due to a similar threshold dynamics, the

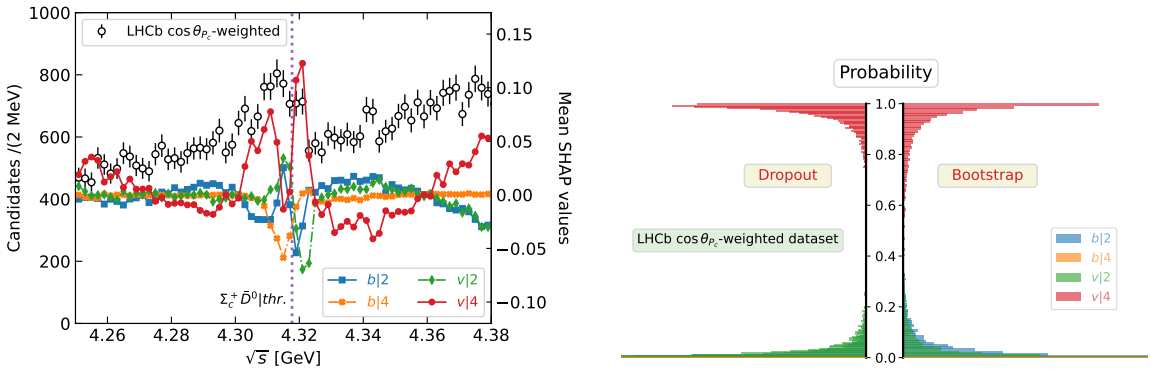

Figure 11: (left) SHAP values for the four classes overlaid on the experimental intensity plot. It is evident that the threshold region is the one impacting the decision. (right) Dropout and bootstrap classification probability densities for the predictions on one of the LHCb datasets for each of the four classes. The x axes are equally cut for the purpose of visibility and comparison. Figures from [83].

recognition ability may still persist. This brings us to the concept of transfer learning which is widely used in Convolutional Neural Networks applied to image recognition [93–95]. One typical application is transferring the ImageNet pretrained convolutional layers to the model one is interested in [96]. In hadron physics, there is no such pretrained "amplitude database". Still, the potential to generate the training sets from amplitudes describing typical situations like a near-threshold peak is practically unlimited. Details of the resulting line shape would depend on the production mechanism, particle masses, detector resolution, etc., but most of the information enabling the translation of the line shape into class assignment comes from a small region, as discussed above. Therefore, identifying layers of the CNN which extract this region and transfer them to other models may result in satisfactory classifier performance. Of course the transferred layers will have to be supplemented with additional trainable layers (either dense or convolutional), to account for non-transferable properties.

Finally, another category of ML methods can also find applications to spectroscopy: generative models, as Variational Autoencoders (VAE) [97], Restricted Boltzmann Machines (RBM) [98] or Generative Adversarial Networks (GAN) [99]. Technically the difference between discriminative and generative models is that the former are designed to capture the differences between groups of data, while the latter compute the joint probability of input and output. In particular GANs recently found application as an alternative to Monte Carlo Event Generators like PYTHIA [100], Herwig [101] or SHERPA [102]. Contrary to these conventional event generators, which are biased by the underlying physical models, the GAN-based generator might learn directly from experimental data. They seem effective in generating inclusive electron-proton scattering events and operated in the range of energies, even beyond those they were trained on [103]. The application to exclusive channels of interest for spectroscopy is presently ongoing [104, 105].

2.4. Light hadron spectroscopy

The light hadron sector has been subject to fierce debate for many decades. Resonances are generally broad and overlap each other; experimental analyses were limited by statistics, and often implemented simplistic methods. All these issues hindered the extraction of robust information. The natures and in some cases even the existence of some states are still under debate [1].

Quark models play a crucial role in guiding the analysis, predicting the number and properties of states to search for [106, 107]. However, since we are entering an era of high-statistics experiments, we are now facing the limits of such models. A complementary path was followed with effective field theories having hadrons as degrees of freedom, in particular Chiral Perturbation Theory (χPT) [108–117]. The low energy constants at a given order can be fixed from experimental data [118–120]. However, fixed order effective theories respect unitarity only perturbatively, and cannot produce resonance poles, if not explicitly incorporated. This

problem was circumvented by various unitarization methods (UχPT) [26, 27, 121–125], at least in the low-energy region. Nevertheless, these methods still suffer from several model dependencies and approximations. This becomes particularly clear when dealing with light scalars, where all the S-matrix principles play a significant role. This is the main reason why dispersive approaches have been gaining attention in recent years [126–138] (for a recent review we refer the reader to [139]). The combination of dispersion relations with experimental data is able to provide us the most robust information about the lightest mesons [140–143]. Unfortunately, partial wave dispersive analyses are usually applicable only up $\sim 1\,\text{GeV}$. At a practical level, most of the data at higher energies come from photo-, electro- and hadroproduction, heavy meson decays, peripheral production, or e^+e^- annihilations. Furthermore, the large number of open channels available make the rigorous application of unitarity unfeasible. For these reasons, loosening the S-matrix constraints, and studying a number of phenomenological amplitudes to assess the systematic uncertainties and reduce the model bias seems the appropriate path to follow.

There are several interesting topics in the light sector. The most fundamental questions concern the existence of resonances where gluons play the role of constituents, as glueball or hybrid mesons [144–146]. The analysis of isoscalar scalar and tensor mesons in the 1–2.5 GeV region—where the lightest glueball is expected—is presented in Section 2.4.1. The $\eta^{(\prime)}\pi$ channel, where the $a_2^{(\prime)}$ and the exotic π_1 are seen, is discussed in Section 2.4.2. The a_1 and π_2 states, for which the three-body dynamics plays a major role, will be discussed later in Sections 3.3.1 and 3.3.2. In the list of states that have received lots of attention in the past, we recall the $\eta(1405)$ as a pseudoscalar glueball candidate [147], the $X(1835)$ that appears at the $p\bar{p}$ threshold [148–150], and the poorly known strangeonium sector.

The baryon sector is even more difficult, despite the efforts by a larger community. We will just mention the longstanding puzzles about the Roper and the $\Lambda(1405)$ [151, 152]. A collective discussion of several baryon resonances [including the $\Lambda(1405)$] is performed by identifying the Regge trajectory they belong to, in Section 2.4.3.

2.4.1. J/ψ radiative decays

As mentioned, the isoscalar-scalar mesons, and -tensor mesons to some extent, have played a central role in spectroscopy. They can mix with the lightest glueball with the same quantum numbers. In pure Yang-Mills, the spectrum is populated by glueballs, the lightest one expected to be around 1.5–2 GeV [153–161]. In nature, glueball production is expected to be enhanced in processes where quarks annihilate into gluons, like $p\bar{p}$ collisions or J/ψ radiative decays.

Most of the literature traces the existence of a significant glueball component with the emergence of a supernumerary state with respect to how many are predicted by the quark model [144, 145, 162]. The PDG lists seven inelastic scalar-isoscalars, in particular the $f_0(1370)$, $f_0(1500)$, $f_0(1710)$ in the 1.2–2 GeV are one more than expected by the quark model, which stimulated an intense work to identify one of them as the glueball [163–170]. The $f_0(1710)$ couples mostly to kaon pairs [171–173]. Since photons do not couple directly to gluons, the poor production of $f_0(1500)$ in $\gamma\gamma$ suggests it may be mainly a glueball. On the other hand, the chiral suppression of the matrix element of a scalar glueball to a $q\bar{q}$ pair, point to the $f_0(1710)$ as a better candidate [169, 174], which is supported by a quenched Lattice QCD calculation [157].

The tensor resonances are better understood. The $f_2(1270)$ and $f_2'(1525)$ are identified as $u\bar{u}+d\bar{d}$ and $s\bar{s}$ mesons, respectively. Indeed, the former couples mostly to $\pi\pi$, and the latter to $K\bar{K}$ [1, 134]. Both resonances are narrow and have also been extracted from lattice QCD [175].

In this section we summarize our efforts to determine these inelastic scalar and tensor resonances from J/ψ radiative decays [38]. We consider the data from the nominal solutions of the $J/\psi \to \gamma\pi^0\pi^0$ [176] and $\to \gamma K_S^0 K_S^0$ [173] mass-independent analyses by BESIII. Bose symmetry requires $J^{PC} = (\text{even})^{++}$; and the isospin zero amplitude is dominant for both channels. We fit the intensities and relative phases of the 0^{++}, 2^{++} E1 multipoles between 1–2.5 GeV.

As mentioned, we use a variety of parametrizations that fulfill as many S-matrix principles as possible, in order to have the model dependencies under control. We follow the coupled-channel N/D formalism [22, 23, 25, 26],

$$a_i^J(s) = E_\gamma\, p_i^J \sum_k n_k^J(s) \left[D^J(s)^{-1}\right]_{ki} , \tag{25}$$

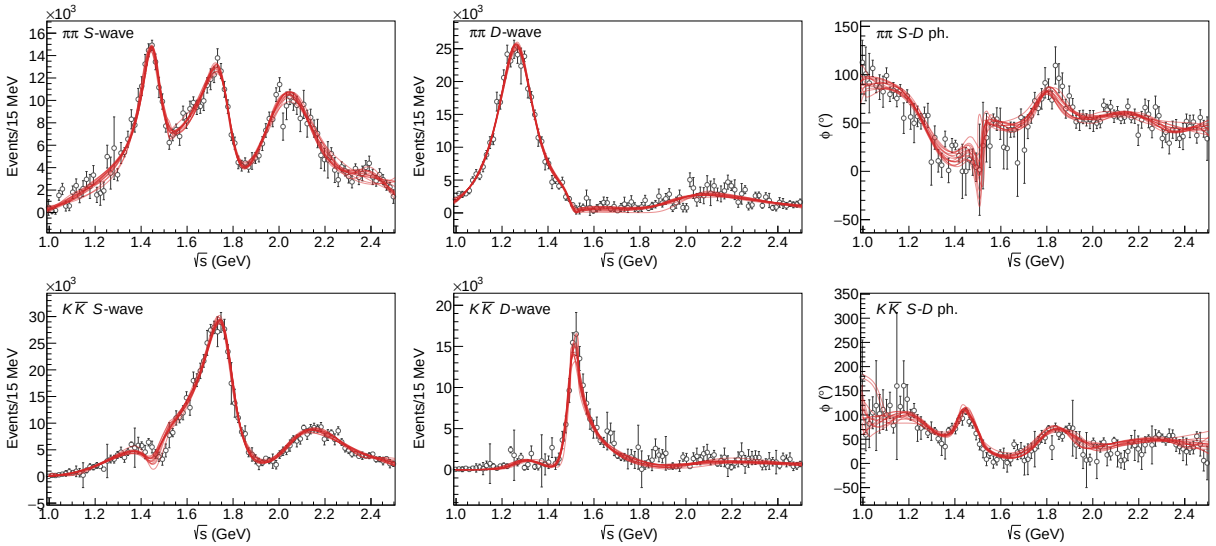

Figure 12: Best 3-channel fits to $\pi\pi$ (top) and $K\bar{K}$ (bottom) final states. The intensities for the S- (left), D-wave (center), and their relative phase (right) are shown. The red lines correspond to the central value of each one of the different fits. All these fits have $\chi^2/\text{dof} \sim 1.1$–$1.2$. Figures from [38].

with $i = h\bar{h}$ the hadron index,s the $h\bar{h}$ invariant mass squared and p_i the breakup momentum in the $h\bar{h}$ rest frame. One power of photon energy E_γ is required.

The $n_k^J(s)$ incorporate exchange forces in the production process and are smooth functions of s in the physical region. It is parametrized by an effective polynomial expansion, possibly including background poles. The matrix $D^J(s)$ represents the $h\bar{h} \to h\bar{h}$ final state interactions, and encodes the resonant content of the $\eta^{(\prime)}\pi$ system. A customary parametrization is given by [22]

$$D^J_{ki}(s) = \left[K^J(s)^{-1}\right]_{ki} - \frac{s}{\pi}\int_{4m_k^2}^{\infty} ds' \frac{\rho N^J_{ki}(s')}{s'(s'-s-i\epsilon)}, \tag{26}$$

where $\rho N^J_{ki}(s')$ is smooth in the physical region, and describes the crossed-channel contribution to the scattering process. For the K-matrix, we consider

$$K^J_{ki}(s)_{\text{nominal}} = \sum_R \frac{g_k^{J,R} g_i^{J,R}}{m_R^2 - s} + c^J_{ki} + d^J_{ki}\, s, \tag{27a}$$

with $c^J_{ki} = c^J_{ik}$ and $d^J_{ki} = d^J_{ik}$. Alternatively, we parametrize the inverse K-matrix as a sum of CDD poles [19, 55],

$$\left[K^J(s)^{-1}\right]^{\text{CDD}}_{ki} = c^J_{ki} - d^J_{ki}\, s - \sum_R \frac{g_k^{J,R} g_i^{J,R}}{m_R^2 - s}\,, \tag{27b}$$

where $c^J_{ki} = c^J_{ik}$ and $d^J_{ki} = d^J_{ik}$ are constrained to be positive. These coefficients are also referred to as "the CDD pole at infinity". For single channel, this choice ensures that no poles can appear on the physical Riemann sheet. Even in the case of coupled channels, their occurrence is scarce, and when they do occur they are deep in the complex plane, far from the physical region.

Initially, we performed a 2-channel analysis using only data on the $\pi^0\pi^0$ and $K^0_S K^0_S$ final states. However these models are too rigid and cannot reproduce fully the local features of data. It is indeed that many of these resonances couple substantially to 4π. For this reason, we extend our model with an unconstrained $\rho\rho$ channel, using the previous results as starting point for the new fits. We identify 14 best fits with different parameterizations, shown in Figure 12. We perform the bootstrap analysis as discussed in Section 2.2.2, generating $\mathcal{O}(10^4)$ pseudodata sets per parameterization.

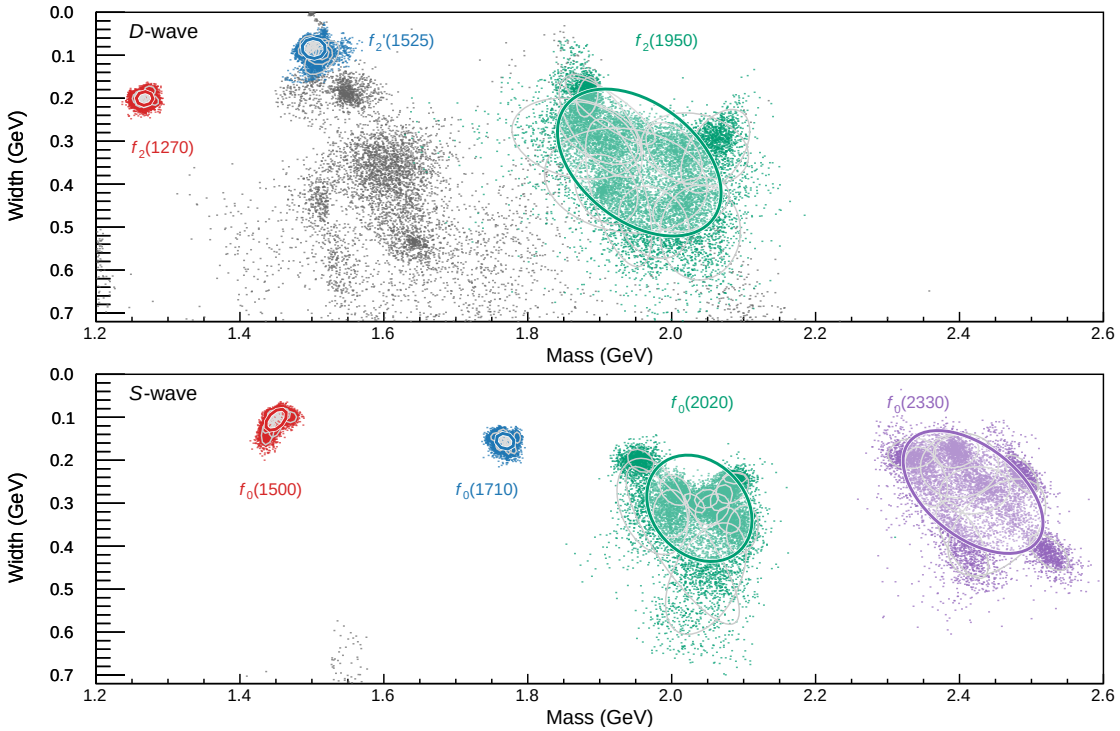

Figure 13: Shown in different colors are the final results for the pole positions, superimposed for the 14 models used int he analysis. A point is drawn for each pole found in each one of the $\mathcal{O}(10^4)$ bootstrap resamples. Gray points are identified as spurious resonances. For each physical resonance and systematic, gray ellipses show the 68% confidence region. Colored ellipses show the final average of all systematics. Figures from [38].

Since our amplitudes respect analyticity and unitarity, we can look for resonant poles in the complex energy plane. Considering the 14 models and the bootstrap resampling, we have $\mathcal{O}(10^5)$ "points" per pole, as shown in Figure 13. As discussed in Section 2.2.3, this analysis allows us to distinguish the spurious model artifacts from the physical ones. We found a total of 4 scalar and 3 tensor stable clusters that can be identified with physical resonances. The four lighter states produce a reasonably Gaussian spread, while the heavier ones have more complicated structures. The results are summarized in Table 1. The scalar resonances are compatible with other recent extractions [177, 178]. We found no evidence for a $f_0(1370)$ in these process. However, it is customarily accepted that this is a $q\bar{q}$ state that couples mostly to 4π, so that our findings do not challenge its existence.

Finally, we also studied the production and scattering couplings of these resonances. The tensor behave nicely, with the $f_2(1270)$ and $f_2'(1525)$ coupling almost entirely to $\pi\pi$ and $K\bar{K}$, respectively. This result is

Table 1: List of final pole position and uncertainties resulting from the combination of the different fits to the data. The errors correspond to the variance of the full samples, by assuming that the spread of results, shown in Figure 13, resembles a Gaussian distribution. Table from [38].

S-wave	$\sqrt{s_p}$ (MeV)	D-wave	$\sqrt{s_p}$ (MeV)
$f_0(1500)$	$(1450 \pm 10) - i(106 \pm 16)/2$	$f_2(1270)$	$(1268 \pm 8) - i(201 \pm 11)/2$
$f_0(1710)$	$(1769 \pm 8) - i(156 \pm 12)/2$	$f_2(1525)$	$(1503 \pm 11) - i(84 \pm 15)/2$
$f_0(2020)$	$(2038 \pm 48) - i(312 \pm 82)/2$	$f_2(1950)$	$(1955 \pm 75) - i(350 \pm 113)/2$
$f_0(2330)$	$(2419 \pm 64) - i(274 \pm 94)/2$		

roughly compatible to those listed in the PDG [1]. The results for the scalar resonances are more involved. Although the scattering couplings are not well constrained, the couplings to the whole radiative process show that the coupling of the $f_0(1710)$ is larger than the $f_0(1500)$, in particular for the $K\bar{K}$ channel, where it becomes almost one order of magnitude greater. As mentioned above, this favors the interpretation for the $f_0(1710)$ to have a sizeable glueball component.

2.4.2. $\eta^{(\prime)}\pi$ spectroscopy at COMPASS

Although the $\eta^{(\prime)}$ belong to the same pseudoscalar nonet as the pion, they are too short-lived to permit any scattering experiment. The information about their interactions comes solely from production experiments, which stimulated an intense theoretical effort to obtain information about their interaction (see *e.g.* [179–181]). The $\eta^{(\prime)}\pi$ system is particularly interesting, as its odd waves have exotic quantum numbers, and could be populated by hybrid mesons. Furthermore, its D-waves could contain the $a_2'(1700)$ resonance, which is poorly known in the literature, due to simplistic model extractions.

The first reported hybrid candidate was the $\pi_1(1400)$ in the $\eta\pi$ final state [182–186]. Another state, the $\pi_1(1600)$, was claimed to appear $\sim 200\,\text{MeV}$ heavier in the $\rho\pi$ and $\eta'\pi$ channels [187, 188]. More refined extractions were not conclusive [189]. Both peaks were confirmed by COMPASS [190, 191]. While the $\pi_1(1600)$ is closer to the theoretical expectations, having two nearby 1^{-+} hybrids below 2 GeV is problematic [192–194]. Establishing whether there exists one or two exotic states in this mass region is thus a stringent test for our understanding of QCD in the nonperturbative regime.

A high statistics dataset of diffractive production $\pi p \to \eta^{(\prime)}\pi p$, with $p_{\text{beam}} = 190\,\text{GeV}$, has been measured by the COMPASS collaboration [195]. In this section we will focus on the analyses of the lowest waves in the resonance region by [39, 55], while we will discuss the high energy region in Section 4.6.

High-energy diffractive production is dominated by an effective Pomeron exchange ($\mathbb{P}$), which allows us to factorize this process into the nuclear target/recoil vertex and the $\pi\mathbb{P} \to \eta^{(\prime)}\pi$ process.[3] In the Gottfried-Jackson (GJ) frame [196], the $\mathbb{P}$ helicity equals the $\eta\pi$ total angular momentum projection M, and the corresponding helicity amplitude $a_M(s,t,t_1)$ can be expanded into partial waves $a_{JM}(s,t)$. Here, s is the invariant mass squared of the $\eta^{(\prime)}\pi$ system, t_1 is the invariant momentum transfer squared between the $\eta^{(\prime)}$ and π, t is the invariant momentum transfer from the π beam to the nuclear target, and J is the total angular momentum of the $\eta^{(\prime)}\pi$ system.

At low transferred momentum, the $\mathbb{P}$ has a predominant coupling to $|M| = 1$ waves, indicating an effective vector coupling to the nuclear vertex. Since the COMPASS analysis integrates over $t \in [-1.0, -0.1]\,\text{GeV}^2$, we will consider a fixed effective $t_{\text{eff}} = -0.1\,\text{GeV}^2$ value in our analysis, and we will vary it to assess systematic uncertainties. The production amplitude can be parametrized following the N/D formalism,

$$a_i^J(s) = q^{J-1} p_i^J \sum_k n_k^J(s) \left[D^J(s)^{-1} \right]_{ki} , \tag{28}$$

where the kinematic prefactors assure proper angular momentum barrier suppression. The $\pi\mathbb{P}$ momentum is represented by q, with the $(J-1)$ power coming from an additional momentum factor from the nuclear vertex as explained in [197]. The parametrizations of $n^J(s)$ and $D^J(s)$ are similar to the ones discussed the previous Section 2.4.1.

As a first study, we perform a single-channel analysis of $\eta\pi$ in the $J^{PC} = 2^{++}$ wave and determine the spectral content of this channel [55]. This serves both as a test for the model, since the tensor wave is the strongest, and an opportunity to investigate radial excitations of the a_2. For $D^J(s)$ we only considered the CDD parametrization, which forces a zero in the amplitude that must be divided out from $n(s)$.

As seen in Figure 14, the COMPASS data shows a dominant peak around $\sqrt{s} \sim 1.2$–$1.3\,\text{GeV}$, and a small enhancement around $\sqrt{s} \sim 1.7\,\text{GeV}$. To assess whether this is actually due to a resonance, we try and fit with just the CDD pole at infinity, or adding a second one. In the former case the fit captures the

[3] As we will discuss in Section 4.6, the contribution of the f_2 is also needed. For the sake of extracting the resonances, the details of the exchanges are not relevant: for example, no information on the trajectory enters the analysis. We will consider here a "Pomeron" exchange that effectively includes all the other ones, whose effective spin one dominates the ϕ distribution.

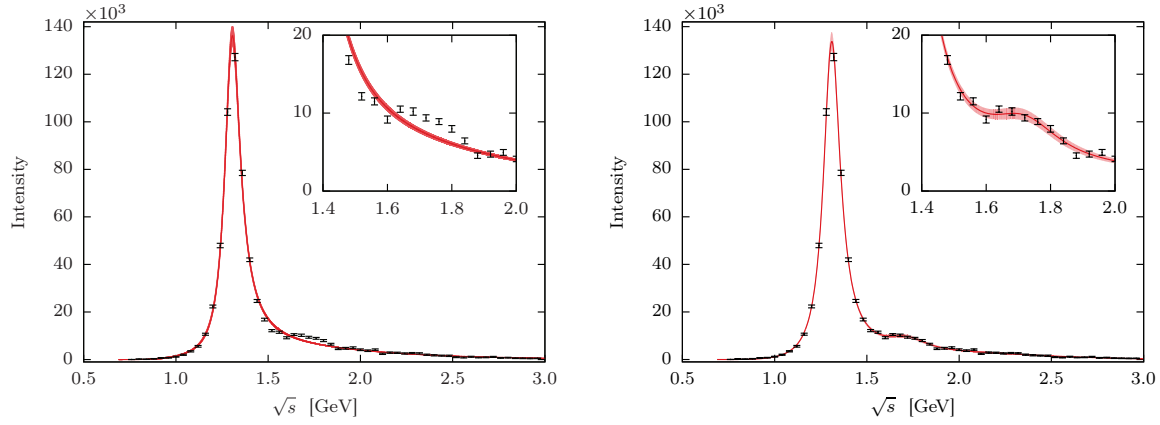

(a) CDD_∞ pole only. (b) Two CDD poles.

Figure 14: Intensity distribution and fits to the $J^{PC} = 2^{++}$ wave for different number of CDD poles, (a) using only CDD_∞ and (b) using CDD_∞ and the CDD pole at $s = c_3$. Red lines show the fit results. Data is taken from Ref. [195]. The inset shows the a_2' region. The error bands correspond to the 3σ (99.7%) confidence level. Figures from [55]

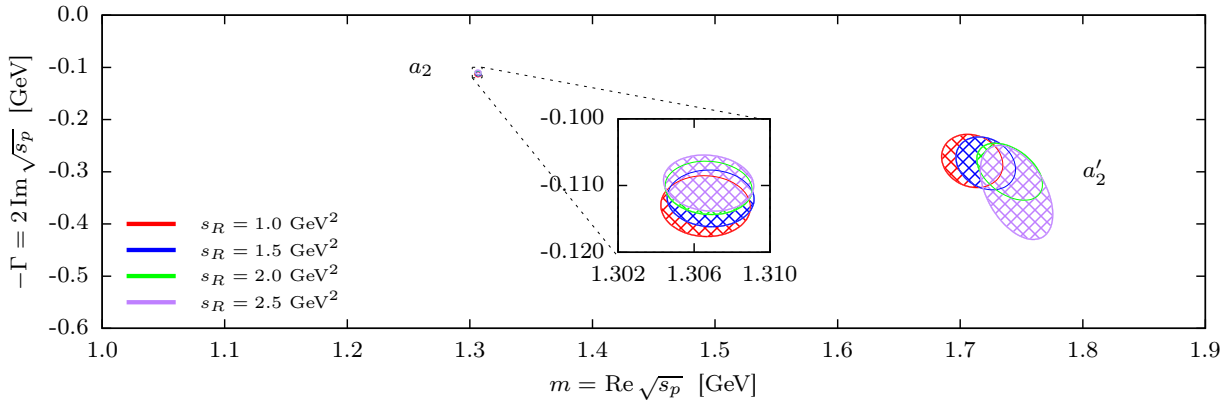

Figure 15: Location of pole positions with two CDD poles. The various ellipses represent the 2σ confidence level for the several model variations. Figure from [55]

dominant a_2 peak, but for reasonable descriptions of the production model the secondary bump cannot be described, see Figure 14(a). In contrast, if we allow both CDD poles, we can resolve both the dominant and subdominant peaks in the spectrum, providing a good description of the data with a $\chi^2/\mathrm{dof} = 1.91$.

The spectral content of the channel can be determined by continuing the amplitude to closest unphysical Riemann sheet, and searching for poles. For the best fit, we find two stable poles, which we identify as the $a_2(1320)$ and $a_2'(1700)$ resonances. We find the $a_2(1320)$ has a mass and width $m = (1307 \pm 1 \pm 6)\,\mathrm{MeV}$ and $\Gamma = (112 \pm 1 \pm 8)\,\mathrm{MeV}$, respectively, while the $a_2'(1700)$ has a mass and width $m = (1720 \pm 10 \pm 60)\,\mathrm{MeV}$ and $\Gamma = (280 \pm 10 \pm 70)\,\mathrm{MeV}$, where the first uncertainty is statistical based on bootstrap, and the second one is a systematic estimate of the model variations.

With this 2^{++} channel under control, we extend the analysis to a coupled-channel study where we investigate the π_1 hybrid candidate with the $\eta^{(\prime)}\pi$ data from COMPASS. To use the information on the relative phase, we have to fit the P- and D-wave data at once. Moreover, we include also the $\eta'\pi$ data, in order to understand both $\pi_1(1400)$ and $\pi_1(1600)$ peaks. We will neglect any other possible decay channels other than the two at hand, even though these are not expected to be the dominant ones [198]. Our reasoning as explained above is that adding new channels should not produce a significant displacement of the pole

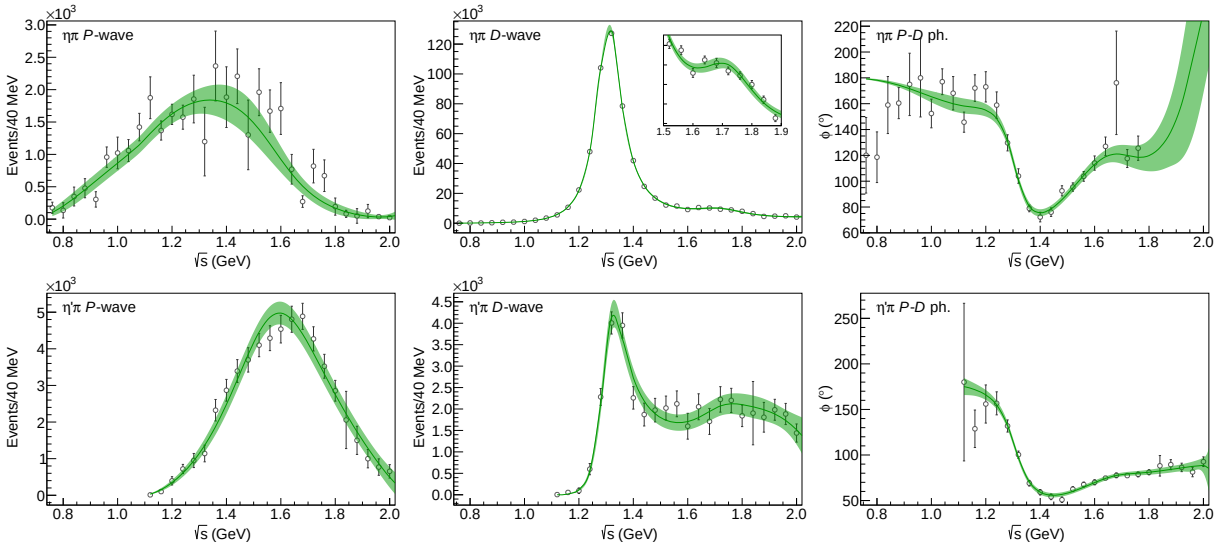

Figure 16: Fits to the $\eta\pi$ (upper row) and $\eta'\pi$ (lower row) data from COMPASS [195]. The intensities of P- (left), D-wave (center), and their relative phase (right) are shown. The inset zooms into the region of the $a_2'(1700)$. The solid line and green band shows the result of the fit and the 2σ confidence level provided by the bootstrap analysis, respectively. The best fit has $\chi^2/\text{dof} = 162/122 = 1.3$. Figures from [39].

positions in this analysis.

The best fit for our nominal model makes use of only a single P-wave K-matrix pole, and it is shown in Figure 16, where the global $\chi^2/\text{dof} = 162/122 = 1.3$. The statistical uncertainties shown correspond to the 2σ confidence level associated to bootstrapping the sample data. This result is remarkable, considering the high precision data on the D-wave, and all the degrees of freedom exhibited on the data. As can be seen in the figure all local features are nicely described by the fit, in particular both P-wave peaks, and even the elusive $a_2'(1700)$ peak.

For systematic checks, fits with different number of K-matrix poles in P-wave have been implemented. The ones with no poles are unable to describe the data, and the ones with more than one do not produce any noticeable different in the goodness of the fit. In the complex plane extra poles can appear, but they are spread all over the place, are generally very broad, and behave erratically when slightly varying the parameters of the fit.

Once again, after obtaining a faithful description of the data, we can make use of our analytic parametrizations to search for poles in the complex plane. The statistical uncertainties are determined via bootstrap. We perform 12 systematic variations of the nominal model and of its parameters. When continuing to the complex plane they all produce an isolated cluster in P-wave, that we identify with the π_1, together with two poles on the D-wave corresponding to the $a_2(1320)$ and $a_2'(1700)$ resonances. Their pole positions are listed in Table 2, and their spread of results is plotted in Figure 17. We conclude that there is no more than one $J^{PC} = 1^{-+}$ hybrid meson decaying to both $\eta^{(\prime)}\pi$ channels. This picture reconciles experimental evidences with phenomenological and Lattice QCD expectations.

Table 2: Pole position from the $\eta^{(\prime)}\pi$ analysis of [39]. The first error is statistical, the second systematic.

Poles	Mass (MeV)	Width (MeV)
$a_2(1320)$	$1306.0 \pm 0.8 \pm 1.3$	$114.4 \pm 1.6 \pm 0.0$
$a_2'(1700)$	$1722 \pm 15 \pm 67$	$247 \pm 17 \pm 63$
π_1	$1564 \pm 24 \pm 86$	$492 \pm 54 \pm 102$

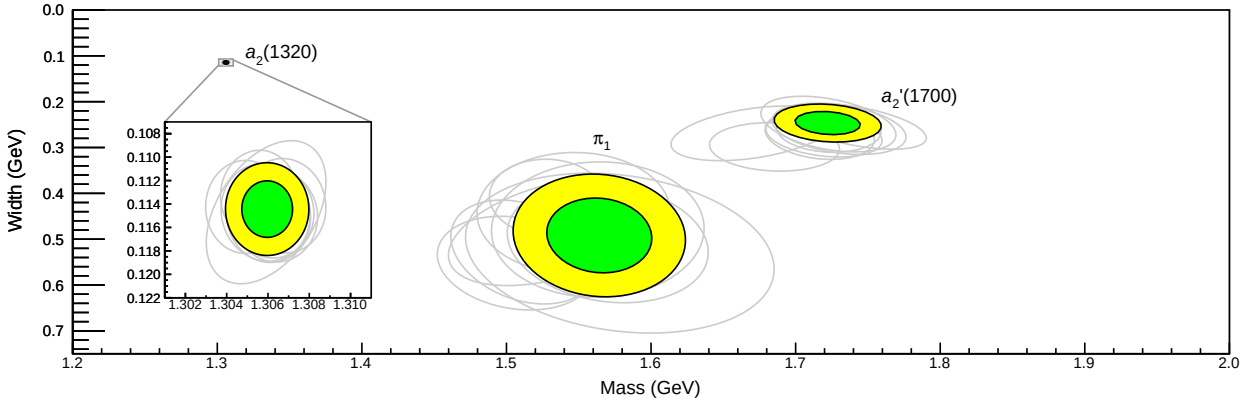

Figure 17: Positions of the poles identified as the $a_2(1320)$, π_1, and $a_2'(1700)$. The inset shows the position of the $a_2(1320)$. The green and yellow ellipses show the 1σ and 2σ confidence levels, respectively. The gray ellipses in the background show, within 2σ, the different pole positions produced by model variations. Figure from [39].

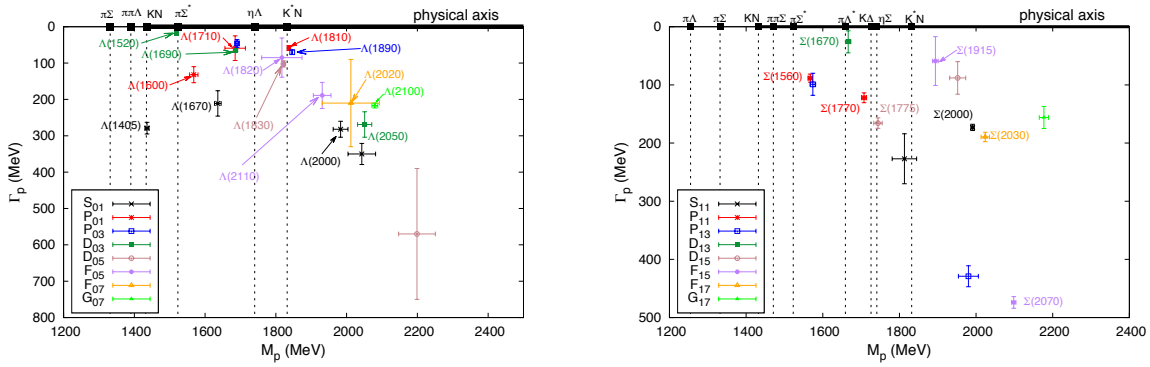

Figure 18: Masses and widths from the Λ (left) and Σ (right) resonances. Figures from [49].

2.4.3. Regge phenomenology of light baryons

The low-lying N^*, Δ, Λ, and Σ resonances, accessible in pion-nucleon and (anti)kaon-nucleon scattering and in photoproduction experiments, are a source of insights into the quark model and the inner works of nonperturbative QCD phenomena [151]. One of the many goals of light baryon spectroscopy is to understand the origin and structure of resonances, in particular whether a compact three-quark interpretation holds for these states or if other components should be considered.

Usually, these resonances are extracted from experimental data through a partial wave analysis, assuming each partial wave independent of the others. Such approach does not take into account the fact that amplitudes are also analytic functions of the angular momentum, as described by Regge theory [199–201]. Therefore, resonances of increasing spin must lie on a so-called Regge trajectory, whose shape can be can be used to gain insight on the microscopic mechanisms responsible for the formation of the resonance [202–207]. In QCD, Regge trajectories are approximately linear, as first shown by Chew and Frautschi [208] by plotting the spin of resonances J_p versus their mass squared M^2, which is one the strongest phenomenological indications of confinement [209]. Constituent quark model predictions for baryons fit nicely in the approximately linear behavior [106, 107, 210–216, 216–218] and so do flux tube models of baryons [219–221]. The emerging pattern can be used to guide a partial wave analyses, for example gaps in the trajectories are usually due to missing states.

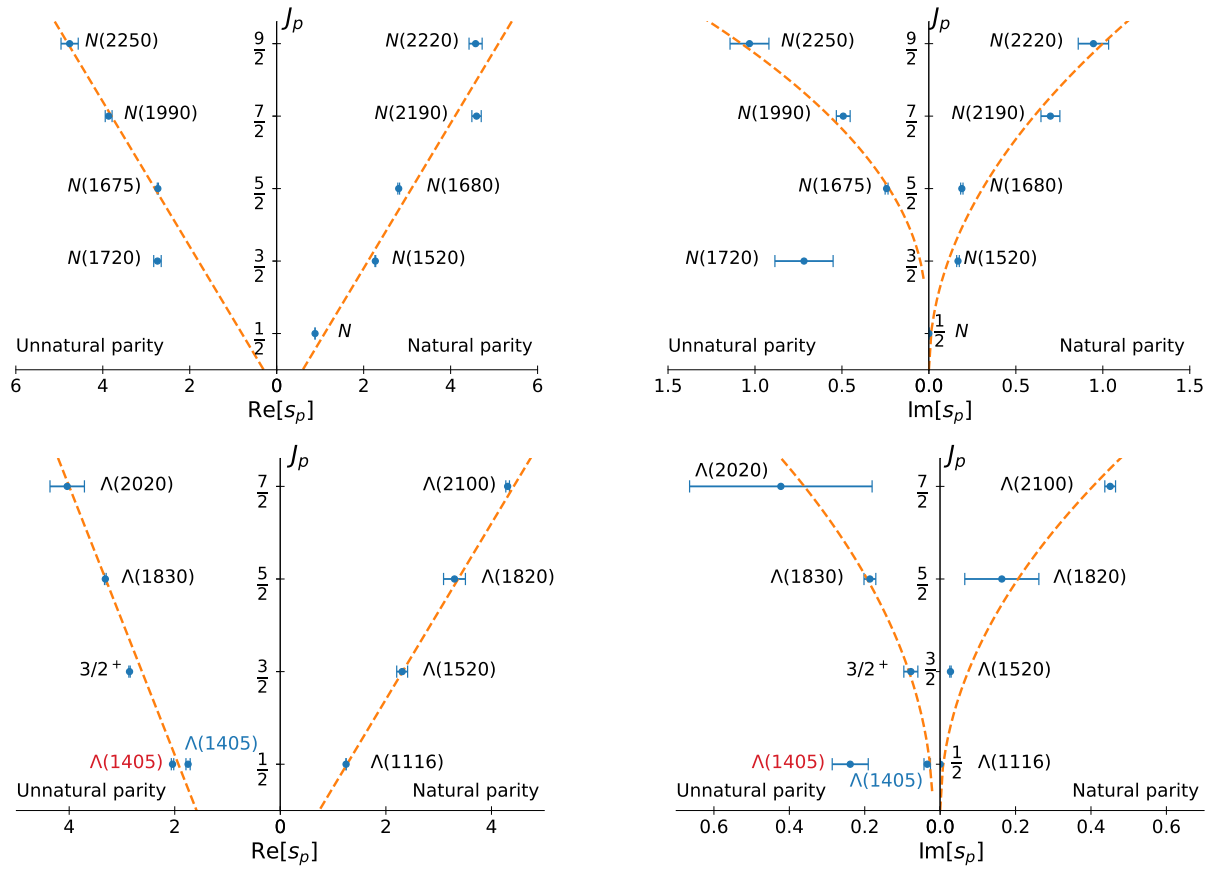

Figure 19: Leading Regge trajectories for N^* (top row) and Λ (bottom row) resonances. Left column shows the Chew-Frautschi plots, while the right column plots the spin as a function of the imaginary part of the pole position (mass times width). The Λ poles are taken from [49, 222]. The N^* poles are taken from [223, 224].

Regge trajectories computed in the Chew-Frautschi plot ignore entirely the resonance widths, *i.e.* the fact that they are poles in the complex s-plane. This is partially inconsistent, as unitarity demands the Regge trajectory $\alpha(s)$ to be a complex function as well [225]. Therefore, one should plot the imaginary part of the pole (*i.e.* the width times the mass of the resonance) as a function of the spin, as proposed in [206]. More details about Regge theory and their implications to study production of hadrons will be given in Section 4.2, while here we focus on using the trajectories as a tool to organize the existing spectrum.

For baryons, Regge trajectories are classified according to isospin I, naturality η, and signature τ.[4] The quantum numbers identify a given $I^{\eta}_{(\tau)}$ trajectory. For example, the nucleon trajectory corresponds to $I^{\eta}_{(\tau)} = \frac{1}{2}{}^{+}_{(+)}$. The Λ and Σ poles were extracted in [49], fitting the single energy partial waves from [226] of $\bar{K}N$ scattering data with a K-matrix model that incorporates analyticity in the angular momentum. The results are summarized in Figure 18. Together with the two $\Lambda(1405)$ poles from [222], their leading Regge trajectories were studied in [206].

Figure 19 plots the spin of the resonance as a function of the real or imaginary part of the pole position. We note that only one of the $\Lambda(1405)$ poles lies on the same trajectory as the higher Λs. The linearity of the Chew-Frautschi plot is apparent, which suggest an interpretation as dominantly three-quark states. The second plot provides additional insight, specially regarding the two $\Lambda(1405)$ poles. In [206, 227] it is argued that linearity in the Chew-Frautschi plot is not enough for a three-quark interpretation, but since most of its width should be due to the phase space contribution, a square-root-like behavior should emerge in when plotting spin *vs.* imaginary part of the pole. It is apparent how a square-root like behavior is generally followed. However, only one of the $\Lambda(1405)$ follows this pattern. This suggests that the heavier $\Lambda(1405)$ is mostly a compact state, while the lightest has a different nature, most likely a molecule [206].

The nonstrange light baryon spectrum can be studied in the same way [227]. The pole extraction can be taken from several partial wave analyses of meson scattering and photoproduction data available in the literature [223, 224, 228–232]. In Figure 19 we show an example of N^* trajectory. The states accommodate nicely to the Regge expectation except for the $N(1720)$, that in [223, 224] has a large width $\Gamma_p \sim 300$–$430\,\text{MeV}$ that would place this state close to the daughter trajectory. Hence, Regge phenomenology demands the existence of another narrower state.

Such a state was actually claimed to be narrower in other analyses [228, 229] with $\Gamma_p = 120\,\text{MeV}$, but no consensus was reached [230, 232, 233]. A recent CLAS analysis finds actually two $N(1720)$ with similar mass and widths, but different Q^2 behavior in electroproduction [234]. The recent ANL-Osaka analysis finds two poles with masses 1703 and 1763 MeV and widths 70 and 159 MeV, respectively [235]. Since quark models predict several $3/2^+$ states in this energy region [107, 211, 212, 214], it is possible that the data analyses are not able to resolve each pole individually. Further research is necessary to establish the number and properties of resonances in this energy region, before discussing their nature.

2.5. Heavy quark spectroscopy

The unexpected discovery of the $X(3872)$ in 2003 ushered in a new era in hadron spectroscopy [236]. Experiments have claimed a long list of states, collectively called XYZ, that appear mostly in the charmonium sector, but do not respect the expectations for ordinary $Q\bar{Q}$ states. Figure 20. An exotic composition is thus likely required [3, 9]. Several of these states appear as relatively narrow peaks in proximity of open charm threshold, suggesting that hadron-hadron dynamics can play a role in their formation [4]. Alternatively, QCD-like models also predict the existence of supernumerary states, by increasing the number of quark/gluon constituents [2]. The recent discovery of a doubly-heavy T^+_{cc} [237, 238] and of a fully-heavy $X(6900)$ [239] states make the whole picture extremely rich. Having a comprehensive description of these states will improve our understanding of the nonperturbative features of QCD. Most of the analyses from Belle and BaBar suffered from limited statistics, and strong claims were sometimes made with simplistic models on a handful of events. Currently running experiments like LHCb and BESIII have overcome this issue, providing extremely precise datasets, that also require more sophisticated analysis methods and theory

[4] For baryons, $\tau = (-1)^{J_p - 1/2}$, for antibaryons $\tau = (-1)^{J_p + 1/2}$. The naturality is $\eta = P\tau$, with P the parity.

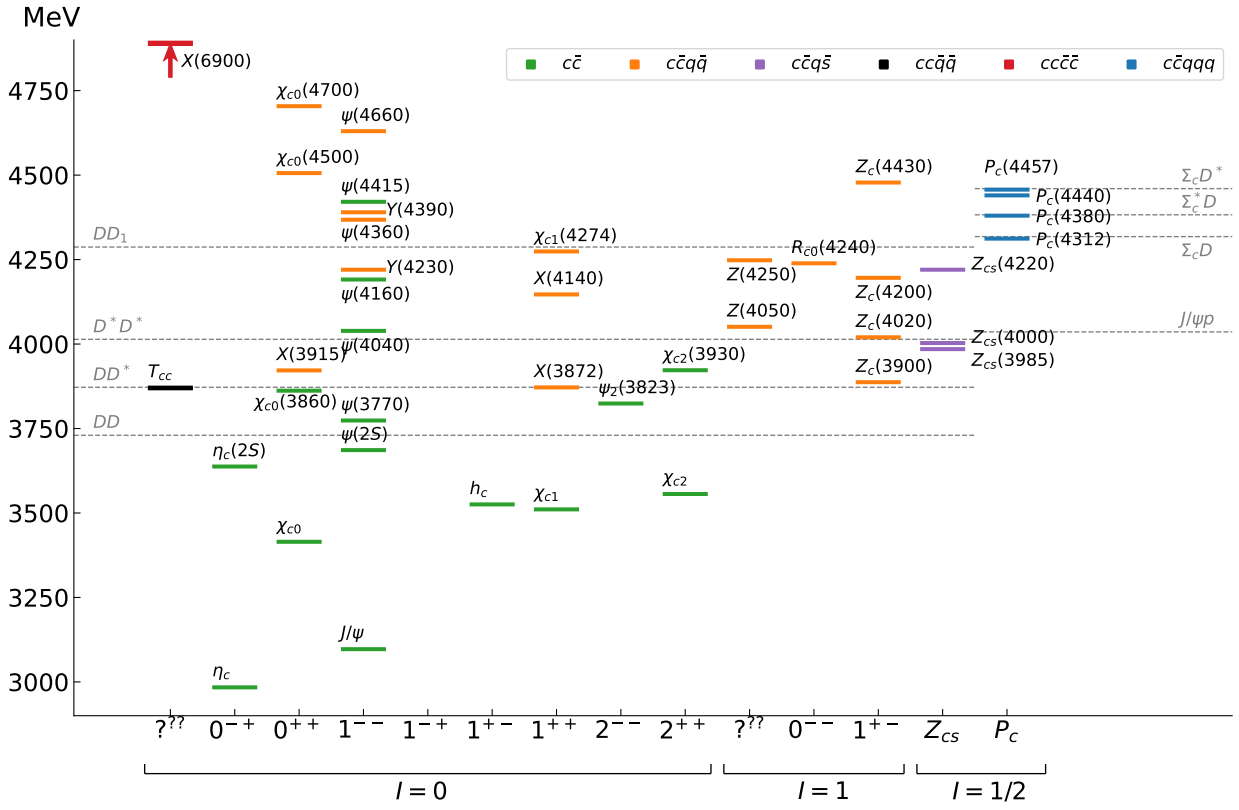

Figure 20: Summary of ordinary charmonia, XYZ and pentaquarks from PDG [1].

inputs. The status of ordinary and exotic charmonia is summarized in Figure 20. Depending on their width and the production mechanism, the states can roughly be classified in:

1. Narrow ($\lesssim 50\,\text{MeV}$) states that appear in b-hadron decays: $X(3872)$, $P_c(4312)$, $P_c(4440)$, $P_c(4457)$, ..., and at e^+e^- colliders: $X(3872)$, $Y(4230)$, $Z_{c,b}^{(\prime)}$, ...
2. Broad ($\gtrsim 50\,\text{MeV}$) states that appear in b-hadron decays: $\chi_{c0}(4140)$, $Z(4430)$, $Z_{cs}(4000)$, ...
3. States produced promptly at hadron machines: $X(3872)$, T_{cc}^+, $X(6900)$, ...

The narrow signals do not require a thorough understanding of interferences with the background. Since they often appear close to some open flavor threshold they call for analysis methods that incorporate such information. To some extent, it is possible to give model-independent statements. The $X(3872)$ is very special. It has $J^{PC} = 1^{++}$, violates isospin substantially decaying into $J/\psi\rho$ and $J/\psi\omega$ with similar rates, and lies exactly at the $\bar{D}^0 D^{*0}$ threshold. Its lineshape was recently studied by LHCb, which triggered several discussions [240–242]. The $Z_c(3900)$ (with $= 1^{+-}$) was seen as a peak in the $J/\psi\,\pi$ invariant mass in the $e^+e^- \to J/\psi\,\pi\pi$ process, and as an enhancement at the $D\bar{D}^*$ threshold in $e^+e^- \to \pi D\bar{D}^*$. Similarly, a $Z_c'(4020)$ with same quantum numbers peaks in $h_c\,\pi$ invariant mass in the $e^+e^- \to h_c\,\pi\pi$ process, and enhances the cross section at the $D^*\bar{D}^*$ threshold in $e^+e^- \to \pi D\bar{D}^*$. The system of two 1^{+-} at the two thresholds seems replicated in the bottomonium sector, by the $Z_b(10610)$ and $Z_b'(10650)$. The proximity to threshold motivated their identification as hadron molecules [243–249], but tetraquark interprations are also viable [250–253].

The discovery of pentaquark candidates in $\Lambda_b^0 \to J/\psi p K^-$ decay in 2015 also boosted the field substantially. The LHCb collaboration reported a narrow and a broad state, the $P_c(4450)$ and the $P_c(4380)$, with

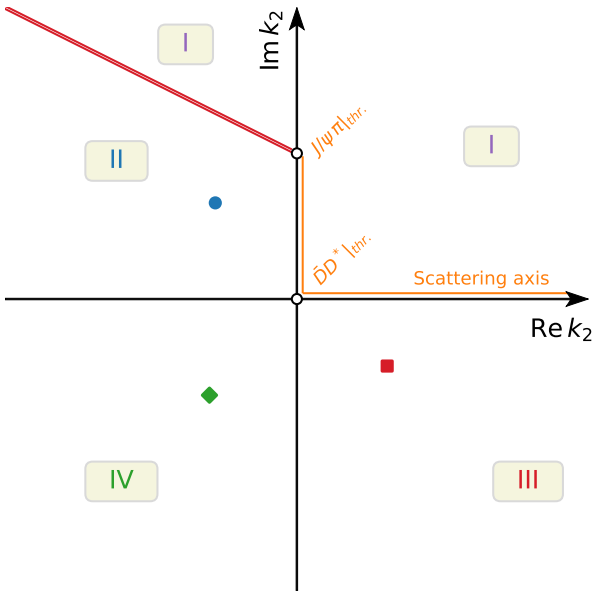

Figure 21: Analytic structure of the $Z_c(3900)$ amplitude near the $\bar{D}D^*$ threshold. The adjacent Riemann sheets are continuously connected along the axes. Several possibilities for the pole to appear. A pole on the III sheet above the DD^* threshold (red square) generates a usual Breit-Wigner-like lineshape, and is likely due to a genuine QCD resonance. A pole on the II sheet below threshold (blue circle) is likely due to a bound state of $\bar{D}D^*$. Similarly, a pole on the IV sheet is not immediately visible on the physical region (orange), but enhances the threshold cusp. This is likely due to a virtual state.

likely opposite parities [254]. The subsequent 1D analysis in 2019, with ten-times higher statistics, reported a composite structure of the narrow peak, that split into $P_c(4440)$ and $P_c(4457)$, and found a new isolated peak, the $P_c(4312)$ [255]. In light of this new information, the quantum numbers reported previously are no longer reliable. Again, the signals can be interpreted as compact five-quark states [256–259], weakly bound meson-baryon molecules [260–266], or triangle singularities [7, 267–272].

We will discuss the examples of the $Z_c(3900)$ in Section 2.5.1 and of the $P_c(4312)$ in Section 2.5.2. In some reactions, it is possible that 3-body dynamics, and in particular triangle singularities can play a role. An example of this will be discussed in Section 2.5.3.

Broad states are much less evident in data, and can be extracted only with sophisticated amplitude analyses, where unitarity is usually neglected. Having a full exploration of the systematic model variations on the lines of what was presented in the previous sections has not been done yet due to limits in computational and human resources. In prompt production, the initial kinematics is uncontrolled. While there is no doubt that strong signals exist, there is a long debate on whether or not one can infer the nature of such states from the production properties at high energies [273–281]. It is worth mentioning that, with the exception of the $X(3872)$, the XYZ have been observed in one specific production channel. Exploring alternative production mechanisms would provide complementary information, that can further shed light on their nature. The study of XYZ photoproduction will be discussed later in Section 4.5.

2.5.1. The $Z_c(3900)$

As we previously stated, the $Z_c(3900)$ peaks in $J/\psi\,\pi$ [282–285], and enhances the $D\bar{D}^*$ cross section at threshold [286–288]. Several possibilities are viable: it might be a bound or virtual state of $D\bar{D}^*$, that moves into the complex plane due to the coupling to $J/\psi\,\pi$; it might be a genuine QCD resonance; it might be a mere threshold cusp enhanced by the presence of a triangle singularity closeby; or a combination of all these. The best candidate to produce a triangle cusp is the $D_1(2420)$ resonance in $D^*\pi$.

Each microscopic interpretation reflects into the analytic properties of the amplitude: bound and virtual states would likely appear on the II and IV sheet, compact states generally lie on the III sheet. This is

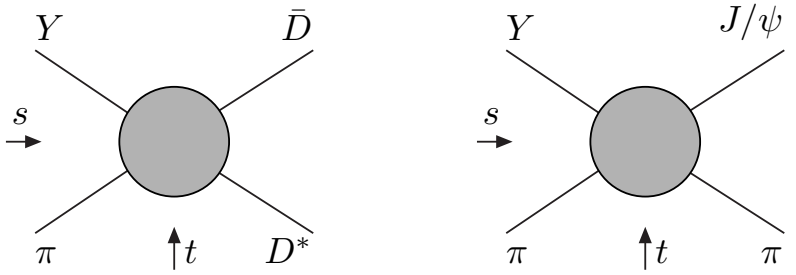

Figure 22: Channel definitions. In channel 1 we consider the exchange of a $D_1(2420)$ in t and of a $\bar{D}_0(2400)$ in u in addition to the possible Z_c in s. In channel 2 we consider the exchange of a $f_0(980)$ and a σ in t, in addition to the possible Z_c in s and u.

schematically represented in Figure 21. A more refined classification based also on the sign of the scattering length will be discussed in Section 2.5.2. Triangle singularities produce a branch point that can also enhance a peak. Such peak cancels in the elastic case. Therefore, studying the inelasticities with a proper coupled channel analysis can constrain the strength of the triangle. Moreover, the details of the line shape are related to the sheet the physical pole is located, and eventually offer a tool to study the nature of the $Z_c(3900)$.

The amplitude can be parametrized in the isobar model:

$$f_i(s,t,u) = 16\pi \left[a_i^{(t)}(t) + a_i^{(u)}(u) + \sum_j t_{ij}(s) \left(c_j + \frac{s}{\pi} \int_{s_j}^{\infty} ds' \frac{\rho_j(s') b_j(s')}{s'\,(s'-s)} \right) \right], \tag{29}$$

with i running over the two channels $\bar{D}D^*$ and $J/\psi\pi$, with Mandelstam variables s,t,u as represented in Figure 22. We are mostly interested in the distribution is s, where the $Z_c(3900)$ is directly observed. Isospin symmetry is assumed, so that the neutral and charged datasets are studied together. Little information is available about the angular distributions, so there is no point in considering spin. Since we are not interested in the nonexotic channels, we fill the $a_i^{(t,u)}$ isobars with simple Breit-Wigners for the $D_1(2420)$, $D_0^*(2400)$, and for two effective $\pi\pi$ resonances whose mass and width are let free in the fit. The s-channel is unitarized *à la* Khuri-Treiman (see Section 3.1), which gives the dispersive integral in Eq. (29), in terms of projections of the isobars in the other channels:

$$b_i(s) = \frac{1}{32\pi} \int_{-1}^{1} dz_s \left[a_i^{(t)}(t(s,z_s)) + a_i^{(u)}\left(u(s,z_s)\right) \right]. \tag{30}$$

The cross channel are not unitarized, so no integral equation has to be solved. The scattering amplitude t_{ij} describes the final state interactions, and can be parametrized with different functional forms, that allow for different singularities in the complex plane. We use the K-matrix parametrization that explicitly encodes unitarity $t_{ij} = \left[K^{-1}(s) - i\rho(s)\right]^{-1}_{ij}$, and consider four scenarios:

1. III: we use Flatté, $K_{ij} = g_i g_j/(M^2 - s)$, and force $b_i(s) \equiv 0$. Although unphysical, this choice is the closest to the parametrization used in the experimental analyses, and eases the comparison;
2. III+tr.: same, restoring the correct $b_i(s)$. These two scenarios naturally produce either a bound state pole below the $\bar{D}D^*$ threshold, or a resonant pole above it, depending on the value of M.
3. IV+tr.: K is a symmetric constant matrix, which produces either bound or virtual states.
4. tr.: same, but forcing the pole to be far from threshold penalizing its position in the fit, to assess whether the triangle singularity alone is able to generate the observed structure.

We perform a minimum χ^2 fit of these models to the $e^+e^- \to J/\psi\,\pi\pi$ [282, 285] and $\to \bar{D}D^*\pi$ [287, 288], for two values of total energy. In Figure 23 we show an example of how the various models result in different lineshapes.

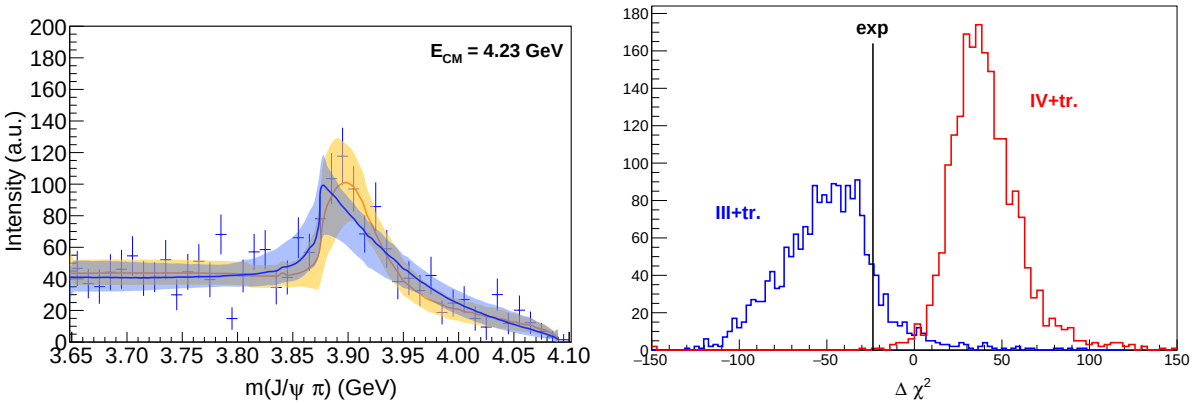

Figure 23: (left) Result of the fit for the scenario III and tr.. The colored lines and bands show the fit result with the relative 1σ error, calculated with bootstrap. Data are the $J/\psi\pi^0$ projection of the $e^+e^- \to J/\psi\pi^0\pi^0$ at $E_{\rm CM} = 4.23\,\text{GeV}$, by BESIII [285]. The errors shown are statistical only. (right) Loglikelihood ratio test. We histogram the χ^2 difference of the III and IV+tr. models, assuming that III (blue) or IV+tr. is the truth. The black line highlights the value of $\Delta\chi^2$ obtained from data. One gets a 2.7σ rejection of IV+tr. over III.

All the models fit reasonably well the data, with χ^2/dof ranging from 1.2 to 1.3. A likelihood ratio test does not give rejections larger than 3σ [289, 290]. We conclude that present statistics prevents us from drawing any strong statements.

In the models where a Z_c pole appears, we can quote its position, and estimate the uncertainties using bootstrap. The results are summarized in Figure 24 and Table 3. We observe that:

1. III: The pole appears above the $\bar{D}D^*$ threshold, on the III sheet, and the width is $\Gamma \simeq 50\,\text{MeV}$, marginally compatible with the value quoted in the PDG, $M = 3886.6 \pm 2.4\,\text{MeV}$, $\Gamma = 28.1 \pm 2.6\,\text{MeV}$ [1].

2. III+tr.: The presence of the logarithmic branching point close to the physical region allows for the pole to be slightly deeper in the complex plane, $\Gamma \simeq 90\,\text{MeV}$. The mass is still safely above threshold.

3. IV+tr.: In this case the peak is generated by the combination of the logarithmic branching point with the virtual state pole on the IV sheet. Given that this sheet is not directly connected with the physical region, and that the triangle singularity contributes to the strength of the signal, the the pole position is not well constrained.

To summarize, we presented a coupled-channel study of the $Z_c(3900)$. We write a unitarized model that takes into account the possible rescattering with the bachelor particle in both channels. We consider several scenarios that, depending on the parametrization chosen, produce singularities that favor different physical interpretations, but present statistics is not able to distinguish between those. Similar conclusions were reached in [291, 292]. In the following Section, we will present a similar analysis where quality of data is actually able to discriminate between the various hypotheses.

Table 3: Mass and width of the $Z_c(3900)$ according to the scenarios which allow for the presence of a pole. Table from [293].

	III	III+tr.	IV+tr.
$M \equiv \text{Re}\,\sqrt{s_P}$ (MeV)	$3893.2^{+5.5}_{-7.7}$	3905^{+11}_{-9}	3900^{+140}_{-90}
$\Gamma \equiv 2\left\lvert\text{Im}\,\sqrt{s_P}\right\rvert$ (MeV)	48^{+19}_{-14}	85^{+45}_{-26}	240^{+230}_{-130}

2.5.2. The $P_c(4312)$

As discussed in Section 2.5, the discovery of two pentaquark resonances, $P_c(4380)$ and $P_c(4450)$ in the $\Lambda^0 \to J/\psi K^- p$ decay by LHCb in 2015 [254] triggered a frenzy of theory work to determine their

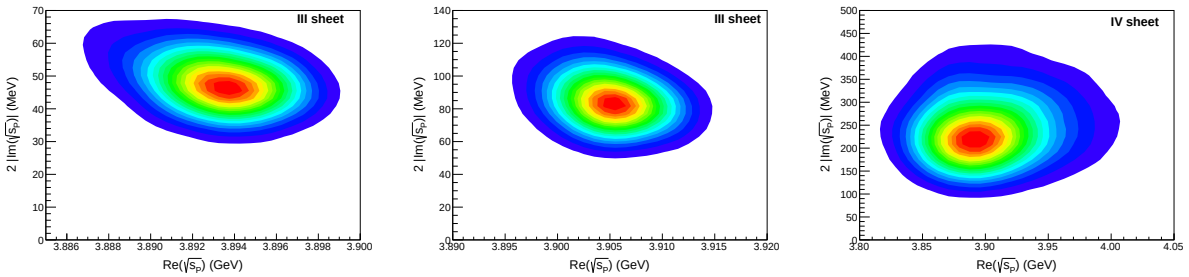

Figure 24: Pole position according to the scenarios which allow for the presence of a pole in the scattering matrix close to the physical region. The colored regions correspond to the 1σ confidence level. Figures from [293].

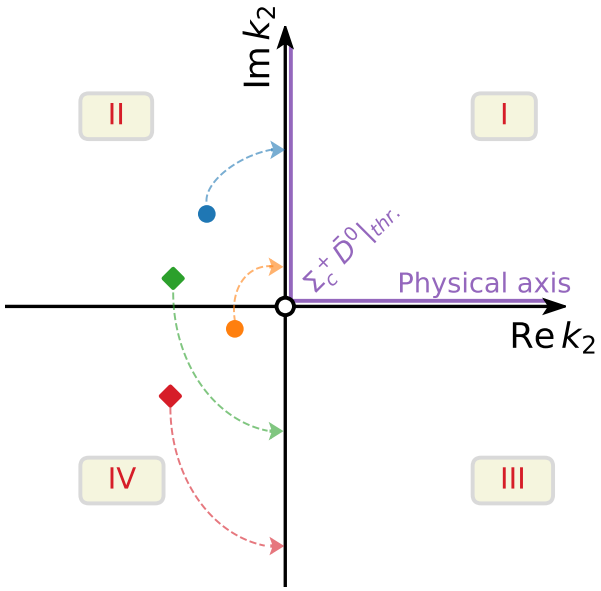

Figure 25: Analytic structure of the $P_c(4312)$ amplitude near the $\Sigma_c^+\bar{D}^0$ threshold. The adjacent Riemann sheets are continuously connected along the axes. The four possibilities for a resonant pole structure are depicted. When the $J/\psi\, p$ and $\Sigma_c^+\bar{D}^0$ channels decouple, the poles move to the imaginary k_2 axis along paths by the arrows. Poles moving to the positive (negative) axis correspond to bound (virtual) states.

nature. Later, with ten times more events [255], the $P_c(4450)$ signal was resolved into two peaks, $P_c(4440)$ and $P_c(4457)$, and a new $P_c(4312)$ was discovered. The latter is particularly interesting as it is a very clean isolated structure that peaks approximately 5 MeV below the $\Sigma_c^+\bar{D}^0$ threshold, making it a prime candidate for a hadron molecule composed of the two particles [264, 265, 294–299]. Such $\Sigma_c^+\bar{D}^0$ molecule with $J^P = 1/2^-$ was predicted in various models [300–305]. However, the opening of a threshold and the $\Sigma_c^+\bar{D}^0$ interaction can also generate a virtual state [306], where the interaction is attractive and generates a signal in the cross section, but is not strong enough to bind a state. A well known example is in neutron-neutron scattering, where the cross section is enhanced at threshold, despite no dineutron bound state exists [307]. The fact that such a narrow (~ 10 MeV) peak appears on top of what seems to be a smooth background permits a simplified analysis of the one-dimensional $J/\psi\, p$ invariant mass distribution. This was done in [308] following a bottom-up approach, favoring a virtual state interpretation.

We consider a two-channel production process, $\Lambda_b^0 \to K^-(J/\psi\, p)$ and $\to K^-(\Sigma_c^+\bar{D}^0)$. The presence of the bachelor antikaon does not create peaking structures, and the three-body effects described in Section 3 can be neglected. Since we focus on events around the $P_c(4312)$ peak only, far away from the $J/\psi\, p$ threshold, we can claim that the latter absorbs all the channels lighter than $\Sigma_c^+\bar{D}^0$. Similarly, the contributions from

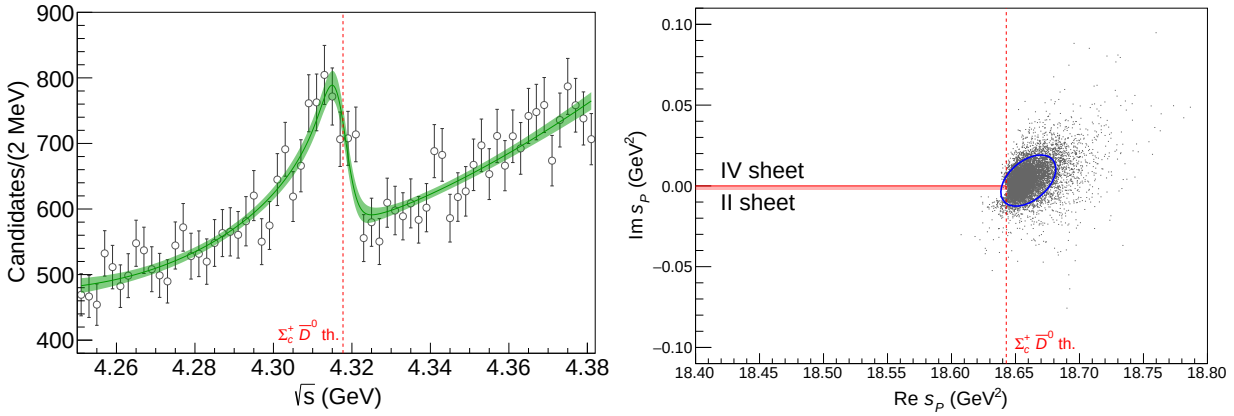

Figure 26: (left) Fit to the $\cos\theta_{P_c}$-weighted $J/\psi\, p$ mass distribution from LHCb in the $P_c(4312)$ region [255]. The solid line and green band show the fit result and the 1σ confidence level. (right) Pole obtained from the 10^4 bootstrap fits. The physical region is highlighted with a pink band. The poles lie on the II and IV Riemann sheets (which are continuously connected above the $\Sigma_c^+ \bar{D}^0$ threshold as shown in Figure 25). The blue ellipse accounts the 68% of the cluster. Figures from [308].

heavier channels can be absorbed by the real parameters of the scattering amplitude. The events distribution is given by [308, 309]

$$\frac{dN}{d\sqrt{s}} = \rho(s)\left[|F(s)|^2 + B(s)\right], \tag{31}$$

where $\rho(s)$ is a phase space factor. The $P_c(4312)$ signal is assumed to have a well-defined spin and, hence, it appears in a single partial wave $F(s)$. The smooth background $B(s)$ is a linear polynomial that parametrizes all the other partial waves that can be added incoherently. The amplitude $F(s) = P_1(s)\, T_{11}(s)$ is a product of a smooth production function $P_1(s)$ that encapsulates both the $J/\psi\, p\, K^-$ production and the cross channel Λ^* resonances projected into the same partial wave as $P_c(4312)$, and of the $J/\psi\, p \to J/\psi\, p$ scattering amplitude $T_{11}(s)$ that contains the details of the $P_c(4312)$. In a P-vector formalism, another term $P_2(s)T_{12}(s)$ would also appear, but since it contains the same singularities as $P_1(s)T_{11}(s)$, it can be reabsorbed there. Close to the $\Sigma_c^+ \bar{D}^0$ threshold, can be expanded as

$$\left(T^{-1}\right)_{ij} = M_{ij} - ik_i\, \delta_{ij}, \tag{32}$$

with $i, j = 1, 2$. The k_i momenta of the two channels are given by $k_1 = \sqrt{s - (m_\psi + m_p)^2}$ and $k_2 = \sqrt{s - (m_{\Sigma_c^+} + m_{\bar{D}^0})^2}$. The M_{ij} are given by

$$M_{ij}(s) = m_{ij} - c_{ij}\, s + \text{higher order terms}, \tag{33}$$

where $c_{ij} = 0$ under the scattering length approximation. The m_{11}, m_{12} and m_{22}, are fitted to the data. The analytical structure of $T_{11}(s)$ is shown in Figure 25. The amplitude has four poles in the complex s plane. Two of them are a conjugated pair that appears either on the II or IV sheet near the $\Sigma_c^+ \bar{D}^0$ threshold where the scattering length expansion is reasonable. The other two poles lie far away from the region of interest and are irrelevant. If $m_{12} \to 0$, the $\Sigma_c^+ \bar{D}^0$ channel decouples from $J/\psi\, p$. In this limit, the $P_c(4312)$ pole would become either a stable bound state on the I sheet, or a virtual state on the II sheet, depending on whether the pole would approach the positive or negative $\mathrm{Im}\, k_2$ axis, as represented in Figure 25. This is controlled by the sign of m_{22}, the inverse scattering length of the $\Sigma_c^+ \bar{D}^0$ chanel: if it is positive (negative) the resonance corresponds to a virtual (bound) state. The fit result is shown in Figure 26 together with the pole position from 10^4 bootstrap fits. For each bootstrap fit only one pole appears in this region. The resulting interpretation was a virtual state with $M_P = 4319.7 \pm 1.6\,\mathrm{MeV}$ and $\Gamma_P = -0.8 \pm 2.4\,\mathrm{MeV}$, where the negative value of the width corresponds to a IV sheet pole. Consistent results are obtained with the three datasets published by LHCb. Still in the scattering length approximation, the nature of the $P_c(4312)$ was

also studied using a deep neural network, employed as described in Section 2.3. The network was trained against four classes of lineshapes: $b|2$, $b|4$, $v|2$, and $v|4$; where the letter stands for the nature of the state, *i.e.* bound or virtual, and the number for the Riemann sheet where the pole is placed. The result for the classification process is shown in Figure 11. The analysis heavily favors the virtual state interpretation [83]. The model can be extended to the effective range approximation, allowing $c_{ij} \neq 0$ with a similar fit quality. The $P_c(4312)$ pole is pushed at $M_P = 4319.8 \pm 1.5\,\text{MeV}$ and $\Gamma_P = 9.2 \pm 2.9\,\text{MeV}$ on the II sheet, but jumps on the IV sheet as soon as m_{12} is made smaller, also favoring a virtual state interpretation.

2.5.3. An example of triangle singularity; the $P_c(4337)$

Triangle singularities have been proposed as a possible explanation of several resonances, and in particular of some of the pentaquark signals [7, 269, 271, 272]. Here we show a simple example of a triangle calculation applied to the new $P_c(4337)$ pentaquark recently reported by LHCb in the $B_s^0 \to J/\psi p\bar{p}$ decay close to the $\chi_{c0}p$ threshold [310]. The signal was found analyzing the Dalitz plot with a significance smaller than 5σ, so discovery was not claimed. A hint of a peak is visible in the $J/\psi p(\bar{p})$ projections, as seen in Figure 27, while no clear resonance is seen in $p\bar{p}$. Hence, one is tempted to perform an analysis of these mass distribution similar to that of the $P_c(4312)$. The low statistics makes an analysis of that kind not worth the effort. Also, a proper analysis should be implemented at the Dalitz plot level rather than on the projections. Nevertheless, we will use these invariant mass distributions to illustrate how a signal can be studied assuming it is generated by a scalar triangle singularity. The possible triangle is shown in Figure 27, where the exchanged f is, in principle, unknown. Here there are two options, the first one is to look up in the PDG tables a suitable state to be exchanged as f. In this case the $f_2(1950)$ seem like an adequate candidate. The second option is to let the data decide the mass and width of the f particle.

The intensity distribution is given by

$$\frac{dN}{d\sqrt{s}} = N_0\,\rho(s)\,|M(s)|^2\,, \tag{34}$$

where N_0 is the normalization parameter, the phase space is given by $\rho(s) = \lambda^{1/2}(s, m_B^2, m_p^2)\,\lambda^{1/2}(s, m_p^2, m_\psi^2)/\sqrt{s}$, and $M(s)$ is the scalar triangle amplitude in Figure 27 given by [269]

$$M(s) = \int_0^1 \frac{dx}{y_+ - y_-}\frac{1}{s}\left[\log\frac{(1-x-y_+)}{-y_+} - \log\frac{(1-x-y_-)}{-y_-}\right], \tag{35}$$

where

$$y_\mp = \frac{1}{2s}\left(-\beta \mp \sqrt{\beta^2 - 4\alpha s}\right), \tag{36a}$$

$$\alpha = x\,m_f^2 + (1-x)^2\,m_p^2\,, \tag{36b}$$

$$\beta = m_\chi^2 - (1-x)\,(s + m_p^2) - x\,m_B^2\,. \tag{36c}$$

To account for the width of the χ_0, we use a complex mass $m_\chi \to m_\chi - i\Gamma_\chi/2$. Hence we perform three different fits: phase space only, $f = f_2(1950)$, and f with mass and width as free parameters. These fits

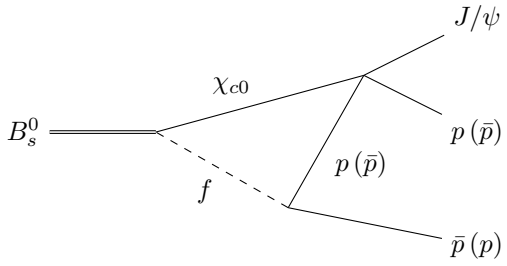

Figure 27: Considered triangle diagram for the $B_s^0 \to J/\psi\,p\bar{p}$ in the region where the $P_c(4337)$ signal appears.

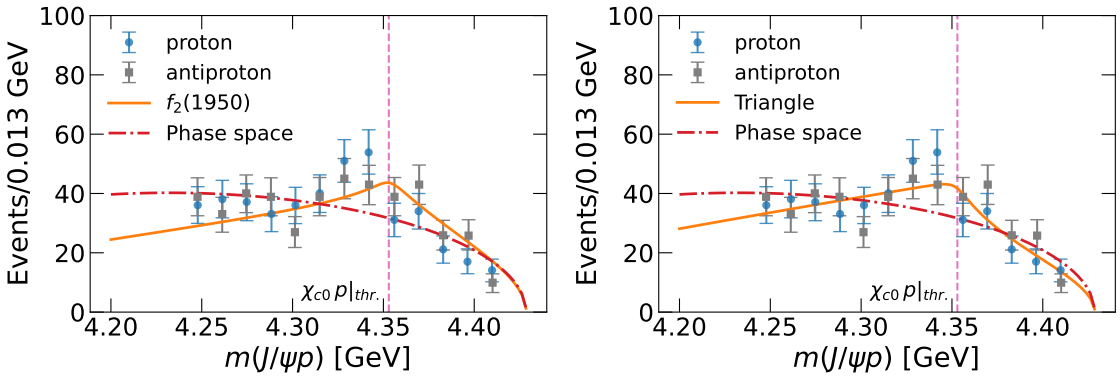

Figure 28: Fits to the $J/\psi p$ and $J/\psi\bar{p}$ projections from LHCb [310] in the energy region of the $\chi_{c0}\,p$ threshold where the $P_c(4337)$ signal appears. (left) fits using phase space only and a triangle with an exchanged $f_2(1950)$. (right) fits using phase space only and a triangle with an exchanged f whose mass and width are fitted to the data.

Table 4: Summary of χ^2/dof for the fits to the $P_c(4337)$ signal in the region of the $\chi_{c0}\,p$ threshold. For the free f fit we obtain $m_f = 1774\,\text{MeV}$ and $\Gamma_f = 217\,\text{MeV}$.

Fitted projection	Phase space	$f_2(1950)$	Free f
$J/\psi p$	1.52	1.73	0.76
$J/\psi\bar{p}$	1.81	1.31	1.25
$J/\psi p$ & $J/\psi\bar{p}$	1.6	1.47	0.95

are to three projection sets in the $(4.25, 4.40)$ GeV range: $J/\psi p$, $J/\psi\bar{p}$, and both combined. The fits are summarized in Table 4. Figure 28 shows the fits of the three models to the combined $J/\psi p$ and $J/\psi\bar{p}$ projections. If we take these results at face value, the phase space alone cannot explain the apparent bump, and the inclusion of the $f_2(1950)$ as a triangle improves the result, although not much. However, the triangle with a fitted mass and with ($m_f = 1774\,\text{MeV}$ and $\Gamma_f = 217\,\text{MeV}$) does improve the agreement between theory and experiment. Actually, this exchanged f lies very close to the $f_0(1710)$ shown in Section 2.4.1. However, this result has to be taken as a simple exercise, given that the statistical significance of the signal is very low.

3. Three-body scattering and decays

3.1. Three-body decay and Khuri-Treiman equations

One of the main issues posed by the presence of hadrons in any reaction is their final-state interactions, which are formally expressed in terms of the unitarity of the amplitude. In two-body scattering, unitarity is usually imposed in the direct channel only, as one is not sensitive to the details of the crossed channels. This is certainly not the case for a three-body decay, where the three possible two-hadron channels are physical, and one ideally wants to impose unitarity in all channels at once. The Khuri-Treiman (KT) formalism is a dispersive approach which indeed allows one to do so. KT equations were first written for $K \to 3\pi$ decays [311]. Soon after several papers appeared discussing different aspects of the formalism [312–316]. For the lightest mesons and lowest waves, KT equations can be justified in chiral perturbation theory at lowest orders via the so-called reconstruction theorem [317–321]. In Ref. [322] the formalism was applied to $\pi\pi$ scattering, and it was found to be equivalent to Roy equations [126, 131] when both formalisms are restricted to S- and P-waves. When higher waves are included in KT equations, still good agreement was found with other dispersive approaches [134]. We also point out that the KT decomposition of $\pi\pi$ scattering

in [322] is compatible with the amplitude decomposition obtained in [323] imposing crossing and chiral symmetries. In Ref. [324] we extended it to arbitrary quantum numbers of the decaying particle, by relating the isobar expansions in the three possible final states with the appropriate helicity crossing matrices (see also the discussion in Section 2.1). The decays of vector mesons to three pions have been studied with this formalism [325–330], and will be discussed in Section 3.1.1. However, the most important application is the study of the $\eta \to 3\pi$ decay [331–345], as we will see in Section 3.1.2. Other recent applications include Refs. [181, 293, 346, 347].

As in Section 2.1, the amplitude can be decomposed in

$$T(s,t,u) = \sum_{j=0}^{\infty} (2j+1) P_j(z_s) t_j(s) \ , \tag{37}$$

Equation (37) is an *infinite* sum of partial waves, each carrying both *left-* and *right-hand* cuts. The essence of the KT approach consists in performing instead an expansion of the amplitude into three (one for each two-meson subsystem) *finite* sums of isobars or single-variable functions, carrying only a *right-hand* cut. Explicitly,

$$T(s,t,u) = \sum_{j=0}^{j_{\max}} (2j+1) P_j(z_s) f_j(s) + \sum_{j=0}^{j_{\max}} (2j+1) P_j(z_t) f_j(t) + \sum_{j=0}^{j_{\max}} (2j+1) P_j(z_u) f_j(u) \ . \tag{38}$$

The "original" partial-wave expansion in Eq. (37) is performed in a single channel, namely the s-channel. In other words, the partial-waves $t_j(s)$ depend solely on the s Mandelstam variable. The dependence on t and u of $T(s,t,u)$ enters only through the Legendre polynomials, which are analytical functions of said variables. Because the sum of a finite number of analytical functions is again an analytical function, the only way in which singularities (such as poles or cuts) in t and u could appear is if the infinite sum in j diverges. However, in practice one can model only a finite number of partial waves, and as a consequence the analytical structure in the t- and u-variables is lost. The KT expansion in Eq. (38) solves the issue, by adding isobars f_j in the three variables, so the analytical structure in t and u can be partially recovered.

Furthermore, the application of dispersion relations to the single-variable functions $f_j(s)$ allows us to impose exact (elastic) unitarity to the two-meson subsystems, which can be essential in a three-body decay. Projecting this *model* decomposition for the amplitude into partial waves through (6), we find

$$t_j(s) = f_j(s) + \hat{f}_j(s) \ , \tag{39}$$

where $\hat{f}_j(s)$ is called the *inhomogeneity*,[5] given by

$$\hat{f}_j(s) = \sum_{j'} \int_{-1}^{+1} \mathrm{d}z \, P_j(z) \, P_{j'} \left(z_t(s, t_z(s,z), u_z(s,z)) \right) \, f_{j'}(t_z(s,z)) \ . \tag{40}$$

The structure of Eq. (39) is thus clear: the partial wave $t_j(s)$ receives a *direct* contribution from the isobar $f_j(s)$, plus an indirect contribution coming from the angular averages of all isobars of the crossed channels. To apply dispersion relations to the $f_j(s)$ functions, one writes its discontinuity,

$$\Delta f_j(s) = \Delta t_j(s) = \rho(s) \, \tau_j^*(s) \left(f_j(s) + \hat{f}_j(s) \right) \ , \tag{41}$$

where $\tau_j(s)$ is the two-meson elastic partial-wave amplitude, and $\rho(s)$ a phase space factor. The solution to

[5] The name inhomogeneity stems from the fact that if $\hat{f}_j = 0$ then the equation for the discontinuity of the isobar $f_j(s)$, Eq. (41) is homogeneous.

the integral equation stemming from the dispersive representation of $f_j(s)$ reads

$$f_j(s) = \Omega_j(s)\left(P_j^{(n)}(s) + I_j^{(n)}(s)\right) \ , \tag{42a}$$

$$I_j^{(n)}(s) = \frac{1}{\pi}\int_{s_{\rm th}}^{\infty} \mathrm{d}s' \left(\frac{s}{s'}\right)^{n+1} \frac{\sin\delta_j(s')\,\hat{f}_j(s')}{|\Omega_j(s')|\,(s'-s)} \ , \tag{42b}$$

$$\Omega_j(s) = \exp\left[\frac{s}{\pi}\int_{s_{\rm th}}^{\infty} \mathrm{d}s' \, \frac{\delta_j(s')}{s'(s'-s)}\right] \ . \tag{42c}$$

with $\Omega_j(s)$ and $\delta_j(s)$ the Omnés function and phase shift associated with the amplitude $\tau_j(s)$, respectively, and $P_j^{(n)}(s)$ a polynomial of n-th order. Above, n represents the number of subtractions performed to the dispersion relation. Determining this number is a rather delicate matter. From a purely mathematical point of view, subtracting the dispersion integral is simply a rearrangement of the equation. As the integral along the infinite circle should vanish, we just have to subtract sufficiently often to make this happen. Oversubtracted dispersion relations still satisfy the same unitarity equation, with the advantage that the more subtractions are used, the more suppressed is the dependence on the scattering shift at high energies. The price to pay is that one modifies the asymptotic behavior of the solution if no sum rule is imposed on the extra coefficients. However, this gives us more freedom than might be required by data. From a physical point of view, the Froissart bound [348, 349] is often invoked to control the asymptotic behavior of the partial waves, hence the number of subtractions.

Equations (42) and (40) represent a coupled system that can be solved, for example, iteratively. Things simplify considerably if one takes into account that the solutions of the dispersion relations are linear in the subtraction constants. This means that one can calculate a set of basis solutions that are independent of the numerical values of the latter.

The equations obtained, Eqs. (42), are valid for the scattering regime, and they have to be analytically continued for masses of the decaying particle $M > 3m$, where m is the mass of the light particle in the final state. The proper prescription was obtained in Refs. [350, 351]. After analytically continuing M_η^2 to its physical value, extra singularities appear, and these must be treated carefully. Also, depending on the solution method, $\hat{f}_j(s)$ could be needed for values of s outside the physical domain, so singularities in the relation of t with s and $\cos\theta$ also need to be taken care of. In this case, the integration path has to be chosen to avoid these extra singularities, see discussions in Refs. [324, 344, 345].

In the example we have discussed the case for all-scalar particles. In more realistic applications of KT equations details on the amplitudes or isobar are different, but the essence of the method remains. Further discussions and references can be found in Refs. [352–354].

3.1.1. $\omega \to 3\pi$ and $\psi \to 3\pi$ decays

The $\omega \to 3\pi$ decay has been previously studied with KT [325–329], and other dispersive approaches [355]. In particular, Refs. [325, 326] predicted the Dalitz plot parameters (to be defined below) of the decay, either considering or neglecting KT effects, but using in both cases unsubtracted dispersion relations to solve KT equations. The BESIII collaboration reported the measurement of the Dalitz plot parameters [356], and found a better agreement with the theoretical predictions of Refs. [325, 326] when the rescattering effects were neglected, as can be seen in Table 5. In view of this seeming disagreement, in Ref. [330] we have reviewed the application of the KT formalism to this decay.

For a vector decaying into three pions, the differential decay width is proportional to $|T(s,t,u)|^2 = \phi(s,t,u)\,|F(s,t,u)|^2$, where $\phi(s,t,u) = s\,t\,u - m_\pi^2(m_V^2 - m_\pi^2)^2$ is the Kibble function [357], and $F(s,t,u)$ is an invariant amplitude. The Dalitz-plot parameters are obtained from a polynomial expansion of $|F(s,t,u)|^2$,

$$|F(s,t,u)|^2 = |N|^2\left[1 + 2\alpha Z + 2\beta Z^{3/2}\sin 3\varphi + 2\gamma Z^2 + \mathcal{O}(Z^{5/2})\right] . \tag{43}$$

$$\sqrt{Z}\,\cos\varphi = \frac{t-u}{\sqrt{3}R_\omega} \, , \quad \sqrt{Z}\,\sin\varphi = \frac{s_c - s}{R_\omega} \, , \tag{44}$$

where $s_c = \frac{1}{3}(m_\omega^2 + 3m_\pi^2)$ and $R_\omega = \frac{2}{3}m_\omega(m_\omega - 3m_\pi)$. In Eq. (43), α, β and γ are the real-valued Dalitz-plot parameters and N is an overall normalization. The experimental determination of these parameters by the WASA-at-COSY [358] and BESIII [356] collaborations are shown in Table 5, together with the theoretical predictions of Refs. [326] and [181].

The partial wave expansion of the amplitude reads

$$F(s,t,u) = \sum_{j\,\text{odd}} (p(s)q(s))^{j-1} P_j'(z_s) f_j(s)\,. \tag{45}$$

Similarly as explained above, the KT formalism is applied to the amplitude $F(s,t,u)$, and truncating the KT expansion to $j_{\max} = 1$ (only $\pi\pi$ $I = J = 1$ wave), we have:

$$F(s,t,u) = F_1(s) + F_1(t) + F_1(u)\ , \tag{46a}$$

$$f_1(s) = F_1(s) + \hat{F}_1(s)\ , \tag{46b}$$

$$\hat{F}_1(s) = 3\int_{-1}^{+1} \mathrm{d}z\, \frac{1-z^2}{2} F_1(t(s,z_s))\ , \tag{46c}$$

$$F_1(s) = \Omega_1^1(s)\left(a + b\,s + \frac{s^2}{\pi}\int_{4m_\pi^2}^{\infty} \mathrm{d}s' \frac{\sin\delta_1^1(s')\,\hat{F}_1(s')}{(s')^2\,|\Omega_1^1(s')|\,(s'-s)}\right)\ . \tag{46d}$$

The above expression for $F_1(s)$ is the solution of the integral equation corresponding to a once-subtracted dispersion relation.

Together with the $\omega \to 3\pi$ Dalitz plot parameters, we also analyze the $\omega\pi^0$ transition form factor, $f_{\omega\pi^0}(s)$, that controls the $\omega \to \pi^0\gamma^*$ amplitude. A once-subtracted dispersion relation for this TFF gives

$$f_{\omega\pi^0}(s) = |f_{\omega\pi^0}(0)|\, e^{i\phi_{\omega\pi^0}(0)} + \frac{s}{12\pi^2}\int_{4m_\pi^2}^{\infty} \frac{ds'}{(s')^{3/2}} \frac{p^3(s')\,F_\pi^{V\,*}(s')\,f_1(s')}{(s'-s)}\ , \tag{47}$$

where $F_\pi^V(s)$ is the pion vector form factor. Because of the low $\pi\pi$ invariant masses explored here, we approximate $F_\pi^V(s) = \Omega_1^1(s)$. Data from the A2 collaboration at MAMI [359] and by the NA60 collaboration at SPS [360, 361] for $|f_{\omega\pi^0}(s)|^2$ (normalized at $s = 0$) for low $\omega\pi^0$ invariant mass are shown in Figure 29. From the NA60 data, we will only consider in our fits the most up to date analysis [361]. The free parameters in Eqs. (46d) and (47) are the complex constant b, the absolute values $|f_{\omega\pi^0}(0)|$ and $|a|$, and the relative phase $\phi_{\omega\pi^0}(0) - \phi_a$, where ϕ_a is the phase of the constant a. We fit these parameters to the experimental data on $|f_{\omega\pi^0}(s)|^2$, the experimental Dalitz plot parameters, and the $\omega \to 3\pi$ and $\omega \to \pi^0\gamma$ widths. Two different best fits are obtained, corresponding to a lower or higher value of the phase $\phi_{\omega\pi^0}(0)$ [330]. In Table 5 we show the Dalitz plot parameters obtained as an output of the fit, in good agreement with the experimental ones. In Figure 29 we show our calculation of $|f_{\omega\pi^0}(s)|^2$ resulting from the fit, also in good agreement with data. Therefore we conclude that the KT equations are capable of describing the low-energy experimental information concerning $\omega \to 3\pi$ and $\omega \to \gamma^*\pi^0$, although a further subtraction has to be performed.

The KT description of $J/\psi \to 3\pi$, proceeds in an identical fashion as the one discussed above. Despite the phase space here is much larger, so the production of excited states other than the $\rho(770)$ is in principle allowed, this decay is vastly dominated by the $\rho\,\pi$ intermediate state. The ρ bands are clearly visible in the Dalitz plot from BESIII [362], while almost no events appear in the center. We perform fits to the BESIII $m_{\pi\pi}$ invariant mass distribution after solving the KT equations for $J/\psi \to 3\pi$ [363] and using the phase parametrization of [364], which is valid up to 2 GeV. The unsubtracted KT equation does not provides a good description of the data. In contrast, a satisfactory result can be achieved performing one subtraction in $F(s)$, with the subtraction constant fitted to data. The result of the fit yields $b = 0.20(1)e^{i2.68(1)}\,\text{GeV}^{-2}$. While this fit provides an excellent description of the data up to ~ 1 GeV, contributions of higher waves seem to be required to describe the intermediate energy region around ~ 1.5 GeV. The next allowed wave is the F-wave, which can be modeled by a resonance $\rho_3(1690)$. The isobar decomposition of the amplitude including F-waves becomes [325]

$$F(s,t,u) = F_1(s) + F_1(t) + F_1(u) + \kappa^2(s)P_3'(z_s)F_3(s) + \kappa^2(t)P_3'(z_t)F_3(t) + \kappa^2(u)P_3'(z_u)F_3(u)\,, \tag{48}$$

Table 5: Dalitz plot parameters α, β, and γ, obtained by previous theoretical [325, 326, 355] and experimental [356, 358] analyses. For the dispersive analyses [325, 326], we show the results obtained with and without KT equations (*i.e.*, with $F_1(s)$ proportional to an Omnés function). Also shown are our results in Ref. [330] for the two solutions found in that work. The quoted uncertainty for Ref. [325] corresponds to the range explored in that work. The uncertainties quoted for Refs. [356, 358] correspond to the experimental statistical one. The first and second uncertainty quoted for Ref. [330] are statistical and systematic ones, respectively.

	Reference	α ($\times 10^{-3}$)	β ($\times 10^{-3}$)	γ ($\times 10^{-3}$)
2 par. (α, β)	Ref. [326], w KT	84	28	–
	Ref. [326], w/o KT	125	30	–
	Ref. [325], w KT	79(5)	26(2)	–
	Ref. [325], w/o KT	130(5)	31(2)	–
	WASA-at-COSY [358]	133(41)	37(54)	–
	BESIII [356]	120.2(8.1)	29.5(9.6)	–
	Ref. [330], low $\phi_{\omega\pi^0}(0)$	121.2(7.7)(0.8)	25.7(3.3)(3.3)	–
	Ref. [330], high $\phi_{\omega\pi^0}(0)$	120.1(7.7)(0.7)	30.2(4.3)(2.5)	–
3 par. (α, β, γ)	Ref. [326], w KT	80	27	8
	Ref. [326], w/o KT	113	27	24
	Ref. [325], w KT	77(4)	26(2)	5(2)
	Ref. [325], w/o KT	116(4)	28(2)	16(2)
	BESIII [356]	111(18)	25(10)	22(29)
	Ref. [330], low $\phi_{\omega\pi^0}(0)$	112(15)(2)	23(6)(2)	29(6)(8)
	Ref. [330], high $\phi_{\omega\pi^0}(0)$	109(14)(2)	26(6)(2)	19(5)(4)

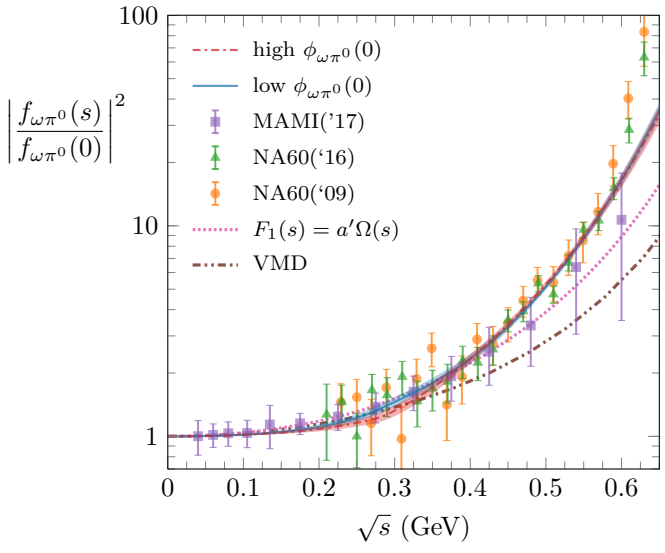

Figure 29: Transition form factor squared, $|f_{\omega\pi^0}(s)|^2 / |f_{\omega\pi^0}(0)|^2$. The experimental data are from the A2 collaboration at MAMI [359] and the NA60 collaboration at SPS [360, 361]. The results of Ref. [330] are shown by the red and blue bands, corresponding to the high and low $\phi_{\omega\pi^0}(0)$ phase fits. The results obtained with the VMD approximation (including an explicit ρ pole as an amplitude) are shown with a double-dotted-dashed brown line, whereas the results obtained when the KT effects are neglected are shown with a dotted pink line. Figure from [330].

where P_3' is the derivative of the Legendre polynomial. The function $F_3(s)$ contains the $\rho_3(1690)$ contribution, which can be represented by a Breit-Wigner,

$$F_3(s) = P(s)\frac{m_{\rho_3}^2}{m_{\rho_3}^2 - s - im_{\rho_3}\Gamma_{\rho_3}(s)}\,, \tag{49}$$

with the energy-dependent width given by

$$\Gamma_{\rho_3}(s) \;=\; \frac{\Gamma_{\rho_3} m_{\rho_3}}{\sqrt{s}}\left(\frac{p_\pi(s)}{p_\pi(m_{\rho_3}^2)}\right)^7 \left(F_R^\ell(s)\right)^2\,, \quad p_\pi(s) = \frac{\sqrt{s}}{2}\sigma_\pi(s)\,. \tag{50}$$

The $F_R^{\ell=3}(s)$ denotes the Blatt-Weisskopf factor that limits the growth of the isobar [365],

$$F_R^{\ell=3}(s) \;=\; \sqrt{\frac{z_0(z_0-15)^2 + 9(2z_0-5)}{z(z-15)^2+9(2z-5)}}\,, \quad z = r_R^2 p_\pi^2(s)\,, \quad z_0 = r_R^2 p_\pi^2(m_{\rho_3}^2)\,, \tag{51}$$

with the hadronic scale $r_R = 2\,\mathrm{GeV}^{-1}$.

The polynomial $P(s)$ in Eq. (49) parametrize some unknown energy dependence not directly related to the propagation of the $\rho_3(1690)$ resonance. Taking it linear, we add two additional (complex) parameters to the fit producing and improved description of the data.

The KT description of the partner reaction $\psi' \to 3\pi$ is formally identical to the one of $J/\psi \to 3\pi$. However, the experimental situation changes drastically for this decay: the $\rho\,\pi$ contribution is subleading and almost all events are found to be in the center of the Dalitz plot [362]. This effect if know as the "$\rho\pi$ puzzle", which remains to be understood. Other important aspects of $J/\psi \to 3\pi$ have been considered in [366, 367]. A description orthogonal to KT, that takes into account the full tower of partial waves as given by the Veneziano amplitude, is found in [368].

3.1.2. $\eta \to 3\pi$

The process $\eta \to 3\pi$ is very interesting because since this decay is forbidden by isospin symmetry–three pions cannot combine to a system with vanishing angular momentum, zero isospin, and even C-parity–it offers an unique experimental access to the light quark mass ratio

$$Q^2 = \frac{m_s^2 - \hat{m}^2}{m_d^2 - m_u^2} \quad \text{and} \quad \hat{m} = \frac{m_u + m_d}{2}. \tag{52}$$

This is done by comparing the experimental measured decay width with the reduced amplitude $M(s,t,u)$ integrated over the phase space:

$$\Gamma\big(\eta \to \pi^+\pi^-\pi^0\big) = \frac{1}{Q^4}\frac{M_K^4(M_K^2 - M_\pi^2)^2}{6912\pi^3 M_\eta^3 M_\pi^4 F_\pi^4}\int_{s_{\min}}^{s_{\max}} \mathrm{d}s \int_{u_-(s)}^{u_+(s)} \mathrm{d}u\,|M(s,t,u)|^2\,. \tag{53}$$

The aim is to compute the amplitude $M(s,t,u)$ with the highest possible accuracy. This is not an easy task since there are strong rescattering effects among the final-state pions. These were initially calculated perturbatively in χPT. The current algebra result is $\Gamma(\eta \to \pi^+\pi^-\pi^0)_{\mathrm{LO}} = 66\,\mathrm{eV}$ [369], and receives a substantial enhancement $\Gamma(\eta \to \pi^+\pi^-\pi^0)_{\mathrm{NLO}} = 160(50)\,\mathrm{eV}$ due to chiral one-loop corrections. The result is still far from the experimental value $\Gamma(\eta \to \pi^+\pi^-\pi^0) = 300 \pm 12\,\mathrm{eV}$ suggesting a convergence problem. Moreover it has been shown that the two-loop calculation [321] may lead to a precise numerical prediction only after the low-energy constants (LECs) appearing in the amplitude are determined reliably. In particular, the role played by the $\mathcal{O}(p^6)$ LECs is nonnegligible and they are largely unknown. A more accurate approach relies on dispersion relations to evaluate rescattering effects to all orders [332–335]. This is not completely independent of χPT, because the dispersive representation requires the subtraction constants as input, and they can be calculated in χPT.

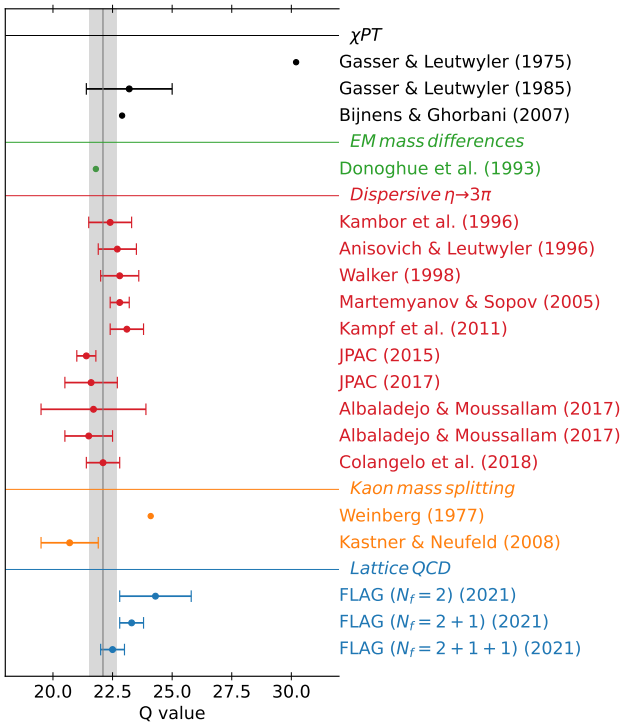

Figure 30: Summary of Q values found in the literature [321, 333–336, 340, 341, 343, 344, 370–376]. The gray line is the weighted average of dispersive $\eta \to 3\pi$ extractions (red) and the grey band its 1σ uncertainty.

There has been a renewed interest in $\eta \to 3\pi$ dispersive analysis due to new and more precise measurements of this decay. In particular recent measurements of the Dalitz plot of the charged ($\eta \to \pi^+\pi^-\pi^0$) channel by KLOE [377, 378] and BESIII [379] and of the neutral channel ($\eta \to \pi^0\pi^0\pi^0$) by A2 [380] have achieved an impressive level of precision. New measurements are planned by BESIII and at JLab by GlueX [381, 382] and CLAS [383], with completely different systematics and even better accuracy.

In the application of KT equations to $\eta \to 3\pi$ decays, one truncates the expansion of the amplitude by neglecting D-and higher single-variable functions, thus writing

$$M(s,t,u) = M_0^0(s) + (s-u)M_1^1(t) + (s-t)M_1^1(u) + M_2^0(t) + M_2^0(u) - \frac{2}{3}M_2^0(s)\,. \tag{54}$$

The functions $M_I^\ell(s)$ have isospin I and angular momentum ℓ. As said before, in the context of light mesons this decomposition is commonly referred to as a *reconstruction theorem* [317–320]. The latter relies on the observation that up to corrections of order $\mathcal{O}(p^8)$ (or three loops) in the chiral expansion, partial waves of any meson–meson scattering process with angular momentum $\ell \geqslant 2$ contain no imaginary parts. Since in Eq. (54) the angular momentum of an isobar is unambiguosly given by its isospin, we will omit ℓ in the following and refer to M_I^ℓ by M_I. The splitting of the full amplitude into these single-variable functions is not unique: there is some ambiguity in the distribution of the polynomial terms over the various M_I due to $s + t + u$ being constant.

As discussed above, using analyticity and unitarity allows one to construct dispersion relations for the

single-variable functions $M_I(s)$, and one arrives to

$$M_I(s) = \Omega_I(s)\left\{P_I(s) + \frac{s^{n_I}}{\pi}\int_{4m_\pi^2}^{\infty}\frac{\mathrm{d}s'}{s'^{n_I}}\frac{\sin\delta_I(s')\hat{M}_I(s')}{|\Omega_I(s')|(s'-s-i\epsilon)}\right\}, \tag{55a}$$

$$\hat{M}_I(s) = \sum_{n,I'}\int_{-1}^{1}\mathrm{d}\cos\theta\ \cos^n\theta\, c_{nII'}M_{I'}\big(t(s,\cos\theta)\big)\ , \tag{55b}$$

completely analogous to Eqs. (42). The explicit forms of the coefficients $c_{nII'}$ can be found *e.g.* in Refs. [334]. To study the convergence behavior of the integrand we have to make assumptions as regards the asymptotic behavior of the phase shifts. It is usually assumed that

$$\delta_0^0(s)\to\pi\,,\quad \delta_1^1(s)\to\pi\,,\quad \text{and}\quad \delta_2^0(s)\to 0\,,\quad \text{as}\quad s\to\infty\,. \tag{56}$$

An asymptotic behavior of $\delta(s)\to k\pi$ implies that the corresponding Omnès function behaves like s^{-k} for high s. If the Froissart bound [348, 349] is assumed as discussed earlier, this implies $M_0(s), M_2(s)\to s$ and $M_1(s)\to$ const., thus four subtractions are required. Since $s+t+u = M_\eta^2+3M_\pi^2$, there exists a five-parameter polynomial transformation of the single-variable functions M_I that leaves the amplitude $M(s,t,u)$ in Eq. (54) invariant. Therefore there is some freedom to assign the subtraction constants to the functions M_I. Taking the phase shifts constant (at multiples of π) at high energies ensures the integrands in Eq. (55a) to vanish above $s > s_{\mathrm{cut}}$, therefore convergence is no longer an issue. We can relax the Froissart bound and oversubtract the dispersive integrals (55a) with the aim of being insensitive, in the physical region, to the high-energy inelastic behavior of the phase, which is unknown. The price to pay is that one has more subtraction constants to be determined. In some recent dispersive analyses [336, 342, 343], 6 subtraction constants have been considered. In Ref. [344] only 4 subtraction constants are considered in the single channel approximation. The subtraction constants are unknown and have to be determined using a combination of experimental information and theory input. In particular since the overall normalization multiplies $1/Q^2$, the quantity that should be extracted from the analysis, it cannot be obtained from data alone and one has to match to χPT. On the other hand, this matching has to be performed in such a way that the problematic convergence of the chiral expansion is not transferred directly to the dispersive representation. This can be achieved by matching the amplitude around the Adler zeros. As discussed in Section 3.1, several dispersive analyses have been performed over the last few years. All these analyses rely on the same theoretical ingredients described above with some subtle differences. For instance the analysis of JPAC [340, 341] uses a different technique to solve the dispersion relation, called the Pasquier inversion [315, 339, 384]. Moreover the left-hand cut is approximated using a Taylor series in the physical region. This allows to reduce the number of subtraction constants from six to three. The result is then matched to NLO χPT near the Adler zero to extract a value for Q. The analysis of Ref. [342, 343] is a modern update of the approach of Anisovich and Leutwyler [334]. There a matching to NLO and NNLO χPT has been performed. Moreover electromagnetic and isospin breaking corrections have been taken into account. Fits to experimental data by KLOE [378], but also to the recent neutral-channel Dalitz plot by A2 [380] have been explored. Finally the analysis of Ref. [344] studies the impact of inelasticities on the dispersive integrals. To this end, the inelastic channels $\eta\pi$ and $K\bar{K}$ have been included. Figure 30 summarizes the results on the extraction of Q from the different analyses. As can be seen in Figure 30, the extracted values of Q agree very well between the different dispersive analyses allowing $\eta\to 3\pi$ to be the golden plate channel to extract the light quark mass ratios.

3.2. $\mathbf{3}\to\mathbf{3}$ *scattering*

In recent years, the problem of describing multihadron scattering processes has generated significant interest. It is well-established experimentally that many resonances couple strongly to three- or more particle channels [385]. Some of the most intriguing particles, which do not fit the naïve quark model predictions, like the Roper resonance $N^*(1440)$, the $a_1(1420)$ seen by COMPASS [386, 387], and the exotic $\pi_1(1600)$ [190, 388], $X(3872)$, and other XYZ states have significant three-particle decay modes [1]. Three-body couplings

might lead to non-standard line shapes and complicated structure of the amplitudes [267, 389], allowing for ambiguities in interpretations of the hadron of interest [3, 7, 390, 391]. To parametrize three-body processes, and in consequence, build and compare phenomenological models properly describing properties of the QCD states, one needs to establish a general theoretical framework of the three-body processes relying on the S-matrix principles.

In addition to phenomenological studies, usually based on particular models and approximations, it is desired to determine the properties of the strongly interacting resonances directly from the underlying theory, using Lattice QCD. The essential challenge to study the resonance physics on the lattice is the fact that resonances are not eigenstates of the QCD Hamiltonian. Moreover, one can not define scattering processes in a finite volume in the usual sense, since there are no asymptotic states, and the continuum spectrum becomes a discrete set of bound states in the box. Fortunately, it was shown by Lüscher [392, 393] that the scattering information is hidden in the volume dependence of the lattice spectrum. In the case of two hadrons being scattered off of each other one can obtain the two-body scattering phase shifts from the so-called two-body *quantization condition* [394–406]. This has been applied to many systems of physical relevance [12]. The three-body generalization of the Lüsher's idea has been developed, leading to different three-particle quantization conditions [407–412]. They allow one to obtain objects called three-body K_{df} matrices, from the three-particle finite-volume spectrum. They are analogous to the two-body K matrix, however, they do not have a simple interpretation of a phase shift. Because of the multi-variable nature of the three-body process, formalisms required to describe the scattering of three hadrons become involved and a three-body K_{df} matrix is related to the genuine three-body infinite-volume amplitude through the set of complicated integral equations. Once they are solved, one obtains the on-shell three-body scattering amplitude computed directly from QCD. In the last step, it has to be continued to the complex energies, to identify complex poles corresponding to three-body resonances.

Two main relativistic on-shell $\mathbf{3} \to \mathbf{3}$ scattering formalisms have been developed and applied to a range of physical problems: **(a)** the relativistic EFT (RFET) established by Hansen, Sharpe, and Briceño in Refs. [408, 413–415], and **(b)** the S-matrix unitarity, also referred to as the B-matrix approach, built by Mai *et al.* [409, 416, 417] and the JPAC group [53, 418, 419]. All of these works have been shown to be equivalent both in their infinite-volume [420] and finite-volume [421] versions. In the following, we summarize both approaches and review the relevant results. Supplementary reviews can be found in Refs. [422, 423].

3.2.1. Relativistic three-body formalisms

Description of the three-body unitarity for the $\mathbf{3} \to \mathbf{3}$ scattering amplitude is considerably more involved than in the two-body case. Parametrizations satisfying unitarity in the three-body systems have been studied by various authors in the '60s and '70s [25, 424–438]. The description of three-body states is usually based on the isobar approximation, in which one represents the amplitude as a sum of truncated partial-wave expansions, one for each pair of particles in the external three-body state [439]. This provides a good description of three-particle final states in the kinematic region, where intermediate two-body resonances dominate over the scattering process. Moreover, the isobar model is capable of reproducing the threshold singularities in two-body subchannels by including only a finite number of partial waves. In the isobar representation, the $\mathbf{3} \to \mathbf{3}$ amplitude is decomposed into $\mathcal{A}_{\boldsymbol{p}'\boldsymbol{p}}$ isobar–spectator amplitudes, where the indices label one of the particles in the initial and final state. This particle is called the *spectator*, whereas the other two form an *isobar* (also called a *pair*), corresponding to the given spectator. The isobar-spectator amplitudes can be pictured as describing a $\mathbf{2} \to \mathbf{2}$ scattering process of a quasi-particle and a stable spectator.

To highlight the features of this parametrization we consider a simplified elastic scattering process in the center of momentum frame (CMF), in which incoming and outgoing state consists of three spinless, indistinguishable particles of mass m and total invariant mass squared s. Let $p = (\omega_{\boldsymbol{p}}, \boldsymbol{p})$ be the four-momentum of the initial spectator in one isobar-spectator configuration, where $\omega_{\boldsymbol{p}} = \sqrt{\boldsymbol{p}^2 + m^2}$, and $\sigma_{\boldsymbol{p}}$ is the invariant mass squared of the corresponding initial isobar. We denote analogous variables for outgoing particles with a prime, e.g., the outgoing spectator's four-momentum is $p' = (\omega_{\boldsymbol{p}'}, \boldsymbol{p}')$. Unitarity constrains the $\mathbf{3} \to \mathbf{3}$ amplitudes on the real energy axis, which restricts the imaginary parts of the partial-wave-projected isobar–spectator amplitudes. Using the notation of Refs. [419, 420], the elastic $\mathbf{3} \to \mathbf{3}$ scattering amplitude, $\mathcal{M}$, is defined as the three-body element of the T matrix. It is convenient to work with the

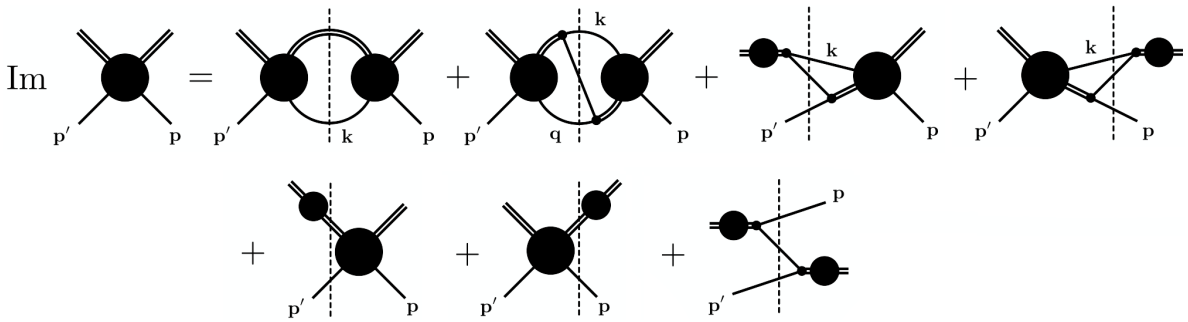

Figure 31: Diagrammatic representation for the $\mathbf{3} \to \mathbf{3}$ unitarity relation, Eq. (57), for the connected isobar-spectator amplitude $\mathcal{A}_{\boldsymbol{p}'\boldsymbol{p}}$. A single external line represents a spectator, while a double external line—an isobar. Closed loops yield three-dimensional integrations over the labeled spectator momentum, and the dashed vertical lines represent placing all three intermediate state particles on their mass-shell. A solid circle with both external isobars and spectators is the amplitude $\mathcal{A}$, and a solid circle only with external isobars is the two-body amplitude $\mathcal{F}$. Momentum flow is from right to left, as before, and each amplitude on the left of the dashed line is hermitian conjugated. Figure adapted from [420].

unsymmetrized isobar-spectator amplitude $[\mathcal{M}_{\boldsymbol{p}'\boldsymbol{p}}]_{\ell' m'_\ell;\, \ell m_\ell}$, written in the so called $(\boldsymbol{p}\ell m_\ell)$ basis in which it can be treated as an infinite-dimensional matrix in the isobars angular momentum space. In the simplified case considered here, the three-body amplitude $\mathcal{M}$ becomes a symmetrized sum of 9 identical isobar-spectator amplitudes $\mathcal{M}_{\boldsymbol{p}'\boldsymbol{p}}$, corresponding to 9 identical divisions of the final and initial state particles into spectator-isobar configurations. The amplitude depends on eight kinematical variables: initial and final isobar invariant masses squared, total invariant mass of the three-body system, the total angular momentum, and angular momenta of isobars (ℓ, m_ℓ) and (ℓ', m'_ℓ). The multi-variable nature of the three-body scattering is the main factor making its description significantly more complicated than in the $\mathbf{2} \to \mathbf{2}$ case. The unsymmetrized partial-wave projected three-body amplitude $\mathcal{M}_{\boldsymbol{p}'\boldsymbol{p}}$ is further separated into a connected and disconnected part, $\mathcal{M}_{\boldsymbol{p}'\boldsymbol{p}} = \mathcal{A}_{\boldsymbol{p}'\boldsymbol{p}} + \mathcal{F}_{\boldsymbol{p}}\, \delta_{\boldsymbol{p}'\boldsymbol{p}}$ where $\delta_{\boldsymbol{p}'\boldsymbol{p}}$ is the properly normalized momentum-conserving δ-function. The disconnected part is given by the two-body scattering amplitude in the isobar sub-channel. It depends on the isobar angular momentum and its invariant mass squared $\sigma_{\boldsymbol{p}}$. Above the isobar threshold, the disconnected amplitude satisfies the usual $\mathbf{2} \to \mathbf{2}$ unitarity relation, $\mathrm{Im}\, \mathcal{F}_{\boldsymbol{p}} = \mathcal{F}^\dagger_{\boldsymbol{p}}\, \bar{\rho}_{\boldsymbol{p}}\, \mathcal{F}_{\boldsymbol{p}}$, where $\bar{\rho}_{\boldsymbol{p}}$ is the two-body phase space multiplied by the threshold Heaviside function indicated with the bar. The unsymmetrized connected $\mathbf{3} \to \mathbf{3}$ amplitude satisfies the three-body unitarity,

$$\mathrm{Im}\, \mathcal{A}_{\boldsymbol{p}'\boldsymbol{p}} = \int_{\boldsymbol{k}} \mathcal{A}^\dagger_{\boldsymbol{p}'\boldsymbol{k}}\, \bar{\rho}_{\boldsymbol{k}}\, \mathcal{A}_{\boldsymbol{k}\boldsymbol{p}} + \int_{\boldsymbol{q}} \int_{\boldsymbol{k}} \mathcal{A}^\dagger_{\boldsymbol{p}'\boldsymbol{q}}\, \mathcal{C}_{\boldsymbol{q}\boldsymbol{k}}\, \mathcal{A}_{\boldsymbol{k}\boldsymbol{p}} + \int_{\boldsymbol{k}} \mathcal{A}^\dagger_{\boldsymbol{p}'\boldsymbol{k}}\, \mathcal{C}_{\boldsymbol{k}\boldsymbol{p}}\, \mathcal{F}_{\boldsymbol{p}} + \int_{\boldsymbol{k}} \mathcal{F}^\dagger_{\boldsymbol{p}'}\, \mathcal{C}_{\boldsymbol{p}'\boldsymbol{k}}\, \mathcal{A}_{\boldsymbol{k}\boldsymbol{p}} \tag{57}$$

$$+ \mathcal{F}^\dagger_{\boldsymbol{p}'}\, \bar{\rho}_{\boldsymbol{p}'}\, \mathcal{A}_{\boldsymbol{p}'\boldsymbol{p}} + \mathcal{A}^\dagger_{\boldsymbol{p}'\boldsymbol{p}}\, \bar{\rho}_{\boldsymbol{p}}\, \mathcal{F}_{\boldsymbol{p}} + \mathcal{F}^\dagger_{\boldsymbol{p}'}\, \mathcal{C}_{\boldsymbol{p}'\boldsymbol{p}}\, \mathcal{F}_{\boldsymbol{p}}\,. \tag{58}$$

where $\mathcal{C}_{\boldsymbol{p}'\boldsymbol{p}}$ is the *recoupling* coefficient between a pair in one state to a different pair in the same state, which is defined as the imaginary part of the amputated one particle exchange (OPE) amplitude $\mathcal{G}_{\boldsymbol{p}'\boldsymbol{p}}$, see Figure 31. The recoupling coefficients are a distinct feature of the three-body scattering unitarity relation.

The most general parametrization satisfying these constraints is provided by the so-called B-matrix equation, which is a linear integral equation, analogous to the Bethe-Salpeter equation. It was introduced first in Ref. [437] and later revisited in Refs. [416, 418, 440], which corrected certain deficiencies of the original formulation related to the unitarity of the formalism above the breakup threshold. In the following, we give a concise overview of the B-matrix formalism, as described in Ref. [420]. The B-matrix parametrization for the connected part $\mathcal{A}_{\boldsymbol{p}'\boldsymbol{p}}$ of the amplitude $\mathcal{M}_{\boldsymbol{p}'\boldsymbol{p}}$ is given by the matrix-integral linear equation,

$$\mathcal{A}_{\boldsymbol{p}'\boldsymbol{p}} = \mathcal{F}_{\boldsymbol{p}'}\, \mathcal{B}_{\boldsymbol{p}'\boldsymbol{p}}\, \mathcal{F}_{\boldsymbol{p}} + \int_{\boldsymbol{k}} \mathcal{F}_{\boldsymbol{p}'}\, \mathcal{B}_{\boldsymbol{p}'\boldsymbol{k}}\, \mathcal{A}_{\boldsymbol{k}\boldsymbol{p}}\,, \tag{59}$$

as demonstrated in Figure 32. The B-matrix kernel is written as a sum of two terms,

$$\mathcal{B}_{\boldsymbol{p}'\boldsymbol{p}} = \mathcal{G}_{\boldsymbol{p}'\boldsymbol{p}} + \mathcal{R}_{\boldsymbol{p}'\boldsymbol{p}}\,, \tag{60}$$

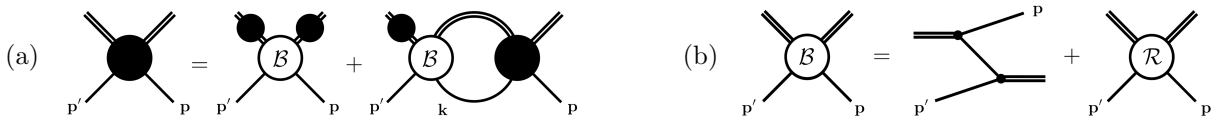

Figure 32: Diagrammatic representation of (a) the B-matrix representation for the on-shell amplitude, Eq. (59), and (b) the B-matrix which is composed of the OPE $\mathcal{G}_{\boldsymbol{p}'\boldsymbol{p}}$, Eq. (60), and the R-matrix. Figure adapted from [420]

where the matrix $\mathcal{G}_{\boldsymbol{p}'\boldsymbol{p}}$ represents the long-range interaction due to one-particle exchange between the isobar and spectator required by unitarity. The amplitude $\mathcal{R}_{\boldsymbol{p}'\boldsymbol{p}}$ is a real matrix that embodies all short-range interactions. It is not constrained by unitarity, and it can be incorporated within a specific model allowing for the freedom to describe QCD resonances. Alternatively, it can be fixed from the lattice data as described below. The B-matrix equation produces a convenient parametrization of the three-body amplitude, reducing it to a three-dimensional integral equation through the isobar assumption. The formalism can accommodate distinguishable spinless particles and was generalized to include the two-body channels [419].

The products of amplitudes present in Eq. (59) formally represent multiplications of infinite matrices in the angular momentum space. For practical use, they are truncated, leading to the finite matrix equation, in which one retains only contributions from dominating two-body sub-channels. Finally, it is worth noting that the integration in the equation goes over the intermediate isobar mass. In Refs. [418, 419] the domain of integration is restricted to physical values of energies. In principle, this requires one to include only the experimentally accessible sub-channel $\mathbf{2} \to \mathbf{2}$ amplitudes without the need for additional assumptions. Moreover, it might be beneficial for a description of states which lie close to their decay thresholds and often are interpreted as molecular systems bound by the nearly physical meson exchanges. However, integration over the physical intermediate energies in the B-matrix formalism results in the non-physical analytic properties of the amplitudes, which may hinder the study of actual three-body singularities and should be cured by an additional, properly chosen dispersion of the interaction kernel. This is in contrast to studies presented in Refs. [416, 440, 441] in which models for dissociation vertex functions are incorporated and the integration includes virtual intermediate energies driving the unphysical singularities away from the physical region.

In the REFT formulation, as developed in Refs. [408, 412–414, 442–446] the connected part of the unsymmetrized three-body amplitude is given as a solution of the equation analogous to Eq. (59). It consists of the sum $\mathcal{D} + \mathcal{M}_{\text{df},3}$, where $\mathcal{D}$ is the *ladder* amplitude driven by one-particle exchanges between $\mathbf{2} \to \mathbf{2}$ subprocesses, while $\mathcal{M}_{\text{df},3}$ is the separate short-range amplitude. The ladder amplitude is obtained by setting $\mathcal{R}_{\boldsymbol{p}'\boldsymbol{p}} = 0$ in the B-matrix equation,

$$\mathcal{D}_{\boldsymbol{p}'\boldsymbol{p}} = \mathcal{F}_{\boldsymbol{p}'}\, \mathcal{G}_{\boldsymbol{p}'\boldsymbol{p}}\, \mathcal{F}_{\boldsymbol{p}} + \int_{\boldsymbol{k}} \mathcal{F}_{\boldsymbol{p}'}\, \mathcal{G}_{\boldsymbol{p}'\boldsymbol{k}}\, \mathcal{D}_{\boldsymbol{k}\boldsymbol{p}}\,. \tag{61}$$

The short-range part is given by an additional double-integral equation, driven by the three-body K matrix called $\mathcal{K}_{\text{df},3}$, representing short-distance three-particle interactions,

$$\mathcal{M}_{\text{df},3;\boldsymbol{p}'\boldsymbol{p}} = \int_{\boldsymbol{k}} \int_{\boldsymbol{k}'} \mathcal{L}_{\boldsymbol{p}'\boldsymbol{k}'}\, \mathcal{T}_{\boldsymbol{k}'\boldsymbol{k}}\, \mathcal{L}^{\top}_{\boldsymbol{k}\boldsymbol{p}}\,, \tag{62}$$

where $\mathcal{L}$ is the *endcap* operator describing incoming and outgoing particles rescatterings, while $\mathcal{T}$ is given by the equation,

$$\mathcal{T}_{\boldsymbol{p}'\boldsymbol{p}} = \mathcal{K}_{\text{df},3;\boldsymbol{p}'\boldsymbol{p}} + \int_{\boldsymbol{k}} \int_{\boldsymbol{k}'} \mathcal{K}_{\text{df},3;\boldsymbol{p}'\boldsymbol{k}}\, i\rho_{\boldsymbol{k}} \mathcal{L}_{\boldsymbol{k}\boldsymbol{k}'}\, \mathcal{T}_{\boldsymbol{k}'\boldsymbol{p}}\,, \tag{63}$$

The $\mathcal{K}_{\text{df},3}$ is the analog of the $\mathcal{R}$ matrix of the B-matrix formalism. In recent lattice studies both the $\mathcal{R}$ and $\mathcal{K}_{\text{df},3}$ have been determined for the realistic three-body systems (see the discussion below). For further details about the REFT formalism, we refer the reader to Ref. [422].

The B-matrix parameterization can be analytically continued to the complex energy plane. The analytical properties of the formalism are discussed in Refs. [418]. One of the most unique characteristics of the three-body equations appears from a kinematic singularity due to the exchange of a real particle. Analytic structure

of the S-wave OPE was studied in Ref. [418]. This process can be isolated from the full $\mathbf{3} \to \mathbf{3}$ scattering amplitude and affects the analytic structure of the interaction kernel. Through a single iteration of Eq. (59) it can be rewritten as a sum of: the bubble ($\mathcal{R} \times \mathcal{R}$), the triangle ($\mathcal{R} \times \mathcal{G}$) and the box ($\mathcal{G} \times \mathcal{G}$) diagrams. The authors of Ref. [418] discuss explicitly the influence of the OPE on the B-matrix triangle amplitude, identifying spurious left-hand cuts. They propose a dispersion approach as a way to eliminate these spurious cuts and compare their result with the analytical structure of the covariant Feynman amplitude. In Ref. [419] the authors perform a comparable analysis, using a model of relativistic three-body scattering with a bound state in the two-body subchannel. They focus on the contact interaction approximation in which the exact solution of the model can be achieved, being effectively a series of bubble diagrams. They show the emergence of similar singularities and eliminate them via the analogous dispersion scheme.

In Ref. [441] the B-matrix equation was applied the coupled-channel case of the decay $a_1(1260) \to \pi^-\pi^-\pi^+$ with the dominant contribution provided by the $\rho\pi$ isobar-spectator channel in the S and D waves. The authors solved the equation by discretizing the particles' momenta on a complex contour, obtaining a matrix equation, which was handled numerically. The obtained amplitude was matched with the experimental data on the $\tau \to (3\pi)\nu_\tau$ to compute $a_1(1260) \to 3\pi$ Dalitz plots and lineshapes. Techniques for solving the B-matrix equation are also discussed in Ref. [447]. There, the authors considered a system of the three-body system with an S-wave bound state in the two-body subchannel, which can be considered as a simplified model of the nucleon-deuteron interaction. They employ the *ladder* approximation and reproduce results obtained using finite-volume spectra of the same model [448].

The three-body equations as presented are complicated to use in practical analyses, as it is necessary to parameterize the short-distance functions and to solve intricate integral equations. Moreover, for extracting the resonant spectrum from data, one is more interested in the short-distance physics than the long-distance rescattering terms which originate from two-body physics. Moreover, real-axis singularities cannot be seen in physical process, since $\mathbf{3} \to \mathbf{3}$ scattering amplitudes are always convoluted with a production source. A reformulation of the B matrix method, similar to the REFT approach, separates these purely rescattering effects from the short-distance physics in order to provide a useful tool for practical data analysis [53]. Resonance physics is a useful application of this approach, as one can focus on constructing dynamical models for the short-distance term and consider the OPE as the "dressing" corrections. Ref. [53] discusses further approximations which can be made to simplify subsequent analyses, such as factorization of the short-distance R matrix or truncation of the partial-wave basis as it is done in Khuri-Treiman approaches.

The phase-space integral of the three-particles final state, which determines the imaginary part of the inverse amplitude, is the integral over the Dalitz plot. The OPE effects the Dalitz plot distribution in a two-folded way. First, the interference of the different decay chains, e.g. a resonance in one pair of particle and in the other pair, is due to the real one-particle exchange. Second, the subchannel-resonance shape might deviate from the one measured in the two-body scattering due to the final-state interaction. Accounting for the interference is straightforward, while the second effect requires modeling and often a fitting of the model parameters to the data.

The Khuri-Treiman equations discussed in section 3.1 offer a good model to address the final-state interaction. The method is based on the analytic continuation of two-body unitarity. Hence, it implements a specific OPE ladder series of the $\mathbf{3} \to \mathbf{3}$ scattering [314]. More importantly, the effect of OPE computed with the KT can be used to complete the three-body unitarity [53].

Similar to the three-body unitarity, the REFT formalism has been studied from various angles by different groups. A threshold expansion and isotropic approximation for the three-body K matrix have been proposed [415, 449, 450] to simplify analyses of the lattice data. The formalism has also been applied to the study of the bound-state toy models in Refs. [448, 451]. In Ref. [420], it was shown that the REFT formulation in the infinite volume can be recovered from the B-matrix representation. This is an expected result in light of Ref. [452] which proved the unitarity of the REFT approach. The differences in both formalisms were proved to be consequences of different parametrization of two-body rescatterings in the initial and final states. Additionally, the authors presented the equivalence of the heavy-mass limit of both representations with the non-relativistic EFT approach by Bedaque, Hammer, and von Kolck [453] and the Faddeev equations [454].

3.2.2. Lattice studies of the three-body scattering

The form of the B-matrix amplitude parametrization is suitable for investigating the three-body finite-volume spectrum in the finite-volume unitarity (FVU) formalism. The integral equation is modified because in the finite cubic volume with periodic boundary conditions the particles' three-momenta become discretized and thus one replaces three-dimensional integrations by the summations over the available lattice momenta. Moreover, in the finite cubic box, the irreducible representations of the rotation group are divided into 10 irreducible representations of the octahedral group and become coupled due to the breaking of rotational symmetry [398, 407, 411, 455, 456]. The FVU approach is rooted in the fact that the three-body subprocesses which lead to the large, finite-volume power-law corrections in the values of observables, are described by amplitudes that contribute only imaginary parts to the three-body unitarity. In this sense, the three- and two-body unitarity imply a three-body quantization condition, that is derived from the finite-volume version of the B-matrix equation and takes the form of the determinant condition including the B matrix and a known geometric function [423].

The first study of the relativistic FVU quantization condition was completed in Ref. [409] for the case of a single isobar and one irreducible representation of the lattice symmetry group, which can be considered an analog of a single partial-wave in the infinite volume limit. In practice, the energy levels extracted on the lattice correspond to a given representation of the group and are determined independently. In Ref. [417] the projection of the quantization condition to a given irreducible representation of the octahedral group was reported. It corresponds to a partial diagonalization of the quantization condition equation and thus greatly simplifies it for practical purposes. Finally, Ref. [457] includes a prediction for the three-pion lattice spectrum from the unitarity quantization condition.

In Ref. [421] it was shown that the quantization conditions corresponding to the REFT and FVU formalisms are equivalent. This was achieved by rewriting the REFT condition in terms of the $\mathcal{R}$ matrix, at the same time producing a generalization of the latter approach to arbitrary angular momenta of isobars, independently of Ref. [458].

The generic lattice-based computation of the three-body amplitude is implemented via the following, simplified procedure. First, one determines the two-body finite-volume amplitude $\mathcal{F}$ through a two-body convenient quantization condition for all relevant isobars in the three-body system. Secondly, one computes a set of three-body energy levels in a given octahedral representation and through the three-body quantization condition determines the three-body $\mathcal{R}$ matrix. In practice, a suitable model is needed to fit the short-range interaction to the finite volume R-matrix data. Finally, one inputs the obtained form of three-body forces into the infinite volume integral equation, Eq. (59), to compute the three-body amplitude.

There is a growing number of results of few-body spectra from lattice QCD [458–466] that can be used to determine the nature of the three-hadron interactions in the QCD. The FVU formalism has been applied to extract three-body forces from various few-particle systems in lattice QCD, all of which were generated at a higher than physical pion mass. In Ref. [467] authors analyse the lattice $\pi^+\pi^+$ and $\pi^+\pi^+\pi^+$ data from Ref. [460], extracting the matrix $\mathcal{R}$. Within the used parametrizations, the authors found the short-range forces to be consistent with zero in this system. This study was continued in Ref. [468], based on the data of Ref. [462] and [465], leading to a more precise determination of the three-body coupling. The authors found the result of their analysis to be small but non-zero, and consistent with the LO ChPT at the heavy pion mass. In the study, the pion mass dependence of the three-body amplitude was studied however a clear conclusion about its agreement with the ChPT prediction could not have been reached.

In Ref. [463], the REFT finite-volume approach was applied to the $3\pi^+$ spectrum computed at three pion masses, including the physical one. The resulting $\mathcal{K}_{\mathrm{df},3}$ term was analyzed in the isotropic approximation and found to be non-zero, showing a reasonable agreement with LO ChPT. The three-body RFT formalism was also employed in Ref. [465], for the same system at large pion mass, producing the three-body term in the isotropic approximation compatible with zero. It is worth noting that in the study the authors used the lattice output in the infinite-volume integral equations for the first time producing scattering amplitudes and Dalitz plots. In Ref. [458], the authors extracted parameters of the $a_1(1260)$ from the Lattice QCD, at pion mass 244 MeV. They generalized the FVU three-body quantization condition to sub-systems with non-zero angular momenta and coupled channels, and performed analytical continuation of the B-matrix

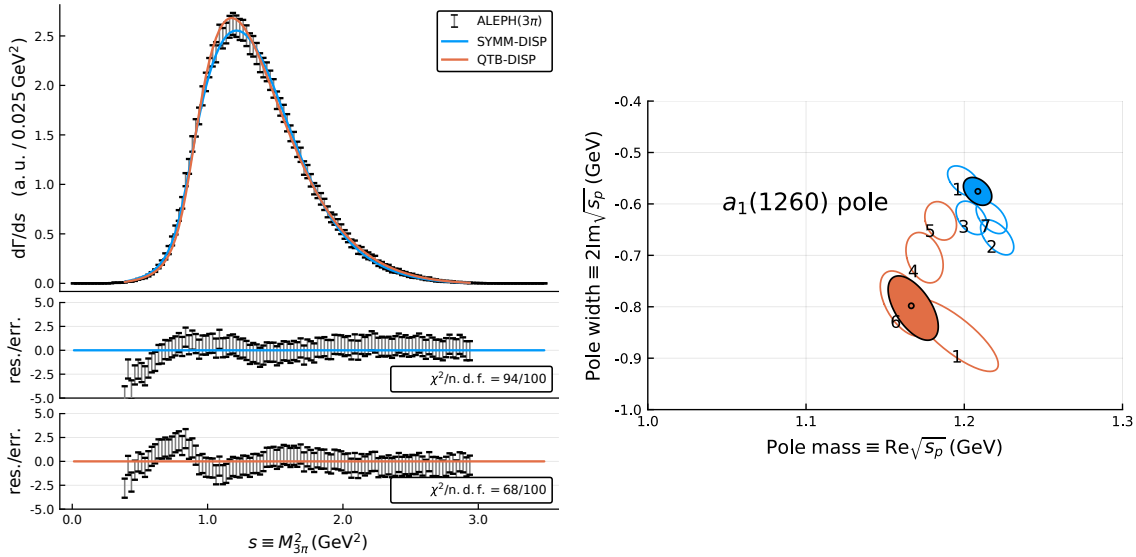

Figure 33: (left) Three-pion spectrum of of the $\tau \to 3\pi\nu$ decay. Data are given by ALEPH [470, 471] The model curves for the two dispersive models are overlayed. (right) Position of the $a_1(1260)$ pole in the complex energy plane for both models: SYMM-DISP (blue) and QTB-DISP (orange). The ellipses account for the 95% confidence level. The results for the main fit are shown by filled ellipses, while the unfilled ellipses provide the systematic studies. Figures from [54].

equations solution to determine the pole position of the resonance. Most recently, Ref. [466] presented a high-precision lattice computation of three-particle systems including either pions or kaons. The authors include the D-wave isobars in their work and determine the three-body K matrix using three different pion masses in the REFT approach. They notice tensions between their results and previous studies and comment on the necessity of more accurate computations in the future.

3.3. Application of three-body unitarity to resonance physics

The construction of dynamical models for three-body resonances can proceed in a way similar to that of two-body amplitudes. Unitarity determines the imaginary part of the inverse amplitude above the particle production threshold. Following the analyticity requirement, the self-energy function can be computed using dispersive techniques. The remaining unknown part of the scattering amplitude is built through the parametrization of a real-valued function (or a matrix in the coupled-channel case) using the K-matrix approach. The OPE needs to be accounted for in the computation of the imaginary part. Firstly, it leads to the contribution of the interference of different chains for a three-body decay, and, secondly, it impacts the lineshape of the subchannel resonances. The inclusion of only the OPE-related interference is referred to as *approximate three-body unitarity*. The approach has been employed in several experimental analysis due to its relative simplicity and as a possibility to test data sensitivity to three-body effects [469].

3.3.1. Studies of $a_1(1260)$ resonance in the 3π system

The $a_1(1260)$ resonance has a prominent role in the $\tau \to 3\pi\nu$ decay, dominating the lineshape structure. Its mass is fairly known, but its width has large uncertainties and is just known to be large [1]. The dominant decay channel is $a_1 \to \rho\pi$ in the S-wave, where the ρ subsequently decays to two pions. The a_1 broad peak spans the range from 0.8 to 1.6 GeV of the three-pion invariant mass, covering the nominal $\rho\pi$ threshold, which makes the explicit inclusion of the threshold essential for the proper analytical continuation of the amplitude to the complex energy plane and pole extraction. The OPE is also significant as shown by the two overlapping ρ bands in the Dalitz plot. The reaction amplitude for the resonant part, *aka* a_1, of the $3\pi \to 3\pi$ rescattering is written as a Breit-Wigner with a nontrivial self-energy function. that account for three-body effects. The imaginary part of the amplitude is computed using the optical theorem for the

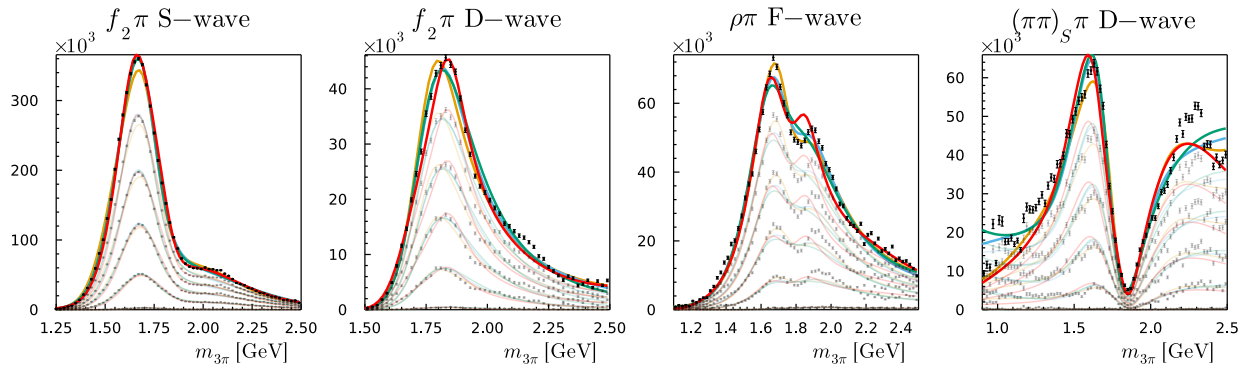

Figure 34: Intensities of the $J^{PC} = 2^{-+}$ waves with the fit model overlaid. Transparent points and the curves corresponds to the partial sum over t' slices starting from the highest t' bin. The data and curves are presented in Refs. [469, 472].

$a_1 \to 3\pi$ decay; then the real part of the self-energy is computed through dispersive integrals. In this way we manage to implement the correct analytical structure. We consider two models. The first one, *aka* symmetrized-dispersive model (SYMM-DISP) incorporates the OPE contribution via the interference of ρ and the self-energy. The second one, *aka* quasi-two-body dispersive model (QTB-DISP), neglects entirely the OPE. Figure 33 shows the fits of both models to the ALEPH dataset [470, 471]. The data are clearly correlated, and the statistics results have be taken with a grain of salt. The models are consistent with the data and provide results of similar quality, however, the parameters and, hence, the pole extractions are quite different. In the figure we also show both pole extractions. Not including the OPE makes the $a_1(1260)$ width larger and the mass lighter. The pole extracted using the QTB-DISP model reads

$$m_p^{a_1(1260)} = 1209 \pm 4^{+12}_{-9}\ \text{MeV}, \qquad \Gamma_p^{a_1(1260)} = 580 \pm 10^{+80}_{-20}\ \text{MeV}, \tag{64}$$

where the first error is statistical and the second error comes from the systematic studies, such as the varying the ρ lineshape.

The $a_1(1260)$ is possibly responsible for the axial resonance-like $a_1(1420)$ signal with mass 1.42 GeV and width 0.15 MeV reported by COMPASS [386]. It was observed in the P-wave of the $f_0(980)\,\pi$ system of the $\pi^- p \to 3\pi\, p$ reaction [472]. The mass of the $a_1(1420)$ is slightly above the $K^*\bar{K}$ threshold. In [473, 474] it was suggested that the signal could be a consequence of final-state interactions in the $a_1(1260)$ decaying to 3π and $K\bar{K}\pi$, in particular, a triangle singularity, finding an excellent agreement with the data [387].

3.3.2. Studies of π_2 resonances in 3π system

The main puzzle of the $J^{PC} = 2^{-+}$ sector is an interplay of the two states called $\pi_2(1670)$ and $\pi_2(1880)$, which have been seen to decay predominantly into 3π [1]. The quark model does not explain two states with same quantum numbers so close in mass: The $\pi_2(1880)$ fits neither the radial-excitation expectations, nor the Regge trajectories, and is a prime candidate for a hybrid meson [194, 475].

The $J^{PC} = 2^{-+}$ sector is very well separated from the other quantum numbers in the COMPASS partial-wave analysis diffractive $\pi^- p \to 3\pi\, p$ reaction [472], allowing to isolate the π_2 candidates. The resonances decay to the 3π final states via f_0, ρ, and f_2. In addition to the $\pi_2(1670)$ and $\pi_2(1880)$, a third overlapping $\pi_2(2005)$ is found.

To study these states, we develop a coupled-channel model that incorporates both the three-body and the resonance-spectator thresholds in the complex plane [469, 476, 477]. The OPE effects are neglected. The model accounts for the production mechanism using the Q-vector approach [1]. The production vector is modeled by a polynomial series of the conformal variable, $\omega(s) = (1 - \sqrt{s})/(1 + \sqrt{s})$. Then, the model is applied to the intensities and interferences of the four major $J^{PC} = 2^{-+}$ waves for eleven $\pi\, p$ transferred momenta [472]. The fits of a model with four K-matrix poles and fourth-order polynomial in ω for each wave and independently for all t' slices are shown in Figure 34 The optimization suffers from multimodality. The colored lines in Figure 34 represent to the four solution for local minima with similar quality.

Table 6: Summary of the parameters of π_2 resonances in the K-matrix model with four poles. The second columns give the results of Ref. [191] using Breit-Wigner model.

	m_p (MeV)	Γ_p (MeV)	$m_{\rm BW}$ (MeV)	$\Gamma_{\rm BW}$ (MeV)
$\pi_2(1670)$	$1650-1750$	$280-380$	1642^{+12}_{-1}	311^{+12}_{-23}
$\pi_2(1880)$	$1770-1870$	$200-450$	1847^{+20}_{-3}	246^{+33}_{-28}
$\pi_2(2005)$	$1890-2190$	$590-1340$	1962^{+17}_{-29}	269^{+16}_{-120}

All the solutions suggest the presence of three poles in vicinity of the fit region. The poles are ordered by their mass values and assigned to $\pi_2(1670)$, $\pi_2(1880)$, and $\pi_2(2005)$. However, the parameters are significantly different across different solutions. Conservative estimates of masses and widths shown in Table 6 are obtained by quoting the extreme values among all the selected solutions.

The results are compared to the conventional approach of the Breit-Wigner model of Ref. [191]. Our studies indicate that both $\pi_2(1670)$ and $\pi_2(1670)$ are required by the data, and their widths are below 450 MeV. The width of the $\pi_2(2005)$ is obtained in the interval from 590 MeV to 1.34 GeV.

The main difficulty in describing the data is related the the nonresonant coherent background process named after Deck [478]. Studies of the Deck mechanism in Refs. [469, 479] showed a large pollution in the $J^{PC} = 2^{-+}$ waves. The unitarization method proposed in Ref. [480] builds in the explicit form of the background while preserving unitarity. The method requires dedicated studies of the partial wave projections of the Deck process. This will be the subject for future research that will lead to a better understanding of the sector.

4. Production mechanisms

The mechanisms that produce hadron resonances in experiments offer another valuable piece of information for understanding their nature. Most of the recent data on XYZ states come from electroweak processes, as heavy meson/baryon decays or e^+e^- annihilation. Matrix elements can most often be studied in terms of form factors [177, 481, 482].

At high energy, (semi-)inclusive production processes enter the perturbative QCD regime. For example, deep inelastic scattering (DIS) of electrons off protons at large Q^2 has been the main experimental tool to scrutinize the inner structure of nucleons. Data on the corresponding cross sections and structure functions have been key ingredients in global QCD analyses of parton distributions [483–492]. At lower energies and Q^2 inclusive data are saturated by a few exclusive channels, and perturbative calculations lose their validity. Having a comprehensive understanding of the low and high energy regimes at once is a highly nontrivial task that will be discussed in Section 4.1.

In peripheral production, where the momentum transferred is much smaller than the energy, forces and resonances themselves are constrained by the same strong interaction dynamics, and one can learn about one by studying the other. This duality is the cornerstone of Regge theory. The most comprehensive study for establishing the role of Reggeons in quasi-elastic two body scattering will be discussed in Section 4.2. These studies are particularly effective in explaining single hadron (or resonance) photoproduction, as shown in Section 4.3 for the light sector. Quarkonia photoproduction will be discussed in Section 4.4 in the context of pentaquark searches, and in Section 4.5 in the context of predicting XYZ rates at electron-proton facilities. At high invariant masses, one enters the so-called double-Regge regime, which we will describe in Section 4.6. Contributions to the amplitude from resonances in the direct channel and Reggeons in the overlapping, crossed channels, cannot be added, as explicit for example in the Veneziano amplitude [493, 494], and one has to take specific care when involving both in amplitude analysis. In $\mathbf{2} \to \mathbf{2}$ scattering, Reggeons dominate the high energy behavior of the cross section at forward (or backward) angles, while resonances are visible at low energies in specific partial waves. Analyticity requires that these two regimes are connected, which allows us to write dispersion relations that can convert the Regge phenomenology at high energies into further constraints for the partial waves in the resonance region. This program of finite energy sum rules

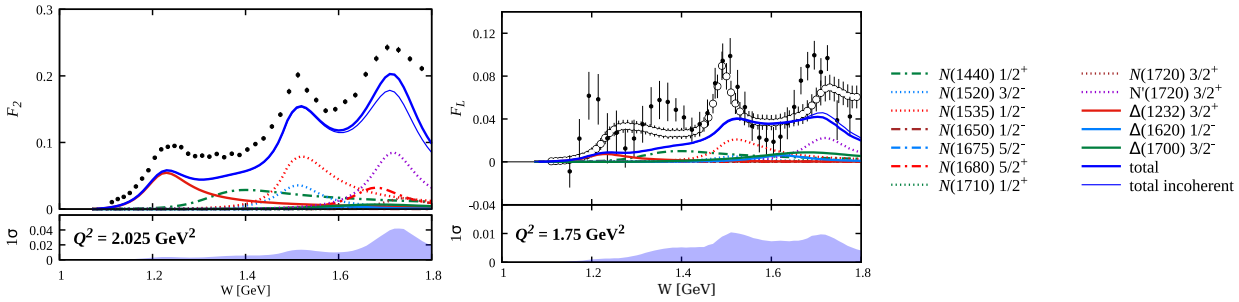

Figure 35: Proton F_2 and F_L structure function in the resonance region at different values of Q^2. The data are compared with the full resonant structure functions computed by adding amplitudes (thick blue curves) and cross sections (thin blue curves) from the contributing resonances, using the central values of their electrocouplings. The contributions from individual resonances are shown separately, as indicated in the legends. Below each panel, we also show the uncertainty sizes of the thick blue curves (full coherent sum of resonant contributions), which are computed by propagating the electrocoupling uncertainties via bootstrap. The data in the left plot come from the interpolation of the CLAS database [516], the data in the right plot come from [514] (filled black circles) and [510] (open black circles). Figure from [508].

(FESR) will be discussed in Section 4.7. This and other forms of duality have found some recent interest because of the discovery of several tetraquark and pentaquark candidates [203, 495]. Although establishing the presence of exotic states in the spectrum through their role as exchange forces might be a long shot, the duality between Reggeons and resonances can play an important role in constraining models of exotics.

4.1. Nucleon resonance contributions to inclusive electron scattering

Being able to describe the strong interaction physics across a broad range of energy and distance scales is crucial, but the nonperturbative regime is still far from being well understood. In inclusive electron-proton scattering, the transition from the low-energy resonance region to the high-energy regime (*i.e.* DIS) offers broad grounds for exploration [488, 490, 496–503]. Leading twist approximations[6] are found to be accurate at describing the region of invariant masses W above the resonances, at sufficiently large photon virtualities, $Q^2 \gtrsim 1$–$2\,\mathrm{GeV}^2$. Therefore, global QCD analyses [488–490] usually involve cuts in both W and Q^2 [484–487, 504–506]. In order to bridge the gap between perturbative and nonperturbative regimes and to assess the parton distributions at large Bjorken-x, target mass corrections, higher twists and factorization-breaking corrections are called for. In addition, due to the resonance peaks appearing in the $W < 2\,\mathrm{GeV}$ region, the electroexcitation amplitudes of the resonances should be incorporated into the description of the structure functions [507, 508]. High-precision measurements of inclusive electron scattering cross sections in the resonance region were made at JLab's Halls B and C [509–515].

A further phenomenological motivation for these studies is the observation of a duality between the structure functions in the nucleon resonance region, when averaged over resonances, and the scaling function extrapolated from the deep-inelastic scattering region [517]. When integrating the structure functions over (finite intervals of) x, one obtains the (truncated) moments of the structure functions [518, 519]. The leading twist term is associated with incoherent scattering with individual partons in the nucleon [520–522], while the higher twist corrections capture elements of long-distance, nonperturbative quark-gluon dynamics associated with color confinement in QCD [523, 524]. Duality is interpreted as the dominance of the leading twist and the consequent suppression of higher twist contributions to the moments [525].

The inclusive structure functions are related to the total virtual photon-nucleon scattering cross sections

[6] Operators contributing to DIS can be organized in terms of their twist, *i.e.* their mass dimension minus the number of Lorentz indices. Higher twist operators are further suppressed by powers of the hard scale Q^2.

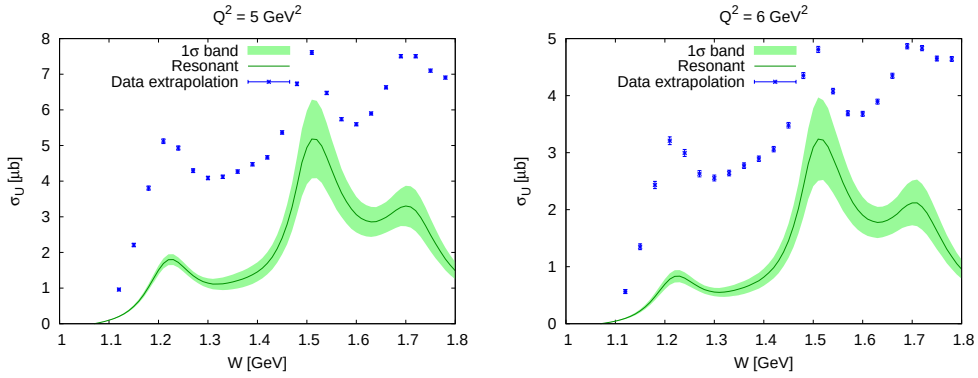

Figure 36: Resonant contributions (green) to the unpolarized σ_U virtual photon-proton cross sections, for an electron beam energy of 10.6 GeV, compared to the predicted inclusive virtual photon-proton cross sections in the kinematic area covered in the measurements with the CLAS12 detector [528]. Figures from [507].

σ_T and σ_L, for transversely and longitudinally polarized photons, respectively [526],

$$F_1(W,Q^2) = \frac{Km}{4\pi^2\alpha}\,\sigma_T(W,Q^2), \tag{65a}$$

$$F_2(W,Q^2) = \frac{Km}{4\pi^2\alpha}\,\frac{2x}{\rho^2}\left(\sigma_T(W,Q^2)+\sigma_L(W,Q^2)\right), \tag{65b}$$

where α is the fine structure constant, $K = (W^2-m^2)/2m$ is the equivalent photon flux in the Hand convention [527], $\rho = \left(1+4m^2x^2/Q^2\right)^{1/2}$ a kinematic parameter, and m the proton mass. The F_2 structure function can also be written in terms of the unpolarized virtual photoproduction cross section σ_U,

$$F_2(W,Q^2) = \frac{Km}{4\pi^2\alpha}\,\frac{2x}{\rho^2}\,\frac{1+R_{LT}}{1+\epsilon R_{LT}}\,\sigma_U(W,Q^2), \tag{66}$$

where

$$\sigma_U(W,Q^2) = \sigma_T(W,Q^2) + \epsilon\,\sigma_L(W,Q^2), \tag{67}$$

ϵ is the degree of transverse virtual photon polarization, determined by the scattered electron angle θ_e,

$$\epsilon = \left(1+\frac{2\rho^2}{\rho^2-1}\tan^2\frac{\theta_e}{2}\right)^{-1}, \tag{68}$$

and $R_{LT} = \sigma_L(W,Q^2)/\sigma_T(W,Q^2)$ is the ratio of longitudinal to transverse virtual photon cross sections. The longitudinal structure function is defined as

$$F_L(W,Q^2) = \frac{Km}{4\pi^2\alpha}2x\,\sigma_L(W,Q^2) = \rho^2F_2(W,Q^2) - 2xF_1(W,Q^2). \tag{69}$$

Here, we focus on the unpolarized structure functions F_1 and F_2, and their combination F_L. A compilation of the data for unpolarized structure functions and inclusive cross sections in the range $1.07 \leq W \leq 2\,\text{GeV}$ and $0.5 \leq Q^2 \leq 7\,\text{GeV}^2$, together with a tool for the interpolation between bins, is available online from the CLAS database [515, 516, 529]. At the same time, the experimental program of exclusive π^+n, π^0p, ηp, and $\pi^+\pi^-p$ electroproduction channels with CLAS at JLab has provided the first and only available results on electroexcitation amplitudes, or electrocouplings of most nucleon resonances in the mass range $W < 1.8\,\text{GeV}$ and $Q^2 < 5.0\,\text{GeV}^2$ [530–532]. This makes it possible to evaluate the resonant contributions to inclusive electron scattering using parameters of the individual nucleon resonances extracted

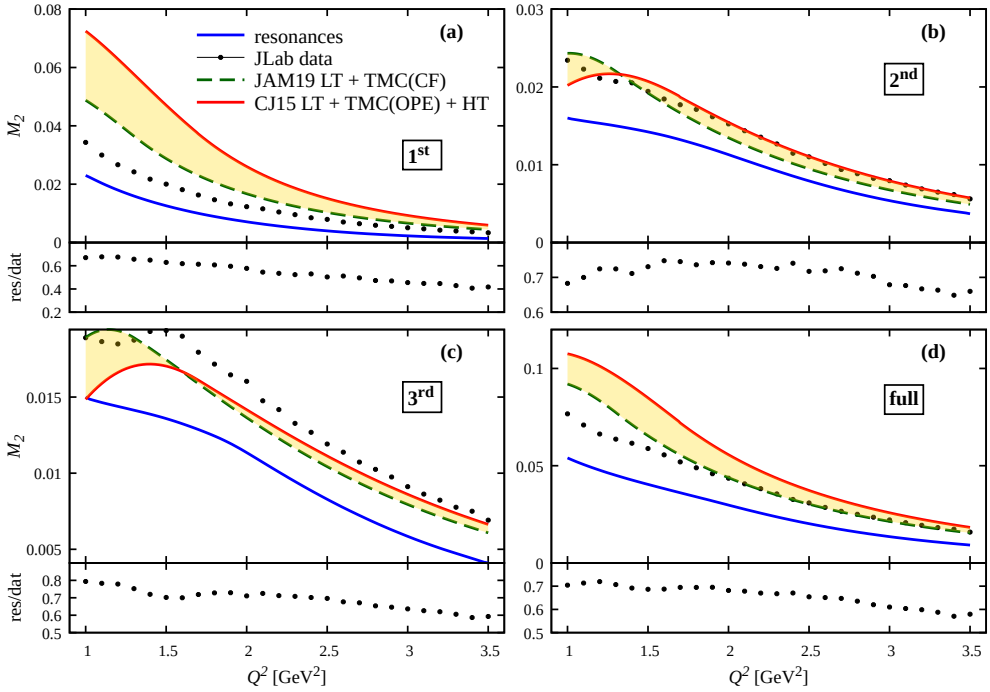

Figure 37: Truncated moments M_2 of the F_2 structure function versus Q^2 for the three resonance regions, as well as for the full range $1.07 < W < 1.75\,\text{GeV}$. The moments from the experimental results [516] (black circles, with uncertainties smaller than the circle sizes) are compared with the resonant contributions (blue lines) and the structure function moments computed from the JAM19 [489] (green lines) and CJ15 [488] (red lines) PDFs, with the latter including also higher twist terms. Also shown beneath each panel is the ratio of the resonant contributions to the data in each W region. Figures from [508].

from data, expressing the amplitudes as a coherent sum over all relevant resonances in the mass range $W < 1.75\,\text{GeV}$ [533, 534],

$$F_1^R = m^2 \sum_{IJ\eta} \left[\left| \sum_{R^{IJ\eta}} G_+^{R^{IJ\eta}} \right|^2 + \left| \sum_{R^{IJ\eta}} G_-^{R^{IJ\eta}} \right|^2 \right] , \tag{70a}$$

$$\rho^2 F_2^R = m\nu \sum_{IJ\eta} \left[\left| \sum_{R^{IJ\eta}} G_+^{R^{IJ\eta}} \right|^2 + 2 \left| \sum_{R^{IJ\eta}} G_0^{R^{IJ\eta}} \right|^2 + \left| \sum_{R^{IJ\eta}} G_-^{R^{IJ\eta}} \right|^2 \right] , \tag{70b}$$

where the outer sum runs over the possible values of spin J, isospin I and intrinsic parity η, and the inner sums run over all those resonances $R^{IJ\eta}$ with same quantum numbers that are added coherently. The electrocouplings are encoded in the functions $G_{0,\pm}^{IJ\eta}$ [508].

Representative examples of $F_2(W, Q^2)$ and $F_L(W, Q^2)$ are shown in Figure 35. Three distinct peaks are clearly seen in their W dependencies and related to the resonant contributions. In the first resonance region, the contribution from the $\Delta(1232)\,3/2^+$ decreases rapidly with Q^2, so that at $Q^2 > 2\,\text{GeV}^2$ the tail from the $N(1440)\,1/2^+$ state becomes essential. This is even more drastically so for the longitudinal F_L. In the second resonance region, the $N(1520)\,3/2^-$ and $N(1535)\,1/2^-$ give the largest contributions to F_2 and the contribution from the $N(1535)\,1/2^-$ becomes dominant as Q^2 increases. Additionally, the tail from $\Delta(1700)\,3/2^-$ becomes the main contribution to F_L as Q^2 increases. Finally, the peak in the third resonance region is generated by contributions from several resonances, one of the largest stemming from the $N'(1720)\,3/2^+$ state discovered recently in combined studies of $\pi^+\pi^- p$ photo- and electroproduction at JLab [234]. Because of the intricate interplay with other resonances, the evolution with Q^2 of the third peak in F_2 becomes rather involved, and the contribution from the $\Delta(1700)\,3/2^-$ dominates the resonant part at

$Q^2 \sim 4\,\mathrm{GeV}^2$. This behavior suggests that further insight can be gained into its structure in the range of high $Q^2 > 4\,\mathrm{GeV}^2$, which will be covered in future nucleon resonance studies with the CLAS12 detector [530, 535]. Therefore, in Figure 36 we also show the unpolarized inclusive cross section [511] $\sigma_U(W, Q^2)$ as predicted for CLAS12 kinematics.

More generally, the pronounced differences seen in the Q^2-evolution of the three peaks are related to the different Q^2 evolutions of the electroexcitation amplitudes of the contributing resonances. Therefore, a credible evaluation of the resonant contributions relies essentially upon the knowledge of the electroexcitation amplitudes of all prominent resonances in the entire mass and Q^2 region under study. The extraction of reliable information from the experimental data on exclusive meson electroproduction will extend the capability of gaining insight into the nucleon parton distribution functions (PDFs) at large x within the resonance excitation region. It also allows us to explore quark-hadron duality.

We quantify the duality by considering the lowest truncated moment of F_2, which in an interval $\Delta x \equiv x_{\mathrm{max}} - x_{\mathrm{min}}$ at fixed Q^2 is given by

$$M_2(x_{\mathrm{min}}, x_{\mathrm{max}}; Q^2) = \int_{x_{\mathrm{min}}}^{x_{\mathrm{max}}} \mathrm{d}x\, F_2(x, Q^2). \tag{71}$$

In Figure 37, we compare the empirical moments with the moments of structure functions computed from the CJ15 [488] and JAM19 [489] PDFs extrapolated from higher W. The differences between parametrizations can be interpreted as systematic theoretical uncertainties associated with the extrapolations. For the moments evaluated for the entire resonance region, from the pion threshold to $W = 1.75\,\mathrm{GeV}$, there is reasonable agreement within uncertainties between the experimental data and the extrapolations from the DIS region for $Q^2 \gtrsim 2\,\mathrm{GeV}^2$. A similar agreement is observed in the second resonance region down to even smaller Q^2 values. In the third region the extrapolated results generally underestimate the data by $\sim 10\% - 30\%$, while in the first region the extrapolated results overestimate the data at all Q^2 considered. Interestingly, the ratio of the resonance contributions to the truncated moments relative to the total remains fairly constant across the range of Q^2 considered. This suggests a similar Q^2 evolution of the resonant and nonresonant contributions to the structure function, thus pointing to a nonvanishing relative resonant *vs.* nonresonant size, even at larger Q^2.

Definitive conclusions about the longitudinal truncated moments are more difficult to draw on account of the greater systematic uncertainties associated with the experimental data extraction and the theoretical analysis prescriptions, motivating the need to complete the understanding of the leading and higher twist contributions to F_L, as well as of obtaining L/T separated data in the resonance region.

On the experimental side, our results motivate extensions of the inclusive electron scattering studies in the resonance region towards $Q^2 > 4\,\mathrm{GeV}^2$, as well as the extraction of the $\gamma^* p N^*$ electrocouplings at high photon virtualities from the exclusive meson electroproduction data [530, 535]. Furthermore, the results suggest the intriguing future avenue of simultaneously describing the resonance and DIS regions, thus providing constraints for nucleon PDFs at large values of x [534]. A further extension is to explore the spin dependence of the exclusive-inclusive duality by analysing the spin-dependent g_1 and g_2 structure functions.

4.2. Regge theory and global fits

As mentioned, Reggeons and resonances are dual and not additive, so one has to be careful when involving both in amplitude analysis. Before exploring the applications of duality in the following sections, we first review the basic of the Regge theory and its recent applications in modern experiments.

Analyticity in angular momentum requires that singularities of partial waves are not independent, but rather connected by an analytic function called *trajectory*. One can show that indeed that poles in the complex angular momentum (Regge poles or *Reggeons*) correspond to the existence of an infinite tower of resonances of increasing mass and spin, as the ones described in Section 2.4.3 (see for example [199–201]). The contribution of a single Reggeon to a $\mathbf{2} \to \mathbf{2}$ process in the high-energy limit $s \gg -t$ can be written as

$$A^{\lambda_b,\lambda_M}_{\lambda_N,\lambda'_N}(s,t) = \beta_{\lambda_\gamma,\lambda_M}(t) \left[\frac{\tau + e^{-i\pi\alpha(t)}}{2\sin\alpha(t)} \left(\frac{s}{s_0} \right)^{\alpha(t)} \right] \beta_{\lambda_N,\lambda'_N}(t)\,, \tag{72}$$

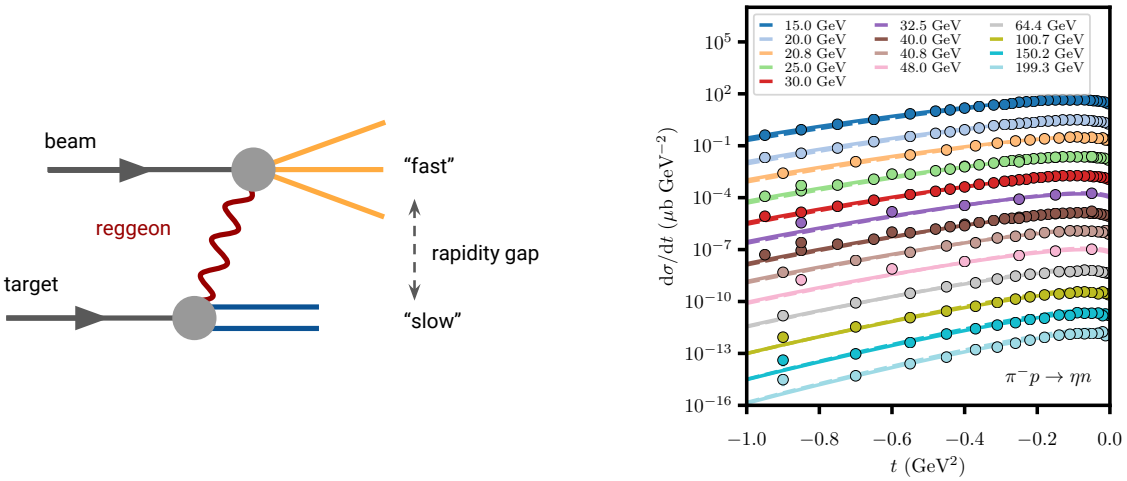

Figure 38: (left) Production of meson via Regge exchange (Reggeon). (right) $\pi^- p \to \eta n$ differential cross sections. Figures from [536].

where $\lambda_b, \lambda_M, \lambda_N$ and λ'_N are the helicities of the beam, produced meson, target and recoil, respectively. The trajectory $\alpha(t)$ gives the pole position of a resonance of given spin J_R solving $\alpha(m_R^2) = J_R$. In the following, we consider $\alpha(t)$ to be real functions, as their imaginary parts are connected to resonance widths and give subleading effects when describing meson production. The effects of the widths and their relation to the nature of light baryon states is studied in Section 2.4.3. The signature of the Reggeon is $\tau = (-1)^J$ with J representing the spin of the lightest particle on the trajectory. Vectors and tensors satisfying $P(-1)^J = +1$ are denoted natural exchanges, while pseudoscalars and axial-vectors with $P(-1)^J = -1$ are denoted unnatural exchanges. Meson production at high energies can thus be explained in terms of Regge exchanges whose quantum numbers determine the energy dependence of the reaction from its trajectory $\alpha(t)$. As shown in Eq. (72) and represented in Figure 38, the production amplitude factorizes into a top (beam-meson) and a bottom (target-recoil) vertex.

The total production amplitude will be a sum over Regge poles (72), and is thus dominated by the exchange having the greatest trajectory $\alpha(t)$. Since, in practice, trajectories are approximately linear $\alpha(t) = \alpha_0 + \alpha' t$, for small $|t|$ the production mechanism is dominated by the trajectory having the highest intercept α_0. In processes having exotic quantum numbers in the s-channel such as pp or $\pi^+\pi^+$ elastic scattering, tensor and vector trajectories are forced to cancel each other since there is no direct resonance produced to be dual to. These vector and tensor exchanges are called degenerate. Exchange degeneracy (EXD) requires not only that vector and tensor trajectories $\alpha(t)$, but also couplings to the exotic channel $\beta(t)$ be equal. Similarly to the natural parity exchange (vector and tensor), one can show that unnatural partity exchange (pseudoscalar and axial-vector trajectories) are also degenerate. There are thus only two different Regge trajectories $\alpha(t)$ for Reggeons built out of mesons.

Natural exchanges have a larger intercept ($\alpha_0 \simeq 0.5$) than unnatural ones ($\alpha_0 \simeq 0$). These values lead to cross sections that decrease with energy, and cannot explain why the total cross section $pp \to$ anything slightly rises with energy. It has been postulated that a Pomeron trajectory ($\mathbb{P}$) with an intercept close to unity and having the quantum numbers of the vacuum is responsible for this phenomena. This trajectory is in principle related to the existence of purely gluonic particles, as glueballs. The t-channel quantum number for various reactions are listed in Table 8, and their Regge trajectories $\alpha(t)$ are listed in Table 7.

For a given process, all quantities appearing in Eq. (72) are known except the couplings $\beta(t)$. These can be approximated to constants, once the t-dependence at small angles is explicitly factored out. Conservation

of angular momentum implies that, in the forward direction,

$$A_{\substack{\lambda_b,\lambda_M \\ \lambda_N,\lambda'_N}}(s,t) \propto \left(\sqrt{-t'}\right)^{|\lambda_b-\lambda_M+\lambda'_N-\lambda_N|} . \tag{73}$$

Where we have defined $t' = t - t_{\min}$ with $t_{\min} = t(\theta = 0)$. The factorized form of the production amplitude implies a stronger constraint

$$A_{\substack{\lambda_b,\lambda_M \\ \lambda_N,\lambda'_N}}(s,t) \propto \left(\sqrt{-t'}\right)^{|\lambda_b-\lambda_M|+|\lambda'_N-\lambda_N|} . \tag{74}$$

By imposing Eq. (74) at the amplitude level, we can thus check whether mesons are photoproduced diffractively by comparing the t-dependence of the data and the model. As said, the constraints in Eq. (74) is only valid near the forward direction. Away from this limit, there are corrections of $\mathcal{O}(-t'/m^2)$, where m is the mass of the produced meson.

The most recent and comprehensive study aimed at establishing the role of Reggeons in quasi-elastic two-body scattering with pion and kaon beams was performed in [536]. It was established that the leading Regge poles which give the high-energy asymptotic behavior of scattering amplitudes (*i.e.* poles with the largest intercept) indeed dominate the charge exchange reactions already for $p_{\text{beam}} > 5\,\text{GeV}$. As can be seen in Figure 38, the model matches perfectly data across a wide energy range. Subleading effects include poles with lower intercept (*daughter trajectories*), or branch cuts in complex angular momentum, for example Reggeon-Pomeron boxes that model final-state interactions, *aka* absorption. These effects are mainly visible when the leading amplitude vanishes, and can also contribute significantly to polarization observables, or in specific cases of pion exchange [537–540]. The latter has indeed long range and can be significantly affected by final-state interactions.

4.3. Single meson photoproduction

The upgrade of the JLab facility has opened a new area for meson photoproduction [546]. With a 12 GeV electron beam, mesons with a mass up to $\sim 4\,\text{GeV}$ are expected to be produced, as depicted on Figure 38.

The GlueX and CLAS detectors are developing a rich meson spectroscopy program, including the study of exotic mesons and of other excited resonances, produced with a real and quasi-real photon beam, respectively [547–549]. However, before undertaking the search of new hadrons, we need to establish the production mechanisms of known mesons. In particular we need to assess whether at these energies they are produced diffractively, *i.e.* the production amplitude factorizes into a photon-meson vertex and a nucleon vertex. This is achieved by comparing diffractive models for pseudoscalar, vector and tensor meson photoproduction to data. The Regge exchanges contributing to photoproduction of mesons on a nucleon target are summarized in Table 8. In these sections, we present several results on single meson photoproduction and their comparison to data. The results are discussed in order of model sophistication.

In this context, the production of vector mesons is an ideal place to start. The ω, the ϕ and, to some extent, the ρ are narrow resonances and so are easy to reconstruct experimentally. The angular distributions of their decay products are given by the Spin Density Matrix Elements (SDME), which are known quadratic combinations of the production amplitudes. We can thus confirm the diffractive nature of vector meson

Table 7: Regge trajectories of the Pomeron, and of other Regge exchanges. Appropriate units of GeV are understood.

Exchange	Regge trajectory $\alpha(t)$
$\mathbb{P}$	$1.08 + 0.2t$
ρ, ω, a_2, f_2	$0.9(t - m_\rho^2) + 1$
π, b_1, h_1, a_1, f_1	$0.7(t - m_\pi^2)$

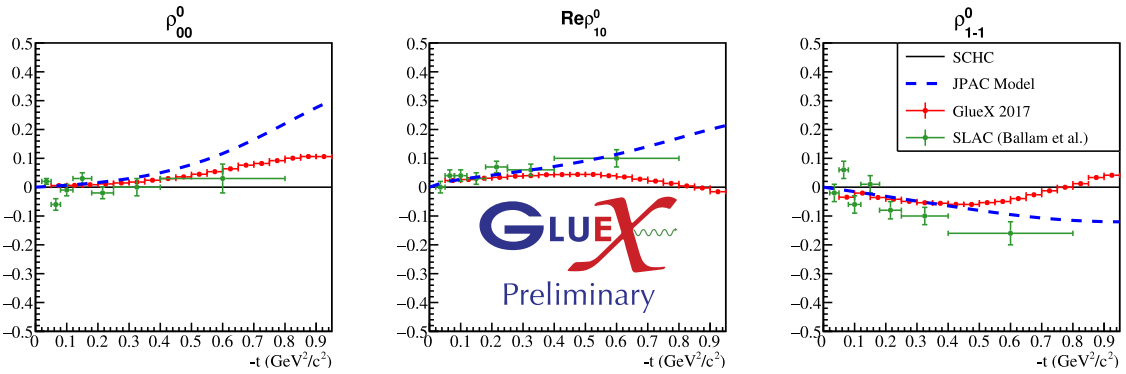

Figure 39: Example of spin density matrix elements in $\rho^0 p$ photoproduction in the helicity frame. Comparison between GlueX preliminary data and the model of Ref. [541]. Figure from [542].

photoproduction by constructing a model based on Regge exchanges that incorporates the small t behavior in Eq. (74), and comparing with JLab data. In Ref. [541], we developed a model for photoproduction of light neutral vector mesons ($V = \rho^0$, ω, ϕ). We considered the only relevant unnatural exchange to be π^0, and determine the coupling from the radiative decay $V \to \gamma\pi^0$. The natural exchanges (Pomeron and tensors), have three distinct helicity couplings to the γV vertex. These are denoted by the difference between the beam helicity and the vector meson one, and called non-flip, single-flip and double-flip couplings. For tensor exchange, the three couplings are related to the partial waves of the radiative decay $T \to V\gamma$ (where $T = f_2$, a_2), and in principle is accessible experimentally. In the absence of such information, we extracted their relative weights from the SLAC measurement of vector meson SDME from Ref. [550]. In the s-channel center-of-mass frame, the Pomeron is assumed to be helicity conserving. A year after the publication the model, GlueX has presented the preliminary version of the ρ^0 SDME [542]. In Figure 39 we show that the comparison between prediction and data is excellent for $-t' < 0.5\,\mathrm{GeV}^2 \simeq m_\rho^2$, in agreement with the range of validity of the expansion (74). Data are compatible with the dominance of the helicity conserving Pomeron coupling, plus the addition of tensor exchanges with complete helicity structures.

In the case just discussed, unnatural exchanges turned out to be almost irrelevant. However, it is well known that pion exchange dominates at low t in charge-exchange reactions such as $\gamma p \to \pi^- \Delta^{++}$. In single pseudoscalar photoproduction, the relative importance between natural and unnatural exchanges can be extracted from the beam asymmetry

$$\Sigma(t) = \frac{\frac{d\sigma_\perp}{dt} - \frac{d\sigma_\parallel}{dt}}{\frac{d\sigma_\perp}{dt} + \frac{d\sigma_\parallel}{dt}}\,, \tag{75}$$

where $\sigma_\perp$ ($\sigma_\parallel$) is the cross section for photon beam with linear polarization, perpendicular (parallel) polarization to the reaction plane. At high energies, natural (unnatural) exchanges contribute only to $\sigma_\perp$ ($\sigma_\parallel$).

Table 8: Regge exchanges in single meson photoproduction on a nucleon target.

Final state	Natural Ex.	Unnatural Ex.	Refs.
$\pi^0 p$, ηp, $\eta' p$	ρ, ω	b_1, h_1	[537, 539, 543]
$\rho^0 p$, ωp, ϕp	$\mathbb{P}$, a_2, f_2	π^0, η, a_1, f_1	[541]
$a_2^0 p$, $f_2 p$	ρ, ω	b_1, h_1	[544]
$\pi^+ n$, $\pi^+\Delta^0$, $\pi^-\Delta^{++}$	ρ, a_2	$\pi^\pm$, b_1	[545]

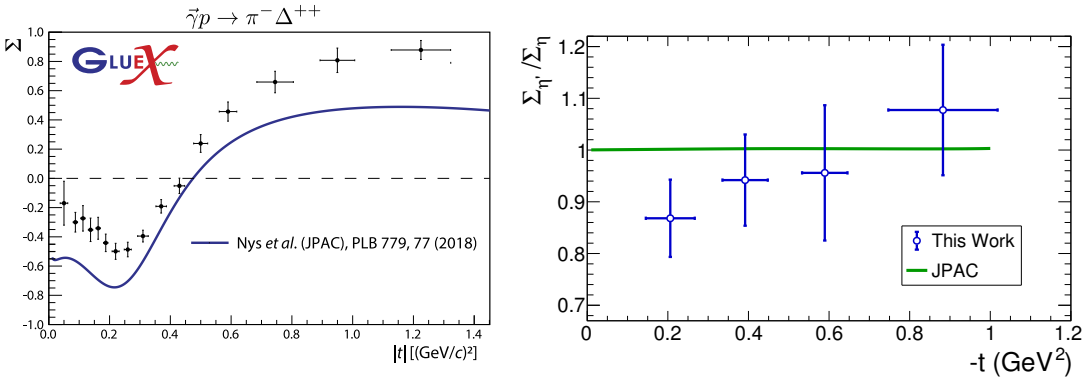

Figure 40: (left) Beam asymmetry in $\pi^- \Delta^{++}$ photoproduction. Comparison between GlueX data and the model in [545]. Figure from [551]. (right) η/η' beam asymmetry ratio compared with the model of [543]. Figure from [552].

Thus, positive (negative) Σ implies the dominance of natural (unnatural) Reggeons.

One observes in Figure 40 that the beam asymmetry turns out to be negative at small $-t$, confirming the dominance of unnatural exchange (pion) in the forward region. Moreover the minimum of Σ around $|t| \simeq 0.25\,\text{GeV}^2$ has been predicted by the model in Ref. [545], which includes ρ and a_2 as dominant natural exchanges. As mentioned in Sec. 4.2, pion exchange suffers from large absorption corrections. We used William's model also known as "Poor's man absorption model", which provide a simple prescription to take these corrections into account. Data on beam asymmetry tend to 1 faster than the model as $-t$ increases, indicating a stronger component of natural exchanges than expected. Nevertheless, the model describe correctly the gross features of the data.

For large $-t$ values, corrections to the leading Regge poles, such as daughter trajectories or Regge cuts, might be important. Their contribution are not easily derived theoretically, but can be estimated from data when available. In Ref. [537], we developed a model for $\gamma p \to \pi^0 p$ that includes Regge cuts, fitting to data measured at $E_\gamma = 6$–$15\,\text{GeV}$ in the range $-t < 1.5\,\text{GeV}^2$. The data display a dip at $t \simeq -0.5\,\text{GeV}^2$ that is described in the model by including a zero in the vector Regge pole. At this point the vector trajectory vanishes, $\alpha(t) = 0$. Such a zero is required to remove the unphysical scalar pole in tensor trajectories. Because of the EXD discussed in Section 4.2, the same zero appears in the vector trajectory as well. This is also called a nonsense wrong-signature zero (NSWSZ). Regge cuts are parametrized in a similar way to Regge pole as in Eq. (72), but with a flatter trajectory $\alpha_c(t) \simeq 0.5 + 0.2t$. In analogy with the Regge vector pole, we included a NSWSZ in the Regge cut couplings $\beta_c(t) \propto \alpha_c(t)$. Consequently, our model predicts a dip at $t \simeq -2.5\,\text{GeV}^2$. New data from the CLAS detector [553] in a wide t range, displayed on Figure 41, confirm the presence of this dip at the same t for several energies, and thus the presence of the NSWSZ in the Regge cut contribution to the production mechanism in π^0 photoproduction.

The presence of corrections to the leading pole approximation can be identified by comparing the beam asymmetries of η and η' photoproduction. Since Regge poles factorize, assuming only Regge exchanges and the absence of hidden strangeness terms as ϕ exchange, lead to the equivalence of η and η' beam asymmetries. In Ref. [543], we modeled the contribution of the ϕ exchange and obtained that the ratio of η and η' beam asymmetries would deviate from 1 by maximum 2% in the range $-t < 1\,\text{GeV}^2$. This ratio, measured recently by the GlueX collaboration [552] and presented in Figure 40 (right), turned out to be compatible with unity indeed. However, uncertainties are still quite large, about 10%, and the data points are centered around a nominal value about 0.95. One should then take this conclusions cautiously, as the data points could change significantly when more statistics are accumulated.

Tensor mesons are photoproduced by the same t-channel quantum numbers as pseudoscalar mesons. Their differencial cross sections indeed present the same pattern. That is, the isovector π^0 and a_2 cross section present a minimum around $t = -0.5\,\text{GeV}^2$, while the isoscalar η and f_2 cross sections do not, see Figure 42. Since the ω exchange dominates the isovector production, it is natural to associate the dip at $t = -0.5\,\text{GeV}^2$ with a zero in the ω amplitudes. In our previous model of $\gamma p \to \pi^0 p$ we introduced a

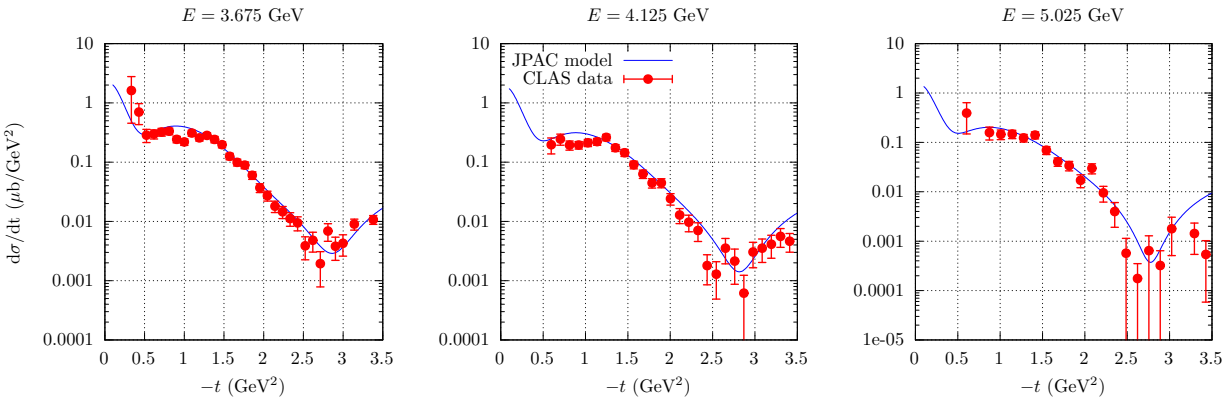

Figure 41: Differential cross section for Regge model at three energies compared to the $\gamma p \to \pi^0 p$ CLAS data [553] Figure from [553].

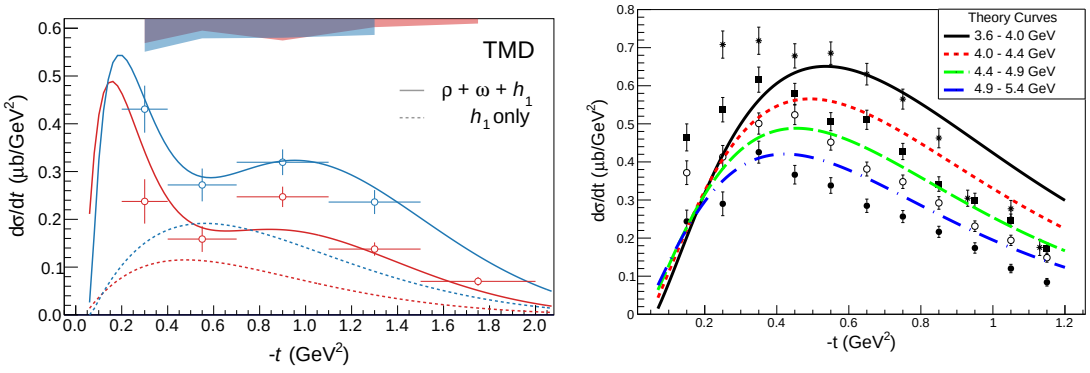

Figure 42: $a_2(1320)$ (left) and $f_2(1270)$ (right) differential cross section extracted by the CLAS collaboration [554, 555] compared to the JPAC model of Ref. [544]. Figures from [544] (left) and [554] (right).

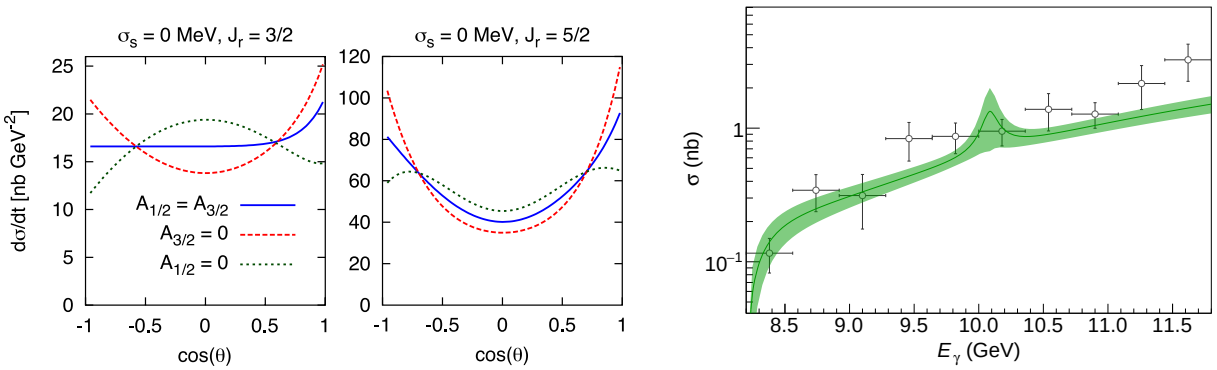

Figure 43: (left) Examples of angular distributions of the pentaquark at the peak, depending on the spin-parity assignment and relative photocoupling sizes. (right) Fit to GlueX [560] data for a spin assignment of the $P_c(4450)$ $J^P = \frac{3}{2}^-$. Figures from [37] (right) and [561] (left).

NSWSZ in both the ω and the ρ amplitudes and explained that it was filled by Regge cut contributions. In Ref. [544] we revised this hypothesis and introduced the NSWSZ only in the ω production, so that the dip at $t = -0.5\,\text{GeV}^2$ is filled by a nonvanishing ρ contribution. In this model, the ρ amplitude does not feature the NSWZ and lead to a nondipping shape of the f_2 differential cross section, in agreement with the recent measurements by the CLAS collaboration [554, 555].

4.4. Photoproduction of J/ψ and pentaquark searches

The use of photon beams to search for or confirm exotic hadrons is appealing since it reduces the role of kinematic effects and minimizes the model dependence of partial-wave analyses [37, 556–559].

As discussed in Section 2.5, the LHCb data on $\Lambda_b^0 \to J/\psi\, p\, K^-$ decay potentially indicate the existence of several baryon resonances in the $J/\psi\, p$ spectrum that do not fit predictions of the valence quark model [254, 255, 562]. These states have the right mass to be produced directly at JLab, through a scan of the J/ψ photoproduction cross sections. Searches proposed at Hall C and CLAS12 are ongoing [563, 564], while the results by GlueX show no evidence of narrow peaks [560]. With fits to these data existing so far, we could provide estimates for the upper limits of the pentaquark coupling sizes. The quantum numbers are not reliably determined yet, so in order to provide an estimate we focus the discussion on the $P_c(4450)$ as determined in the older analysis [254].

We describe the diffractive J/ψ production background with an effective Pomeron exchange [37, 561]. We adopt the vector Pomeron model [565, 566],

$$\langle \lambda_\psi \lambda_{p'} | T_P | \lambda_\gamma \lambda_p \rangle = F(s,t)\, \bar{u}(p_f, \lambda_{p'}) \gamma_\mu u(p_i, \lambda_p) [\varepsilon^\mu(q,\lambda_\gamma) q^\nu - \varepsilon^\nu(q,\lambda_\gamma) q^\mu] \varepsilon^*_\nu(p_\psi, \lambda_\psi)\,, \tag{76}$$

with

$$F(s,t) = iA \left(\frac{s - s_{\text{th}}}{s_0} \right)^{\alpha(t)} \frac{e^{b_0 (t - t_{\text{min}})}}{s}\,, \tag{77}$$

that was successful in reproducing the azimuthal angular dependencies (see Sections 2.4.2 and 4.6). Since this is just an effective description, the Pomeron parameters are refitted to data. The pentaquark contribution is given by a simple Breit-Wigner amplitude

$$\langle \lambda_\psi \lambda_{p'} | T_R | \lambda_\gamma \lambda_p \rangle = f_{\text{th}}(s) \frac{\langle \lambda_\psi \lambda_{p'} | T_{\text{dec}} | \lambda_R \rangle \langle \lambda_R | T^\dagger_{\text{em}} | \lambda_\gamma \lambda_p \rangle}{M_R^2 - s - i \Gamma_R M_R}\,, \tag{78}$$

where $f_{\text{th}}(s)$ further suppresses the amplitude at threshold. The strong decay $\langle \lambda_\psi \lambda_{p'} | T_{\text{dec}} | \lambda_R \rangle$ is determined by the spin-parity of the state, while $\langle \lambda_R | T^\dagger_{\text{em}} | \lambda_\gamma \lambda_p \rangle$ depends on the unknown pentaquark photocouplings.

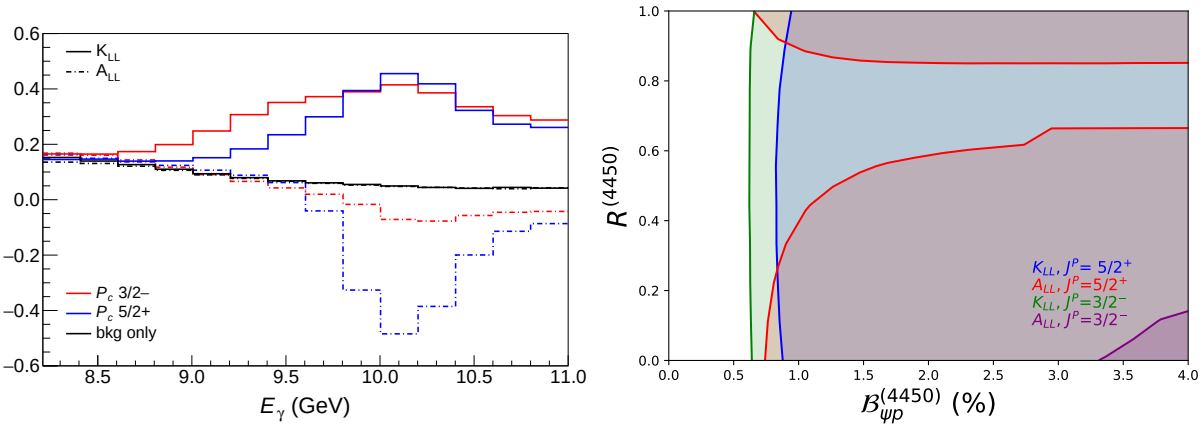

Figure 44: (left) Predictions for K_{LL} (solid line) and A_{LL} (dash-dotted line) in the SBS acceptance in bins of energy in the presence of two pentaquarks, considering hadronic branching ratios $\mathcal{B}_{\psi p}^{(4450)} = \mathcal{B}_{\psi p}^{(4380)} = 1.3\%$, and photocouplings ratio $R^{(4450)} = 0.2$, $R^{(4380)} = 1/\sqrt{2}$ and an experimental resolution of 125 MeV. (right) 5σ sensitivity map of the dependence of the double polarization observables on the photocoupling ratio R and the branching fraction $\mathcal{B}_{\psi p}$ of the $P_c(4450)$. Figures from [561].

According to vector meson dominance, one can relate the two matrix elements assuming

$$\langle \lambda_\gamma \lambda_p | \, T_{\rm em} \, | \lambda_R \rangle = \frac{\sqrt{4\pi\alpha} f_\psi}{M_\psi} \langle \lambda_\psi = \lambda_\gamma, \lambda_p | \, T_{\rm dec} \, | \lambda_R \rangle \,, \tag{79}$$

and with this provide an upper limit to the branching ratio of the $P_c(4450)$ to the final state where it is actually observed. Before GlueX data were published, most of J/ψ photoproduction data were taken by HERA at higher energies [567, 568], which we analyzed in the first publication [37]. After GlueX data were made available, we noticed that our simple model is not able to fit consistently the low and high energy region. We therefore selected the data at $E_\gamma \lesssim 25\,\text{GeV}$ by GlueX and SLAC [569]. The results are summarized in Table 9 for different spin-parity hypotheses [561], and a fit example is given in Figure 43.

Furthermore, we could provide estimates of the angular distributions of the differential cross sections depending on the relative size of the photocouplings, see Figure 43. These kinds of studies will help pin down the quantum numbers of the pentaquarks if their signals are to be found in photoproduction experiments.

The use of polarization observables has been proposed for an experiment at the Super BigBite Spectrometer (SBS) in Hall A at JLab [570]. It has been argued that these may reach higher signal-to-background ratios than differential cross sections, which is particularly appealing due to the discovery of double-peak structures in the LHCb spectrum. Furthermore, the polarization data offer new and complementary information relevant in the evaluation of the resonance photo- and hadronic couplings. In Ref. [561], we provided sensitivity studies for the planned experiments on extracting the beam-target asymmetry A_{LL},

Table 9: Parameters of the fits for different J^P assignments for the $P_c(4450)$ state. Uncertainties are at the 68% confidence level, except for the branching ratio, whose upper limit is quoted at 95%. Table from [561].

J^P	$\frac{3}{2}^-$	$\frac{5}{2}^+$	$\frac{3}{2}^+$	$\frac{5}{2}^-$
A	0.379 ± 0.051	0.380 ± 0.053	0.378 ± 0.049	0.381 ± 0.053
α_0	0.941 ± 0.047	0.941 ± 0.049	0.942 ± 0.045	0.941 ± 0.048
α' (GeV^{-2})	0.364 ± 0.037	0.367 ± 0.039	0.363 ± 0.035	0.365 ± 0.037
b_0 (GeV^{-2})	0.12 ± 0.14	0.13 ± 0.15	0.12 ± 0.14	0.13 ± 0.15
$\mathcal{B}_{\psi p}^{(4450)}$ (95%)	$\leq 4.3\%$	$\leq 1.4\%$	$\leq 1.8\%$	$\leq 0.71\%$

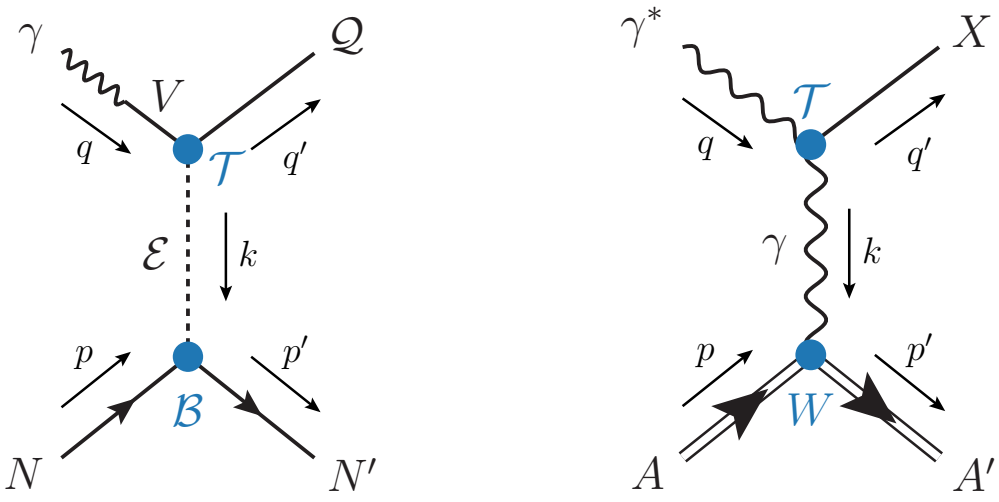

Figure 45: (left) Photoproduction of a quarkonium-like meson, $\mathcal{Q}$ via an exchange $\mathcal{E}$ in the t-channel. (right) Quasi-real photon production of $X(3872)$ via Primakoff effect. Figures from [571].

and the beam-recoil asymmetry K_{LL}, scanning the observable behaviour with the relative coupling sizes, and mapping it as functions of the scattering angles and energies, to find the optimal experimental settings. The results are summarized in Figure 44, where the presence of a broad $P_c(4380)$ with parity opposite to the $P_c(4450)$ was also considered. We found that 250 days of collected data with the SBS experiment would give more than 5σ sensitivity to the P_c signals in large regions of the parameter space, in particular for K_{LL}.

Another possibility is to produce P_c's in backward J/ψ photoproduction. The cross sections can be estimated employing the techniques shown in the following section. Unfortunately, searches of hidden-charm pentaquarks in this way are hindered by large N^* contributions [571].

In view of the experiments in the electron-ion collider (EIC) era, it is instructive and timely to extend these studies to other polarization observables as well, and to investigate pentaquark photo- and electroproduction also in semi-inclusive reactions. Furthermore, EIC colliders are unique factories for hidden-beauty P_b searches [572], hence it is important to provide theoretical studies for these states as well. Ultimately, for the signals to be found in photo- and electroproduction experiments, it shall be important to use the combined knowledge of different observables in order to draw conclusions about the quantum numbers, couplings, and nature of these exotic states.

4.5. XYZ production in electron-proton collisions

Electromagnetic probes are expected to be essential in the near future to provide insight on the nature of exotic hadrons. Besides providing independent confirmation of exotica, at high energies these reactions are not affected by three-body dynamics and constitute efficient probes to determine exotic hadrons' quantum numbers and internal structure. The use of real and quasi-real photon beams to search for exotic hadrons is currently being surveyed in the light sector at JLab, with some incursion into reachable low-lying charmonia, in particular pentaquarks as was shown in the previous section.

The next generation of electron-hadron colliders, the EIC [573, 574] and the EicC [575], promise to open new possibilities of a spectroscopy program with higher energy and luminosity to study the plethora of the XYZ states. In preparation for these new facilities, it is necessary to provide theoretical estimates for the production of quarkonium(-like) states. In particular, we are interested in exclusive processes where $\mathcal{Q}$ is produced through photon fragmentation from threshold to the expected EIC and EicC energies. We aim at providing predictions that are as based on data as possible, in order to minimize the model assumptions related to the microscopic nature of the XYZ states. Moreover we also give predictions for the ordinary quarkonia generated by the production mechanism, in order to provide candles to assess the goodness of the model.

Table 10: List of XYZ states studied, with the corresponding branching ratios into vector quarkonia and light meson.

$\mathcal{Q}$	$\Gamma_{\mathcal{Q}}$ (MeV)	V	$\mathcal{E}$	$\mathcal{B}(\mathcal{Q} \to V\,\mathcal{E})$ (%)
$X(3872)$	1.19 ± 0.19	J/ψ	ρ	$4.9^{+1.9}_{-1.1}$
			ω	$4.4^{+2.3}_{-1.3}$
$Z_c(3900)$	28.3 ± 2.5	J/ψ	π	10.5 ± 3.5
$Z_{cs}(4000)$	131 ± 41	J/ψ	K	~ 10
$X(6900)$	168 ± 102	J/ψ	ω	$\sim 1 - 4$
$Z_b(10610)$	18.4 ± 2.4	$\Upsilon(1S)$	π	$0.54^{+0.19}_{-0.15}$
		$\Upsilon(2S)$		$3.6^{+1.1}_{-0.8}$
		$\Upsilon(3S)$		$2.1^{+0.8}_{-0.6}$
$Z_b(10650)$	11.5 ± 2.2	$\Upsilon(1S)$	π	$0.17^{+0.08}_{-0.06}$
		$\Upsilon(2S)$		$1.4^{+0.6}_{-0.4}$
		$\Upsilon(3S)$		$1.6^{+0.7}_{-0.5}$

We write a helicity amplitude for the production process $\gamma N \to \mathcal{Q} N'$ (see Figure 45),

$$\langle \lambda_{\mathcal{Q}}, \lambda_{N'} | T_{\mathcal{E}} | \lambda_\gamma, \lambda_N \rangle = \mathcal{T}^{\alpha_1 \ldots \alpha_J}_{\lambda_\gamma \lambda_{\mathcal{Q}}}\; \mathcal{P}^{(\mathcal{E})}_{\alpha_1 \ldots \alpha_J ; \beta_1 \ldots \beta_J}\; \mathcal{B}^{\beta_1 \ldots \beta_J}_{\lambda_N \lambda_{N'}}\,, \tag{80}$$

where the rank-J Lorentz tensors associated to the spin J of the exchanged $\mathcal{E}$, $\mathcal{T}$ (top vertex) and $\mathcal{B}$ (bottom vertex) are derived from assumed forms of the $\gamma\mathcal{Q}\mathcal{E}$ and $\mathcal{E}NN'$ interactions, say from effective Lagrangians consistent with expected symmetries of the reactions. The helicity structure is simplified when needed in order to make the amplitude depend on a single coupling. Since most of the XYZ states have been observed to decay into a vector quarkonium, one can assume vector meson dominance to calculate the photon-$\mathcal{Q}$-$\mathcal{E}$ coupling from the measurement of the branching ratio $\mathcal{B}(\mathcal{Q} \to V\,\mathcal{E})$. The phenomenology of the bottom vertex is well constrained by photoproduction phenomenology. Table 10 summarizes the exchanges and branching ratios for the considered exotics.

We note that we are dealing with two energy regimes that require different treatments. We expect that a model with exchange of a fixed-spin particle is valid from threshold to moderate values of s. However, it can be shown that this amplitude behaves as

$$\left\langle \mu_{\mathcal{Q}} \mu_\gamma \middle| T \middle| \mu'_{\tilde{N}} \mu_N \right\rangle \propto \frac{d^j_{\mu'_{\tilde{N}} - \mu_N, \mu_{\mathcal{Q}} - \mu_\gamma}(\theta_t)}{t - m^2_{\mathcal{E}}}\,, \tag{81}$$

where $\cos\theta_t$ is the t-channel scattering angle, and depends linearly on s. At high energies, this expression grows as s^j, which exceeds the unitarity bound. The reason for this is that a fixed-spin exchange amplitude is not analytic in angular momentum. Assuming that the large-s behavior is dominated by a Regge pole rather than a fixed pole, we obtain the standard form of the Regge propagator of Eq. (72). This can be interpreted as originating from the resummation of the leading powers of s^j in the t-channel amplitude, which originate from the exchange of a tower of particles with increasing spin. In the high-energy regime, the $\mathcal{P}^{(\mathcal{E})}_{\alpha_1 \ldots \alpha_J ; \beta_1 \ldots \beta_J}$ is thus replaced by a Regge propagator.

For the Pomeron-dominated $Y(4260)$ production, a fixed-spin description is no longer possible. However, we can use the results discussed in Section 4.4 from Refs. [37, 561], that were fitted to low-energy and high-energy J/ψ photoproduction data separately. Together with a rescaling of couplings, and an upper limit on $Y(4260)$ production from HERA data [576], one can obtain predictions also for this state.

An example of results is shown in Figure 46. We note that the strengths of the amplitudes do not necessarily match in the two regimes. The expectation is that the cross section decreases faster and matches the Regge prediction at $W_{\gamma p} \sim 20\,\text{GeV}$.

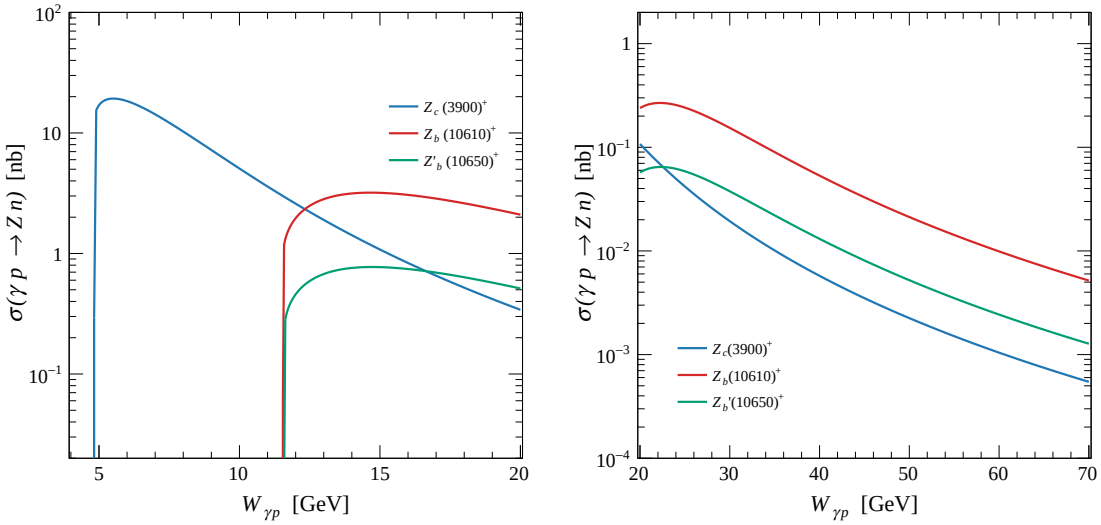

Figure 46: Integrated cross sections for the axial Z_c and $Z_b^{(\prime)}$ states according to the low-energy fixed-spin model (left), and to the high-energy Regge exchange (right). Figures from [571].

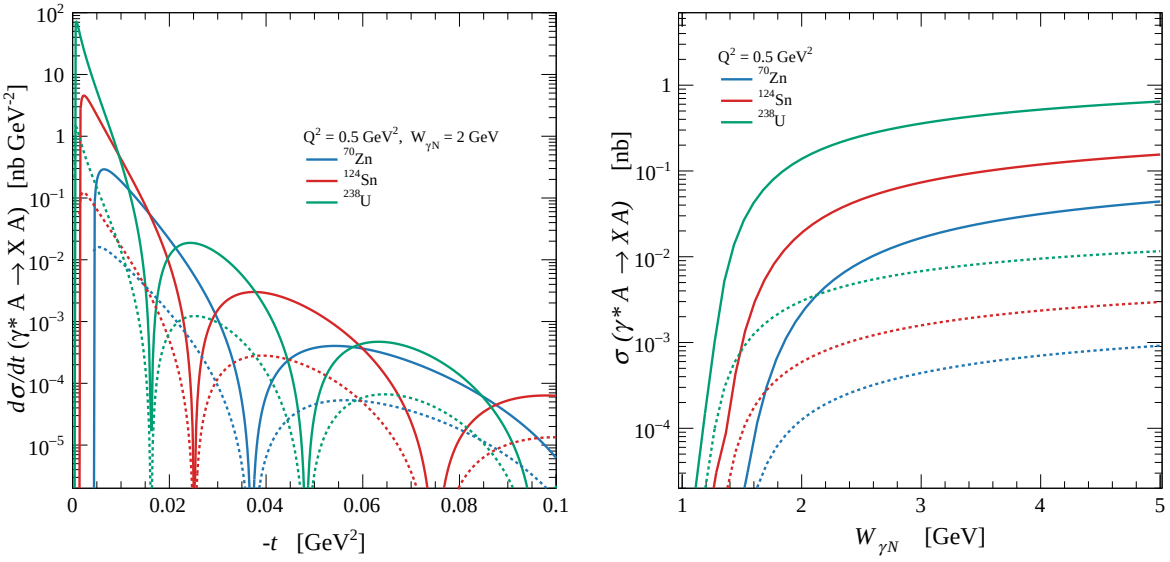

Figure 47: Differential cross sections for $W_{\gamma N} = 2\,\text{GeV}$ (left) and integrated cross sections (right) for Primakoff production of $X(3872)$ off various nuclei. Solid and dashed curves correspond to longitudinal and transverse incoming photons, respectively. Figures from [571].

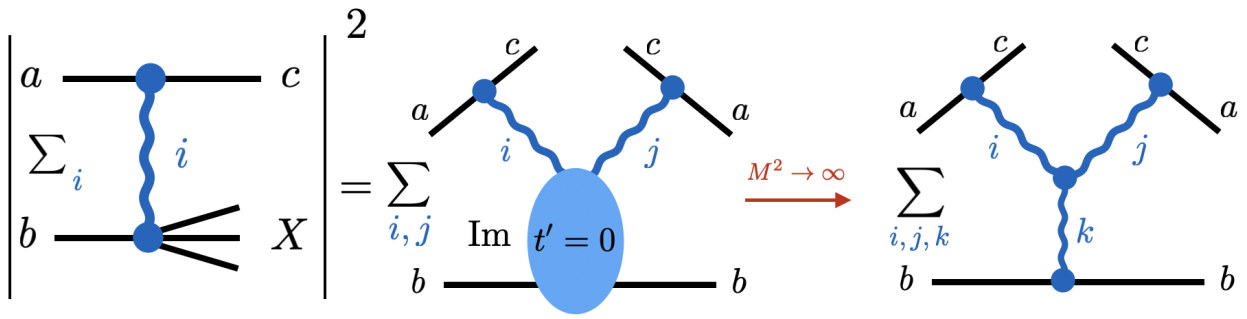

Figure 48: Diagrammatic representation of triple-Regge interactions in the $s, M^2 \to \infty$ limit.

Another possible mechanism to produce the $X(3872)$ at the EIC is through Primakoff effect exploiting the planned nuclear beams, ranging from the proton to uranium. The diagram is shown in Figure 45. The Landau-Yang theorem [577, 578] prohibits the $X(3872)$ to couple to two real photons, but nothing prevents it from coupling to a real and a virtual one. Actually, a recent measurement by Belle found $\tilde{\Gamma}^X_{\gamma\gamma} \times \mathcal{B}(X(3872) \to J/\psi\,\pi^+\pi^-) = 5.5^{+4.1}_{-3.8} \pm 0.7\,\text{eV}$ [579]. The virtuality of the exchanged photon is suppressed for $-t \gg R^{-2} \sim \mathcal{O}(10^{-3})\,\text{GeV}^2$, R being the nuclear radius, so that the exchanged photon is quasi-real. The $X\gamma\gamma^*$ coupling can be estimated from Belle's width and the absolute branching ratios in [580], obtaining $g_{X\gamma\gamma^*} \sim 3.2 \times 10^{-3}$. The cross section is enhanced by the square of the atomic number of the nuclear beam, so we expect this production mechanism to be possible for high Z beams. Figure 47 shows differential and integrated cross section predictions for a variety of nuclei for $Q^2 = 0.5\,\text{GeV}^2$ for an average photon nucleon energy $W_{\gamma N} = W_{\gamma A}/A = 2\,\text{GeV}$, with A being the mass number of the ion.

The integrated cross-section estimations show that the near-threshold production of the $X(3872)$ and Z states might be promising for the EIC or other electron-proton facilities. The $X(3872)$ may see production cross-sections of tens of nanobarn close to threhsold, while charged quarkonium states near-threshold are predicted to be $\mathcal{O}(1\text{nb})$ which are well positioned for a high-luminosity spectroscopy program at the EIC. Additionally, diffractive vector production of vector states was also computed and shown to increase with energy, meaning the higher center-of-mass reach of the EIC is also beneficial for the production of $Y(4260)$ states.

When compared to exclusive reactions, semi-inclusive production can, among others, offer the advantage of easier experimental accessibility. We therefore aim to extend the work described in the previous section to general $\gamma N \to \mathcal{Q}X$ processes, where X represents any combination of final states with total invariant mass M (*aka* missing mass) that are produced in addition to the scrutinized $\mathcal{Q}$. We shall focus on the region characterized by large center-of-mass energy and missing masses, with $s \gg M^2 \gg m_p$. In this limit the $\mathcal{Q}$ meson is produced with high momentum in the near-forward region with $x \sim p_L/p \approx 1$. This region is dominated primarily by "triple-Regge" interactions as shown in Figure 48, where the sum over i, j and k refers to the possible exchanges contributing to the triple Regge vertex. As can be seen, the top and bottom vertices can be taken from our previous work on exclusive reactions. The novel information to be given as input is the triple-Regge vertex itself. Here, production of neutral states is assumed to primarily proceed through a triple-Pomeron interaction [581]. For the charged Z states, on the other hand, pion exchanges dominate the top vertices, and therefore in order to describe the triple-Regge exchange one needs to estimate the total πN scattering cross section, for which one can take the asymptotic Regge approximation [1]. This way, we aim to provide estimates and feasibility studies for semi-inclusive production of heavy quarkonia, which is particularly timely and promising in view of the EIC era.

4.6. Two-meson production in the double-Regge region

As discussed in Section 2.4.2 the $\eta\pi$ spectrum is of particular interest, since the odd partial waves have exotic quantum numbers and specifically, the $J^{PC} = 1^{-+}$ partial wave hosts the π_1 hybrid candidate. To

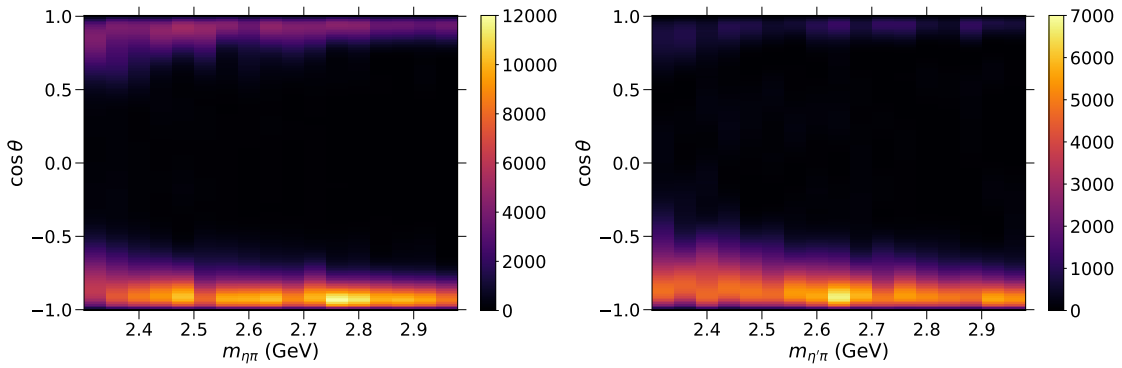

Figure 49: Intensity $I_\theta(m, \cos\theta)$ density distribution computed from the $\eta\pi$ (upper) and $\eta'\pi$ (lower) COMPASS partial waves. Figure from [36].

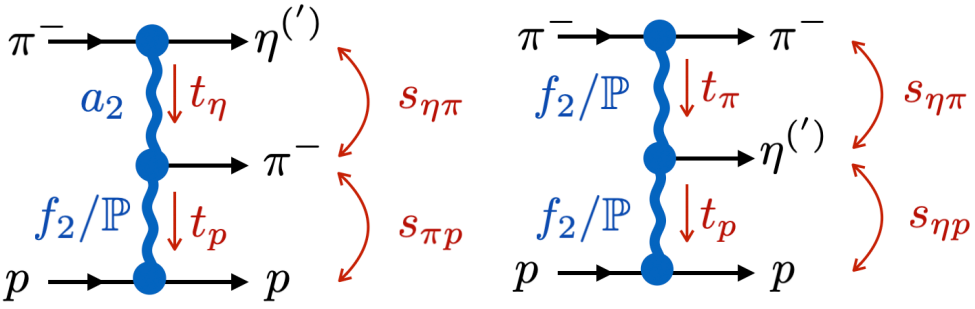

Figure 50: Fast-η (left) and fast-π (rigth) amplitudes. Figure from [36].

further understand the exotic meson production in this channel, one can invoke the Regge-resonance duality to relate the process $\pi p \to R\, p \to \eta^{(\prime)}\pi p$, where R stands for an $\eta^{(\prime)}\pi$ resonance, to the double Regge region where the $\eta^{(\prime)}\pi$ invariant mass is large.

In general the multi-Regge exchange formalism has been extensively studied theoretically in the past [199, 582–587]; more recently the double-Regge exchange was used to study two-kaon photoproduction off the proton [588], and to describe the central meson production in the high energy proton-proton collisions [589–591].

In Ref. [36], we studied the $\pi^- p \to \eta^{(\prime)}\pi^- p$ data measured at COMPASS [195]. The experimental $\eta^{(\prime)}\pi$ m-binned intensity distribution $I(m, \cos\theta, \phi)$, where m is the $\eta^{(\prime)}\pi$ invariant mass, can be computed from the published partial waves [195]. We focus on the $2.4 < m < 3.0\,\text{GeV}$ region, where the double Regge is expected to dominate. The angular variables determine the direction of the $\eta^{(\prime)}$ in the Gottfried-Jackson frame. The ϕ-integrated distributions

$$I_\theta(m, \cos\theta) = \int_0^{2\pi} \mathrm{d}\phi\, I(m, \cos\theta, \phi)\,, \tag{82}$$

are shown in Figure 49 for a total of seventeen mass bins in each channel. We note that the intensity peaks in the forward $\cos\theta \sim 1$ and backward $\cos\theta \sim -1$ regions and both become narrower as the invariant mass m increases. In the forward region, most of the beam momentum is carried by the $\eta^{(\prime)}$ ("fast-η" region), and in the backward region by the pion ("fast-π" region). These features are typical of diffractive processes, pointing to the dominance of double-Regge exchanges for $m \gtrsim 2.3\,\text{GeV}$.

The existence of a forward-backward asymmetry is apparent in Figure 49 and by itself is proof of the existence of resonances with exotic quantum numbers in that m range. This asymmetry can be quantified

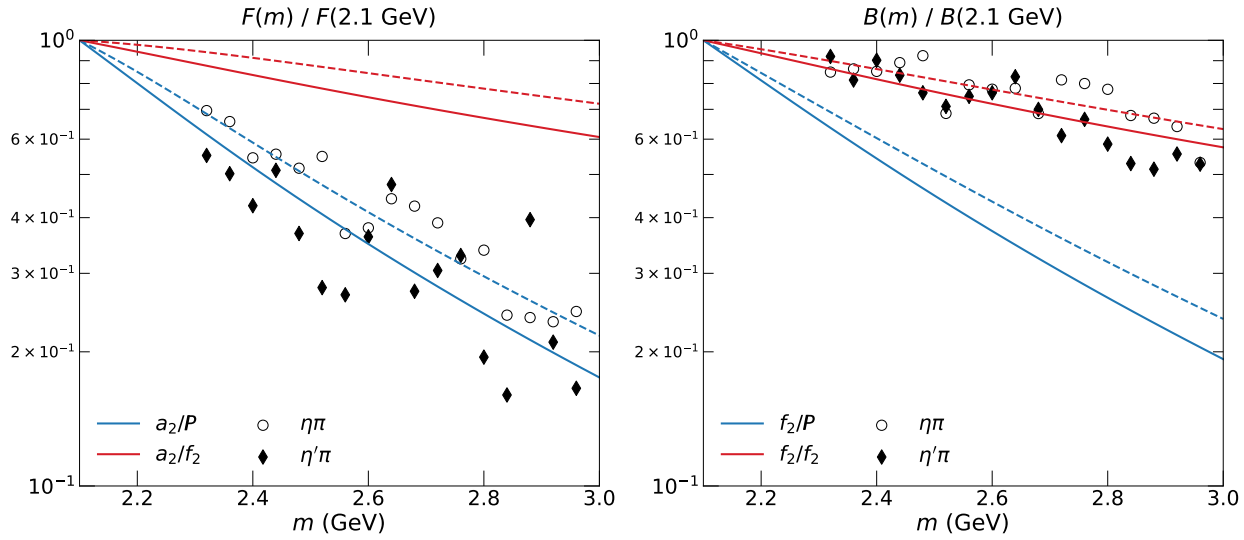

Figure 51: Forward (left) and backward (right) intensities as defined in Eq. (84) for the top-a_2 and top-f_2 amplitudes, respectively. Solid lines correspond to $\eta\pi$ and dashed to $\eta'\pi$. Each theoretical intensity is normalized to its value at $m = 2.1\,\text{GeV}$. In circles and diamonds we show the experimental data arbitrarily rescaled. Figures from [36].

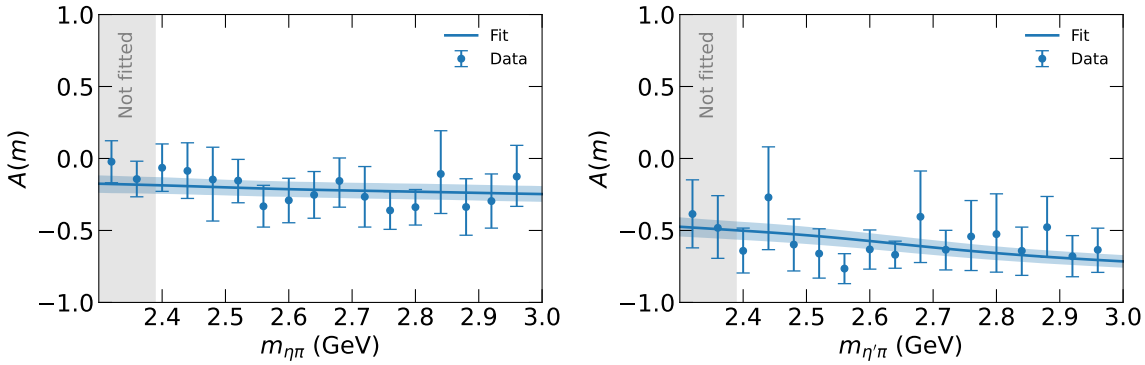

Figure 52: Forward-backward intensity asymmetry as defined in Eq. (83) for $\eta\pi$ (left) and $\eta'\pi$ (right).

through

$$A(m) \equiv \frac{F(m) - B(m)}{F(m) + B(m)}\,, \tag{83}$$

where

$$F(m) \equiv \int_0^1 \mathrm{d}\cos\theta\, I_\theta(m, \cos\theta)\,,\; B(m) \equiv \int_{-1}^0 \mathrm{d}\cos\theta\, I_\theta(m, \cos\theta)\,, \tag{84}$$

with $F(m)$ and $B(m)$ being the forward and backward intensities, respectively.

COMPASS data were correctly described by model of [36]. Specifically, the double-Regge exchange amplitudes depicted in Figure 50 were considered, assuming the dominance of leading Regge poles. The intensity is given by

$$I_{\text{Th}}(m, \Omega) = k(m)\, |A_{\text{Th}}(m, \Omega)|^2, \tag{85}$$

where $k(m) = \lambda^{\frac{1}{2}}(m^2, m^2_{\eta^{(\prime)}}, m^2_\pi)/(2m)$ is the breakup momentum between the π and the $\eta^{(\prime)}$ and the total amplitude $A_{\text{Th}}(m, \Omega)$ is the sum of six double-Regge amplitudes,

$$A_{\text{Th}}(m,\Omega) = c_{a_2\mathbb{P}}\, A_{a_2\mathbb{P}} + c_{a_2 f_2}\, A_{a_2 f_2} + c_{f_2\mathbb{P}}\, A_{f_2\mathbb{P}} + c_{f_2 f_2}\, A_{f_2 f_2} + c_{\mathbb{P}\mathbb{P}}\, A_{\mathbb{P}\mathbb{P}} + c_{\mathbb{P} f_2}\, A_{\mathbb{P} f_2}\,, \tag{86}$$

where the $\{c\}$ are constants fitted to the data.

An important property of multiperipheral amplitudes is the absence of simultaneous singularities in overlapping channels. For example, it is possible to identify that, for fast-η production, the first two terms in Eq. (86) are dual to resonances decaying to $\eta\pi$ and πN, and it is possible to write dispersion relations that enable us to independently study resonances in the beam and target fragmentation region.

The top exchange is dominated by the a_2 trajectory for fast-η, and by f_2 or $\mathbb{P}$ trajectories for fast-π. The bottom exchange is either f_2 or $\mathbb{P}$ for both amplitudes. Given the high energy of the COMPASS pion beam, the $\mathbb{P}$ was expected to be the relevant bottom exchange. We found this to be true for the forward peak, where the slope of the $F(m)$ intensity is dominated by the $a_2/\mathbb{P}$ amplitude as shown in Figure 51. However, for the backward peak we find that the slope of the $B(m)$ intensity is dominated by the bottom f_2 exchange, as also shown in Figure 51.

The $\eta\pi$ intensity can be well described with four amplitudes, either $a_2/\mathbb{P}$ or a_2/f_2, f_2/f_2, $f_2/\mathbb{P}$ or $\mathbb{P}/\mathbb{P}$. The inclusion of either bottom-$\mathbb{P}$ amplitude is necessary to describe the forward region, but the data do not show a clear preference between $f_2/\mathbb{P}$ and $\mathbb{P}/\mathbb{P}$. Figure 52 compares the asymmetry intensity $A(m)$ to the fitted model. The existence of a nonzero asymmetry is clear. The $\eta'\pi$ data are consistently described by the $a_2/\mathbb{P}$, a_2/f_2, f_2/f_2, and $\mathbb{P}/\mathbb{P}$ amplitudes. The $\mathbb{P}/\mathbb{P}$ contribution is necessary to describe the data and is an indication of the large gluon impact on the $\eta'\pi$ system, which relates to the existence of hybrid mesons. This result is consistent with exchange degeneracy breaking between a_2 and f_2 in $\eta'\pi$ production.

Additionally, the double-Regge amplitude model contains an infinite number of partial waves and hence, these cannot be directly matched to the truncated waves from COMPASS. However, both partial waves can be reconciled performing a partial wave analysis on the theoretical amplitudes constrained to the same partial waves employed by COMPASS. Hence, once the double-Regge regime is reached, it is important to study the full amplitude rather than a truncated partial wave decomposition.

4.7. Finite energy sum rules

In the previous sections, we provided models for Regge amplitudes and compared to experimental data. As said, at low energies the $\mathbf{2} \to \mathbf{2}$ amplitude is saturated by a finite number of s-channel partial waves, dominated by resonances, while at high energies it can be represented by a sum over a finite number of leading Regge poles exchanged in the crossed channels. Both are representations of the same analytical amplitudes, so they must be related by a dispersion relation, which can be used to provide strong constraints on resonance parameters by imposing that the sum of partial waves at low energies matches the Regge amplitude at high energies. The dispersion relations are written for invariant amplitudes that are free of kinematic singularities. These are four in pseudoscalar photoproduction and two in πN scattering. We will denote generically those amplitudes as A_i and refer to [539, 592] and [538] for their definition and their relation to observables. For πN scattering, where the s- and u-channel both represent the $\pi N \to \pi N$ reaction, the A_i have definite parity in the variable $\nu = (s-u)/2$.

For each A_i, one writes an integral over the contour depicted in Figure 53. This gives a relation between the imaginary part of the amplitude integrated over the resonance region, and an integral evaluated at complex high energies. In the latter, the amplitude is represented by Regge exchanges, and the integral can be computed analytically. Powers of ν can be multiplied to the amplitude, in order to calculate higher moments. These relations are generally called finite-energy sum rules (FESR) and for pseudoscalar photoproduction they read

$$\frac{1}{\Lambda^{k+1}} \int_0^\Lambda \text{Im}\, A_i(\nu, t) \nu^k \mathrm{d}\nu = \beta(t) \frac{(\Lambda/s_0)^{\alpha(t)-1}}{\alpha(t)+k}\,, \tag{87}$$

where $k \in \mathbb{Z}$. The *r.h.s.* of Eq. (87) includes the nucleon pole and the discontinuity above the πN threshold up to $\nu = \Lambda$ as depicted in Figure 53. The cutoff Λ should be chosen large enough that for $\nu \gtrsim \Lambda$ the

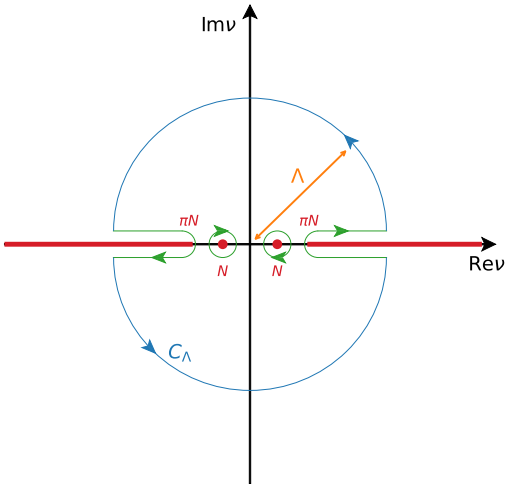

Figure 53: Contour integration in the $\nu = (s-u)/2$ plane for the πN FESR. The contour across the positive real axis accounts for the integral over $\mathrm{Im}\, A_i(\nu, t)$ in the resonance region. At large Λ, the amplitude is saturated by a finite number of Regge poles, so that the integral over C_Λ can be analytically computed.

amplitude is saturated by Reggeons. In the *r.h.s.* of Eq. (87), a sum over the leading Regge poles is understood.

These relations between the low and high energy regimes can be exploited in different ways. One use is to provide further constraints to the resonance parametrization using high energy data. Another utilization would be to predict the cross section at high energies from the reactions at low energies.

As an example, in Figure 54 the differential cross section for π^0 photoproduction at high energies is compared with predictions based on FESR. The low-energy amplitude is calculated from the partial waves extracted by SAID [596]. Analogous application of FESR to η photoproduction [539], using the partial wave from η-MAID [597]. This study revealed a discrepancy between data and predictions in the forward $-t < 0.25\,\mathrm{GeV}^2$ region, which was traced to the A_4 amplitude. In this region indeed the various PWA extractions available in the literature have strong disagreements, and other constraints like the one discussed here can be crucial to resolve the issue.

When precise data in the high energy regime are available, the Regge couplings $\beta_i(t)$ can be determined as explained in the previous section and both sides of Eq. (87) can be compared. In the case of πN scattering we observed an excellent agreement in all invariant amplitudes for both isospin channels [538]. The relations between the pattern of zeroes in the low-energy and high-energy regimes is made apparent thanks to the FESR. For instance, the *l.h.s.* of Eq. (87) for the charged exchange amplitudes helicity nonflip and flip vanish at $t = -0.1$ and $-0.5\,\mathrm{GeV}^2$ respectively, which correspond to zeroes of the ρ exchange residues. The zero in the nonflip amplitude implies that the elastic $\pi^+ p$ and $\pi^- p$ cross sections coincide at that value of t (cf Fig. 54 left panel), while the zero in the flip amplitude produces a dip in the $\pi^- p \to \pi^0 n$ cross section.

The very good agreement of both sides of the FESR allowed us to reconstruct the real part of the amplitudes via the dispersion relation

$$A_i(\nu, t) = \frac{1}{\pi} \int_0^\infty \mathrm{d}\nu' \;\; \mathrm{Im}\, A_i(\nu', t) \left(\frac{1}{\nu' - \nu} \pm \frac{1}{\nu' + \nu} \right) , \tag{88}$$

where the relative sign depends on the parity properties of A_i. In Ref. [538], the imaginary part of the amplitudes in Eq. (88) were taken from SAID in the low energy region and smoothly continued to the Regge parametrization matching the data and satisfying the FESR. The resulting real part of the amplitudes reconstructed from Eq. (88) is in excellent agreement with the original real part from the SAID analysis, *cf.*

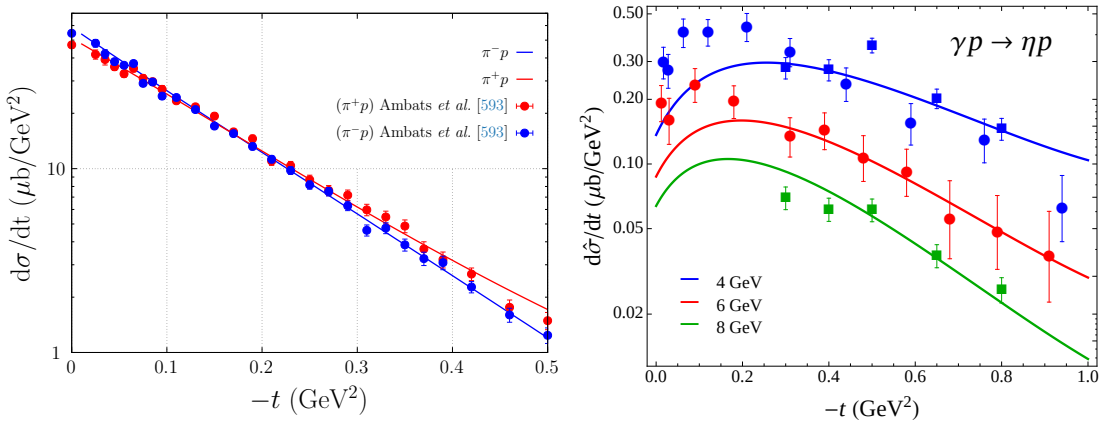

Figure 54: (left) Differential cross sections for $\pi^+ p$ (red) and $\pi^- p$ (blue) elastic scattering at $p_{\rm lab} = 5\,$GeV. Data from [593]. Figure adapted from [538]. (right) η photoproduction differential cross section computed from the low energy models using FESR. Data from [594] (circles) and [595] (squares). Figure from [592].

Figure 55. This result exemplifies how one can determine the complete amplitudes in the complex plane by only fitting its imaginary part on the real axis, together with an appropriate description of the high energy region with Regge poles.

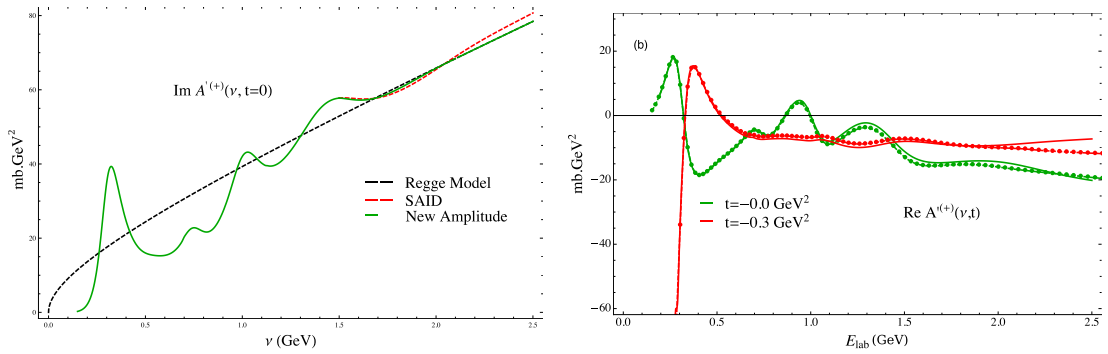

Figure 55: (left) Illustration of FESR in Eq. (87): the Regge parametrization is equivalent to the average of the imaginary part of the amplitude. (right) The real part of the amplitude reconstructed from the dispersion relation in Eq. (88) (dots) matches the original real part from SAID (solid line) [596] . Figures from [538].

In pion photoproduction, the situation is more complicated. The simultaneous inclusion of all three isospin channels leads to 12 invariant amplitudes. In Ref. [592] we computed the *l.h.s.* of the FESR using five independent partial wave analyses in the resonance region. We then performed a global fit of the high energy data constrained by the FESR. The inclusion of Regge daughters was necessary to accommodate both the data and the features of the FESR. Finally our solution involves the minimum Regge content in each amplitude: a leading Regge pole, whose trajectory is constrained around the expected values, and a second subleading term in the natural exchange amplitudes. The latter allowed us to match the position of zeroes in the two sides of the FESR, and to describe the high-energy observables.

5. Summary

A lot of new and unexpected hadrons have been discovered in the last twenty years. To exploit fully the potential of present and future high-statistics datasets, one has to combine knowledge of reaction theory,

hadron phenomenology, and data analysis. The ultimate goal is to reduce the model dependence as much as possible. In this respect, machine learning techniques have the potential to contribute to this objective.

Since its foundation in 2013, the Joint Physics Analysis Center (JPAC) has focused its research on developing the necessary tools to tackle some of the many open challenges in hadron spectroscopy. JPAC has contributed to understand several aspects of the hadron spectrum and of resonance production, as well as of three-body dynamics.

Continuing this work in close cooperation with experimental collaborations will allow to improve the level of rigor on how to assess the properties of resonances in QCD, and eventually to understand why the microscopic constituents of matter arrange themselves into the rich picture one observes in nature.

Acknowledgments

We dedicate this review to the memory of our colleague and friend Mike Pennington, who was instrumental in the inception and development of the Joint Physics Analysis Center. We thank our numerous colleagues within both the theory and experiment hadron physics communities for all their input, keen insight, and encouraging discussions that helped unfold all the physics discussed in this review.

This work was supported by the U.S. Department of Energy under Grant No. DE-AC05-06OR23177 under which Jefferson Science Associates, LLC, manages and operates Jefferson Lab, No. DE-FG02-87ER40365 at Indiana University, and No. DE-SC0018416 at the College of William & Mary, National Science Foundation under Grant No. PHY-2013184, Polish Science Center (NCN) under Grant No. 2018/29/B/ST2/02576, Spanish Ministerio de Economía y Competitividad and Ministerio de Ciencia e Innovación under Grants No. PID2019–106080 GB-C21, No. PID2019-105439G-C22, No. PID2020-118758GB-I00 and No. PID2020-112777GB-I00 (Ref. 10.13039/501100011033), UNAM-PAPIIT under Grant No. IN106921, CONACYT under Grant No. A1-S-21389, National Natural Science Foundation of China Grant No. 12035007 and the NSFC and the Deutsche Forschungsgemeinschaft (DFG, German Research Foundation) through the funds provided to the Sino-German Collaborative Research Center TRR110 "Symmetries and the Emergence of Structure in QCD" (NSFC Grant No. 12070131001, DFG Project-ID 196253076-TRR 110). MA is supported by Generalitat Valenciana under Grant No. CIDEGENT/2020/002. CFR is supported by Spanish Ministerio de Educación y Formación Profesional under Grant No. BG20/00133. VM is a Serra Húnter fellow. JASC is supported by CONACYT under Grant No. 734789. SGS is supported by the Laboratory Directed Research and Development program of Los Alamos National Laboratory under project No. 20210944PRD2, and by the U.S. Department of Energy through the Los Alamos National Laboratory. Los Alamos National Laboratory is operated by Triad National Security, LLC, for the National Nuclear Security Administration of U.S. Department of Energy (Contract No. 89233218CNA000001).

References

[1] P. A. Zyla, et al., Review of Particle Physics, PTEP 2020 (8) (2020) 083C01. doi:10.1093/ptep/ptaa104.

[2] A. Esposito, A. Pilloni, A. D. Polosa, Multiquark Resonances, Phys.Rept. 668 (2017) 1–97. arXiv:1611.07920, doi:10.1016/j.physrep.2016.11.002.

[3] S. L. Olsen, T. Skwarnicki, D. Zieminska, Nonstandard heavy mesons and baryons: Experimental evidence, Rev.Mod.Phys. 90 (1) (2018) 015003. arXiv:1708.04012, doi:10.1103/RevModPhys.90.015003.

[4] F.-K. Guo, C. Hanhart, U.-G. Meißner, Q. Wang, Q. Zhao, B.-S. Zou, Hadronic molecules, Rev.Mod.Phys. 90 (1) (2018) 015004. arXiv:1705.00141, doi:10.1103/RevModPhys.90.015004.

[5] R. F. Lebed, R. E. Mitchell, E. S. Swanson, Heavy-Quark QCD Exotica, Prog.Part.Nucl.Phys. 93 (2017) 143–194. arXiv:1610.04528, doi:10.1016/j.ppnp.2016.11.003.

[6] M. Karliner, J. L. Rosner, T. Skwarnicki, Multiquark States, Ann.Rev.Nucl.Part.Sci 68 (1) (2018) 17–44. arXiv:1711.10626, doi:10.1146/annurev-nucl-101917-020902.

[7] F.-K. Guo, X.-H. Liu, S. Sakai, Threshold cusps and triangle singularities in hadronic reactions, Prog.Part.Nucl.Phys. 112 (2020) 103757. arXiv:1912.07030, doi:10.1016/j.ppnp.2020.103757.

[8] A. Ali, L. Maiani, A. D. Polosa, Multiquark Hadrons, Cambridge University Press, 2019. doi:10.1017/9781316761465.

[9] N. Brambilla, S. Eidelman, C. Hanhart, A. Nefediev, C.-P. Shen, C. E. Thomas, A. Vairo, C.-Z. Yuan, The XYZ states: experimental and theoretical status and perspectives, Phys.Rept. 873 (2020) 1–154. arXiv:1907.07583, doi:10.1016/j.physrep.2020.05.001.

[10] W. Altmannshofer, et al., The Belle II Physics Book, PTEP 2019 (12) (2019) 123C01, [Erratum: PTEP 2020, 029201 (2020)]. arXiv:1808.10567, doi:10.1093/ptep/ptz106.
[11] M. R. Shepherd, J. J. Dudek, R. E. Mitchell, Searching for the rules that govern hadron construction, Nature 534 (7608) (2016) 487–493. doi:10.1038/nature18011.
[12] R. A. Briceño, J. J. Dudek, R. D. Young, Scattering processes and resonances from lattice QCD, Rev.Mod.Phys. 90 (2) (2018) 025001. arXiv:1706.06223, doi:10.1103/RevModPhys.90.025001.
[13] J. Polonyi, Lectures on the functional renormalization group method, Central Eur.J.Phys. 1 (2003) 1–71. arXiv:hep-th/0110026, doi:10.2478/BF02475552.
[14] P. Maris, C. D. Roberts, Dyson-Schwinger equations: A Tool for hadron physics, Int.J.Mod.Phys. E12 (2003) 297–365. arXiv:nucl-th/0301049, doi:10.1142/S0218301303001326.
[15] W. Plessas, The constituent-quark model – Nowadays, Int.J.Mod.Phys. A30 (02) (2015) 1530013. doi:10.1142/S0217751X15300136.
[16] S. J. Brodsky, G. F. de Teramond, H. G. Dosch, J. Erlich, Light-Front Holographic QCD and Emerging Confinement, Phys.Rept. 584 (2015) 1–105. arXiv:1407.8131, doi:10.1016/j.physrep.2015.05.001.
[17] L. D. Landau, On analytic properties of vertex parts in quantum field theory, Nucl.Phys. 13 (1) (1959) 181–192. doi:10.1016/B978-0-08-010586-4.50103-6.
[18] T. Regge, Introduction to complex orbital momenta, Nuovo Cim. 14 (1959) 951. doi:10.1007/BF02728177.
[19] L. Castillejo, R. H. Dalitz, F. J. Dyson, Low's scattering equation for the charged and neutral scalar theories, Phys.Rev. 101 (1956) 453–458. doi:10.1103/PhysRev.101.453.
[20] G. Källén, Elementary particle physics, Addison-Wesley, Reading, MA, 1964.
[21] L. Rosenfeld, Unitarity of the collision matrix and interdependence of resonance parameters, Acta Phys.Polon. A38 (1970) 603–619.
[22] I. J. R. Aitchison, K-matrix formalism for overlapping resonances, Nucl.Phys. A189 (1972) 417–423. doi:10.1016/0375-9474(72)90305-3.
[23] G. F. Chew, S. Mandelstam, Theory of low-energy pion pion interactions, Phys.Rev. 119 (1960) 467–477. doi:10.1103/PhysRev.119.467.
[24] A. Martin, T. Spearman, Elementary particle theory, North-Holland Pub. Co., 1970.
URL https://books.google.com/books?id=sxAzAAAAMAAJ
[25] J. D. Bjorken, Construction of Coupled Scattering and Production Amplitudes Satisfying Analyticity and Unitarity, Phys.Rev.Lett. 4 (1960) 473–474. doi:10.1103/PhysRevLett.4.473.
[26] J. A. Oller, E. Oset, J. R. Peláez, Meson meson interaction in a nonperturbative chiral approach, Phys.Rev. D59 (1999) 074001, [Erratum: Phys.Rev.D 60, 099906 (1999), Erratum: Phys.Rev.D 75, 099903 (2007)]. arXiv:hep-ph/9804209, doi:10.1103/PhysRevD.59.074001.
[27] J. A. Oller, E. Oset, N/D description of two meson amplitudes and chiral symmetry, Phys.Rev. D60 (1999) 074023. arXiv:hep-ph/9809337, doi:10.1103/PhysRevD.60.074023.
[28] M. Wang, Y. Jiang, Y. Liu, W. Qian, X. Lyu, L. Zhang, A novel method to test particle ordering and final state alignment in helicity formalism, Chin.Phys. C45 (6) (2021) 063103. arXiv:2012.03699, doi:10.1088/1674-1137/abf139.
[29] D. Marangotto, Helicity Amplitudes for Generic Multibody Particle Decays Featuring Multiple Decay Chains, Adv.High Energy Phys. 2020 (2020) 6674595. arXiv:1911.10025, doi:10.1155/2020/6674595.
[30] M. Mikhasenko, M. Albaladejo, L. Bibrzycki, C. Fernández-Ramírez, V. Mathieu, S. Mitchell, M. Pappagallo, A. Pilloni, D. Winney, T. Skwarnicki, A. Szczepaniak, Dalitz-plot decomposition for three-body decays, Phys.Rev. D101 (3) (2020) 034033. arXiv:1910.04566, doi:10.1103/PhysRevD.101.034033.
[31] M. Jacob, G. C. Wick, On the general theory of collisions for particles with spin, Annals Phys. 7 (1959) 404–428, [Annals Phys.281,774(2000)]. doi:10.1016/0003-4916(59)90051-X.
[32] M. Mikhasenko, A. Pilloni, J. Nys, M. Albaladejo, C. Fernández-Ramírez, A. Jackura, V. Mathieu, N. Sherrill, T. Skwarnicki, A. P. Szczepaniak, What is the right formalism to search for resonances?, Eur.Phys.J. C78 (3) (2018) 229. arXiv:1712.02815, doi:10.1140/epjc/s10052-018-5670-y.
[33] A. Pilloni, J. Nys, M. Mikhasenko, M. Albaladejo, C. Fernández-Ramírez, A. Jackura, V. Mathieu, N. Sherrill, T. Skwarnicki, A. P. Szczepaniak, What is the right formalism to search for resonances? II. The pentaquark chain, Eur.Phys.J. C78 (9) (2018) 727. arXiv:1805.02113, doi:10.1140/epjc/s10052-018-6177-2.
[34] G. Cowan, K. Cranmer, E. Gross, O. Vitells, Asymptotic formulae for likelihood-based tests of new physics, Eur.Phys.J. C71 (2011) 1554, [Erratum: Eur.Phys.J.C 73, 2501 (2013)]. arXiv:1007.1727, doi:10.1140/epjc/s10052-011-1554-0.
[35] G. Cowan, Statistical Models with Uncertain Error Parameters, Eur.Phys.J. C79 (2) (2019) 133. arXiv:1809.05778, doi:10.1140/epjc/s10052-019-6644-4.
[36] Ł. Bibrzycki, C. Fernández-Ramírez, V. Mathieu, M. Mikhasenko, M. Albaladejo, A. N. Hiller Blin, A. Pilloni, A. P. Szczepaniak, $\pi^- p \to \eta^{(\prime)} \pi^- p$ in the double-Regge region, Eur.Phys.J. C81 (7) (2021) 647. doi:10.1140/epjc/s10052-021-09420-1.
[37] A. N. Hiller Blin, C. Fernández-Ramírez, A. Jackura, V. Mathieu, V. I. Mokeev, A. Pilloni, A. P. Szczepaniak, Studying the $P_c(4450)$ resonance in J/ψ photoproduction off protons, Phys.Rev. D94 (3) (2016) 034002. arXiv:1606.08912, doi:10.1103/PhysRevD.94.034002.
[38] A. Rodas, A. Pilloni, M. Albaladejo, C. Fernandez-Ramirez, V. Mathieu, A. P. Szczepaniak, Scalar and tensor resonances in J/ψ radiative decays (9 2021). arXiv:2110.00027.
[39] A. Rodas, et al., Determination of the pole position of the lightest hybrid meson candidate, Phys.Rev.Lett. 122 (4) (2019) 042002. arXiv:1810.04171, doi:10.1103/PhysRevLett.122.042002.
[40] L. Lyons, W. Allison, Maximum Likelihood or Extended Maximum Likelihood?, Nucl.Instrum.Meth. A245 (1986) 530–

534. doi:10.1016/0168-9002(86)91293-3.
[41] R. J. Barlow, Extended maximum likelihood, Nucl.Instrum.Meth. A297 (1990) 496–506. doi:10.1016/0168-9002(90)91334-8.
[42] F. James, Statistical methods in experimental physics, 2006.
[43] G. D'Agostini, On the use of the covariance matrix to fit correlated data, Nucl.Instrum.Meth. A346 (1994) 306–311. doi:10.1016/0168-9002(94)90719-6.
[44] F. James, M. Roos, Minuit: A System for Function Minimization and Analysis of the Parameter Errors and Correlations, Comput.Phys.Commun. 10 (1975) 343–367. doi:10.1016/0010-4655(75)90039-9.
[45] K. Levenberg, A method for the solution of certain non-linear problems in least squares, Quart.Appl.Math. 2 (1944) 164–168. doi:10.1090/qam/10666.
[46] D. W. Marquardt, An Algorithm for Least-Squares Estimation of Nonlinear Parameters, SIAM Journal on Applied Mathematics 11 (1963) 431–441. doi:10.1137/0111030.
[47] D. G. Ireland, S. Janssen, J. Ryckebusch, A genetic algorithm analysis of N^* resonances in $p(\gamma, K^+)\Lambda$ reactions, Nucl.Phys. A740 (2004) 147–167. arXiv:nucl-th/0312103, doi:10.1016/j.nuclphysa.2004.05.007.
[48] C. Fernández-Ramírez, E. Moya de Guerra, A. Udías, J. M. Udías, Properties of Nucleon Resonances by means of a Genetic Algorithm, Phys.Rev. C77 (2008) 065212. arXiv:0805.4178, doi:10.1103/PhysRevC.77.065212.
[49] C. Fernández-Ramírez, I. V. Danilkin, D. M. Manley, V. Mathieu, A. P. Szczepaniak, Coupled-channel model for $\bar{K}N$ scattering in the resonant region, Phys.Rev. D93 (3) (2016) 034029. arXiv:1510.07065, doi:10.1103/PhysRevD.93.034029.
[50] B. Efron, R. Tibshirani, An Introduction to the Bootstrap, Chapman & Hall/CRC Monographs on Statistics & Applied Probability, Taylor & Francis, 1994.
URL https://www.crcpress.com/An-Introduction-to-the-Bootstrap/Efron-Tibshirani/p/book/9780412042317
[51] J. Landay, M. Döring, C. Fernández-Ramírez, B. Hu, R. Molina, Model Selection for Pion Photoproduction, Phys.Rev. C95 (1) (2017) 015203. arXiv:1610.07547, doi:10.1103/PhysRevC.95.015203.
[52] C. Fernández-Ramírez, A simple example of MIGRAD vs. bootstrap (2021).
URL https://github.com/JointPhysicsAnalysisCenter/SimpleMIGRADvsBS
[53] M. Mikhasenko, Y. Wunderlich, A. Jackura, V. Mathieu, A. Pilloni, B. Ketzer, A. Szczepaniak, Three-body scattering: Ladders and Resonances, JHEP 08 (2019) 080. arXiv:1904.11894, doi:10.1007/JHEP08(2019)080.
[54] M. Mikhasenko, A. Pilloni, M. Albaladejo, C. Fernández-Ramírez, A. Jackura, V. Mathieu, J. Nys, A. Rodas, B. Ketzer, A. P. Szczepaniak, Pole position of the $a_1(1260)$ from τ-decay, Phys.Rev. D98 (9) (2018) 096021. arXiv:1810.00016, doi:10.1103/PhysRevD.98.096021.
[55] A. Jackura, et al., New analysis of $\eta\pi$ tensor resonances measured at the COMPASS experiment, Phys.Lett. B779 (2018) 464–472. arXiv:1707.02848, doi:10.1016/j.physletb.2018.01.017.
[56] A. Krizhevsky, I. Sutskever, G. Hinton, Imagenet classification with deep convolutional neural networks, in: Advances in Neural Information Processing Systems, Vol. 2, 2012, pp. 1097–1105.
URL https://www.scopus.com/inward/record.uri?eid=2-s2.0-84876231242&partnerID=40&md5=621b2cd1757ccc77341281f8a2f2ecaf
[57] Y. LeCun, L. Bottou, Y. Bengio, P. Haffner, Gradient-based learning applied to document recognition, Proc. IEEE 86 (11) (1998) 2278–2323. doi:10.1109/5.726791.
[58] V. Nair, G. E. Hinton, Rectified linear units improve restricted boltzmann machines, in: Proceedings of the 27th International Conference on International Conference on Machine Learning, ICML'10, Omnipress, Madison, WI, USA, 2010, p. 807–814. doi:10.5555/3104322.3104425.
[59] X. Glorot, A. Bordes, Y. Bengio, Deep sparse rectifier neural networks, in: Proceedings of the Fourteenth International Conference on Artificial Intelligence and Statistics, Vol. 15 of Proceedings of Machine Learning Research, PMLR, 2011, pp. 315–323.
URL https://proceedings.mlr.press/v15/glorot11a.html
[60] D. P. Kingma, J. Ba, Adam: A method for stochastic optimization, in: Y. Bengio, Y. LeCun (Eds.), 3rd International Conference on Learning Representations, ICLR 2015, San Diego, CA, USA, May 7-9, 2015, Conference Track Proceedings, 2015. arXiv:1412.6980.
[61] S. Ioffe, C. Szegedy, Batch normalization: Accelerating deep network training by reducing internal covariate shift, in: F. Bach, D. Blei (Eds.), Proceedings of the 32nd International Conference on Machine Learning, Vol. 37 of Proceedings of Machine Learning Research, PMLR, 2015, pp. 448–456. arXiv:1502.03167.
URL https://proceedings.mlr.press/v37/ioffe15.html
[62] V. V. Gligorov, M. Williams, Efficient, reliable and fast high-level triggering using a bonsai boosted decision tree, JINST 8 (2013) P02013. arXiv:1210.6861, doi:10.1088/1748-0221/8/02/P02013.
[63] P. Baldi, P. Sadowski, D. Whiteson, Searching for Exotic Particles in High-Energy Physics with Deep Learning, Nature Commun. 5 (2014) 4308. arXiv:1402.4735, doi:10.1038/ncomms5308.
[64] R. Santos, M. Nguyen, J. Webster, S. Ryu, J. Adelman, S. Chekanov, J. Zhou, Machine learning techniques in searches for $t\bar{t}h$ in the $h \to b\bar{b}$ decay channel, JINST 12 (04) (2017) P04014. arXiv:1610.03088, doi:10.1088/1748-0221/12/04/P04014.
[65] C. Peterson, T. Rognvaldsson, L. Lonnblad, JETNET 3.0: A Versatile artificial neural network package, Comput.Phys.Commun. 81 (1994) 185–220. doi:10.1016/0010-4655(94)90120-1.
[66] G. Aad, et al., Performance of b-Jet Identification in the ATLAS Experiment, JINST 11 (04) (2016) P04008. arXiv:1512.01094, doi:10.1088/1748-0221/11/04/P04008.
[67] W. Adam, R. Fruhwirth, A. Strandlie, T. Todorov, Reconstruction of electrons with the Gaussian sum filter in the CMS

tracker at LHC, eConf C0303241 (2003) TULT009. arXiv:physics/0306087, doi:10.1088/0954-3899/31/9/N01.
[68] M. Aaboud, et al., Performance of the ATLAS Track Reconstruction Algorithms in Dense Environments in LHC Run 2, Eur.Phys.J. C77 (10) (2017) 673. arXiv:1704.07983, doi:10.1140/epjc/s10052-017-5225-7.
[69] M. Lazzarin, S. Alioli, S. Carrazza, MCNNTUNES: Tuning Shower Monte Carlo generators with machine learning, Comput.Phys.Commun. 263 (2021) 107908. arXiv:2010.02213, doi:10.1016/j.cpc.2021.107908.
[70] A. Buckley, Computational challenges for MC event generation, J.Phys.Conf.Ser. 1525 (1) (2020) 012023. arXiv:1908.00167, doi:10.1088/1742-6596/1525/1/012023.
[71] R. D. Ball, et al., Parton distributions for the LHC Run II, JHEP 04 (2015) 040. arXiv:1410.8849, doi:10.1007/JHEP04(2015)040.
[72] S. Forte, L. Garrido, J. I. Latorre, A. Piccione, Neural network parametrization of deep inelastic structure functions, JHEP 05 (2002) 062. arXiv:hep-ph/0204232, doi:10.1088/1126-6708/2002/05/062.
[73] J. Rojo, J. I. Latorre, Neural network parametrization of spectral functions from hadronic tau decays and determination of QCD vacuum condensates, JHEP 01 (2004) 055. arXiv:hep-ph/0401047, doi:10.1088/1126-6708/2004/01/055.
[74] J. W. T. Keeble, A. Rios, Machine learning the deuteron, Phys.Lett. B809 (2020) 135743. arXiv:1911.13092, doi:10.1016/j.physletb.2020.135743.
[75] C. Adams, G. Carleo, A. Lovato, N. Rocco, Variational Monte Carlo Calculations of $A \leq 4$ Nuclei with an Artificial Neural-Network Correlator Ansatz, Phys.Rev.Lett. 127 (2) (2021) 022502. arXiv:2007.14282, doi:10.1103/PhysRevLett.127.022502.
[76] R. D. Ball, S. Forte, A. Guffanti, E. R. Nocera, G. Ridolfi, J. Rojo, Unbiased determination of polarized parton distributions and their uncertainties, Nucl.Phys. B874 (2013) 36–84. arXiv:1303.7236, doi:10.1016/j.nuclphysb.2013.05.007.
[77] L. Del Debbio, S. Forte, J. I. Latorre, A. Piccione, J. Rojo, Neural network determination of parton distributions: The Nonsinglet case, JHEP 03 (2007) 039. arXiv:hep-ph/0701127, doi:10.1088/1126-6708/2007/03/039.
[78] M. Abdughani, J. Ren, L. Wu, J. M. Yang, J. Zhao, Supervised deep learning in high energy phenomenology: a mini review, Commun.Theor.Phys. 71 (8) (2019) 955. arXiv:1905.06047, doi:10.1088/0253-6102/71/8/955.
[79] D. Guest, K. Cranmer, D. Whiteson, Deep Learning and its Application to LHC Physics, Ann.Rev.Nucl.Part.Sci. 68 (2018) 161–181. arXiv:1806.11484, doi:10.1146/annurev-nucl-101917-021019.
[80] D. L. B. Sombillo, Y. Ikeda, T. Sato, A. Hosaka, Classifying the pole of an amplitude using a deep neural network, Phys.Rev. D102 (1) (2020) 016024. arXiv:2003.10770, doi:10.1103/PhysRevD.102.016024.
[81] D. L. B. Sombillo, Y. Ikeda, T. Sato, A. Hosaka, Model independent analysis of coupled-channel scattering: A deep learning approach, Phys.Rev. D104 (3) (2021) 036001. arXiv:2105.04898, doi:10.1103/PhysRevD.104.036001.
[82] D. L. B. Sombillo, Y. Ikeda, T. Sato, A. Hosaka, Unveiling the pole structure of S-matrix using deep learning (4 2021). arXiv:2104.14182.
[83] L. Ng, L. Bibrzycki, J. Nys, C. Fernandez-Ramirez, A. Pilloni, V. Mathieu, A. J. Rasmusson, A. P. Szczepaniak, Deep Learning Exotic Hadrons (10 2021). arXiv:2110.13742.
[84] C. M. Bishop, Pattern Recognition and Machine Learning (Information Science and Statistics), Springer-Verlag, Berlin, Heidelberg, 2006.
[85] B. D. Ripley, Pattern Recognition and Neural Networks, Cambridge University Press, 1996. doi:10.1017/CBO9780511812651.
[86] G. James, D. Witten, T. Hastie, R. Tibshirani, An Introduction to Statistical Learning, Springer, 2017.
URL https://faculty.marshall.usc.edu/gareth-james/ISL/
[87] I. Goodfellow, Y. Bengio, A. Courville, Deep Learning, MIT Press, 2016, http://www.deeplearningbook.org.
[88] C. C. Aggarwal, Neural Networks and Deep Learning: A Textbook, 1st Edition, Springer Publishing Company, Incorporated, 2018.
[89] M. P. Deisenroth, A. A. Faisal, C. S. Ong, Mathematics for Machine Learning, Cambridge University Press, 2020. doi:10.1017/9781108679930.
[90] T. Hastie, R. Tibshirani, J. Friedman, The Elements of Statistical Learning: Data Mining, Inference, and Prediction, Springer series in statistics, Springer, 2009.
URL https://books.google.pl/books?id=eBSgoAEACAAJ
[91] S. M. Lundberg, S.-I. Lee, A unified approach to interpreting model predictions, in: I. Guyon, U. V. Luxburg, S. Bengio, H. Wallach, R. Fergus, S. Vishwanathan, R. Garnett (Eds.), Advances in Neural Information Processing Systems, Vol. 30, Curran Associates, Inc., 2017. arXiv:1705.07874.
URL https://proceedings.neurips.cc/paper/2017/file/8a20a8621978632d76c43dfd28b67767-Paper.pdf
[92] Y. Gal, Z. Ghahramani, Dropout as a bayesian approximation: Representing model uncertainty in deep learning, in: M. F. Balcan, K. Q. Weinberger (Eds.), Proceedings of The 33rd International Conference on Machine Learning, Vol. 48 of Proceedings of Machine Learning Research, PMLR, New York, New York, USA, 2016, pp. 1050–1059. arXiv:1506.02142.
URL https://proceedings.mlr.press/v48/gal16.html
[93] S. J. Pan, Q. Yang, A survey on transfer learning, IEEE Transactions on Knowledge and Data Engineering 22 (10) (2010) 1345–1359. doi:10.1109/TKDE.2009.191.
[94] D. S. Maitra, U. Bhattacharya, S. K. Parui, Cnn based common approach to handwritten character recognition of multiple scripts, in: 2015 13th International Conference on Document Analysis and Recognition (ICDAR), 2015, pp. 1021–1025. doi:10.1109/ICDAR.2015.7333916.
[95] H. T. H. Phan, A. Kumar, J. Kim, D. Feng, Transfer learning of a convolutional neural network for hep-2 cell image classification, in: 2016 IEEE 13th International Symposium on Biomedical Imaging (ISBI), 2016, pp. 1208–1211. doi:10.1109/ISBI.2016.7493483.
[96] T. Hachaj, Ł. Bibrzycki, M. Piekarczyk, Recognition of cosmic ray images obtained from cmos sensors used in mobile

phones by approximation of uncertain class assignment with deep convolutional neural network, Sensors 21 (6) (2021). doi:10.3390/s21061963.
URL https://www.mdpi.com/1424-8220/21/6/1963
[97] D. P. Kingma, M. Welling, Auto-Encoding Variational Bayes (12 2013). arXiv:1312.6114.
[98] G. E. Hinton, R. Salakhutdinov, Reducing the dimensionality of data with neural networks, Science 313 (2006) 504–507. doi:10.1126/science.1127647.
[99] I. Goodfellow, J. Pouget-Abadie, M. Mirza, B. Xu, D. Warde-Farley, S. Ozair, A. Courville, Y. Bengio, Generative adversarial networks, Commun. ACM 63 (11) (2020) 139–144. doi:10.1145/3422622.
URL https://doi.org/10.1145/3422622
[100] T. Sjostrand, S. Mrenna, P. Z. Skands, A Brief Introduction to PYTHIA 8.1, Comput.Phys.Commun. 178 (2008) 852–867. arXiv:0710.3820, doi:10.1016/j.cpc.2008.01.036.
[101] J. Bellm, et al., Herwig 7.0/Herwig++ 3.0 release note, Eur.Phys.J. C76 (4) (2016) 196. arXiv:1512.01178, doi:10.1140/epjc/s10052-016-4018-8.
[102] T. Gleisberg, S. Hoeche, F. Krauss, M. Schonherr, S. Schumann, F. Siegert, J. Winter, Event generation with SHERPA 1.1, JHEP 02 (2009) 007. arXiv:0811.4622, doi:10.1088/1126-6708/2009/02/007.
[103] L. Velasco, E. McClellan, N. Sato, P. Ambrozewicz, T. Liu, W. Melnitchouk, M. P. Kuchera, Y. Alanazi, Y. Li, cFAT-GAN: Conditional Simulation of Electron-Proton Scattering Events with Variate Beam Energies by a Feature Augmented and Transformed Generative Adversarial Network, in: 19th IEEE International Conference on Machine Learning and Applications, 2020, pp. 372–375. doi:10.1109/icmla51294.2020.00066.
[104] Y. Alanazi, et al., AI-based Monte Carlo event generator for electron-proton scattering (8 2020). arXiv:2008.03151.
[105] Y. Alanazi, N. Sato, P. Ambrozewicz, A. N. H. Blin, W. Melnitchouk, M. Battaglieri, T. Liu, Y. Li, A survey of machine learning-based physics event generation (6 2021). arXiv:2106.00643.
[106] S. Godfrey, N. Isgur, Mesons in a Relativized Quark Model with Chromodynamics, Phys.Rev. D32 (1985) 189–231. doi:10.1103/PhysRevD.32.189.
[107] S. Capstick, N. Isgur, Baryons in a Relativized Quark Model with Chromodynamics, Phys.Rev. D34 (1986) 2809. doi:10.1103/PhysRevD.34.2809.
[108] S. Weinberg, Phenomenological Lagrangians, Physica A 96 (1-2) (1979) 327–340. doi:10.1016/0378-4371(79)90223-1.
[109] E. E. Jenkins, A. V. Manohar, Baryon chiral perturbation theory using a heavy fermion Lagrangian, Phys.Lett. B255 (1991) 558–562. doi:10.1016/0370-2693(91)90266-S.
[110] C. Ordonez, U. van Kolck, Chiral lagrangians and nuclear forces, Phys.Lett. B291 (1992) 459–464. doi:10.1016/0370-2693(92)91404-W.
[111] C. Ordonez, L. Ray, U. van Kolck, Nucleon-nucleon potential from an effective chiral Lagrangian, Phys.Rev.Lett. 72 (1994) 1982–1985. doi:10.1103/PhysRevLett.72.1982.
[112] J. Bijnens, G. Colangelo, G. Ecker, J. Gasser, M. E. Sainio, Elastic $\pi\pi$ scattering to two loops, Phys.Lett. B374 (1996) 210–216. arXiv:hep-ph/9511397, doi:10.1016/0370-2693(96)00165-7.
[113] J. Bijnens, G. Colangelo, G. Ecker, J. Gasser, M. E. Sainio, Pion-pion scattering at low energy, Nucl.Phys. B508 (1997) 263–310, [Erratum: Nucl.Phys.B 517, 639–639 (1998)]. arXiv:hep-ph/9707291, doi:10.1016/S0550-3213(97)00621-4.
[114] J. Bijnens, G. Colangelo, G. Ecker, The Mesonic chiral Lagrangian of order p^6, JHEP 02 (1999) 020. arXiv:hep-ph/9902437, doi:10.1088/1126-6708/1999/02/020.
[115] J. Bijnens, G. Ecker, Mesonic low-energy constants, Ann.Rev.Nucl.Part.Sci. 64 (2014) 149–174. arXiv:1405.6488, doi:10.1146/annurev-nucl-102313-025528.
[116] V. Bernard, N. Kaiser, U.-G. Meissner, Chiral dynamics in nucleons and nuclei, Int.J.Mod.Phys. E4 (1995) 193–346. arXiv:hep-ph/9501384, doi:10.1142/S0218301395000092.
[117] E. Epelbaum, H.-W. Hammer, U.-G. Meißner, Modern Theory of Nuclear Forces, Rev.Mod.Phys. 81 (2009) 1773–1825. arXiv:0811.1338, doi:10.1103/RevModPhys.81.1773.
[118] J. Gasser, H. Leutwyler, Chiral Perturbation Theory to One Loop, Annals Phys. 158 (1984) 142. doi:10.1016/0003-4916(84)90242-2.
[119] J. Gasser, H. Leutwyler, Chiral Perturbation Theory: Expansions in the Mass of the Strange Quark, Nucl.Phys. B250 (1985) 465–516. doi:10.1016/0550-3213(85)90492-4.
[120] V. Bernard, N. Kaiser, U.-G. Meißner, πK scattering in chiral perturbation theory to one loop, Nucl.Phys. B357 (1991) 129–152. doi:10.1016/0550-3213(91)90461-6.
[121] A. Dobado, M. J. Herrero, T. N. Truong, Unitarized Chiral Perturbation Theory for Elastic Pion-Pion Scattering, Phys.Lett. B235 (1990) 134–140. doi:10.1016/0370-2693(90)90109-J.
[122] T. N. Truong, Remarks on the unitarization methods, Phys.Rev.Lett. 67 (1991) 2260–2263. doi:10.1103/PhysRevLett.67.2260.
[123] A. Dobado, J. R. Peláez, The Inverse amplitude method in chiral perturbation theory, Phys.Rev. D56 (1997) 3057–3073. arXiv:hep-ph/9604416, doi:10.1103/PhysRevD.56.3057.
[124] J. A. Oller, E. Oset, J. R. Peláez, Nonperturbative approach to effective chiral Lagrangians and meson interactions, Phys.Rev.Lett. 80 (1998) 3452–3455. arXiv:hep-ph/9803242, doi:10.1103/PhysRevLett.80.3452.
[125] A. Gomez Nicola, J. R. Peláez, Meson meson scattering within one loop chiral perturbation theory and its unitarization, Phys.Rev. D65 (2002) 054009. arXiv:hep-ph/0109056, doi:10.1103/PhysRevD.65.054009.
[126] S. M. Roy, Exact integral equation for pion pion scattering involving only physical region partial waves, Phys.Lett. 36B (1971) 353–356. doi:10.1016/0370-2693(71)90724-6.
[127] F. Steiner, On the convergence of finite energy sum rules in non-forward directions, Phys.Lett. B32 (1970) 294–296. doi:10.1016/0370-2693(70)90531-9.

[128] F. Steiner, Partial wave crossing relations for meson-baryon scattering, Fortsch. Phys. 19 (1971) 115–159. doi:10.1002/prop.19710190302.
[129] G. E. Hite, F. Steiner, New dispersion relations and their application to partial-wave amplitudes, Nuovo Cim. A 18 (1973) 237–270. doi:10.1007/BF02722827.
[130] N. Johannesson, G. Nilsson, An Analysis of Low-Energy πK Scattering, Nuovo Cim. A43 (1978) 376. doi:10.1007/BF02730436.
[131] B. Ananthanarayan, G. Colangelo, J. Gasser, H. Leutwyler, Roy equation analysis of $\pi\pi$ scattering, Phys.Rept. 353 (2001) 207–279. arXiv:hep-ph/0005297, doi:10.1016/S0370-1573(01)00009-6.
[132] G. Colangelo, J. Gasser, H. Leutwyler, $\pi\pi$ scattering, Nucl.Phys. B603 (2001) 125–179. arXiv:hep-ph/0103088, doi:10.1016/S0550-3213(01)00147-X.
[133] S. Descotes-Genon, B. Moussallam, The $K_0^*(800)$ scalar resonance from Roy-Steiner representations of πK scattering, Eur.Phys.J. C48 (2006) 553. arXiv:hep-ph/0607133, doi:10.1140/epjc/s10052-006-0036-2.
[134] R. García-Martín, R. Kamiński, J. R. Peláez, J. Ruiz de Elvira, F. J. Ynduráin, The Pion-pion scattering amplitude. IV: Improved analysis with once subtracted Roy-like equations up to 1100 MeV, Phys.Rev. D83 (2011) 074004. arXiv:1102.2183, doi:10.1103/PhysRevD.83.074004.
[135] M. Hoferichter, D. R. Phillips, C. Schat, Roy-Steiner equations for $\gamma\gamma \to \pi\pi$, Eur.Phys.J. C71 (2011) 1743. arXiv:1106.4147, doi:10.1140/epjc/s10052-011-1743-x.
[136] C. Ditsche, M. Hoferichter, B. Kubis, U.-G. Meißner, Roy-Steiner equations for pion-nucleon scattering, JHEP 06 (2012) 043. arXiv:1203.4758, doi:10.1007/JHEP06(2012)043.
[137] J. R. Peláez, A. Rodas, $\pi\pi \to K\bar{K}$ scattering up to 1.47 GeV with hyperbolic dispersion relations, Eur.Phys.J. C78 (11) (2018) 897. arXiv:1807.04543, doi:10.1140/epjc/s10052-018-6296-9.
[138] J. Peláez, A. Rodas, Dispersive $\pi K \to \pi K$ and $\pi\pi \to K\bar{K}$ amplitudes from scattering data, threshold parameters and the lightest strange resonance κ or $K_0^*(700)$ (10 2020). arXiv:2010.11222.
[139] J. R. Peláez, From controversy to precision on the σ meson: a review on the status of the non-ordinary $f_0(500)$ resonance, Phys.Rept. 658 (2016) 1. arXiv:1510.00653, doi:10.1016/j.physrep.2016.09.001.
[140] I. Caprini, G. Colangelo, H. Leutwyler, Mass and width of the lowest resonance in QCD, Phys.Rev.Lett. 96 (2006) 132001. arXiv:hep-ph/0512364, doi:10.1103/PhysRevLett.96.132001.
[141] R. García-Martín, R. Kaminski, J. R. Peláez, J. Ruiz de Elvira, Precise determination of the $f_0(600)$ and $f_0(980)$ pole parameters from a dispersive data analysis, Phys.Rev.Lett. 107 (2011) 072001. arXiv:1107.1635, doi:10.1103/PhysRevLett.107.072001.
[142] B. Moussallam, Couplings of light $I = 0$ scalar mesons to simple operators in the complex plane, Eur.Phys.J. C71 (2011) 1814. arXiv:1110.6074, doi:10.1140/epjc/s10052-011-1814-z.
[143] J. Peláez, A. Rodas, Determination of the lightest strange resonance $K_0^*(700)$ or κ, from a dispersive data analysis, Phys.Rev.Lett. 124 (17) (2020) 172001. arXiv:2001.08153, doi:10.1103/PhysRevLett.124.172001.
[144] V. Mathieu, N. Kochelev, V. Vento, The Physics of Glueballs, Int.J.Mod.Phys. E18 (2009) 1–49. arXiv:0810.4453, doi:10.1142/S0218301309012124.
[145] F. J. Llanes-Estrada, Glueballs as the Ithaca of meson spectroscopy, Eur.Phys.J.ST (1 2021). arXiv:2101.05366, doi:10.1140/epjs/s11734-021-00143-8.
[146] C. A. Meyer, E. S. Swanson, Hybrid Mesons, Prog.Part.Nucl.Phys. 82 (2015) 21–58. arXiv:1502.07276, doi:10.1016/j.ppnp.2015.03.001.
[147] T. Gutsche, V. E. Lyubovitskij, M. C. Tichy, $\eta(1405)$ in a chiral approach based on mixing of the pseudoscalar glueball with the first radial excitations of η and eta', Phys.Rev. D80 (2009) 014014. arXiv:0904.3414, doi:10.1103/PhysRevD.80.014014.
[148] M. Ablikim, et al., Observation of a resonance $X(1835)$ in $J/\psi \to \gamma\pi^+\pi^-\eta'$, Phys.Rev.Lett. 95 (2005) 262001. arXiv:hep-ex/0508025, doi:10.1103/PhysRevLett.95.262001.
[149] N. Kochelev, D.-P. Min, $X(1835)$ as the lowest mass pseudoscalar glueball and proton spin problem, Phys.Lett. B633 (2006) 283–288. arXiv:hep-ph/0508288, doi:10.1016/j.physletb.2005.11.079.
[150] S.-L. Zhu, C.-S. Gao, $X(1835)$: A Possible baryonium?, Commun.Theor.Phys. 46 (2006) 291. arXiv:hep-ph/0507050, doi:10.1088/0253-6102/46/2/021.
[151] V. D. Burkert, C. D. Roberts, Colloquium : Roper resonance: Toward a solution to the fifty year puzzle, Rev.Mod.Phys. 91 (1) (2019) 011003. arXiv:1710.02549, doi:10.1103/RevModPhys.91.011003.
[152] D. Jido, J. A. Oller, E. Oset, A. Ramos, U.-G. Meißner, Chiral dynamics of the two $\Lambda(1405)$ states, Nucl.Phys. A725 (2003) 181–200. arXiv:nucl-th/0303062, doi:10.1016/S0375-9474(03)01598-7.
[153] G. S. Bali, K. Schilling, A. Hulsebos, A. C. Irving, C. Michael, P. W. Stephenson, A Comprehensive lattice study of SU(3) glueballs, Phys.Lett. B309 (1993) 378–384. arXiv:hep-lat/9304012, doi:10.1016/0370-2693(93)90948-H.
[154] A. Patel, R. Gupta, G. Guralnik, G. W. Kilcup, S. R. Sharpe, An Improved Estimate of the Scalar Glueball Mass, Phys.Rev.Lett. 57 (1986) 1288. doi:10.1103/PhysRevLett.57.1288.
[155] M. Albanese, et al., Glueball Masses and String Tension in Lattice QCD, Phys.Lett. B192 (1987) 163–169. doi:10.1016/0370-2693(87)91160-9.
[156] C. Michael, M. Teper, The Glueball Spectrum in $SU(3)$, Nucl.Phys. B314 (1989) 347–362. doi:10.1016/0550-3213(89)90156-9.
[157] J. Sexton, A. Vaccarino, D. Weingarten, Numerical evidence for the observation of a scalar glueball, Phys.Rev.Lett. 75 (1995) 4563–4566. arXiv:hep-lat/9510022, doi:10.1103/PhysRevLett.75.4563.
[158] C. J. Morningstar, M. J. Peardon, The Glueball spectrum from an anisotropic lattice study, Phys.Rev. D60 (1999) 034509. arXiv:hep-lat/9901004, doi:10.1103/PhysRevD.60.034509.

[159] A. P. Szczepaniak, E. S. Swanson, The Low lying glueball spectrum, Phys.Lett. B577 (2003) 61–66. arXiv:hep-ph/0308268, doi:10.1016/j.physletb.2003.10.008.
[160] Y. Chen, et al., Glueball spectrum and matrix elements on anisotropic lattices, Phys.Rev. D73 (2006) 014516. arXiv:hep-lat/0510074.
[161] A. Athenodorou, M. Teper, The glueball spectrum of $SU(3)$ gauge theory in $3+1$ dimensions, JHEP 11 (2020) 172. arXiv:2007.06422, doi:10.1007/JHEP11(2020)172.
[162] W. Ochs, The Status of Glueballs, J.Phys. G40 (2013) 043001. arXiv:1301.5183, doi:10.1088/0954-3899/40/4/043001.
[163] M. S. Chanowitz, Have We Seen Our First Glueball?, Phys.Rev.Lett. 46 (1981) 981. doi:10.1103/PhysRevLett.46.981.
[164] C. Amsler, F. E. Close, Is $f_0(1500)$ a scalar glueball?, Phys.Rev. D53 (1996) 295–311. arXiv:hep-ph/9507326, doi:10.1103/PhysRevD.53.295.
[165] C. Amsler, F. E. Close, Evidence for a scalar glueball, Phys.Lett. B353 (1995) 385–390. arXiv:hep-ph/9505219, doi:10.1016/0370-2693(95)00579-A.
[166] W.-J. Lee, D. Weingarten, Scalar quarkonium masses and mixing with the lightest scalar glueball, Phys.Rev. D61 (2000) 014015. arXiv:hep-lat/9910008, doi:10.1103/PhysRevD.61.014015.
[167] F. Giacosa, T. Gutsche, V. Lyubovitskij, A. Faessler, Scalar nonet quarkonia and the scalar glueball: Mixing and decays in an effective chiral approach, Phys.Rev. D72 (2005) 094006. arXiv:hep-ph/0509247, doi:10.1103/PhysRevD.72.094006.
[168] F. Giacosa, T. Gutsche, V. E. Lyubovitskij, A. Faessler, Scalar meson and glueball decays within a effective chiral approach, Phys.Lett. B622 (2005) 277–285. arXiv:hep-ph/0504033, doi:10.1016/j.physletb.2005.07.016.
[169] M. Albaladejo, J. A. Oller, Identification of a Scalar Glueball, Phys.Rev.Lett. 101 (2008) 252002. arXiv:0801.4929, doi:10.1103/PhysRevLett.101.252002.
[170] S. Janowski, F. Giacosa, D. H. Rischke, Is $f_0(1710)$ a glueball?, Phys.Rev. D90 (11) (2014) 114005. arXiv:1408.4921, doi:10.1103/PhysRevD.90.114005.
[171] D. Barberis, et al., A Partial wave analysis of the centrally produced K^+K^- and $K^0_SK^0_S$ systems in pp interactions at 450 GeV/c and new information on the spin of the $f_J(1710)$, Phys.Lett. B453 (1999) 305–315. arXiv:hep-ex/9903042, doi:10.1016/S0370-2693(99)00365-2.
[172] S. Uehara, et al., High-statistics study of K^0_S pair production in two-photon collisions, PTEP 2013 (12) (2013) 123C01. arXiv:1307.7457, doi:10.1093/ptep/ptt097.
[173] M. Ablikim, et al., Amplitude analysis of the K_SK_S system produced in radiative J/ψ decays, Phys.Rev. D98 (7) (2018) 072003. arXiv:1808.06946, doi:10.1103/PhysRevD.98.072003.
[174] M. Chanowitz, Chiral suppression of scalar glueball decay, Phys.Rev.Lett. 95 (2005) 172001. arXiv:hep-ph/0506125, doi:10.1103/PhysRevLett.95.172001.
[175] R. A. Briceño, J. J. Dudek, R. G. Edwards, D. J. Wilson, Isoscalar $\pi\pi, K\overline{K}, \eta\eta$ scattering and the σ, f_0, f_2 mesons from QCD, Phys.Rev. D97 (5) (2018) 054513. arXiv:1708.06667, doi:10.1103/PhysRevD.97.054513.
[176] M. Ablikim, et al., Amplitude analysis of the $\pi^0\pi^0$ system produced in radiative J/ψ decays, Phys.Rev. D92 (5) (2015) 052003, [Erratum: Phys.Rev.D93,no.3,039906(2016)]. arXiv:1506.00546, doi:10.1103/PhysRevD.92.052003.
[177] S. Ropertz, C. Hanhart, B. Kubis, A new parametrization for the scalar pion form factors, Eur.Phys.J. C78 (12) (2018) 1000. arXiv:1809.06867, doi:10.1140/epjc/s10052-018-6416-6.
[178] A. V. Sarantsev, I. Denisenko, U. Thoma, E. Klempt, Scalar isoscalar mesons and the scalar glueball from radiative J/ψ decays, Phys.Lett. B816 (2021) 136227. arXiv:2103.09680, doi:10.1016/j.physletb.2021.136227.
[179] M. Albaladejo, B. Moussallam, Form factors of the isovector scalar current and the $\eta\pi$ scattering phase shifts, Eur.Phys.J. C75 (10) (2015) 488. arXiv:1507.04526, doi:10.1140/epjc/s10052-015-3715-z.
[180] M. Albaladejo, J. T. Daub, C. Hanhart, B. Kubis, B. Moussallam, How to employ $\overline{B}^0_d \to J/\psi\left(\pi\eta, \overline{K}K\right)$ decays to extract information on $\pi\eta$ scattering, JHEP 04 (2017) 010. arXiv:1611.03502, doi:10.1007/JHEP04(2017)010.
[181] T. Isken, B. Kubis, S. P. Schneider, P. Stoffer, Dispersion relations for $\eta' \to \eta\pi\pi$, Eur.Phys.J. C77 (7) (2017) 489. arXiv:1705.04339, doi:10.1140/epjc/s10052-017-5024-1.
[182] D. R. Thompson, et al., Evidence for exotic meson production in the reaction $\pi^-p \to \eta\pi^-p$ at 18 GeV/c, Phys.Rev.Lett. 79 (1997) 1630–1633. arXiv:hep-ex/9705011, doi:10.1103/PhysRevLett.79.1630.
[183] S. U. Chung, et al., Evidence for exotic $J^{PC} = 1^{-+}$ meson production in the reaction $\pi^-p \to \eta\pi^-p$ at 18 GeV/c, Phys.Rev. D60 (1999) 092001. arXiv:hep-ex/9902003, doi:10.1103/PhysRevD.60.092001.
[184] G. S. Adams, et al., Confirmation of a π^0_1 Exotic Meson in the $\eta\pi^0$ System, Phys.Lett. B657 (2007) 27–31. arXiv:hep-ex/0612062, doi:10.1016/j.physletb.2007.07.068.
[185] A. Abele, et al., Exotic $\eta\pi$ state in $\bar{p}d$ annihilation at rest into $\pi^-\pi^0\eta p$(spectator), Phys.Lett. B423 (1998) 175–184. doi:10.1016/S0370-2693(98)00123-3.
[186] A. Abele, et al., Evidence for a $\pi\eta$ P-wave in $\bar{p}p$ annihilations at rest into $\pi^0\pi^0\eta$, Phys.Lett. B446 (1999) 349–355. doi:10.1016/S0370-2693(98)01544-5.
[187] E. I. Ivanov, et al., Observation of exotic meson production in the reaction $\pi^-p \to \eta'\pi^-p$ at 18 GeV/c, Phys.Rev.Lett. 86 (2001) 3977–3980. arXiv:hep-ex/0101058, doi:10.1103/PhysRevLett.86.3977.
[188] Yu. A. Khokhlov, Study of $X(1600)$ 1^{-+} hybrid, Nucl.Phys. A663 (2000) 596–599, Particles and nuclei. Proceedings, 15th International Conference, PANIC '99, Uppsala, Sweden, June 10-16, 1999. doi:10.1016/S0375-9474(99)00663-6.
[189] A. P. Szczepaniak, M. Swat, A. R. Dzierba, S. Teige, Study of the $\eta\pi$ and $\eta'\pi$ spectra and interpretation of possible exotic $J^{PC} = 1^{-+}$ mesons, Phys.Rev.Lett. 91 (2003) 092002. arXiv:hep-ph/0304095, doi:10.1103/PhysRevLett.91.092002.
[190] M. Alekseev, et al., Observation of a $J^{PC} = 1^{-+}$ exotic resonance in diffractive dissociation of 190 GeV/c π^- into $\pi^-\pi^-\pi^+$, Phys.Rev.Lett. 104 (2010) 241803. arXiv:0910.5842, doi:10.1103/PhysRevLett.104.241803.
[191] M. Aghasyan, et al., Light isovector resonances in $\pi^-p \to \pi^-\pi^-\pi^+p$ at 190 GeV/c, Phys.Rev. D98 (9) (2018) 092003. arXiv:1802.05913, doi:10.1103/PhysRevD.98.092003.

[192] F. E. Close, H. J. Lipkin, New Experimental Evidence for Four Quark Exotics: The Serpukhov $\phi\pi$ Resonance and the Gams $\eta\pi$ Enhancement, Phys.Lett. B196 (1987) 245. doi:10.1016/0370-2693(87)90613-7.
[193] S. U. Chung, E. Klempt, J. G. Korner, $SU(3)$ classification of P-wave $\eta\pi$ and $\eta'\pi$ systems, Eur.Phys.J. A15 (2002) 539–542. arXiv:hep-ph/0211100, doi:10.1140/epja/i2002-10058-0.
[194] J. J. Dudek, The lightest hybrid meson supermultiplet in QCD, Phys.Rev. D84 (2011) 074023. arXiv:1106.5515, doi:10.1103/PhysRevD.84.074023.
[195] C. Adolph, et al., Odd and even partial waves of $\eta\pi^-$ and $\eta'\pi^-$ in $\pi^- p \to \eta^{(\prime)}\pi^- p$ at 191 GeV/c, Phys.Lett. B740 (2015) 303–311, [Corrigendum: Phys.Lett.B 811, 135913 (2020)]. arXiv:1408.4286, doi:10.1016/j.physletb.2014.11.058.
[196] K. Gottfried, J. D. Jackson, On the Connection between production mechanism and decay of resonances at high-energies, Nuovo Cim. 33 (1964) 309–330. doi:10.1007/BF02750195.
[197] A. W. Jackura, Studies in Multiparticle Scattering Theory, Ph.D. thesis, Indiana U. (2019). doi:10.2172/1570367.
[198] A. J. Woss, J. J. Dudek, R. G. Edwards, C. E. Thomas, D. J. Wilson, Decays of an exotic 1^{-+} hybrid meson resonance in QCD, Phys.Rev. D103 (5) (2021) 054502. arXiv:2009.10034, doi:10.1103/PhysRevD.103.054502.
[199] P. D. B. Collins, An Introduction to Regge Theory and High-Energy Physics, Cambridge Monographs on Mathematical Physics, Cambridge Univ. Press, Cambridge, UK, 2009.
URL http://www-spires.fnal.gov/spires/find/books/www?cl=QC793.3.R4C695
[200] V. N. Gribov, The theory of complex angular momenta: Gribov lectures on theoretical physics, Cambridge Monographs on Mathematical Physics, Cambridge University Press, 2007. doi:10.1017/CBO9780511534959.
URL http://www.cambridge.org/uk/catalogue/catalogue.asp?isbn=0521307848
[201] V. N. Gribov, Strong interactions of hadrons at high energies: Gribov lectures on Theoretical Physics, Cambridge University Press, 2012.
URL http://cambridge.org/catalogue/catalogue.asp?isbn=9780521856096
[202] G. Rossi, G. Veneziano, A Possible Description of Baryon Dynamics in Dual and Gauge Theories, Nucl.Phys. B123 (1977) 507. doi:10.1016/0550-3213(77)90178-X.
[203] L. Montanet, G. Rossi, G. Veneziano, Baryonium Physics, Phys.Rept. 63 (1980) 149–222.
[204] J. T. Londergan, J. Nebreda, J. R. Pelgaez, A. Szczepaniak, Identification of non-ordinary mesons from the dispersive connection between their poles and their Regge trajectories: The $f_0(500)$ resonance, Phys.Lett. B729 (2014) 9–14. arXiv:1311.7552, doi:10.1016/j.physletb.2013.12.061.
[205] J. A. Carrasco, J. Nebreda, J. R. Peláez, A. P. Szczepaniak, Dispersive calculation of complex Regge trajectories for the lightest f_2 resonances and the $K^*(892)$, Phys.Lett. B749 (2015) 399–406. arXiv:1504.03248, doi:10.1016/j.physletb.2015.08.019.
[206] C. Fernández-Ramírez, I. V. Danilkin, V. Mathieu, A. P. Szczepaniak, Understanding the Nature of $\Lambda(1405)$ through Regge Physics, Phys.Rev. D93 (7) (2016) 074015. arXiv:1512.03136, doi:10.1103/PhysRevD.93.074015.
[207] J. R. Peláez, A. Rodas, The non-ordinary Regge behavior of the $K_0^*(800)$ or κ -meson versus the ordinary $K_0^*(1430)$, Eur.Phys.J. C77 (6) (2017) 431. arXiv:1703.07661, doi:10.1140/epjc/s10052-017-4994-3.
[208] G. F. Chew, S. C. Frautschi, Regge Trajectories and the Principle of Maximum Strength for Strong Interactions, Phys.Rev.Lett. 8 (1962) 41–44. doi:10.1103/PhysRevLett.8.41.
[209] J. Greensite, An introduction to the confinement problem, Vol. 821, 2011. doi:10.1007/978-3-642-14382-3.
[210] H. Nakkagawa, K. Yamawaki, S. Machida, Quark-orbital regge trajectories, Prog.Theor.Phys. 48 (1972) 939–963. doi:10.1143/PTP.48.939.
[211] R. Bijker, F. Iachello, A. Leviatan, Algebraic models of hadron structure. 1. Nonstrange baryons, Annals Phys. 236 (1994) 69–116. arXiv:nucl-th/9402012, doi:10.1006/aphy.1994.1108.
[212] R. Bijker, F. Iachello, A. Leviatan, Algebraic models of hadron structure. 2. Strange baryons, Annals Phys. 284 (2000) 89–133. arXiv:nucl-th/0004034, doi:10.1006/aphy.2000.6064.
[213] E. Ortiz-Pacheco, R. Bijker, C. Fernández-Ramírez, Hidden charm pentaquarks: mass spectrum, magnetic moments, and photocouplings, J.Phys. G46 (06) (2019) 065104. arXiv:1808.10512, doi:10.1088/1361-6471/ab096d.
[214] U. Loring, B. C. Metsch, H. R. Petry, The Light baryon spectrum in a relativistic quark model with instanton induced quark forces: The Nonstrange baryon spectrum and ground states, Eur.Phys.J. A10 (2001) 395–446. arXiv:hep-ph/0103289, doi:10.1007/s100500170105.
[215] A. Inopin, G. S. Sharov, Hadronic Regge trajectories: Problems and approaches, Phys.Rev. D63 (2001) 054023. arXiv:hep-ph/9905499, doi:10.1103/PhysRevD.63.054023.
[216] A. Tang, J. W. Norbury, Properties of Regge trajectories, Phys.Rev. D62 (2000) 016006. arXiv:hep-ph/0004078, doi:10.1103/PhysRevD.62.016006.
[217] M. Koll, R. Ricken, D. Merten, B. C. Metsch, H. R. Petry, A Relativistic quark model for mesons with an instanton induced interaction, Eur.Phys.J. A9 (2000) 73–94. arXiv:hep-ph/0008220, doi:10.1007/PL00013675.
[218] D. Ebert, R. N. Faustov, V. O. Galkin, Mass spectra and Regge trajectories of light mesons in the relativistic quark model, Phys.Rev. D79 (2009) 114029. arXiv:0903.5183, doi:10.1103/PhysRevD.79.114029.
[219] N. Isgur, J. E. Paton, A Flux Tube Model for Hadrons in QCD, Phys.Rev. D31 (1985) 2910. doi:10.1103/PhysRevD.31.2910.
[220] M. G. Olsson, S. Veseli, K. Williams, Fermion confinement by a relativistic flux tube, Phys.Rev. D53 (1996) 4006. arXiv:hep-ph/9501323, doi:10.1103/PhysRevD.53.4006.
[221] C. Semay, F. Buisseret, N. Matagne, F. Stancu, Baryonic mass formula in large N_c QCD versus quark model, Phys.Rev. D75 (2007) 096001. arXiv:hep-ph/0702075, doi:10.1103/PhysRevD.75.096001.
[222] M. Mai, U.-G. Meißner, Constraints on the chiral unitary $\bar{K}N$ amplitude from $\pi\Sigma K^+$ photoproduction data, Eur.Phys.J. A51 (3) (2015) 30. arXiv:1411.7884, doi:10.1140/epja/i2015-15030-3.

[223] A. V. Anisovich, R. Beck, E. Klempt, V. A. Nikonov, A. V. Sarantsev, U. Thoma, Properties of baryon resonances from a multichannel partial wave analysis, Eur.Phys.J. A48 (2012) 15. arXiv:1112.4937, doi:10.1140/epja/i2012-12015-8.
[224] V. Sokhoyan, et al., High-statistics study of the reaction $\gamma p \to p 2\pi^0$, Eur.Phys.J. A51 (8) (2015) 95, [Erratum: Eur. Phys. J.A51,no.12,187(2015)]. arXiv:1507.02488, doi:10.1140/epja/i2015-15187-7,10.1140/epja/i2015-15095-x.
[225] V. N. Gribov, Analytic properties of the partial wave amplitudes and the asymptotic behavior of the scattering amplitude, Sov.Phys.JETP 15 (1962) 873. doi:10.1016/0029-5582(63)90256-6.
[226] H. Zhang, J. Tulpan, M. Shrestha, D. M. Manley, Multichannel parametrization of $\bar{K}N$ scattering amplitudes and extraction of resonance parameters, Phys.Rev. C88 (3) (2013) 035205. arXiv:1305.4575, doi:10.1103/PhysRevC.88.035205.
[227] J. Silva-Castro, C. Fernández-Ramírez, M. Albaladejo, I. Danilkin, A. Jackura, V. Mathieu, J. Nys, A. Pilloni, A. Szczepaniak, G. Fox, Regge phenomenology of the N^* and Δ^* poles, Phys.Rev. D99 (3) (2019) 034003. arXiv:1809.01954, doi:10.1103/PhysRevD.99.034003.
[228] R. E. Cutkosky, C. P. Forsyth, R. E. Hendrick, R. L. Kelly, Pion-Nucleon Partial Wave Amplitudes, Phys.Rev. D20 (1979) 2839. doi:10.1103/PhysRevD.20.2839.
[229] R. E. Cutkosky, C. P. Forsyth, J. B. Babcock, R. L. Kelly, R. E. Hendrick, Pion-nucleon partial wave analysis, in: Baryon 1980. Proceedings, 4th International Conference on Baryon Resonances, Toronto, Canada, July 14-16, 1980, 1980, p. 19.
[230] D. Rönchen, M. Döring, U. G. Meißner, The impact of $\mathbf{K^+\Lambda}$ photoproduction on the resonance spectrum, Eur.Phys.J. A54 (6) (2018) 110. arXiv:1801.10458, doi:10.1140/epja/i2018-12541-3.
[231] A. Švarc, M. Hadžimehmedović, H. Osmanović, J. Stahov, R. L. Workman, Pole structure from energy-dependent and single-energy fits to GWU-SAID πN elastic scattering data, Phys.Rev. C91 (1) (2015) 015207. arXiv:1405.6474, doi:10.1103/PhysRevC.91.015207.
[232] A. Švarc, M. Hadžimehmedović, R. Omerović, H. Osmanović, J. Stahov, Poles of Karlsruhe-Helsinki KH80 and KA84 solutions extracted by using the Laurent-Pietarinen method, Phys.Rev. C89 (4) (2014) 045205. arXiv:1401.1947, doi:10.1103/PhysRevC.89.045205.
[233] G. Höhler, Pion Nucleon Scattering. Part 2: Methods and Results of Phenomenological Analyses, Landolt-Bornstein, Springer-Verlag Berlin Heidelberg, 1983. doi:10.1007/10201161_90.
URL https://materials.springer.com/lb/docs/sm_lbs_978-3-540-39059-6_90
[234] V. Mokeev, et al., Evidence for the $N'(1720)3/2^+$ Nucleon Resonance from Combined Studies of CLAS $\pi^+\pi^- p$ Photo- and Electroproduction Data, Phys.Lett. B805 (2020) 135457. arXiv:2004.13531, doi:10.1016/j.physletb.2020.135457.
[235] H. Kamano, S. X. Nakamura, T. S. H. Lee, T. Sato, Nucleon resonances within a dynamical coupled-channels model of πN and γN reactions, Phys.Rev. C88 (3) (2013) 035209. arXiv:1305.4351, doi:10.1103/PhysRevC.88.035209.
[236] S.-K. Choi, et al., Observation of a new narrow charmonium state in exclusive $B^\pm \to K^\pm\pi^+\pi^- J/\psi$ decays, Phys.Rev.Lett. 91 (2003) 262001. arXiv:hep-ex/0309032, doi:10.1103/PhysRevLett.91.262001.
[237] R. Aaij, et al., Observation of an exotic narrow doubly charmed tetraquark (9 2021). arXiv:2109.01038.
[238] R. Aaij, et al., Study of the doubly charmed tetraquark T_{cc}^+ (9 2021). arXiv:2109.01056.
[239] R. Aaij, et al., Observation of structure in the J/ψ -pair mass spectrum, Sci.Bull. 65 (23) (2020) 1983–1993. arXiv:2006.16957, doi:10.1016/j.scib.2020.08.032.
[240] R. Aaij, et al., Study of the lineshape of the $\chi_{c1}(3872)$ state, Phys.Rev. D102 (9) (2020) 092005. arXiv:2005.13419, doi:10.1103/PhysRevD.102.092005.
[241] A. Esposito, L. Maiani, A. Pilloni, A. D. Polosa, V. Riquer, From the lineshape of the $X(3872)$ to its structure (8 2021). arXiv:2108.11413.
[242] V. Baru, X.-K. Dong, M.-L. Du, A. Filin, F.-K. Guo, C. Hanhart, A. Nefediev, J. Nieves, Q. Wang, Effective range expansion for narrow near-threshold resonances (10 2021). arXiv:2110.07484.
[243] N. A. Tornqvist, From the deuteron to deusons, an analysis of deuteron-like meson meson bound states, Z.Phys. C61 (1994) 525–537. arXiv:hep-ph/9310247, doi:10.1007/BF01413192.
[244] E. Braaten, M. Kusunoki, Low-energy universality and the new charmonium resonance at 3870 MeV , Phys.Rev. D69 (2004) 074005. arXiv:hep-ph/0311147, doi:10.1103/PhysRevD.69.074005.
[245] M. Voloshin, Interference and binding effects in decays of possible molecular component of $X(3872)$, Phys.Lett. B579 (2004) 316–320. arXiv:hep-ph/0309307, doi:10.1016/j.physletb.2003.11.014.
[246] F. E. Close, P. R. Page, The $D^{*0}\bar{D}^0$ threshold resonance, Phys.Lett. B578 (2004) 119–123. arXiv:hep-ph/0309253, doi:10.1016/j.physletb.2003.10.032.
[247] E. S. Swanson, The New heavy mesons: A Status report, Phys.Rept. 429 (2006) 243–305. arXiv:hep-ph/0601110, doi:10.1016/j.physrep.2006.04.003.
[248] M. Cleven, F.-K. Guo, C. Hanhart, U.-G. Meißner, Bound state nature of the exotic Z_b states, Eur.Phys.J. A47 (2011) 120. arXiv:1107.0254, doi:10.1140/epja/i2011-11120-6.
[249] Q. Wang, C. Hanhart, Q. Zhao, Decoding the riddle of $Y(4260)$ and $Z_c(3900)$, Phys.Rev.Lett. 111 (13) (2013) 132003. arXiv:1303.6355, doi:10.1103/PhysRevLett.111.132003.
[250] L. Maiani, F. Piccinini, A. D. Polosa, V. Riquer, Diquark-antidiquarks with hidden or open charm and the nature of $X(3872)$, Phys.Rev. D71 (2005) 014028. arXiv:hep-ph/0412098, doi:10.1103/PhysRevD.71.014028.
[251] A. Ali, C. Hambrock, W. Wang, Tetraquark Interpretation of the Charged Bottomonium-like states $Z_b^\pm(10610)$ and $Z_b^\pm(10650)$ and Implications, Phys.Rev. D85 (2012) 054011. arXiv:1110.1333, doi:10.1103/PhysRevD.85.054011.
[252] A. Ali, L. Maiani, A. Polosa, V. Riquer, Hidden-Beauty Charged Tetraquarks and Heavy Quark Spin Conservation, Phys.Rev. D91 (1) (2015) 017502. arXiv:1412.2049, doi:10.1103/PhysRevD.91.017502.
[253] L. Maiani, A. D. Polosa, V. Riquer, Hydrogen bond of QCD, Phys.Rev. D100 (1) (2019) 014002. arXiv:1903.10253, doi:10.1103/PhysRevD.100.014002.

[254] R. Aaij, et al., Observation of $J/\psi p$ resonances consistent with pentaquark states in $\Lambda_b^0 \to J/\psi K^- p$ decays, Phys.Rev.Lett. 115 (2015) 072001. arXiv:1507.03414, doi:10.1103/PhysRevLett.115.072001.
[255] R. Aaij, et al., Observation of a narrow pentaquark state, $P_c(4312)^+$, and of two-peak structure of the $P_c(4450)^+$, Phys.Rev.Lett 122 (2019) 222001. arXiv:1904.03947, doi:10.1103/PhysRevLett.122.222001.
[256] L. Maiani, A. D. Polosa, V. Riquer, The New Pentaquarks in the Diquark Model, Phys.Lett. B749 (2015) 289–291. arXiv:1507.04980, doi:10.1016/j.physletb.2015.08.008.
[257] R. F. Lebed, The Pentaquark Candidates in the Dynamical Diquark Picture, Phys.Lett. B749 (2015) 454–457. arXiv:1507.05867, doi:10.1016/j.physletb.2015.08.032.
[258] V. V. Anisovich, M. A. Matveev, J. Nyiri, A. V. Sarantsev, A. N. Semenova, Pentaquarks and resonances in the pJ/ψ spectrum (2015). arXiv:1507.07652.
[259] A. Ali, A. Ya. Parkhomenko, Interpretation of the Narrow $J/\psi p$ Peaks in $\Lambda_b \to J/\psi p K^-$ Decay in the Compact Diquark Model, Phys.Lett. B793 (2019) 365–371. arXiv:1904.00446, doi:10.1016/j.physletb.2019.05.002.
[260] R. Chen, X. Liu, X.-Q. Li, S.-L. Zhu, Identifying exotic hidden-charm pentaquarks, Phys.Rev.Lett. 115 (13) (2015) 132002. arXiv:1507.03704, doi:10.1103/PhysRevLett.115.132002.
[261] H.-X. Chen, W. Chen, X. Liu, T. G. Steele, S.-L. Zhu, Towards exotic hidden-charm pentaquarks in QCD, Phys.Rev.Lett. 115 (17) (2015) 172001. arXiv:1507.03717, doi:10.1103/PhysRevLett.115.172001.
[262] L. Roca, J. Nieves, E. Oset, LHCb pentaquark as a $\bar{D}^*\Sigma_c - \bar{D}^*\Sigma_c^*$ molecular state, Phys.Rev. D92 (9) (2015) 094003. arXiv:1507.04249, doi:10.1103/PhysRevD.92.094003.
[263] F.-K. Guo, H.-J. Jing, U.-G. Meißner, S. Sakai, Isospin breaking decays as a diagnosis of the hadronic molecular structure of the $P_c(4457)$, Phys.Rev. D99 (9) (2019) 091501. arXiv:1903.11503, doi:10.1103/PhysRevD.99.091501.
[264] Z.-H. Guo, J. A. Oller, Anatomy of the newly observed hidden-charm pentaquark states: $P_c(4312)$, $P_c(4440)$ and $P_c(4457)$, Phys.Lett. B793 (2019) 144–149. arXiv:1904.00851, doi:10.1016/j.physletb.2019.04.053.
[265] C. W. Xiao, J. Nieves, E. Oset, Heavy quark spin symmetric molecular states from $\bar{D}^{(*)}\Sigma_c^{(*)}$ and other coupled channels in the light of the recent LHCb pentaquarks, Phys.Rev. D100 (1) (2019) 014021. arXiv:1904.01296, doi:10.1103/PhysRevD.100.014021.
[266] M.-Z. Liu, Y.-W. Pan, F.-Z. Peng, M. Sanchez Sanchez, L.-S. Geng, A. Hosaka, M. Pavon Valderrama, Emergence of a complete heavy-quark spin symmetry multiplet: seven molecular pentaquarks in light of the latest LHCb analysis, Phys.Rev.Lett. 122 (24) (2019) 242001. arXiv:1903.11560, doi:10.1103/PhysRevLett.122.242001.
[267] A. P. Szczepaniak, Dalitz plot distributions in presence of triangle singularities, Phys.Lett. B757 (2016) 61–64. arXiv:1510.01789, doi:10.1016/j.physletb.2016.03.064.
[268] U.-G. Meißner, J. A. Oller, Testing the $\chi_{c1}\, p$ composite nature of the $P_c(4450)$, Phys.Lett. B751 (2015) 59–62. arXiv:1507.07478, doi:10.1016/j.physletb.2015.10.015.
[269] M. Mikhasenko, A triangle singularity and the LHCb pentaquarks (2015). arXiv:1507.06552.
[270] F.-K. Guo, U.-G. Meißner, J. Nieves, Z. Yang, Remarks on the P_c structures and triangle singularities, Eur.Phys.J. A52 (10) (2016) 318. arXiv:1605.05113, doi:10.1140/epja/i2016-16318-4.
[271] M. Bayar, F. Aceti, F.-K. Guo, E. Oset, A Discussion on Triangle Singularities in the $\Lambda_b \to J/\psi K^- p$ Reaction, Phys.Rev. D94 (7) (2016) 074039. arXiv:1609.04133, doi:10.1103/PhysRevD.94.074039.
[272] S. X. Nakamura, $P_c(4312)^+$, $P_c(4380)^+$, and $P_c(4457)^+$ as double triangle cusps, Phys.Rev. D103 (2021) 111503. arXiv:2103.06817, doi:10.1103/PhysRevD.103.L111503.
[273] C. Bignamini, B. Grinstein, F. Piccinini, A. Polosa, C. Sabelli, Is the $X(3872)$ Production Cross Section at Tevatron Compatible with a Hadron Molecule Interpretation?, Phys.Rev.Lett. 103 (2009) 162001. arXiv:0906.0882, doi:10.1103/PhysRevLett.103.162001.
[274] P. Artoisenet, E. Braaten, Production of the $X(3872)$ at the Tevatron and the LHC, Phys.Rev. D81 (2010) 114018. arXiv:0911.2016, doi:10.1103/PhysRevD.81.114018.
[275] C. Bignamini, B. Grinstein, F. Piccinini, A. Polosa, V. Riquer, et al., More loosely bound hadron molecules at CDF?, Phys.Lett. B684 (2010) 228–230. arXiv:0912.5064, doi:10.1016/j.physletb.2010.01.037.
[276] P. Artoisenet, E. Braaten, Estimating the Production Rate of Loosely-bound Hadronic Molecules using Event Generators, Phys.Rev. D83 (2011) 014019. arXiv:1007.2868, doi:10.1103/PhysRevD.83.014019.
[277] M. Albaladejo, F.-K. Guo, C. Hanhart, U.-G. Meißner, J. Nieves, A. Nogga, Z. Yang, Note on $X(3872)$ production at hadron colliders and its molecular structure, Chin.Phys. C41 (2017) 121001. arXiv:1709.09101, doi:10.1088/1674-1137/41/12/121001.
[278] A. Esposito, B. Grinstein, L. Maiani, F. Piccinini, A. Pilloni, A. D. Polosa, V. Riquer, Comment on 'Note on $X(3872)$ production at hadron colliders and its molecular structure', Chin.Phys. C42 (11) (2018) 114107. arXiv:1709.09631, doi:10.1088/1674-1137/42/11/114107.
[279] W. Wang, On the production of hidden-flavored hadronic states at high energy, Chin.Phys. 42 (2018) 043103. arXiv:1709.10382, doi:10.1088/1674-1137/42/4/043103.
[280] A. Esposito, E. G. Ferreiro, A. Pilloni, A. D. Polosa, C. A. Salgado, The nature of $X(3872)$ from high-multiplicity pp collisions (6 2021). arXiv:2006.15044, doi:10.1140/epjc/s10052-021-09425-w.
[281] E. Braaten, L.-P. He, K. Ingles, J. Jiang, Production of $X(3872)$ at High Multiplicity, Phys.Rev. D103 (7) (2021) L071901. arXiv:2012.13499, doi:10.1103/PhysRevD.103.L071901.
[282] M. Ablikim, et al., Observation of a Charged Charmoniumlike Structure in $e^+e^- \to \pi^+\pi^- J/\psi$ at $\sqrt{s} = 4.26\,\text{GeV}$, Phys.Rev.Lett. 110 (25) (2013) 252001. arXiv:1303.5949, doi:10.1103/PhysRevLett.110.252001.
[283] Z. Liu, et al., Study of $e^+e^- \to \pi^+\pi^- J/\psi$ and Observation of a Charged Charmoniumlike State at Belle, Phys.Rev.Lett. 110 (25) (2013) 252002. arXiv:1304.0121, doi:10.1103/PhysRevLett.110.252002.
[284] T. Xiao, S. Dobbs, A. Tomaradze, K. K. Seth, Observation of the Charged Hadron $Z_c^{\pm}(3900)$ and Evidence for the

Neutral $Z_c^0(3900)$ in $e^+e^- \to \pi\pi J/\psi$ at $\sqrt{s} = 4170$ MeV, Phys.Lett. B727 (2013) 366–370. arXiv:1304.3036, doi:10.1016/j.physletb.2013.10.041.
[285] M. Ablikim, et al., Observation of $Z_c(3900)^0$ in $e^+e^- \to \pi^0\pi^0 J/\psi$, Phys.Rev.Lett. 115 (11) (2015) 112003. arXiv:1506.06018, doi:10.1103/PhysRevLett.115.112003.
[286] M. Ablikim, et al., Observation of a charged $(D\bar{D}^*)^\pm$ mass peak in $e^+e^- \to \pi^+ D\bar{D}^*$ at $\sqrt{s} = 4.26$ GeV, Phys.Rev.Lett. 112 (2014) 022001. arXiv:1310.1163, doi:10.1103/PhysRevLett.112.022001.
[287] M. Ablikim, et al., Confirmation of a charged charmoniumlike state $Z_c(3885)^\mp$ in $e^+e^- \to \pi^\pm(D\bar{D}^*)^\mp$ with double D tag, Phys.Rev. D92 (9) (2015) 092006. arXiv:1509.01398, doi:10.1103/PhysRevD.92.092006.
[288] M. Ablikim, et al., Observation of a Neutral Structure near the $D\bar{D}^*$ Mass Threshold in $e^+e^- \to (D\bar{D}^*)^0\pi^0$ at $\sqrt{s} = 4.226$ and 4.257 GeV, Phys.Rev.Lett. 115 (22) (2015) 222002. arXiv:1509.05620, doi:10.1103/PhysRevLett.115.222002.
[289] L. Demortier, P values and nuisance parameters, in: Statistical issues for LHC physics. Proceedings, Workshop, PHYSTAT-LHC, Geneva, Switzerland, June 27-29, 2007, 2007, pp. 23–33. URL http://cds.cern.ch/record/1099967/files/p23.pdf
[290] R. Faccini, F. Piccinini, A. Pilloni, A. Polosa, The Spin of the $X(3872)$, Phys.Rev. D86 (2012) 054012. arXiv:1204.1223, doi:10.1103/PhysRevD.86.054012.
[291] M. Albaladejo, F.-K. Guo, C. Hidalgo-Duque, J. Nieves, $Z_c(3900)$: What has been really seen?, Phys.Lett. B755 (2016) 337–342. arXiv:1512.03638, doi:10.1016/j.physletb.2016.02.025.
[292] M. Albaladejo, P. Fernández-Soler, J. Nieves, $Z_c(3900)$: Confronting theory and lattice simulations, Eur.Phys.J. C76 (10) (2016) 573. arXiv:1606.03008, doi:10.1140/epjc/s10052-016-4427-8.
[293] A. Pilloni, C. Fernández-Ramírez, A. Jackura, V. Mathieu, M. Mikhasenko, J. Nys, A. P. Szczepaniak, Amplitude analysis and the nature of the $Z_c(3900)$, Phys.Lett. B772 (2017) 200–209. arXiv:1612.06490, doi:10.1016/j.physletb.2017.06.030.
[294] H.-X. Chen, W. Chen, S.-L. Zhu, Possible interpretations of the $P_c(4312)$, $P_c(4440)$, and $P_c(4457)$, Phys.Rev. D100 (5) (2019) 051501. arXiv:1903.11001, doi:10.1103/PhysRevD.100.051501.
[295] R. Chen, Z.-F. Sun, X. Liu, S.-L. Zhu, Strong LHCb evidence supporting the existence of the hidden-charm molecular pentaquarks, Phys.Rev. D100 (1) (2019) 011502. arXiv:1903.11013, doi:10.1103/PhysRevD.100.011502.
[296] J. He, Study of $P_c(4457)$, $P_c(4440)$, and $P_c(4312)$ in a quasipotential Bethe-Salpeter equation approach, Eur.Phys.J. C79 (5) (2019) 393. arXiv:1903.11872, doi:10.1140/epjc/s10052-019-6906-1.
[297] C.-J. Xiao, Y. Huang, Y.-B. Dong, L.-S. Geng, D.-Y. Chen, Exploring the molecular scenario of $P_c(4312)$, $P_c(4440)$, and $P_c(4457)$, Phys.Rev. D100 (1) (2019) 014022. arXiv:1904.00872, doi:10.1103/PhysRevD.100.014022.
[298] M.-L. Du, V. Baru, F.-K. Guo, C. Hanhart, U.-G. Meißner, J. A. Oller, Q. Wang, Interpretation of the LHCb P_c States as Hadronic Molecules and Hints of a Narrow $P_c(4380)$, Phys.Rev.Lett. 124 (7) (2020) 072001. arXiv:1910.11846, doi:10.1103/PhysRevLett.124.072001.
[299] M.-L. Du, V. Baru, F.-K. Guo, C. Hanhart, U.-G. Meißner, J. A. Oller, Q. Wang, Revisiting the nature of the P_c pentaquarks, JHEP 08 (2021) 157. arXiv:2102.07159, doi:10.1007/JHEP08(2021)157.
[300] J.-J. Wu, R. Molina, E. Oset, B. S. Zou, Prediction of narrow N^* and Λ^* resonances with hidden charm above 4 GeV, Phys.Rev.Lett. 105 (2010) 232001. arXiv:1007.0573, doi:10.1103/PhysRevLett.105.232001.
[301] J.-J. Wu, R. Molina, E. Oset, B. S. Zou, Dynamically generated N^* and Λ^* resonances in the hidden charm sector around 4.3 GeV, Phys.Rev. C84 (2011) 015202. arXiv:1011.2399, doi:10.1103/PhysRevC.84.015202.
[302] W. L. Wang, F. Huang, Z. Y. Zhang, B. S. Zou, $\Sigma_c\bar{D}$ and $\Lambda_c\bar{D}$ states in a chiral quark model, Phys.Rev. C84 (2011) 015203. arXiv:1101.0453, doi:10.1103/PhysRevC.84.015203.
[303] Z.-C. Yang, Z.-F. Sun, J. He, X. Liu, S.-L. Zhu, The possible hidden-charm molecular baryons composed of anti-charmed meson and charmed baryon, Chin.Phys. C36 (2012) 6–13. arXiv:1105.2901, doi:10.1088/1674-1137/36/1/002.
[304] C. W. Xiao, J. Nieves, E. Oset, Combining heavy quark spin and local hidden gauge symmetries in the dynamical generation of hidden charm baryons, Phys.Rev. D88 (2013) 056012. arXiv:1304.5368, doi:10.1103/PhysRevD.88.056012.
[305] Y. Yamaguchi, A. Giachino, A. Hosaka, E. Santopinto, S. Takeuchi, M. Takizawa, Hidden-charm and bottom meson-baryon molecules coupled with five-quark states, Phys.Rev. D96 (11) (2017) 114031. arXiv:1709.00819, doi:10.1103/PhysRevD.96.114031.
[306] R. J. Eden, J. R. Taylor, Poles and Shadow Poles in the Many-Channel S Matrix, Phys.Rev. 133 (1964) B1575–B1580. doi:10.1103/PhysRev.133.B1575.
[307] H. W. Hammer, S. König, Constraints on a possible dineutron state from pionless EFT, Phys.Lett. B736 (2014) 208–213. arXiv:1406.1359, doi:10.1016/j.physletb.2014.07.015.
[308] C. Fernández-Ramírez, A. Pilloni, M. Albaladejo, A. Jackura, V. Mathieu, M. Mikhasenko, J. A. Silva-Castro, A. P. Szczepaniak, Interpretation of the LHCb $P_c(4312)$ Signal, Phys.Rev.Lett. 123 (9) (2019) 092001. arXiv:1904.10021, doi:10.1103/PhysRevLett.123.092001.
[309] W. R. Frazer, A. W. Hendry, S-Matrix Poles Close to Threshold, Phys.Rev. 134 (1964) B1307–B1314. doi:10.1103/PhysRev.134.B1307.
[310] R. Aaij, et al., Evidence for a new structure in the $J/\psi p$ and $J/\psi\bar{p}$ systems in $B_s^0 \to J/\psi p\bar{p}$ decays (8 2021). arXiv:2108.04720.
[311] N. N. Khuri, S. B. Treiman, Pion-Pion Scattering and $K^\pm \to 3\pi$ Decay, Phys.Rev. 119 (1960) 1115–1121. doi:10.1103/PhysRev.119.1115.
[312] J. B. Bronzan, C. Kacser, Khuri-Treiman Representation and Perturbation Theory, Phys.Rev. 132 (6) (1963) 2703. doi:10.1103/PhysRev.132.2703.
[313] I. J. R. Aitchison, Dispersion Theory Model of Three-Body Production and Decay Processes, Phys.Rev. 137 (1965) B1070–B1084. doi:10.1103/PhysRev.137.B1070.

[314] I. J. R. Aitchison, R. Pasquier, Three-Body Unitarity and Khuri-Treiman Amplitudes, Phys.Rev. 152 (4) (1966) 1274. doi:10.1103/PhysRev.152.1274.
[315] R. Pasquier, J. Y. Pasquier, Khuri-Treiman-Type Equations for Three-Body Decay and Production Processes, Phys.Rev. 170 (1968) 1294–1309. doi:10.1103/PhysRev.170.1294.
[316] R. Pasquier, J. Y. Pasquier, Khuri-Treiman-type equations for three-body decay and production processes. 2., Phys.Rev. 177 (1969) 2482–2493. doi:10.1103/PhysRev.177.2482.
[317] J. Stern, H. Sazdjian, N. H. Fuchs, What $\pi\pi$ scattering tells us about chiral perturbation theory, Phys.Rev. D47 (1993) 3814–3838. arXiv:hep-ph/9301244, doi:10.1103/PhysRevD.47.3814.
[318] M. Knecht, B. Moussallam, J. Stern, N. H. Fuchs, The Low-energy $\pi\pi$ amplitude to one and two loops, Nucl.Phys. B457 (1995) 513–576. arXiv:hep-ph/9507319, doi:10.1016/0550-3213(95)00515-3.
[319] B. Ananthanarayan, P. Buettiker, Comparison of pion kaon scattering in $SU(3)$ chiral perturbation theory and dispersion relations, Eur.Phys.J. C19 (2001) 517–528. arXiv:hep-ph/0012023, doi:10.1007/s100520100629.
[320] M. Zdrahal, J. Novotny, Dispersive Approach to Chiral Perturbation Theory, Phys.Rev. D78 (2008) 116016. arXiv:0806.4529, doi:10.1103/PhysRevD.78.116016.
[321] J. Bijnens, K. Ghorbani, $\eta \to 3\pi$ at Two Loops In Chiral Perturbation Theory, JHEP 11 (2007) 030. arXiv:0709.0230, doi:10.1088/1126-6708/2007/11/030.
[322] M. Albaladejo, N. Sherrill, C. Fernández-Ramírez, A. Jackura, V. Mathieu, M. Mikhasenko, J. Nys, A. Pilloni, A. P. Szczepaniak, Khuri-Treiman equations for $\pi\pi$ scattering, Eur.Phys.J. C78 (7) (2018) 574. arXiv:1803.06027, doi:10.1140/epjc/s10052-018-6045-0.
[323] H. Yamagishi, I. Zahed, A Master formula for chiral symmetry breaking, Annals Phys. 247 (1996) 292–413. arXiv:hep-ph/9503413, doi:10.1006/aphy.1996.0045.
[324] M. Albaladejo, D. Winney, I. Danilkin, C. Fernández-Ramírez, V. Mathieu, M. Mikhasenko, A. Pilloni, J. Silva-Castro, A. Szczepaniak, Khuri-Treiman equations for 3π decays of particles with spin, Phys.Rev. D101 (5) (2020) 054018. arXiv:1910.03107, doi:10.1103/PhysRevD.101.054018.
[325] F. Niecknig, B. Kubis, S. P. Schneider, Dispersive analysis of $\omega \to 3\pi$ and $\phi \to 3\pi$ decays, Eur.Phys.J. C72 (2012) 2014. arXiv:1203.2501, doi:10.1140/epjc/s10052-012-2014-1.
[326] I. V. Danilkin, C. Fernández-Ramírez, P. Guo, V. Mathieu, D. Schott, M. Shi, A. P. Szczepaniak, Dispersive analysis of $\omega/\phi \to 3\pi$, $\pi\gamma^*$, Phys.Rev. D91 (9) (2015) 094029. arXiv:1409.7708, doi:10.1103/PhysRevD.91.094029.
[327] B. Ananthanarayan, I. Caprini, B. Kubis, Constraints on the $\omega\pi$ form factor from analyticity and unitarity, Eur.Phys.J. C74 (12) (2014) 3209. arXiv:1410.6276, doi:10.1140/epjc/s10052-014-3209-4.
[328] I. Caprini, Testing the consistency of the $\omega\pi$ transition form factor with unitarity and analyticity, Phys.Rev. D92 (1) (2015) 014014. arXiv:1505.05282, doi:10.1103/PhysRevD.92.014014.
[329] M. Dax, T. Isken, B. Kubis, Quark-mass dependence in $\omega \to 3\pi$ decays, Eur.Phys.J. C78 (10) (2018) 859. arXiv:1808.08957, doi:10.1140/epjc/s10052-018-6346-3.
[330] M. Albaladejo, I. Danilkin, S. Gonzàlez-Solís, D. Winney, C. Fernández-Ramírez, A. Hiller Blin, V. Mathieu, M. Mikhasenko, A. Pilloni, A. Szczepaniak, $\omega \to 3\pi$ and $\omega\pi^0$ transition form factor revisited, Eur.Phys.J. C80 (12) (2020) 1107. arXiv:2006.01058, doi:10.1140/epjc/s10052-020-08576-6.
[331] A. Neveu, J. Scherk, Final-state interaction and current algebra in $K \to 3\pi$ and $\eta \to 3\pi$ decays, Annals Phys. 57 (1970) 39–64. doi:10.1016/0003-4916(70)90268-X.
[332] A. V. Anisovich, Dispersion relation technique for three pion system and the P-wave interaction in $\eta \to 3\pi$ decay, Phys. Atom. Nucl. 58 (1995) 1383–1397.
[333] J. Kambor, C. Wiesendanger, D. Wyler, Final state interactions and Khuri-Treiman equations in $\eta \to 3\pi$ decays, Nucl.Phys. B465 (1996) 215–266. arXiv:hep-ph/9509374, doi:10.1016/0550-3213(95)00676-1.
[334] A. V. Anisovich, H. Leutwyler, Dispersive analysis of the decay $\eta \to 3\pi$, Phys.Lett. B375 (1996) 335–342. arXiv:hep-ph/9601237, doi:10.1016/0370-2693(96)00192-X.
[335] M. Walker, $\eta \to 3\pi$, Other thesis (1998).
[336] K. Kampf, M. Knecht, J. Novotny, M. Zdrahal, Analytical dispersive construction of $\eta \to 3\pi$ amplitude: first order in isospin breaking, Phys.Rev. D84 (2011) 114015. arXiv:1103.0982, doi:10.1103/PhysRevD.84.114015.
[337] S. Lanz, $\eta \to 3\pi$ and quark masses, PoS CD12 (2013) 007. arXiv:1301.7282, doi:10.22323/1.172.0007.
[338] S. Descotes-Genon, B. Moussallam, Analyticity of $\eta\pi$ isospin-violating form factors and the $\tau \to \eta\pi\nu$ second-class decay, Eur.Phys.J. C74 (2014) 2946. arXiv:1404.0251, doi:10.1140/epjc/s10052-014-2946-8.
[339] P. Guo, I. V. Danilkin, A. P. Szczepaniak, Dispersive approaches for three-particle final state interaction, Eur.Phys.J. A51 (10) (2015) 135. arXiv:1409.8652, doi:10.1140/epja/i2015-15135-7.
[340] P. Guo, I. V. Danilkin, D. Schott, C. Fernández-Ramírez, V. Mathieu, A. P. Szczepaniak, Three-body final state interaction in $\eta \to 3\pi$, Phys.Rev. D92 (5) (2015) 054016. arXiv:1505.01715, doi:10.1103/PhysRevD.92.054016.
[341] P. Guo, I. V. Danilkin, C. Fernández-Ramírez, V. Mathieu, A. P. Szczepaniak, Three-body final state interaction in $\eta \to 3\pi$ revisited, Phys.Lett. B771 (2017) 497–502. arXiv:1608.01447, doi:10.1016/j.physletb.2017.05.092.
[342] G. Colangelo, S. Lanz, H. Leutwyler, E. Passemar, $\eta \to 3\pi$: Study of the Dalitz plot and extraction of the quark mass ratio Q, Phys.Rev.Lett. 118 (2) (2017) 022001. arXiv:1610.03494, doi:10.1103/PhysRevLett.118.022001.
[343] G. Colangelo, S. Lanz, H. Leutwyler, E. Passemar, Dispersive analysis of $\eta \to 3\pi$, Eur.Phys.J. C78 (11) (2018) 947. arXiv:1807.11937, doi:10.1140/epjc/s10052-018-6377-9.
[344] M. Albaladejo, B. Moussallam, Extended chiral Khuri-Treiman formalism for $\eta \to 3\pi$ and the role of the $a_0(980)$, $f_0(980)$ resonances, Eur.Phys.J. C77 (2017) 508. arXiv:1702.04931, doi:10.1140/epjc/s10052-017-5052-x.
[345] J. Gasser, A. Rusetsky, Solving integral equations in $\eta \to 3\pi$, Eur.Phys.J. C78 (11) (2018) 906. arXiv:1809.06399, doi:10.1140/epjc/s10052-018-6378-8.

[346] F. Niecknig, B. Kubis, Dispersion-theoretical analysis of the $D^+ \to K^-\pi^+\pi^+$ Dalitz plot, JHEP 10 (2015) 142. arXiv:1509.03188, doi:10.1007/JHEP10(2015)142.
[347] F. Niecknig, B. Kubis, Consistent Dalitz plot analysis of Cabibbo-favored $D^+ \to \bar{K}\pi\pi^+$ decays, Phys.Lett. B780 (2017) 471–478. arXiv:1708.00446, doi:10.1016/j.physletb.2018.03.048.
[348] M. Froissart, Asymptotic behavior and subtractions in the Mandelstam representation, Phys.Rev. 123 (1961) 1053–1057. doi:10.1103/PhysRev.123.1053.
[349] A. Martin, Unitarity and high-energy behavior of scattering amplitudes, Phys.Rev. 129 (1963) 1432–1436. doi:10.1103/PhysRev.129.1432.
[350] S. Mandelstam, Unitarity Condition Below Physical Thresholds in the Normal and Anomalous Cases, Phys.Rev.Lett. 4 (1960) 84–87. doi:10.1103/PhysRevLett.4.84.
[351] C. Kacser, Analytic Structure of Partial-Wave Amplitudes for Production and Decay Processes, Phys.Rev. 132 (6) (1963) 2712. doi:10.1103/PhysRev.132.2712.
[352] I. J. R. Aitchison, Unitarity, Analyticity and Crossing Symmetry in Two- and Three-hadron Final State Interactions (2015). arXiv:1507.02697.
[353] J. Oller, Coupled-channel approach in hadron–hadron scattering, Prog.Part.Nucl.Phys. 110 (2020) 103728. arXiv:1909.00370, doi:10.1016/j.ppnp.2019.103728.
[354] S.-s. Fang, B. Kubis, A. Kupsc, What can we learn about light-meson interactions at electron-positron colliders?, Prog.Part.Nucl.Phys. 120 (2021) 103884. arXiv:2102.05922, doi:10.1016/j.ppnp.2021.103884.
[355] C. Terschlüsen, B. Strandberg, S. Leupold, F. Eichstädt, Reactions with pions and vector mesons in the sector of odd intrinsic parity, Eur.Phys.J. A49 (2013) 116. arXiv:1305.1181, doi:10.1140/epja/i2013-13116-6.
[356] M. Ablikim, et al., Dalitz Plot Analysis of the Decay $\omega \to \pi^+\pi^-\pi^0$, Phys.Rev. D98 (11) (2018) 112007. arXiv:1811.03817, doi:10.1103/PhysRevD.98.112007.
[357] T. W. B. Kibble, Kinematics of General Scattering Processes and the Mandelstam Representation, Phys.Rev. 117 (1960) 1159–1162. doi:10.1103/PhysRev.117.1159.
[358] P. Adlarson, et al., Measurement of the $\omega \to \pi^+\pi^-\pi^0$ Dalitz plot distribution, Phys.Lett. B770 (2017) 418–425. arXiv:1610.02187, doi:10.1016/j.physletb.2017.03.050.
[359] P. Adlarson, et al., Measurement of the $\omega \to \pi^0 e^+ e^-$ and $\eta \to e^+ e^- \gamma$ Dalitz decays with the A2 setup at MAMI, Phys.Rev. C95 (3) (2017) 035208. arXiv:1609.04503, doi:10.1103/PhysRevC.95.035208.
[360] R. Arnaldi, et al., Study of the electromagnetic transition form-factors in $\eta \to \mu^+\mu^-\gamma$ and $\omega \to \mu^+\mu^-\pi^0$ decays with NA60, Phys.Lett. B677 (2009) 260–266. arXiv:0902.2547, doi:10.1016/j.physletb.2009.05.029.
[361] R. Arnaldi, et al., Precision study of the $\eta \to \mu^+\mu^-\gamma$ and $\omega \to \mu^+\mu^-\pi^0$ electromagnetic transition form-factors and of the $\rho \to \mu^+\mu^-$ line shape in NA60, Phys.Lett. B757 (2016) 437–444. arXiv:1608.07898, doi:10.1016/j.physletb.2016.04.013.
[362] M. Ablikim, et al., Precision measurement of the branching fractions of $J/\psi \to \pi^+\pi^-\pi^0$ and $\psi' \to \pi^+\pi^-\pi^0$, Phys.Lett. B710 (2012) 594–599. arXiv:1202.2048, doi:10.1016/j.physletb.2012.03.036.
[363] JPAC Collaboration, in preparation (2022).
[364] J. Pelaez, A. Rodas, J. Ruiz De Elvira, Global parameterization of $\pi\pi$ scattering up to 2 GeV, Eur.Phys.J. C79 (12) (2019) 1008. arXiv:1907.13162, doi:10.1140/epjc/s10052-019-7509-6.
[365] J. M. Blatt, V. F. Weisskopf, Theoretical nuclear physics, Springer, New York, 1952. doi:10.1007/978-1-4612-9959-2.
[366] P. Guo, R. Mitchell, A. P. Szczepaniak, The Role of P-wave inelasticity in $J/\psi to \pi^+\pi^-\pi^0$, Phys.Rev. D82 (2010) 094002. arXiv:1006.4371, doi:10.1103/PhysRevD.82.094002.
[367] P. Guo, R. Mitchell, M. Shepherd, A. P. Szczepaniak, Amplitudes for the analysis of the decay $J/\psi \to K^+K^-\pi^0$, Phys.Rev. D85 (2012) 056003. arXiv:1112.3284, doi:10.1103/PhysRevD.85.056003.
[368] A. P. Szczepaniak, M. R. Pennington, Application of the Veneziano Model in Charmonium Dalitz Plot Analysis, Phys.Lett. B737 (2014) 283–288. arXiv:1403.5782, doi:10.1016/j.physletb.2014.08.060.
[369] H. Osborn, D. J. Wallace, η-X mixing, $\eta \to 3\pi$ and chiral lagrangians, Nucl.Phys. B20 (1970) 23–44. doi:10.1016/0550-3213(70)90194-X.
[370] J. Gasser, H. Leutwyler, Implications of scaling for the proton-neutron mass difference, Nucl.Phys. B94 (1975) 269–310. doi:10.1016/0550-3213(75)90493-9.
[371] S. Weinberg, The Problem of Mass, Trans.New York Acad.Sci. 38 (1977) 185–201. doi:10.1111/j.2164-0947.1977.tb02958.x.
[372] J. Gasser, H. Leutwyler, $\eta \to \pi$ to One Loop, Nucl.Phys. B250 (1985) 539–560. doi:10.1016/0550-3213(85)90494-8.
[373] J. F. Donoghue, B. R. Holstein, D. Wyler, Electromagnetic selfenergies of pseudoscalar mesons and Dashen's theorem, Phys.Rev. D47 (1993) 2089–2097. doi:10.1103/PhysRevD.47.2089.
[374] B. V. Martemyanov, V. S. Sopov, Light quark mass ratio from Dalitz plot of $\eta \to \pi^+\pi^-\pi^0$ decay, Phys.Rev. D71 (2005) 017501. arXiv:hep-ph/0502023, doi:10.1103/PhysRevD.71.017501.
[375] A. Kastner, H. Neufeld, The $K_{\ell 3}$ scalar form factors in the standard model, Eur.Phys.J. C57 (2008) 541–556. arXiv:0805.2222, doi:10.1140/epjc/s10052-008-0703-6.
[376] Y. Aoki, et al., FLAG Review 2021 (11 2021). arXiv:2111.09849.
[377] F. Ambrosino, et al., Determination of $\eta \to \pi^+\pi^-\pi^0$ Dalitz plot slopes and asymmetries with the KLOE detector, JHEP 05 (2008) 006. arXiv:0801.2642, doi:10.1088/1126-6708/2008/05/006.
[378] A. Anastasi, et al., Precision measurement of the $\eta \to \pi^+\pi^-\pi^0$ Dalitz plot distribution with the KLOE detector, JHEP 05 (2016) 019. arXiv:1601.06985, doi:10.1007/JHEP05(2016)019.
[379] M. Ablikim, et al., Measurement of the Matrix Elements for the Decays $\eta \to \pi^+\pi^-\pi^0$ and $\eta/\eta' \to \pi^0\pi^0\pi^0$, Phys.Rev. D92 (2015) 012014. arXiv:1506.05360, doi:10.1103/PhysRevD.92.012014.

[380] S. Prakhov, et al., High-statistics measurement of the $\eta \to 3\pi^0$ decay at the Mainz Microtron, Phys.Rev. C97 (6) (2018) 065203. arXiv:1803.02502, doi:10.1103/PhysRevC.97.065203.
[381] Probes for Fundamental QCD Symmetries and a Dark Gauge Boson via Light Meson Decays, Vol. CD15. doi:10.22323/1.253.0017.
[382] L. Gan, et al., Eta decays with emphasis on rare neutral modes: The jlab eta factory (jef) experiment, proposal approved by PAC42 (2014).
URL https://www.jlab.org/exp_prog/proposals/14/PR12-14-004.pdf
[383] J. Goity, J. Chen (Eds.), Photoproduction and Decay of Light Mesons in CLAS, Vol. CD12, 2013. doi:10.22323/1.172.0061.
[384] I. J. R. Aitchison, J. J. Brehm, Unitary Analytic Isobar Model for the Reaction Nucleon-Meson to Nucleon-Meson-Meson, Phys.Rev. D17 (1978) 3072. doi:10.1103/PhysRevD.17.3072.
[385] B. Ketzer, B. Grube, D. Ryabchikov, Light-Meson Spectroscopy with COMPASS, Prog.Part.Nucl.Phys. 113 (2020) 103755. arXiv:1909.06366, doi:10.1016/j.ppnp.2020.103755.
[386] C. Adolph, et al., Observation of a New Narrow Axial-Vector Meson $a_1(1420)$, Phys.Rev.Lett. 115 (8) (2015) 082001. arXiv:1501.05732, doi:10.1103/PhysRevLett.115.082001.
[387] G. D. Alexeev, et al., Triangle Singularity as the Origin of the $a_1(1420)$, Phys.Rev.Lett. 127 (8) (2021) 082501. arXiv:2006.05342, doi:10.1103/PhysRevLett.127.082501.
[388] M. G. Alexeev, et al., The exotic meson $\pi_1(1600)$ with $J^{PC} = 1^{-+}$ and its decay into $\rho(770)\pi$ (8 2021). arXiv:2108.01744.
[389] I. J. R. Aitchison, J. J. Brehm, Are there important unitary corrections to the isobar model?, Phys.Lett. 84B (1979) 349–353. doi:10.1016/0370-2693(79)90056-X.
[390] A. P. Szczepaniak, Triangle Singularities and XYZ Quarkonium Peaks, Phys.Lett. B747 (2015) 410–416. arXiv:1501.01691, doi:10.1016/j.physletb.2015.06.029.
[391] S. Nakamura, K. Tsushima, $Z_c(4430)$ and $Z_c(4200)$ as triangle singularities, Phys.Rev. D100 (5) (2019) 051502. arXiv:1901.07385, doi:10.1103/PhysRevD.100.051502.
[392] M. Luscher, Volume Dependence of the Energy Spectrum in Massive Quantum Field Theories. 2. Scattering States, Commun.Math.Phys. 105 (1986) 153–188. doi:10.1007/BF01211097.
[393] M. Lüscher, Two particle states on a torus and their relation to the scattering matrix, Nucl.Phys. B354 (1991) 531–578. doi:10.1016/0550-3213(91)90366-6.
[394] C. h. Kim, C. T. Sachrajda, S. R. Sharpe, Finite-volume effects for two-hadron states in moving frames, Nucl.Phys. B727 (2005) 218–243. arXiv:hep-lat/0507006, doi:10.1016/j.nuclphysb.2005.08.029.
[395] K. Rummukainen, S. A. Gottlieb, Resonance scattering phase shifts on a nonrest frame lattice, Nucl.Phys. B450 (1995) 397–436. arXiv:hep-lat/9503028, doi:10.1016/0550-3213(95)00313-H.
[396] C. Liu, X. Feng, S. He, Two particle states in a box and the S-matrix in multi-channel scattering, Int.J.Mod.Phys. A21 (2006) 847–850. arXiv:hep-lat/0508022, doi:10.1142/S0217751X06032150.
[397] N. Li, C. Liu, Generalized Lüscher formula in multichannel baryon-meson scattering, Phys.Rev. D87 (1) (2013) 014502. arXiv:1209.2201, doi:10.1103/PhysRevD.87.014502.
[398] L. Leskovec, S. Prelovsek, Scattering phase shifts for two particles of different mass and non-zero total momentum in lattice QCD, Phys.Rev. D85 (2012) 114507. arXiv:1202.2145, doi:10.1103/PhysRevD.85.114507.
[399] M. Lage, U.-G. Meissner, A. Rusetsky, A Method to measure the antikaon-nucleon scattering length in lattice QCD, Phys.Lett. B681 (2009) 439–443. arXiv:0905.0069, doi:10.1016/j.physletb.2009.10.055.
[400] S. He, X. Feng, C. Liu, Two particle states and the S-matrix elements in multi-channel scattering, JHEP 07 (2005) 011. arXiv:hep-lat/0504019, doi:10.1088/1126-6708/2005/07/011.
[401] X. Feng, X. Li, C. Liu, Two particle states in an asymmetric box and the elastic scattering phases, Phys.Rev. D70 (2004) 014505. arXiv:hep-lat/0404001, doi:10.1103/PhysRevD.70.014505.
[402] N. H. Christ, C. Kim, T. Yamazaki, Finite volume corrections to the two-particle decay of states with non-zero momentum, Phys.Rev. D72 (2005) 114506. arXiv:hep-lat/0507009, doi:10.1103/PhysRevD.72.114506.
[403] P. F. Bedaque, Aharonov-Bohm effect and nucleon nucleon phase shifts on the lattice, Phys.Lett. B593 (2004) 82–88. arXiv:nucl-th/0402051, doi:10.1016/j.physletb.2004.04.045.
[404] V. Bernard, M. Lage, U. G. Meißner, A. Rusetsky, Scalar mesons in a finite volume, JHEP 01 (2011) 019. arXiv:1010.6018, doi:10.1007/JHEP01(2011)019.
[405] M. T. Hansen, S. R. Sharpe, Multiple-channel generalization of Lellouch-Luscher formula, Phys.Rev. D86 (2012) 016007. arXiv:1204.0826, doi:10.1103/PhysRevD.86.016007.
[406] P. Guo, J. Dudek, R. Edwards, A. P. Szczepaniak, Coupled-channel scattering on a torus, Phys.Rev. D88 (1) (2013) 014501. arXiv:1211.0929, doi:10.1103/PhysRevD.88.014501.
[407] K. Polejaeva, A. Rusetsky, Three particles in a finite volume, Eur.Phys.J. A48 (2012) 67. arXiv:1203.1241, doi:10.1140/epja/i2012-12067-8.
[408] M. T. Hansen, S. R. Sharpe, Expressing the three-particle finite-volume spectrum in terms of the three-to-three scattering amplitude, Phys.Rev. D92 (11) (2015) 114509. arXiv:1504.04248, doi:10.1103/PhysRevD.92.114509.
[409] M. Mai, M. Döring, Three-body Unitarity in the Finite Volume, Eur.Phys.J. A53 (12) (2017) 240. arXiv:1709.08222, doi:10.1140/epja/i2017-12440-1.
[410] H.-W. Hammer, J.-Y. Pang, A. Rusetsky, Three-particle quantization condition in a finite volume: 1. The role of the three-particle force, JHEP 09 (2017) 109. arXiv:1706.07700, doi:10.1007/JHEP09(2017)109.
[411] H. W. Hammer, J. Y. Pang, A. Rusetsky, Three particle quantization condition in a finite volume: 2. general formalism and the analysis of data, JHEP 10 (2017) 115. arXiv:1707.02176, doi:10.1007/JHEP10(2017)115.
[412] T. D. Blanton, S. R. Sharpe, Alternative derivation of the relativistic three-particle quantization condition, Phys.Rev.

D102 (5) (2020) 054520. arXiv:2007.16188, doi:10.1103/PhysRevD.102.054520.
[413] M. T. Hansen, S. R. Sharpe, Relativistic, model-independent, three-particle quantization condition, Phys.Rev. D90 (11) (2014) 116003. arXiv:1408.5933, doi:10.1103/PhysRevD.90.116003.
[414] R. A. Briceño, M. T. Hansen, S. R. Sharpe, Relating the finite-volume spectrum and the two-and-three-particle S matrix for relativistic systems of identical scalar particles, Phys.Rev. D95 (7) (2017) 074510. arXiv:1701.07465, doi:10.1103/PhysRevD.95.074510.
[415] R. A. Briceño, M. T. Hansen, S. R. Sharpe, Three-particle systems with resonant subprocesses in a finite volume, Phys.Rev. D99 (1) (2019) 014516. arXiv:1810.01429, doi:10.1103/PhysRevD.99.014516.
[416] M. Mai, B. Hu, M. Döring, A. Pilloni, A. Szczepaniak, Three-body Unitarity with Isobars Revisited, Eur.Phys.J. A53 (2017) 177. arXiv:1706.06118, doi:10.1140/epja/i2017-12368-4.
[417] M. Döring, H. W. Hammer, M. Mai, J. Y. Pang, t. A. Rusetsky, J. Wu, Three-body spectrum in a finite volume: the role of cubic symmetry, Phys.Rev. D97 (11) (2018) 114508. arXiv:1802.03362, doi:10.1103/PhysRevD.97.114508.
[418] A. Jackura, C. Fernández-Ramírez, V. Mathieu, M. Mikhasenko, J. Nys, A. Pilloni, K. Saldaña, N. Sherrill, A. P. Szczepaniak, Phenomenology of Relativistic $\mathbf{3} \to \mathbf{3}$ Reaction Amplitudes within the Isobar Approximation, Eur.Phys.J. C79 (1) (2019) 56. arXiv:1809.10523, doi:10.1140/epjc/s10052-019-6566-1.
[419] S. M. Dawid, A. P. Szczepaniak, Bound states in the B-matrix formalism for the three-body scattering, Phys.Rev. D103 (1) (2021) 014009. arXiv:2010.08084, doi:10.1103/PhysRevD.103.014009.
[420] A. W. Jackura, S. M. Dawid, C. Fernández-Ramírez, V. Mathieu, M. Mikhasenko, A. Pilloni, S. R. Sharpe, A. P. Szczepaniak, Equivalence of three-particle scattering formalisms, Phys.Rev. D100 (3) (2019) 034508. arXiv:1905.12007, doi:10.1103/PhysRevD.100.034508.
[421] T. D. Blanton, S. R. Sharpe, Equivalence of relativistic three-particle quantization conditions, Phys.Rev. D102 (5) (2020) 054515. arXiv:2007.16190, doi:10.1103/PhysRevD.102.054515.
[422] M. T. Hansen, S. R. Sharpe, Lattice QCD and Three-particle Decays of Resonances, Ann.Rev.Nucl.Part.Sci. 69 (2019) 65–107. arXiv:1901.00483, doi:10.1146/annurev-nucl-101918-023723.
[423] M. Mai, M. Döring, A. Rusetsky, Multi-particle systems on the lattice and chiral extrapolations: a brief review, Eur.Phys.J. ST230 (6) (2021) 1623. arXiv:2103.00577, doi:10.1140/epjs/s11734-021-00146-5.
[424] M. T. Grisaru, Three-particle contributions to elastic scattering, Phys.Rev. 146 (1966) 1098–1106. doi:10.1103/PhysRev.146.1098.
[425] S. Mandelstam, J. Paton, R. Peierls, A. Sarker, Isobar approximation of production processes, Annals Phys. 18 (2) (1962) 198–225. doi:https://doi.org/10.1016/0003-4916(62)90067-2.
[426] D. R. Harrington, Two-particle approximation for the three-pion amplitude, Phys.Rev. 127 (1962) 2235–2240. doi:10.1103/PhysRev.127.2235.
[427] G. N. Fleming, Recoupling Effects in the Isobar Model. 1. General Formalism for Three-Pion Scattering, Phys.Rev. 135 (1964) B551–B560. doi:10.1103/PhysRev.135.B551.
[428] W. R. Frazer, D. Y. Wong, Width of three-pion resonances, Phys.Rev. 128 (1962) 1927–1929. doi:10.1103/PhysRev.128.1927.
[429] W. J. Holman, Modified isobar approximation for $\pi\rho$ scattering, Phys.Rev. 138 (1965) B1286–B1303. doi:10.1103/PhysRev.138.B1286.
[430] L. F. Cook, B. W. Lee, Unitarity and Production Amplitudes, Phys.Rev. 127 (1962) 283–296. doi:10.1103/PhysRev.127.283.
[431] J. S. Ball, W. R. Frazer, M. Nauenberg, Scattering and production amplitudes with unstable particles, in: High-energy physics. Proceedings, 11th International Conference, ICHEP'62, Geneva, Switzerland, Jul 4-11, 1962, 1962, pp. 141–143.
[432] R. C. Hwa, On the analytic structure of production amplitudes, Phys.Rev. 134 (1964) B1086–B1098. doi:10.1103/PhysRev.134.B1086.
[433] R. Blankenbecler, R. Sugar, Linear integral equations for relativistic multichannel scattering, Phys.Rev. 142 (1966) 1051–1059. doi:10.1103/PhysRev.142.1051.
[434] R. D. Amado, Minimal three-body scattering theory, Phys.Rev.Lett. 33 (1974) 333–336. doi:10.1103/PhysRevLett.33.333.
[435] R. Aaron, R. D. Amado, Analysis of three-hadron final states, Phys.Rev.Lett. 31 (1973) 1157–1159. doi:10.1103/PhysRevLett.31.1157.
[436] R. D. Amado, Minimal three-body equations with finite-range effects, Phys.Rev. C12 (1975) 1354–1357. doi:10.1103/PhysRevC.12.1354.
[437] R. Aaron, R. D. Amado, J. E. Young, Relativistic three-body theory with applications to πN scattering, Phys.Rev. 174 (1968) 2022–2032. doi:10.1103/PhysRev.174.2022.
[438] J. M. Greben, L. P. Kok, Three Particle Aspects in an N/D Approach to Nuclear Reactions, Phys.Rev. C13 (1976) 1352. doi:10.1103/PhysRevC.13.1352.
[439] D. Herndon, P. Soding, R. J. Cashmore, A generalized isobar model formalism, Phys.Rev. D11 (1975) 3165. doi:10.1103/PhysRevD.11.3165.
[440] M. Mai, B. Hu, M. Doring, A. Pilloni, A. Szczepaniak, Three-body scattering in isobar ansatz, PoS Hadron2017 (2018) 140. doi:10.22323/1.310.0140.
[441] D. Sadasivan, M. Mai, H. Akdag, M. Döring, Dalitz plots and lineshape of $a_1(1260)$ from a relativistic three-body unitary approach, Phys.Rev. D101 (9) (2020) 094018, [Erratum: Phys.Rev.D 103, 019901 (2021)]. arXiv:2002.12431, doi:10.1103/PhysRevD.101.094018.
[442] M. T. Hansen, S. R. Sharpe, Perturbative results for two and three particle threshold energies in finite volume, Phys.Rev. D93 (2016) 014506. arXiv:1509.07929, doi:10.1103/PhysRevD.93.014506.

[443] T. D. Blanton, F. Romero-López, S. R. Sharpe, Implementing the three-particle quantization condition including higher partial waves, JHEP 03 (2019) 106. arXiv:1901.07095, doi:10.1007/JHEP03(2019)106.
[444] M. T. Hansen, F. Romero-López, S. R. Sharpe, Generalizing the relativistic quantization condition to include all three-pion isospin channels, JHEP 07 (2020) 047, [Erratum: JHEP 02, 014 (2021)]. arXiv:2003.10974, doi:10.1007/JHEP07(2020)047.
[445] T. D. Blanton, S. R. Sharpe, Relativistic three-particle quantization condition for nondegenerate scalars, Phys.Rev. D103 (5) (2021) 054503. arXiv:2011.05520, doi:10.1103/PhysRevD.103.054503.
[446] T. D. Blanton, S. R. Sharpe, Three-particle finite-volume formalism for $\pi^+\pi^+K^+$ and related systems, Phys.Rev. D104 (3) (2021) 034509. arXiv:2105.12094, doi:10.1103/PhysRevD.104.034509.
[447] A. W. Jackura, R. A. Briceño, S. M. Dawid, M. H. E. Islam, C. McCarty, Solving relativistic three-body integral equations in the presence of bound states, Phys.Rev. D104 (1) (2021) 014507. arXiv:2010.09820, doi:10.1103/PhysRevD.104.014507.
[448] F. Romero-López, S. R. Sharpe, T. D. Blanton, R. A. Briceño, M. T. Hansen, Numerical exploration of three relativistic particles in a finite volume including two-particle resonances and bound states, JHEP 10 (2019) 007. arXiv:1908.02411, doi:10.1007/JHEP10(2019)007.
[449] M. T. Hansen, S. R. Sharpe, Threshold expansion of the three-particle quantization condition, Phys.Rev. D93 (9) (2016) 096006, [Erratum: Phys.Rev.D 96, 039901 (2017)]. arXiv:1602.00324, doi:10.1103/PhysRevD.93.096006.
[450] R. A. Briceño, M. T. Hansen, S. R. Sharpe, Numerical study of the relativistic three-body quantization condition in the isotropic approximation, Phys.Rev. D98 (1) (2018) 014506. arXiv:1803.04169, doi:10.1103/PhysRevD.98.014506.
[451] M. T. Hansen, S. R. Sharpe, Applying the relativistic quantization condition to a three-particle bound state in a periodic box, Phys.Rev. D95 (3) (2017) 034501. arXiv:1609.04317, doi:10.1103/PhysRevD.95.034501.
[452] R. A. Briceño, M. T. Hansen, S. R. Sharpe, A. P. Szczepaniak, Unitarity of the infinite-volume three-particle scattering amplitude arising from a finite-volume formalism, Phys.Rev. D100 (5) (2019) 054508. arXiv:1905.11188, doi:10.1103/PhysRevD.100.054508.
[453] P. F. Bedaque, H. W. Hammer, U. van Kolck, Renormalization of the three-body system with short range interactions, Phys.Rev.Lett. 82 (1999) 463. arXiv:nucl-th/9809025, doi:10.1103/PhysRevLett.82.463.
[454] C. Elster, W. Glockle, H. Witala, A New Approach to the 3D Faddeev Equation for Three-Body Scattering, Few Body Syst. 45 (2009) 1–10. arXiv:0807.1421, doi:10.1007/s00601-008-0003-6.
[455] V. Bernard, M. Lage, U.-G. Meißner, A. Rusetsky, Resonance properties from the finite-volume energy spectrum, JHEP 08 (2008) 024. arXiv:0806.4495, doi:10.1088/1126-6708/2008/08/024.
[456] M. Doring, U. G. Meißner, E. Oset, A. Rusetsky, Scalar mesons moving in a finite volume and the role of partial wave mixing, Eur.Phys.J. A48 (2012) 114. arXiv:1205.4838, doi:10.1140/epja/i2012-12114-6.
[457] M. Mai, M. Döring, C. Culver, A. Alexandru, Three-body unitarity versus finite-volume $\pi^+\pi^+\pi^+$ spectrum from lattice QCD, Phys.Rev. D101 (5) (2020) 054510. arXiv:1909.05749, doi:10.1103/PhysRevD.101.054510.
[458] M. Mai, A. Alexandru, R. Brett, C. Culver, M. Döring, F. X. Lee, D. Sadasivan, Three-body dynamics of the $a_1(1260)$ resonance from lattice QCD (7 2021). arXiv:2107.03973.
[459] W. Detmold, K. Orginos, M. J. Savage, A. Walker-Loud, Kaon Condensation with Lattice QCD, Phys.Rev. D78 (2008) 054514. arXiv:0807.1856, doi:10.1103/PhysRevD.78.054514.
[460] W. Detmold, M. J. Savage, A. Torok, S. R. Beane, T. C. Luu, K. Orginos, A. Parreno, Multi-Pion States in Lattice QCD and the Charged-Pion Condensate, Phys.Rev. D78 (2008) 014507. arXiv:0803.2728, doi:10.1103/PhysRevD.78.014507.
[461] B. Hörz, A. Hanlon, Two- and three-pion finite-volume spectra at maximal isospin from lattice QCD, Phys.Rev.Lett. 123 (14) (2019) 142002. arXiv:1905.04277, doi:10.1103/PhysRevLett.123.142002.
[462] C. Culver, M. Mai, R. Brett, A. Alexandru, M. Döring, Three body spectrum from lattice QCD, Phys.Rev. D101 (11) (2020) 114507. arXiv:1911.09047, doi:10.1103/PhysRevD.101.114507.
[463] M. Fischer, B. Kostrzewa, L. Liu, F. Romero-López, M. Ueding, C. Urbach, Scattering of two and three physical pions at maximal isospin from lattice QCD, Eur.Phys.J. C81 (5) (2021) 436. arXiv:2008.03035, doi:10.1140/epjc/s10052-021-09206-5.
[464] A. Alexandru, R. Brett, C. Culver, M. Döring, D. Guo, F. X. Lee, M. Mai, Finite-volume energy spectrum of the $K^-K^-K^-$ system, Phys.Rev. D102 (11) (2020) 114523. arXiv:2009.12358, doi:10.1103/PhysRevD.102.114523.
[465] M. T. Hansen, R. A. Briceño, R. G. Edwards, C. E. Thomas, D. J. Wilson, Energy-Dependent $\pi^+\pi^+\pi^+$ Scattering Amplitude from QCD, Phys.Rev.Lett. 126 (2021) 012001. arXiv:2009.04931, doi:10.1103/PhysRevLett.126.012001.
[466] T. D. Blanton, A. D. Hanlon, B. Hörz, C. Morningstar, F. Romero-López, S. R. Sharpe, Interactions of two and three mesons including higher partial waves from lattice QCD, JHEP 10 (2021) 023. arXiv:2106.05590, doi:10.1007/JHEP10(2021)023.
[467] M. Mai, M. Döring, Finite-volume spectrum of $\pi^+\pi^+$ and $\pi^+\pi^+\pi^+$ systems, Phys.Rev.Lett. 122 (6) (2019) 062503. arXiv:1807.04746, doi:10.1103/PhysRevLett.122.062503.
[468] R. Brett, C. Culver, M. Mai, A. Alexandru, M. Döring, F. X. Lee, Three-body interactions from the finite-volume QCD spectrum, Phys.Rev. D104 (1) (2021) 014501. arXiv:2101.06144, doi:10.1103/PhysRevD.104.014501.
[469] M. Mikhasenko, Three-pion dynamics at COMPASS: resonances, rescattering and non-resonant processes, Ph.D. thesis, U. Bonn (main) (2019).
[470] M. Davier, A. Höcker, B. Malaescu, C.-Z. Yuan, Z. Zhang, Update of the ALEPH non-strange spectral functions from hadronic τ decays, Eur.Phys.J. C74 (3) (2014) 2803. arXiv:1312.1501, doi:10.1140/epjc/s10052-014-2803-9.
[471] S. Schael, et al., Branching ratios and spectral functions of tau decays: Final ALEPH measurements and physics implications, Phys.Rept. 421 (2005) 191–284. arXiv:hep-ex/0506072, doi:10.1016/j.physrep.2005.06.007.
[472] C. Adolph, et al., Resonance Production and $\pi\pi$ S-wave in $\pi^- + p \to \pi^-\pi^-\pi^+ + p_{recoil}$ at 190 GeV/c, Phys.Rev. D95 (3)

(2017) 032004. arXiv:1509.00992, doi:10.1103/PhysRevD.95.032004.
[473] M. Mikhasenko, B. Ketzer, A. Sarantsev, Nature of the $a_1(1420)$, Phys.Rev. D91 (9) (2015) 094015. arXiv:1501.07023, doi:10.1103/PhysRevD.91.094015.
[474] F. Aceti, L. R. Dai, E. Oset, $a_1(1420)$ peak as the $\pi f_0(980)$ decay mode of the $a_1(1260)$, Phys.Rev. D94 (9) (2016) 096015. arXiv:1606.06893, doi:10.1103/PhysRevD.94.096015.
[475] E. Klempt, A. Zaitsev, Glueballs, Hybrids, Multiquarks. Experimental facts versus QCD inspired concepts, Phys.Rept. 454 (2007) 1–202. arXiv:0708.4016, doi:10.1016/j.physrep.2007.07.006.
[476] M. Mikhasenko, A. Jackura, B. Ketzer, A. Szczepaniak, Unitarity approach to the mass-dependent fit of 3π resonance production data from the COMPASS experiment, in: Proceedings, 12th Conference on Quark Confinement and the Hadron Spectrum (Confinement XII): Thessaloniki, Greece, Vol. 137, 2017, p. 05017. doi:10.1051/epjconf/201713705017.
[477] A. Jackura, M. Mikhasenko, A. Szczepaniak, Amplitude analysis of resonant production in three pions, in: Proceedings, 14th International Workshop on Meson Production, Properties and Interaction (MESON 2016): Cracow, Poland, June 2-7, 2016, Vol. 130, 2016, p. 05008. arXiv:1610.04567, doi:10.1051/epjconf/201613005008.
[478] R. T. Deck, Kinematical interpretation of the first $\pi\rho$ resonance, Phys.Rev.Lett. 13 (1964) 169–173. doi:10.1103/PhysRevLett.13.169.
[479] G. Ascoli, R. Cutler, L. M. Jones, U. Kruse, T. Roberts, B. Weinstein, H. W. Wyld, Deck-model calculation of $\pi^- p \to \pi^-\pi^+\pi^- p$, Phys.Rev. D9 (1974) 1963–1979. doi:10.1103/PhysRevD.9.1963.
[480] J. L. Basdevant, E. L. Berger, Unitary Coupled-Channel Analysis of Diffractive Production of the a_1 Resonance, Phys.Rev. D16 (1977) 657. doi:10.1103/PhysRevD.16.657.
[481] C. Hanhart, A New Parameterization for the Pion Vector Form Factor, Phys.Lett. B715 (2012) 170–177. arXiv:1203.6839, doi:10.1016/j.physletb.2012.07.038.
[482] L. Von Detten, F. Noël, C. Hanhart, M. Hoferichter, B. Kubis, On the scalar πK form factor beyond the elastic region, Eur.Phys.J. C81 (5) (2021) 420. arXiv:2103.01966, doi:10.1140/epjc/s10052-021-09169-7.
[483] J. C. Collins, D. E. Soper, G. F. Sterman, Factorization of Hard Processes in QCD, Adv.Ser.Direct.High Energy Phys. 5 (1989) 1–91. arXiv:hep-ph/0409313, doi:10.1142/9789814503266_0001.
[484] L. A. Harland-Lang, A. D. Martin, P. Motylinski, R. S. Thorne, Parton distributions in the LHC era: MMHT 2014 PDFs, Eur.Phys.J. C75 (5) (2015) 204. arXiv:1412.3989, doi:10.1140/epjc/s10052-015-3397-6.
[485] S. Dulat, T.-J. Hou, J. Gao, M. Guzzi, J. Huston, P. Nadolsky, J. Pumplin, C. Schmidt, D. Stump, C. P. Yuan, New parton distribution functions from a global analysis of quantum chromodynamics, Phys.Rev. D93 (3) (2016) 033006. arXiv:1506.07443, doi:10.1103/PhysRevD.93.033006.
[486] R. D. Ball, et al., Parton distributions from high-precision collider data, Eur.Phys.J. C77 (10) (2017) 663. arXiv:1706.00428, doi:10.1140/epjc/s10052-017-5199-5.
[487] E. Moffat, W. Melnitchouk, T. C. Rogers, N. Sato, Simultaneous Monte Carlo analysis of parton densities and fragmentation functions, Phys.Rev. D104 (1) (2021) 016015. arXiv:2101.04664, doi:10.1103/PhysRevD.104.016015.
[488] A. Accardi, L. T. Brady, W. Melnitchouk, J. F. Owens, N. Sato, Constraints on large-x parton distributions from new weak boson production and deep-inelastic scattering data, Phys.Rev. D93 (11) (2016) 114017. arXiv:1602.03154, doi:10.1103/PhysRevD.93.114017.
[489] N. Sato, C. Andres, J. J. Ethier, W. Melnitchouk, Strange quark suppression from a simultaneous Monte Carlo analysis of parton distributions and fragmentation functions, Phys.Rev. D101 (7) (2020) 074020. arXiv:1905.03788, doi:10.1103/PhysRevD.101.074020.
[490] S. Alekhin, J. Blümlein, S. Moch, R. Placakyte, Parton distribution functions, α_s, and heavy-quark masses for LHC Run II, Phys.Rev. D96 (1) (2017) 014011. arXiv:1701.05838, doi:10.1103/PhysRevD.96.014011.
[491] M. Abele, D. de Florian, W. Vogelsang, Approximate NNLO QCD corrections to semi-inclusive DIS (9 2021). arXiv:2109.00847.
[492] T. Liu, W. Melnitchouk, J.-W. Qiu, N. Sato, A new approach to semi-inclusive deep-inelastic scattering with QED and QCD factorization (8 2021). arXiv:2108.13371.
[493] G. Veneziano, Construction of a crossing-symmetric, Regge behaved amplitude for linearly rising trajectories, Nuovo Cim. A57 (1968) 190–197. doi:10.1007/BF02824451.
[494] G. Veneziano, An Introduction to Dual Models of Strong Interactions and Their Physical Motivations, Phys.Rept. 9 (1974) 199–242. doi:10.1016/0370-1573(74)90027-1.
[495] G. Rossi, G. Veneziano, The string-junction picture of multiquark states: an update, JHEP 06 (2016) 041. arXiv:1603.05830, doi:10.1007/JHEP06(2016)041.
[496] R. P. Feynman, What neutrinos can tell us about partons., in: 1st Europhysics Conference on Neutrinos – Neutrino '72 Balatonfured, Hungary, June 11-17, 1972, Vol. C720611, 1972, pp. 75–100.
[497] G. R. Farrar, D. R. Jackson, Pion and Nucleon Structure Functions Near x=1, Phys.Rev.Lett. 35 (1975) 1416. doi:10.1103/PhysRevLett.35.1416.
[498] F. E. Close, A. W. Thomas, The Spin and Flavor Dependence of Parton Distribution Functions, Phys.Lett. B212 (1988) 227–230. doi:10.1016/0370-2693(88)90530-8.
[499] W. Melnitchouk, A. W. Thomas, Neutron/proton structure function ratio at large x, Phys.Lett. B377 (1996) 11–17. arXiv:nucl-th/9602038, doi:10.1016/0370-2693(96)00292-4.
[500] L. T. Brady, A. Accardi, T. J. Hobbs, W. Melnitchouk, Next-to leading order analysis of target mass corrections to structure functions and asymmetries, Phys.Rev. D84 (2011) 074008, [Erratum: Phys.Rev.D85, 039902 (2012)]. arXiv:1108.4734, doi:10.1103/PhysRevD.84.074008.
[501] J. F. Owens, A. Accardi, W. Melnitchouk, Global parton distributions with nuclear and finite-Q^2 corrections, Phys.Rev. D87 (9) (2013) 094012. arXiv:1212.1702, doi:10.1103/PhysRevD.87.094012.

[502] E. R. Nocera, Small- and large-x nucleon spin structure from a global QCD analysis of polarized Parton Distribution Functions, Phys.Lett. B742 (2015) 117–125. arXiv:1410.7290, doi:10.1016/j.physletb.2015.01.021.
[503] E. Moffat, T. C. Rogers, W. Melnitchouk, N. Sato, F. Steffens, What does kinematical target mass sensitivity in DIS reveal about hadron structure?, Phys.Rev. D99 (9) (2019) 096008. arXiv:1901.09016, doi:10.1103/PhysRevD.99.096008.
[504] P. Jimenez-Delgado, W. Melnitchouk, J. F. Owens, Parton momentum and helicity distributions in the nucleon, J.Phys. G40 (2013) 093102. arXiv:1306.6515, doi:10.1088/0954-3899/40/9/093102.
[505] J. Gao, L. Harland-Lang, J. Rojo, The Structure of the Proton in the LHC Precision Era, Phys.Rept. 742 (2018) 1–121. arXiv:1709.04922, doi:10.1016/j.physrep.2018.03.002.
[506] J. J. Ethier, E. R. Nocera, Parton Distributions in Nucleons and Nuclei, Ann.Rev.Nucl.Part.Sci. 70 (2020) 43–76. arXiv:2001.07722, doi:10.1146/annurev-nucl-011720-042725.
[507] A. N. Hiller Blin, et al., Nucleon resonance contributions to unpolarised inclusive electron scattering, Phys.Rev. C100 (3) (2019) 035201. arXiv:1904.08016, doi:10.1103/PhysRevC.100.035201.
[508] A. N. Hiller Blin, W. Melnitchouk, V. I. Mokeev, V. D. Burkert, V. V. Chesnokov, A. Pilloni, A. P. Szczepaniak, Resonant contributions to inclusive nucleon structure functions from exclusive meson electroproduction data, Phys.Rev. C104 (2) (2021) 025201. arXiv:2105.05834, doi:10.1103/PhysRevC.104.025201.
[509] M. Osipenko, et al., A Kinematically complete measurement of the proton structure function F_2 in the resonance region and evaluation of its moments, Phys.Rev. D67 (2003) 092001. arXiv:hep-ph/0301204, doi:10.1103/PhysRevD.67.092001.
[510] Y. Liang, et al., Measurement of $R = \sigma_L/\sigma_T$ and the separated longitudinal and transverse structure functions in the nucleon resonance region (2004). arXiv:nucl-ex/0410027.
[511] M. E. Christy, P. E. Bosted, Empirical fit to precision inclusive electron-proton cross sections in the resonance region, Phys.Rev. C81 (2010) 055213. arXiv:0712.3731, doi:10.1103/PhysRevC.81.055213.
[512] S. P. Malace, et al., Applications of quark-hadron duality in F_2 structure function, Phys.Rev. C80 (2009) 035207. arXiv:0905.2374, doi:10.1103/PhysRevC.80.035207.
[513] Y. Prok, et al., Precision measurements of g_1 of the proton and the deuteron with 6 GeV electrons, Phys.Rev. C90 (2) (2014) 025212. arXiv:1404.6231, doi:10.1103/PhysRevC.90.025212.
[514] V. Tvaskis, et al., Measurements of the separated longitudinal structure function F_L from hydrogen and deuterium targets at low Q^2, Phys.Rev. C97 (4) (2018) 045204. arXiv:1606.02614, doi:10.1103/PhysRevC.97.045204.
[515] A. A. Golubenko, V. V. Chesnokov, B. S. Ishkhanov, V. I. Mokeev, Evaluation of the inclusive electron scattering observables in the resonance region from the experimental data, Phys.Part.Nucl. 50 (5) (2019) 587–592. arXiv:1902.02900, doi:10.1134/S1063779619050083.
[516] Structure functions and cross-sections Database, http://clas.sinp.msu.ru/strfun/.
URL http://clas.sinp.msu.ru/strfun/
[517] E. D. Bloom, F. J. Gilman, Scaling, Duality, and the Behavior of Resonances in Inelastic electron-Proton Scattering, Phys.Rev.Lett. 25 (1970) 1140. doi:10.1103/PhysRevLett.25.1140.
[518] S. Forte, L. Magnea, Truncated moments of parton distributions, Phys.Lett. B448 (1999) 295–302. arXiv:hep-ph/9812479, doi:10.1016/S0370-2693(99)00065-9.
[519] S. Forte, L. Magnea, A. Piccione, G. Ridolfi, Evolution of truncated moments of singlet parton distributions, Nucl.Phys. B594 (2001) 46–70. arXiv:hep-ph/0006273, doi:10.1016/S0550-3213(00)00670-2.
[520] A. Piccione, Solving the Altarelli-Parisi equations with truncated moments, Phys.Lett. B518 (2001) 207–213. arXiv:hep-ph/0107108, doi:10.1016/S0370-2693(01)01059-0.
[521] D. Kotlorz, A. Kotlorz, Evolution equations for truncated moments of the parton distributions, Phys.Lett. B644 (2007) 284–287. arXiv:hep-ph/0610282, doi:10.1016/j.physletb.2006.11.054.
[522] D. Kotlorz, A. Kotlorz, Analysis of DIS structure functions of the nucleon within truncated Mellin moments approach, Int.J.Mod.Phys. A31 (34) (2016) 1650181. arXiv:1607.08397, doi:10.1142/S0217751X16501815.
[523] X.-D. Ji, P. Unrau, Parton-hadron duality: Resonances and higher twists, Phys.Rev. D52 (1995) 72–77. arXiv:hep-ph/9408317, doi:10.1103/PhysRevD.52.72.
[524] A. Psaker, W. Melnitchouk, M. E. Christy, C. Keppel, Quark-hadron duality and truncated moments of nucleon structure functions, Phys.Rev. C78 (2008) 025206. arXiv:0803.2055, doi:10.1103/PhysRevC.78.025206.
[525] A. De Rujula, H. Georgi, H. D. Politzer, Demythification of Electroproduction, Local Duality and Precocious Scaling, Annals Phys. 103 (1977) 315. doi:10.1016/S0003-4916(97)90003-8.
[526] D. Drechsel, B. Pasquini, M. Vanderhaeghen, Dispersion relations in real and virtual Compton scattering, Phys.Rept. 378 (2003) 99–205. arXiv:hep-ph/0212124, doi:10.1016/S0370-1573(02)00636-1.
[527] L. Hand, Experimental investigation of pion electroproduction, Phys.Rev. 129 (1963) 1834–1846. doi:10.1103/PhysRev.129.1834.
[528] V. D. Burkert, Jefferson Lab at 12 GeV: The Science Program, Ann.Rev.Nucl.Part.Sci. 68 (2018) 405–428. doi:10.1146/annurev-nucl-101917-021129.
[529] CLAS Physics Database, https://clasweb.jlab.org/physicsdb/.
URL https://clasweb.jlab.org/physicsdb/
[530] D. S. Carman, K. Joo, V. I. Mokeev, Strong QCD Insights from Excited Nucleon Structure Studies with CLAS and CLAS12, Few Body Syst. 61 (3) (2020) 29. arXiv:2006.15566, doi:10.1007/s00601-020-01563-3.
[531] V. I. Mokeev, Two Pion Photo- and Electroproduction with CLAS, EPJ Web Conf. 241 (2020) 03003. doi:10.1051/epjconf/202024103003.
[532] I. G. Aznauryan, V. D. Burkert, Electroexcitation of nucleon resonances, Prog.Part.Nucl.Phys. 67 (2012) 1–54. arXiv:1109.1720, doi:10.1016/j.ppnp.2011.08.001.
[533] C. E. Carlson, N. C. Mukhopadhyay, Bloom-Gilman duality in the resonance spin structure functions, Phys.Rev. D58

(1998) 094029. arXiv:hep-ph/9801205, doi:10.1103/PhysRevD.58.094029.
[534] W. Melnitchouk, R. Ent, C. Keppel, Quark-hadron duality in electron scattering, Phys.Rept. 406 (2005) 127–301. arXiv:hep-ph/0501217, doi:10.1016/j.physrep.2004.10.004.
[535] Strong QCD from Hadron Structure Experiments, Vol. E29. arXiv:2006.06802, doi:10.1142/S0218301320300064.
[536] J. Nys, A. Hiller Blin, V. Mathieu, C. Fernández-Ramírez, A. Jackura, A. Pilloni, J. Ryckebusch, A. Szczepaniak, G. Fox, Global analysis of charge exchange meson production at high energies, Phys.Rev. D98 (3) (2018) 034020. arXiv:1806.01891, doi:10.1103/PhysRevD.98.034020.
[537] V. Mathieu, G. Fox, A. P. Szczepaniak, Neutral Pion Photoproduction in a Regge Model, Phys.Rev. D92 (7) (2015) 074013. arXiv:1505.02321, doi:10.1103/PhysRevD.92.074013.
[538] V. Mathieu, I. V. Danilkin, C. Fernández-Ramírez, M. R. Pennington, D. Schott, A. P. Szczepaniak, G. Fox, Toward Complete Pion Nucleon Amplitudes, Phys.Rev. D92 (7) (2015) 074004. arXiv:1506.01764, doi:10.1103/PhysRevD.92.074004.
[539] J. Nys, V. Mathieu, C. Fernández-Ramírez, A. N. Hiller Blin, A. Jackura, M. Mikhasenko, A. Pilloni, A. P. Szczepaniak, G. Fox, J. Ryckebusch, Finite-energy sum rules in eta photoproduction off a nucleon, Phys.Rev. D95 (3) (2017) 034014. arXiv:1611.04658, doi:10.1103/PhysRevD.95.034014.
[540] V. Mathieu, J. Nys, C. Fernández-Ramírez, A. N. Hiller Blin, A. Jackura, A. Pilloni, A. P. Szczepaniak, G. Fox, Structure of Pion Photoproduction Amplitudes, Phys.Rev. D98 (2018) 014041. arXiv:1806.08414.
[541] V. Mathieu, J. Nys, C. Fernández-Ramírez, A. Jackura, A. Pilloni, N. Sherrill, A. P. Szczepaniak, G. Fox, Vector Meson Photoproduction with a Linearly Polarized Beam, Phys.Rev. D97 (9) (2018) 094003. arXiv:1802.09403, doi:10.1103/PhysRevD.97.094003.
[542] A. Austregesilo, Spin-density matrix elements for vector meson photoproduction at GlueX, AIP Conf. Proc. 2249 (1) (2020) 030005. arXiv:1908.07275, doi:10.1063/5.0008585.
[543] V. Mathieu, J. Nys, C. Fernández-Ramírez, A. Jackura, M. Mikhasenko, A. Pilloni, A. P. Szczepaniak, G. Fox, On the η and η' Photoproduction Beam Asymmetry at High Energies, Phys.Lett. B774 (2017) 362–367. arXiv:1704.07684, doi:10.1016/j.physletb.2017.09.081.
[544] V. Mathieu, A. Pilloni, M. Albaladejo, L. Bibrzycki, A. Celentano, C. Fernández-Ramírez, A. Szczepaniak, Exclusive tensor meson photoproduction, Phys.Rev. D102 (1) (2020) 014003. arXiv:2005.01617, doi:10.1103/PhysRevD.102.014003.
[545] J. Nys, V. Mathieu, C. Fernández-Ramírez, A. Jackura, M. Mikhasenko, A. Pilloni, N. Sherrill, J. Ryckebusch, A. P. Szczepaniak, G. Fox, Features of $\pi\Delta$ Photoproduction at High Energies, Phys.Lett. B779 (2018) 77–81. arXiv:1710.09394, doi:10.1016/j.physletb.2018.01.075.
[546] J. Dudek, et al., Physics Opportunities with the 12 GeV Upgrade at Jefferson Lab, Eur.Phys.J. A48 (2012) 187. arXiv:1208.1244, doi:10.1140/epja/i2012-12187-1.
[547] M. Battaglieri, et al., Jlab approved experiment e12-11-005, https://www.jlab.org/exp_prog/proposals/11/PR12-11-005.pdf (2011).
[548] M. Battaglieri, et al., JLab approved experiment E12-11-005: Meson Spectroscopy with low Q^2 electron scattering in CLAS12 (2011).
[549] H. Al Ghoul, et al., First Results from The GlueX Experiment, AIP Conf.Proc. 1735 (2016) 020001. arXiv:1512.03699, doi:10.1063/1.4949369.
[550] J. Ballam, et al., Vector Meson Production by Polarized Photons at 2.8 GeV, 4.7 GeV, and 9.3 GeV, Phys.Rev. D7 (1973) 3150. doi:10.1103/PhysRevD.7.3150.
[551] S. Adhikari, et al., Measurement of beam asymmetry for $\pi^-\Delta^{++}$ photoproduction on the proton at E_γ=8.5 GeV, Phys.Rev. C103 (2) (2021) L022201. arXiv:2009.07326, doi:10.1103/PhysRevC.103.L022201.
[552] S. Adhikari, et al., Beam Asymmetry $\mathbf{\Sigma}$ for the Photoproduction of η and η' Mesons at $\mathbf{E}_\gamma = \mathbf{8.8}$GeV, Phys.Rev. C100 (5) (2019) 052201. arXiv:1908.05563, doi:10.1103/PhysRevC.100.052201.
[553] M. C. Kunkel, et al., Exclusive photoproduction of π^0 up to large values of Mandelstam variables s, t and u with CLAS, Phys.Rev. C98 (1) (2018) 015207. arXiv:1712.10314, doi:10.1103/PhysRevC.98.015207.
[554] M. Carver, et al., Photoproduction of the $f_2(1270)$ meson using the CLAS detector, Phys.Rev.Lett. 126 (8) (2021) 082002. arXiv:2010.16006, doi:10.1103/PhysRevLett.126.082002.
[555] A. Celentano, et al., First measurement of direct photoproduction of the $a_2(1320)^0$ meson on the proton, Phys.Rev. C102 (3) (2020) 032201. arXiv:2004.05359, doi:10.1103/PhysRevC.102.032201.
[556] V. Kubarovsky, M. B. Voloshin, Formation of hidden-charm pentaquarks in photon-nucleon collisions, Phys.Rev. D92 (3) (2015) 031502. arXiv:1508.00888, doi:10.1103/PhysRevD.92.031502.
[557] Q. Wang, X.-H. Liu, Q. Zhao, Photoproduction of hidden charm pentaquark states $P_c^+(4380)$ and $P_c^+(4450)$, Phys.Rev. D92 (2015) 034022. arXiv:1508.00339, doi:10.1103/PhysRevD.92.034022.
[558] M. Karliner, J. L. Rosner, Photoproduction of Exotic Baryon Resonances, Phys.Lett. B752 (2016) 329–332. arXiv:1508.01496, doi:10.1016/j.physletb.2015.11.068.
[559] X.-Y. Wang, X.-R. Chen, J. He, Possibility to study pentaquark states $P_c(4312), P_c(4440)$ and $P_c(4457)$ in $\gamma p \to J/\psi p$ reaction, Phys.Rev. D99 (11) (2019) 114007. arXiv:1904.11706, doi:10.1103/PhysRevD.99.114007.
[560] A. Ali, et al., First measurement of near-threshold J/ψ exclusive photoproduction off the proton, Phys.Rev.Lett. 123 (7) (2019) 072001. arXiv:1905.10811, doi:10.1103/PhysRevLett.123.072001.
[561] D. Winney, C. Fanelli, A. Pilloni, A. N. Hiller Blin, C. Fernández-Ramírez, M. Albaladejo, V. Mathieu, V. I. Mokeev, A. P. Szczepaniak, Double polarization observables in pentaquark photoproduction, Phys.Rev. D100 (3) (2019) 034019. arXiv:1907.09393, doi:10.1103/PhysRevD.100.034019.
[562] R. Aaij, et al., Model-independent evidence for $J/\psi p$ contributions to $\Lambda_b^0 \to J/\psi p K^-$ decays, Phys.Rev.Lett. 117 (8)

(2016) 082002. arXiv:1604.05708, doi:10.1103/PhysRevLett.117.082002.
[563] Z. E. Meziani, et al., A Search for the LHCb Charmed 'Pentaquark' using Photo-Production of J/ψ at Threshold in Hall C at Jefferson Lab (2016). arXiv:1609.00676.
[564] S. Stepanyan, et al., JLab approved experiment E12-12-001A, JLab approved experiment E12-12-001A (2017).
[565] D. Barberis, et al., Experimental evidence for a vector like behavior of Pomeron exchange, Phys.Lett. B467 (1999) 165–170. arXiv:hep-ex/9909013, doi:10.1016/S0370-2693(99)01186-7.
[566] L. Lesniak, A. P. Szczepaniak, Theoretical model of the ϕ meson photoproduction amplitudes, Acta Phys.Polon. B34 (2003) 3389–3400. arXiv:hep-ph/0304007.
[567] S. Chekanov, et al., Exclusive photoproduction of J/ψ mesons at HERA, Eur.Phys.J. C24 (2002) 345–360. arXiv:hep-ex/0201043, doi:10.1007/s10052-002-0953-7.
[568] A. Aktas, et al., Elastic J/ψ production at HERA, Eur.Phys.J. C46 (2006) 585–603. arXiv:hep-ex/0510016, doi:10.1140/epjc/s2006-02519-5.
[569] U. Camerini, J. G. Learned, R. Prepost, C. M. Spencer, D. E. Wiser, W. Ash, R. L. Anderson, D. Ritson, D. Sherden, C. K. Sinclair, Photoproduction of the ψ Particles, Phys.Rev.Lett. 35 (1975) 483. doi:10.1103/PhysRevLett.35.483.
[570] C. Fanelli, L. Pentchev, B. Wojtsekhowski, Measurement of the parameters of the LHCb pentaquark states through double polarization asymmetries with SBS in Hall A, LoI12-18-001 (PAC 46) (2018).
URL https://www.jlab.org/exp_prog/proposals/18/LOI12-18-001.pdf
[571] M. Albaladejo, A. N. Hiller Blin, A. Pilloni, D. Winney, C. Fernández-Ramírez, V. Mathieu, A. Szczepaniak, XYZ spectroscopy at electron-hadron facilities: Exclusive processes, Phys.Rev. D102 (2020) 114010. arXiv:2008.01001, doi:10.1103/PhysRevD.102.114010.
[572] X. Cao, F.-K. Guo, Y.-T. Liang, J.-J. Wu, J.-J. Xie, Y.-P. Xie, Z. Yang, B.-S. Zou, Photoproduction of hidden-bottom pentaquark and related topics, Phys.Rev. D101 (7) (2020) 074010. arXiv:1912.12054, doi:10.1103/PhysRevD.101.074010.
[573] A. Accardi, et al., Electron Ion Collider: The Next QCD Frontier: Understanding the glue that binds us all, Eur.Phys.J. A52 (9) (2016) 268. arXiv:1212.1701, doi:10.1140/epja/i2016-16268-9.
[574] R. Abdul Khalek, et al., Science Requirements and Detector Concepts for the Electron-Ion Collider: EIC Yellow Report (3 2021). arXiv:2103.05419.
[575] D. P. Anderle, et al., Electron-ion collider in China, Front.Phys. 16 (6) (2021) 64701. arXiv:2102.09222, doi:10.1007/s11467-021-1062-0.
[576] C. Adloff, et al., Diffractive photoproduction of $\psi(2S)$ mesons at HERA, Phys.Lett. B541 (2002) 251–264. arXiv:hep-ex/0205107, doi:10.1016/S0370-2693(02)02275-X.
[577] L. Landau, On the angular momentum of a system of two photons, Dokl.Akad.Nauk SSSR 60 (2) (1948) 207–209. doi:10.1016/B978-0-08-010586-4.50070-5.
[578] C.-N. Yang, Selection Rules for the Dematerialization of a Particle Into Two Photons, Phys.Rev. 77 (1950) 242–245. doi:10.1103/PhysRev.77.242.
[579] Y. Teramoto, et al., Evidence for $X(3872) \to J/\psi\pi^+\pi^-$ Produced in Single-Tag Two-Photon Interactions, Phys.Rev.Lett. 126 (12) (2021) 122001. arXiv:2007.05696, doi:10.1103/PhysRevLett.126.122001.
[580] C. Li, C.-Z. Yuan, Determination of the absolute branching fractions of $X(3872)$ decays, Phys.Rev. D100 (9) (2019) 094003. arXiv:1907.09149, doi:10.1103/PhysRevD.100.094003.
[581] R. D. Field, G. C. Fox, Triple Regge and Finite Mass Sum Rule Analysis of the Inclusive Reaction $pp \to pX$, Nucl.Phys. B80 (1974) 367–402. doi:10.1016/0550-3213(74)90495-7.
[582] R. Brower, C. E. DeTar, J. Weis, Regge Theory for Multiparticle Amplitudes, Phys.Rept. 14 (1974) 257. doi:10.1016/0370-1573(74)90012-X.
[583] I. Drummond, P. Landshoff, W. Zakrzewski, The two-reggeon/particle coupling, Nucl.Phys. B11 (1969) 383–405. doi:10.1016/0550-3213(69)90088-1.
[584] N. F. Bali, G. F. Chew, A. Pignotti, Multiple-Production Theory Via Toller Variables, Phys.Rev.Lett. 19 (1967) 614–618. doi:10.1103/PhysRevLett.19.614.
[585] I. Drummond, P. Landshoff, W. Zakrzewski, Signature in production amplitudes, Phys.Lett. B28 (1969) 676–678. doi:10.1016/0370-2693(69)90220-2.
[586] J. Weis, Singularities in complex angular momentum and helicity, Phys.Rev. D6 (1972) 2823–2841. doi:10.1103/PhysRevD.6.2823.
[587] T. Shimada, A. D. Martin, A. C. Irving, Double Regge Exchange Phenomenology, Nucl.Phys. B142 (1978) 344–364. doi:10.1016/0550-3213(78)90209-2.
[588] M. Shi, I. V. Danilkin, C. Fernández-Ramírez, V. Mathieu, M. R. Pennington, D. Schott, A. P. Szczepaniak, Double-Regge Exchange Limit for the $\gamma p \to K^+K^-p$ Reaction, Phys.Rev. D91 (3) (2015) 034007. arXiv:1411.6237, doi:10.1103/PhysRevD.91.034007.
[589] P. Lebiedowicz, O. Nachtmann, A. Szczurek, Central exclusive diffractive production of $K^+K^-K^+K^-$ via the intermediate $\phi\phi$ state in proton-proton collisions, Phys.Rev. D99 (9) (2019) 094034. arXiv:1901.11490, doi:10.1103/PhysRevD.99.094034.
[590] P. Lebiedowicz, J. Leutgeb, O. Nachtmann, A. Rebhan, A. Szczurek, Central exclusive diffractive production of axial-vector $f_1(1285)$ and $f_1(1420)$ mesons in proton-proton collisions, Phys.Rev. D102 (11) (2020) 114003. arXiv:2008.07452, doi:10.1103/PhysRevD.102.114003.
[591] A. Cisek, A. Szczurek, Two-gluon production of ϕ and η' mesons in proton-proton collisions at high energies, Phys.Rev. D103 (2021) 114008. arXiv:2103.08954, doi:10.1103/PhysRevD.103.114008.
[592] V. Mathieu, J. Nys, A. Pilloni, C. Fernández-Ramírez, A. Jackura, M. Mikhasenko, V. Pauk, A. Szczepaniak, G. Fox,

Analyticity Constraints for Hadron Amplitudes: Going High to Heal Low Energy Issues, Europhys.Lett. 122 (4) (2018) 41001. arXiv:1708.07779, doi:10.1209/0295-5075/122/41001.

[593] I. Ambats, D. S. Ayres, R. Diebold, A. F. Greene, S. L. Kramer, A. Lesnik, D. R. Rust, C. E. W. Ward, A. B. Wicklund, D. D. Yovanovitch, Comparison of particle-antiparticle elastic scattering from 3 to 6 GeV/c, Phys.Rev.Lett. 29 (1972) 1415–1419. doi:10.1103/PhysRevLett.29.1415.

[594] W. Braunschweig, W. Erlewein, H. Frese, K. Luebelsmeyer, H. Meyer-Wachsmuth, D. Schmitz, A. Schultz Von Dratzig, G. Wessels, Single photoproduction of η mesons on hydrogen in the forward direction at 4 and 6 GeV, Phys.Lett. B33 (1970) 236–240. doi:10.1016/0370-2693(70)90583-6.

[595] J. Dewire, B. Gittelman, R. Loe, E. C. Loh, D. J. Ritchie, R. A. Lewis, Photoproduction of η mesons from hydrogen, Phys.Lett. B37 (1971) 326–328. doi:10.1016/0370-2693(71)90030-X.

[596] R. L. Workman, M. W. Paris, W. J. Briscoe, I. I. Strakovsky, Unified Chew-Mandelstam SAID analysis of pion photoproduction data, Phys.Rev. C86 (2012) 015202. arXiv:1202.0845, doi:10.1103/PhysRevC.86.015202.

[597] W.-T. Chiang, S.-N. Yang, L. Tiator, D. Drechsel, An Isobar model for eta photoproduction and electroproduction on the nucleon, Nucl.Phys. A700 (2002) 429–453. arXiv:nucl-th/0110034, doi:10.1016/S0375-9474(01)01325-2.